NASA Contractor Report 3740

240

Radiative Properties of Advanced Spacecraft Heat Shield Materials

G. R. Cunnington, A. I. Funai,
and T. K. McNab

CONTRACT NAS1-16423
NOVEMBER 1983

BEST DOCUMENT AVAILABLE

NASA-2-3740

NASA Contractor Report 3740

Radiative Properties of Advanced Spacecraft Heat Shield Materials

G. R. Cunnington, A. I. Funai,
and T. K. McNab
Lockheed Missiles and Space Company, Inc.
Palo Alto, California

Prepared for
Langley Research Center
under Contract NAS1-16423

National Aeronautics
and Space Administration

**Scientific and Technical
Information Branch**

1983

BLANK PAGE

FOREWORD

This document was prepared by the Lockheed Palo Alto Research Laboratories (LPARL) of the Lockheed Missiles and Space Company, Inc., for the Langley Research Center of the National Aeronautics and Space Administration as the final report of the research activities carried out under Contract NAS1-16423 from October 1980 through September 1982. The research was to define the effects of simulated reentry exposure conditions on the thermal emittance properties of statically oxidized Inconel 617 and Haynes alloy 188 (HS188) and coated columbium and to relate any changes in radiative properties to morphology and chemistry of the surface oxides and the coating.

The NASA project Manager was Dr. Ronald K. Clark, Langley Research Center. The Lockheed Program Manager was Mr. George R. Cunnington. The authors gratefully acknowledge the following persons for their special assistance and services during the program: Mr. E. Fretter of Aerotherm Division, Acurex Corporation, for arc plasma testing; Mr. Ian Ward and Mr. R. J. Blattner of Charles Evans Associates for Auger electron spectroscopy; Dr. Carl Lampert of Lawrence Berkeley Laboratory, University of California, for Auger electron and secondary ion mass spectrometry; Mr. John Robinson and Ms. Andrea Ambrosia of LPARL for x-ray diffraction and Auger electron spectroscopy studies; Mr. George Martin of LPARL for electron microprobe studies; and Mr. Lawrence Gilliam of LPARL for emittance measurements.

ABSTRACT

Experimental results are presented to show the effects of simulated reentry exposure by convective heating and by radiant heating on spectral and total emittance of statically oxidized Inconel 617 and Haynes HS188 superalloys to 1260 K and a silicide coated (R512E) columbium 752 alloy to 1590 K. Convective heating exposures were conducted in a supersonic arc plasma wind tunnel using a wedge-shaped specimen configuration. Radiant tests were conducted at a pressure of 3×10^{-3} atmospheres of dry air at a flow velocity of several meters per second. Convective heating specimens were subjected to 8, 20, and 38 15-min heating cycles, and radiant heating specimens were tested for 10, 20, 50, and 100 30-min heating cycles. Changes in radiative properties are explained in terms of changes in composition resulting from simulated reentry tests.

The methods used to evaluate morphological, compositional and crystallographic changes include: Auger Electron Spectroscopy (AES); Scanning Electron Microscopy (SEM); X-Ray Diffraction Analysis (XRDA); and Electron Microprobe (EP) analysis. Total normal emittance of oxidized Inconel 617 and HS188 did not significantly change from the statically oxidized conditions after either exposure. Total normal emittance of both materials remained above 0.80 at 1260 K. Significant spectral changes were observed at wavelengths less than 2.0 μm and greater than 15 μm, but these had no significant influence on total emittance at 1260 K. The changes in radiative properties were qualitatively correlated to compositional changes observed after the exposure cycles.

CONTENTS

Section		Page
	FOREWORD	iii
	ABSTRACT	iv
	ILLUSTRATIONS	vii
	TABLES	xiii
	NOMENCLATURE	xv
1	INTRODUCTION AND SUMMARY	1
2	SAMPLE PREPARATION	3
	2.1 Test Specimen Geometry	3
	2.2 Static Oxidation Procedure	3
	2.3 R512E Coating on Columbium 752	7
3	EXPERIMENTAL APPARATUS AND PROCEDURES	12
	3.1 Supersonic Arc Plasma Wind Tunnel	12
	3.2 Radiant Heating Apparatus	16
	3.3 Emittance Apparatus	18
	3.4 Reflectance Apparatus	25
	3.5 Morphological and Compositional Analysis	26
	3.5.1 Imaging	26
	3.5.2 Compositional Analysis	26
	3.5.3 Oxide Layer Thickness	27
4	EXPERIMENTAL RESULTS	29
	4.1 Simulated Reentry Exposures	29
	4.1.1 Supersonic Arc Plasma Wind Tunnel Tests	29
	4.1.2 Radiant Heating Tests	35
	4.1.3 Sonic Velocity-Cold Air Tests	37
	4.2 Radiative Properties	39
	4.2.1 Stability of Specimens in HTEA	39
	4.2.2 Inconel 617 Simulated Reentry Tests	45
	4.2.3 HS188 Simulated Reentry Tests	65
	4.2.4 R512E Coated Cb752 Simulated Reentry Tests	68
	4.3 Morphology, Composition, and Structure	72
	4.3.1 Inconel 617	76
	4.3.2 Haynes 188	106
	4.3.3 R512E Coated Cb752	128
5	DISCUSSION AND RECOMMENDATIONS	136
	5.1 Thermal Radiative Properties	136
	5.2 Oxide Layers on Inconel 617 and HS188	139
	5.3 Recommendations	141
	5.3.1 Environmental Stability	142
	5.3.2 Thermal Radiative Properties	142
6	CONCLUSIONS	143
7	REFERENCES	144

Section		Page
Appendix		
A	SUMMARY OF TEST CONDITIONS AND SPECIMEN TEMPERATURES FOR ARC PLASMA TESTING	A-1
B	EMITTANCE AND REFLECTANCE DATA FOR OXIDIZED INCONEL 617 AND HS188 AND R512E COATED COLUMBIUM 752	B-1

ILLUSTRATIONS

Figure		Page
1	Specimen design for convective heating tests	5
2	Visual appearance of statically oxidized superalloy specimens	6
3	Room temperature (294 K) spectral normal reflectance of statically oxidized Inconel 617 and HS188	9
4	Visual appearances of R512E coated Cb752 specimens	10
5	Room temperature (294 K) spectral normal reflectance of R512E coated Cb752 before simulated reentry testing . . .	11
6	Schematic of Acurex 1 MW supersonic arc plasma wind tunnel	13
7	Acurex calibration wedge showing locations of instrumentation	14
8	Configuration of sample holder for convective heating tests	15
9	Radiant heating apparatus	17
10	High temperature emittance apparatus (HTEA)	19
11	HTEA sample mounting	19
12	Schematic of optical system of HTEA	22
13	Schematic of oxide thickness measurement using the cylindrical grinding technique	28
14	Visual representation of surface temperature gradients during supersonic arc plasma wind tunnel testing	34
15	Typical post-exposure appearance of supersonic arc plasma wind tunnel specimens	36
16	Supersonic arc plasma wind tunnel specimen showing a typical test failure	37
17	Schematic of sonic velocity cold air test	38
18	Comparison of room temperature spectral reflectance data for statically oxidized Inconel 617 with reflectance computed from elevated temperature spectral emittance data	43

Figure		Page
19	Comparison of room temperature spectral reflectance data for statically oxidized HS188 with reflectance computed from elevated temperature spectral emittance data	44
20	Comparison of pre- and post-HETA test room temperature spectral reflectance data for R512E coated columbium 752 . . .	48
21	Total normal emittance of Inconel 617 as a function of temperature for the statically oxidized and reentry simulation test specimens	50
22	Spectral normal emittance of statically oxidized Inconel 617 as a function of temperature	50
23	Spectral normal emittance of Inconel 617 as a function of temperature for 20 and 38 cycle supersonic arc plasma wind tunnel tests	51
24	Spectral normal emittance of Inconel 617 as a function of temperature for 10, 50, and 100 cycle radiant heating tests	51
25	Temperature dependence of spectral normal emittance of Inconel 617 after simulated reentry tests	53
26	Room temperature (294 K) spectral normal reflectance of statically oxidized Inconel 617 after radiant heating tests and measurement in the HTEA	56
27	Room temperature (294 K) spectral normal reflectance of statically oxidized Inconel 617 after supersonic arc plasma wind tunnel tests and measurement in the HTEA	57
28	Room temperature (294 K) spectral normal reflectance of statically oxidized Inconel 617 and plasma sprayed Cr_2O_3	58
29	Spectral normal emittance of statically oxidized Inconel 617 at 1260 K after simulated reentry tests	59
30	Spectral normal emittance of statically oxidizeu Inconel specimens 617-2 and 617-3 after arc plasma wind tunnel testing, stagnation flow	63
31	Room temperature (294 K) spectral normal reflectance of statically oxidized Inconel 617 specimens before and after testing in an arc plasma wind tunnel, stagnation model	64

Figure		Page
32	Change in total normal emittance of statically oxidized HS188 at 1260 K with exposure time in supersonic arc plasma wind tunnel and radiant heating tests	66
33	Temperature dependence of total normal emittance of statically oxidized HS188 after supersonic arc plasma wind tunnel tests	67
34	Spectral normal emittance of statically oxidized HS188 at 1260 K before and after supersonic arc plasma wind tunnel and radiant heating tests	67
35	Temperature dependence of spectral normal emittance of statically oxidized HS188	69
36	Temperature dependence of spectral normal emittance of statically oxidized HS188 after supersonic arc plasma wind tunnel tests	69
37	Room temperature (294 K) spectral normal reflectance of statically oxidized HS188 after supersonic arc plasma wind tunnel tests	70
38	Room temperature (294 K) spectral normal reflectance of statically oxidized HS188 after radiant heating tests	71
39	Spectral normal emittance of R512E coated Cb752 at 1260 K, no simulated reentry exposure	73
40	Spectral normal emittance of R512E coated Cb752 at 1590 K, no simulated reentry exposure	73
41	Spectral normal emittance of R512E coated Cb752 at 1260 K after supersonic arc plasma wind tunnel and radiant heating tests	74
42	Spectral normal emittance of R512E coated Cb752 at 1590 K after supersonic arc plasma wind tunnel and radiant heating tests	74
43	Room temperature (294 K) spectral normal reflectance of R512E coated Cb752 after reentry and HTEA testing	75
44	Surface of Inconel 617 before static oxidation at 2000X . . .	77
45	Surface of statically oxidized Inconel 617	78

Figure		Page
46	Photomicrographs of cylindrical grinding region on surface of statically oxidized Inconel 617	79
47	Boundary layer surface of statically oxidized Inconel 617 after 8 cycles in supersonic arc plasma wind tunnel	81
48	Rear surface of statically oxidized Inconel 617 after 8 cycles in supersonic arc plasma wind tunnel	82
49	Boundary layer surface of statically oxidized Inconel 617 after 20 cycles in supersonic arc plasma wind tunnel	85
50	Boundary layer and rear surfaces of statically oxidized Inconel 617 after 38 cycles in supersonic arc plasma wind tunnel	86
51	Photomicrographs of cylindrical grinding regions on surfaces of statically oxidized Inconel 617 after 38 cycles in supersonic arc plasma wind tunnel	87
52	Boundary layer surface of statically oxidized Inconel 617 after 8 h at 1260 K in supersonic arc plasma wind tunnel, stagnation model low enthalpy test (specimen 617-2)	89
53	Boundary layer surface of statically oxidized Inconel 617 after 8 h at 1260 K in arc plasma wind tunnel, stagnation model high enthalpy test (specimen 617-3)	90
54	Cross section photomicrographs of Inconel 617 supersonic arc plasma wind tunnel test specimens	91
55	Photomicrographs of surface of statically oxidized Inconel 617 after 100 radiant heating cycles	91
56	AES depth profile of statically oxidized Inconel 617	95
57	AES depth profile of statically oxidized Inconel 617 after 20 radiant heating test cycles.	97
58	AES depth profile of boundary layer surface of statically oxidized Inconel 617 after 8 supersonic arc plasma wind tunnel test cycles	98
59	AES depth profile of rear surface of statically oxidized Inconel 617 after 8 supersonic arc plasma wind tunnel test cycles	98

Figure		Page
60	AES depth profile of boundary layer surface of oxidized Inconel 617 after 38 supersonic arc plasma wind tunnel test cycles	99
61	AES depth profile of rear surface of statically oxidized Inconel 617 after 38 supersonic arc plasma wind tunnel test cycles	100
62	Inconel 617 oxide layer chromium, cobalt, nickel, and titanium concentrations as a function of reentry test condition . . .	101
63	SIMS depth profile of statically oxidized Inconel 617	103
64	Surface topography of statically oxidized HS188	107
65	Photomicrographs of cylindrical grinding region on the surface of statically oxidized HS188.	109
66	Boundary layer surface of statically oxidized HS188 after 8 cycles in supersonic arc plasma wind tunnel	110
67	Boundary layer surface of statically oxidized HS188 after 38 cycles in supersonic arc plasma wind tunnel	110
68	Rear surface of statically oxidized HS188 after 8 cycles in supersonic arc plasma wind tunnel	111
69	Rear surface of statically oxidized HS188 after 38 cycles in supersonic arc plasma wind tunnel	111
70	Surface of statically oxidized HS188 after 20 radiant heating test cycles	112
71	Photomicrographs of the cylindrical grinding areas on both surfaces of the HS188 38 cycle supersonic arc plasma wind tunnel test specimen	113
72	EP analysis locations for the statically oxidized HS188 specimen.	117
73	EP Analysis locations for boundary layer surface of the HS188 38 cycle supersonic arc plasma wind tunnel test specimen	117
74	SIMS depth profiles of statically oxidized HS188	119
75	AES deptn profile of statically oxidized HS188	120

Figure		Page
76	AES depth profiles of the HS188 8 cycle supersonic arc plasma wind test specimen	121
77	AES depth profile of the HS188 20 cycle supersonic arc plasma wind tunnel test specimen, boundary layer surface . .	122
78	AES depth profiles of the HS188 38 cycle supersonic arc plasma wind tunnel test specimen	123
79	SIMS depth profile of the HS188 8 cycle supersonic arc plasma wind tunnel test specimen, boundary layer surface . .	124
80	SIMS depth profile of the HS188 20 cycle supersonic arc plasma wind tunnel test specimen, boundary layer surface . .	124
81	SIMS depth profile of the HS188 38 cycle supersonic arc plasma wind tunnel test specimen, boundary layer surface . .	125
82	Determination of the cobalt oxide/nickel oxide ratio in the HS188 mixed metal oxide phase using the Taylor-Sinclair function method	127
83	SEM images of surface of R512E coated Cb752 (as prepared)	129
84	SEM images of boundary layer surface of R512E coated Cb752 after 8 cycles in supersonic arc plasma wind tunnel	130
85	SEM images of the boundary layer surface of R512E coated Cb752 after 20 test cycles in supersonic arc plasma wind tunnel	130
86	SEM images of the boundary layer surface of R512E coated Cb752 after 38 test cycles in supersonic arc plasma wind tunnel	131
87	Calculated optical constants for Cr_2O_3	138
88	Comparison of spectral reflectance calculated for Cr_2O_3 (from optical constants) with data measured for statically oxidized Inconel 617 and HS188	139

TABLES

Table		Page
1	High Temperature Alloys	4
2	Vendor's Compositional Analysis of Inconel 617 and Haynes 188	4
3	Compositional Analysis of Oxide on Statically Oxidized Inconel 617 and HS188	8
4	Total Normal Emittance of Statically Oxidized Inconel 617 and HS188 as Calculated From Spectral Reflectance Measurements at 294 K	8
5	Instrumentation for Supersonic Arc Plasma Wind Tunnel Tests	16
6	Argon Gas Analysis	21
7	Calculated Boundary Layer Edge Conditions for Supersonic Arc Plasma Wind Tunnel Tests	30
8	Wedge-Specimen Position and Cycle History of Supersonic Arc Plasma Wind Tunnel Tests	32
9	Summary of Supersonic Arc Plasma Wind Tunnel Tests	33
10	Spectral Normal Emittance Data for Statically Oxidized Inconel 617 After Exposures for 90 min in the HTEA at 1367 K	40
11	Spectral Normal Emittance Data for Statically Oxidized HS188 After Exposures for 90 min in the HTEA	41
12	Change in Total Normal Emittance of Statically Oxidized Inconel 617 and HS188 After 90 min Exposures at 1260 K and 1367 K in Several Types of Atmosphere in the HTEA	46
13	Change in Spectral Normal and Total Normal Emittance of R512E Coated Cb752 in Dried Air and Argon Atmospheres After 90 min Exposures at 1590 K in the HTEA	47
14	Total Normal Emittance of Statically Oxidized Inconel 617 After Simulated Reentry Tests	52
15	Comparison of Directly Measured Total Normal Emittance With Total Normal Emittance Calculated by Integration of Spectral Normal Emittance Data for Statically Oxidized Inconel 617	61

Table		Page
16	Total Hemispherical Emittance and Total Directional Emittance of Statically Oxidized Inconel 617	61
17	Total Normal Emittance of Statically Oxidized HS188 at 1260 K as a Function of Exposure Time in Supersonic Arc Plasma Wind Tunnel and Radiant Heating Tests	66
18	Total Normal Emittance of R512E Columbium 752 as a Function of Type of Simulated Reentry Test and Number of Test Cycles	72
19	Relative Line Intensities for Electron Microprobe Analysis of Surface of Statically Oxidized Inconel 617	80
20	Relative Line Intensities for Electron Microprobe Analysis of Boundary Layer and Rear Surfaces of Statically Oxidized Inconel 617 Specimen After 8 Supersonic Arc Plasma Wind tunnel cycles	84
21	Overall Thickness and Oxide Layer Thickness Data for Inconel 617 Specimens	93
22	X-Ray Diffraction Analysis of Inconel 617 Specimens	104
23	Overall Thickness and Oxide Layer Thickness Data for HS188 Specimens	115
24	Relative Line Intensities for Electron Microprobe Analysis of HS188 Specimens	116
25	Quantitative EP Analysis of HS188 Oxide Layers	118
26	X-Ray Diffraction Analysis of HS188 Specimens	126
27	Overall Thickness Data for R512E Coated Cb752 Specimens . . .	133
28	Elemental Surface Analyses of R512E Coated Cb752 After Supersonic Arc Plasma Wind Tunnel Tests	134
29	AES Intensity Ratios for R512E Coated Cb752	135

NOMENCLATURE

Å	angstrom
A	area
a_o	lattice parameter
C_H	heat transfer coefficient
E	blackbody radiance
F	optical transfer coefficient
H	enthalpy
h	responsivity
I	current
P	power loss
q	heat flux
T	absolute temperature
V	voltage
ε	emittance
θ	angle measured from normal to surface
λ	wavelength
μ	thickness
ρ	reflectance
σ	Stefan-Boltzmann constant
τ	transmittance

Subscripts

a	ambient
b	blackbody
c	chamber, convective
N	normal
o	stream
s	signal, system, sample
TH	total hemispherical
TN	total normal
w	window, wall
θ	angle
λ	wavelength

Section 1

INTRODUCTION AND SUMMARY

The metallic heat shield is a promising concept for the radiatively cooled thermal protection system (TPS) for reusable advanced space transportation system vehicles (ref. 1) and hypersonic aircraft (ref. 2). Because of their high temperature strength properties and excellent long-term oxidation resistance the nickel-chromium and cobalt base superalloys (refs. 3 and 4) and coated refractory metals (ref. 5) are attractive candidates for the external surface of the TPS.

In addition to these properties, materials used in a radiatively cooled TPS must have a high value of total hemispherical emittance at elevated temperature. The reusability aspect further imposes the requirement of high stability of emittance for many flights (100 or more). Inconel 617 and HS188 superalloys, and columbium 752 meet the high-temperature strength criteria. The oxide layers formed during static oxidation of these superalloys have a relatively high emittance value and impart excellent oxidation resistance to the base metal. Some of the silicide base coatings have a high emittance and give acceptable oxidation resistance to the columbium alloy (refs. 6 and 7). However, the stability of the thermal radiative properties of these surfaces after multiple exposures to earth reentry conditions has not been demonstrated.

The purpose of this research study was to experimentally evaluate the effects of simulated reentry exposures on the thermal emittance properties of Inconel 617 and HS188, starting with an initial statically oxidized surface, and a columbium silicide coating (designated as R512E) fused on columbium 752 alloy and subsequently oxidized in air. Two reentry simulation facilities were used; one, a supersonic arc plasma wind tunnel and, two, a radiant heating facility using low-velocity air. The radiant apparatus was used to evaluate the utility of a low-cost exposure test for studies of radiative properties stability. Multiple cycle tests were conducted in both environments and the results compared in terms of spectral emittance and surface composition and morphology at equivalent exposure times. Convective heating tests were run for 8, 20, and 38 cycles, each of 15 min duration in the supersonic arc plasma wind tunnel stream followed by 15 min of cooling. Radiant tests were 10, 20, 50, and 100 cycles of 30 min heating and 30 min cooling. The results from the supersonic arc plasma wind tunnel were used as the baseline as this is a much better simulation of the environment parameters of surface mass flux, boundary layer species, and surface shear.

The data show differences in spectral emittance of the materials between the two types of exposure. However, total normal emittance (ϵ_{TN}) at maximum temperature was relatively insensitive to exposure conditions because of a consistency of spectral emittance in the 2- to 10-μm region. For statically oxidized Inconel 617, total normal emittance at 1260 K was greater than 0.84, and it increased by increments ranging from 0.02 to 0.06 with subsequent exposures. For HS188, ϵ_{TN} was 0.81 or greater at 1260 K, with little change

after the various exposure tests. Similar results were observed for the coated Cb752 specimens with $\epsilon_{TN} \geq 0.81$ at 1590 K after exposure tests. Compositional and morphological differences were observed between specimens tested in the two types of environments. A significant visual appearance change occurred for all materials after supersonic arc plasma wind tunnel testing. The Inconel 617 specimens changed from a uniform gray color to a blue-green with several brownish areas. The HS188 went from a uniform gray to a black appearance with a soot-like outer surface layer. The coated Cb752 generally darkened with mottled areas of yellow to red-brown. Appearance of the specimens did not change significantly with radiant testing.

Section 2

SAMPLE PREPARATION

The materials investigated in this program were selected by NASA and specified in the Contract Statement of Work. A description and an analysis of the alloys used to prepare test specimens are given in Tables 1 and 2, respectively. The static oxidation procedure used to initially oxidize the Inconel 617 and HS188 specimens was specified by NASA. The silicide coating for the columbium 752 alloy was recommended by LMSC on the basis of prior simulated environmental exposure results for this system (refs. 6 and 7). Test specimen geometry and oxidation/coating procedures are discussed in the following subsections.

2.1 TEST SPECIMEN GEOMETRY

Two specimen configurations were used for the environmental exposure tests. Radiant exposure specimens were flat strips 188 mm long by 25.4 mm wide which fit directly into the electrode clamps of the high temperature emittance apparatus (HTEA). Specimens for the convective heating tests (arc plasma) were in the form of 96.5 mm wide by 108 mm long plates having 9.6 mm deep flanged edges (figure 1) that fit into the test wedge specimen holder and are secured by tungsten pins.

For the post-convective exposure emittance measurements in the HTEA, a strip specimen 25.4 mm wide by 96 mm long was cut from the plate in the location shown by Note A of figure 2. Specimen cutting was done dry with a hand held rotary tool and a diamond blade. The spanwise specimen was chosen to give a more isothermal exposure area for emittance measurement. To accommodate the electrode clamp spacing of the HTEA, extender bars of the same material (statically oxidized) and cross-sectional dimensions as the test specimen were heliarc welded to each end. The heat-effected zone at a weld extended less than 5 mm diameter from the joint and did not approach the emittance measurement area of the specimen. A similar procedure was used for the 25.4 mm diameter specimens of Inconel 617 that were tested by Langley Research Center.

2.2 STATIC OXIDATION PROCEDURE

The fabricated test specimens were cleaned with trichloroethylene in an ultrasonic bath then rinsed with acetone followed by hot water and ethanol and then forced-air dried. Oxidation of both Inconel 617 and HS188 specimens was carried out in a nearly static atmosphere of dried air in an electrically heated alumina lined furnace. Air to the furnace was dried to <1 ppm by passing it through a column of P_2O_5. The furnace temperature was stabilized at 1256 K prior to insertion of the cleaned specimens, which were supported on alumina rods during oxidization and cooling. After 12 h at 1256 ± 3 K, the specimens were removed and allowed to cool to ambient temperature. Only one alloy was oxidized at a time to minimize the possibility of cross-contamination .

Table 1. High Temperature Alloys

Alloy	Supplier	Heat No.	As Received Condition
Inconel 617	Castle Metals	XX01A4UK	Smooth clean surface, annealed
	Castle Metals	XX04A8UK (Huntington)	Smooth clean surface, annealed
Haynes Alloy 188 (HS188)	Stellite Div., Cabot. Corp.	1880-00159	Smooth clean surface, annealed and cooled in dry H_2
Columbium Alloy Cb752	Teledyne, Wah Chang	Not known	Smooth clean surface, annealed, 100 percent recrystallized, average ASTM grain size 8

Table 2. Vendor's Compositional Analysis of Inconel 617 and Haynes 188

	Composition (weight percent)		
	Inconel 617		
Element	XX01A4UK	XX04A8UK	HS188
Cr	21.6	22.4	22.1
Ni	53.6	55.5	23.4
Co	12.2	11.0	37.5
Mn	0.04	0.03	0.7
Mo	10.0	8.3	----
Fe	1.5	0.3	1.7
Ti	----	0.3	----
Al	1.0	0.9	----
Si	0.1	0.2	0.4
La	----	----	0.05
Cb	----	----	----
W	----	----	14.1

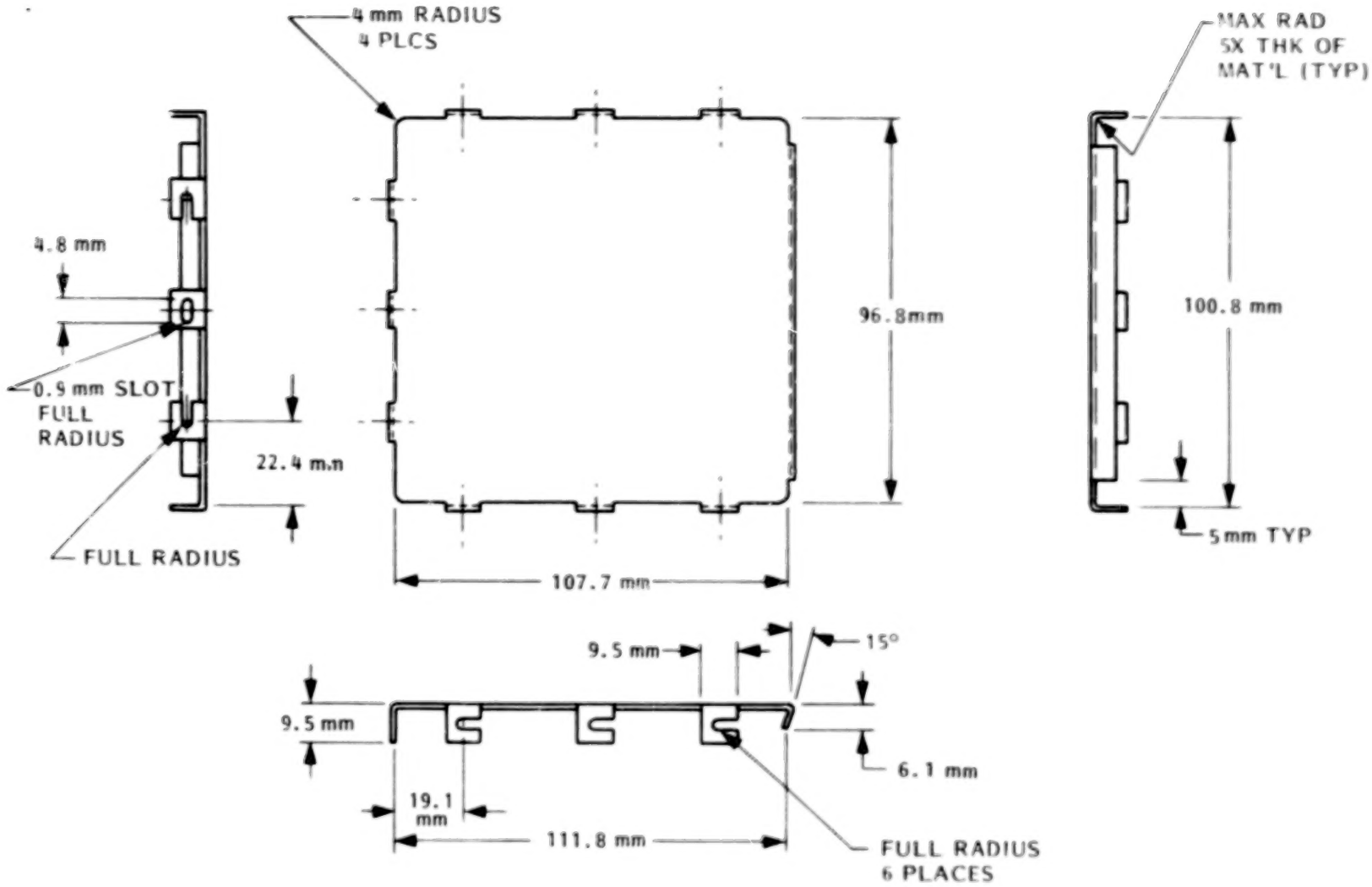

Figure 1. Specimen design for convective heating tests.

BEST DOCUMENT AVAILABLE

BEST DOCUMENT AVAILABLE

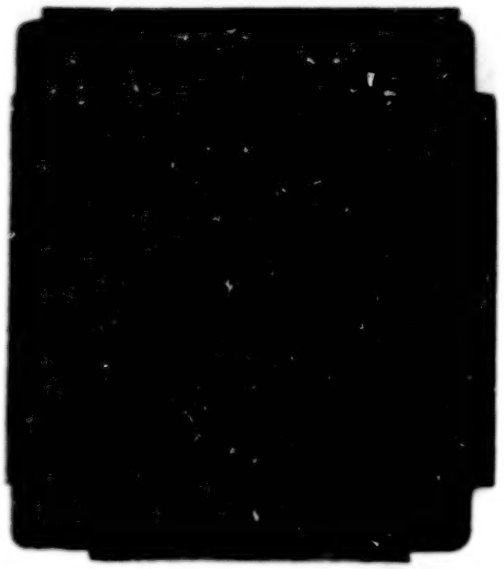

(a) Inconel 617 wedge specimen A

(b) HS188 wedge specimen E

Figure 2. Visual appearance of statically oxidized superalloy specimens.

Figure 2 shows statically oxidized specimens of the two superalloys. Both are a relatively uniform dark dull-gray color with the Inconel 617 having a slightly blue-gray tone. No visual evidence of any spalling of the oxide for either alloy was observed. Cross sectional micrographs show a 3 to 4 μm thick oxide layer for Inconel 617 and a 1 to 2 μm thick oxide for the HS188. Bulk oxide layer elemental compositions are given in Table 3. Inconel 617 shows a chromium rich oxide with significant amounts of nickel, whereas the HS188 oxide layer is cobalt rich. A detailed discussion of the oxide compositions is given in section 4.3.

Measurements of near normal spectral reflectance were made at room temperature on statically oxidized witness disks; the data are summarized in figure 3. The curves shown are the average values of three specimens of each superalloy. All data fell within ±0.03 of the average. Reflectance of the Inconel 617 is significantly lower than that of the HS188 specimens in the 2 to 12 μm region. This should result in a higher emittance for Inconel 617 at elevated temperatures. The reflectance data for HS188 are similar to those reported in reference 7 for this alloy oxidized in air for 3 h at 1310 K. Integration of the spectral reflectance data for several blackbody temperatures gives the total normal emittance values as a function of temperature that are shown in Table 4. Assuming no changes in the spectral optical constants with increasing temperatures, the total emittance of statically oxidized Inconel 617 would be greater than the design goal of 0.80 at 1260 K, whereas the statically oxidized HS188 total emittance would be significantly lower than the goal.

2.3 R512E COATING ON COLUMBIUM 752

The columbium 752 specimens were prepared for coating by pickling for 30 to 60 s in a solution of two parts nitric acid, two parts sulfuric acid, and one part hydrofluoric acid at room temperature. The specimens were then slurry coated with the basic R512E coating mix as follows:

60 g chromium powder - 200 mesh
60 g iron powder - 200 mesh
180 g silicon powder - 200 mesh
42 cm^3 nitrocellulose solution (Superior Finishes, Grade 200-2, A. H. Thompson Co., Berkeley, California)
82 cm^3 acetone
12 g Baker MPA60 (Baker Castor Oil Co., Bavonne, New Jersey)

The ingredients were blended into a slurry by ball milling for 30 min. Each specimen was then dip coated to obtain a green coating weight (air dried) of 0.20 to 0.25 kg/m^2. The green coating was then fused by heating for 30 min at 1690 K in a vacuum of 1×10^{-3} Pa. The specimens were brought to fusion temperature at a rate of 50 K/min. After fusion, the specimens were heated in air at atmospheric pressure for 15 min at 1645 K. The fused coating thickness is 0.07 to 0.10 mm. After coating, the specimens were inspected with a low power (15x) binocular microscope to ensure they were free of large edge fissures and coating defects. The coating and firing procedure has been used for several years at LMSC for the coating of missile propulsion system components.

Table 3. Compositional Analysis of Oxide on Statically Oxidized Inconel 617 and HS188

Element	Concentration* (atomic percent)	
	Inconel 617	HS188
O	52.8	44.2
Cr	30.7	12.2
Ni	10.2	7.4
Co	2.3	29.4
Mn	0.6	5.0
Mo	0.06	----
Fe	1.0	1.1
Ti	2.2	----
Si	----	0.1
La	----	0.1
Al	0.2	0.3
W	----	0.2

*Quantitative electron beam microprobe analysis

Table 4. Total Normal Emittance of Statically Oxidized Inconel 617 and HS188 as Calculated from Spectral Reflectance Masurements at 294 K

Temperature (K)	Total Normal Emittance	
	Inconel 617	HS188
294	0.67	0.51
533	0.76	0.53
811	0.80	0.59
1089	0.83	0.66
1255	0.94	0.68
1367	0.84	0.70

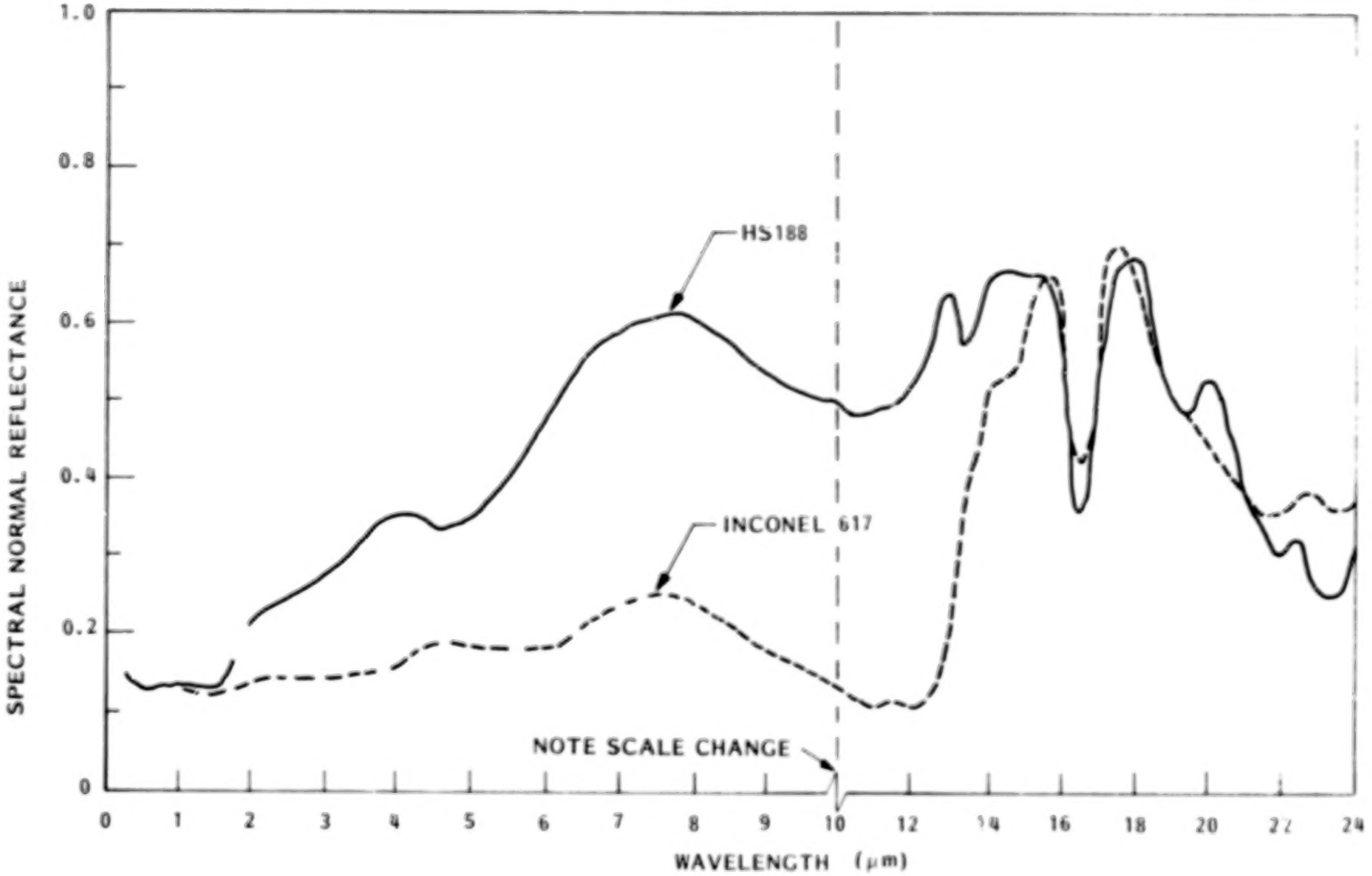

Figure 3. Room temperature (294 K) spectral normal reflectance of statically oxidized Inconel 617 and HS188.

BEST DOCUMENT AVAILABLE

BEST DOCUMENT AVAILABLE

Figure 4 is a photograph of a coated specimen ready for supersonic arc plasma wind tunnel testing. The surface is mottled tan to dark brown with a loosely adhering layer of granular material which is easily removed by rubbing. The sublayer is hard and has a diffuse, glass-like character. The bulk layer elemental composition, as determined by quantitative electron beam microprobe analysis, is:

Element	Composition (atomic percent)
Si	67
Cb	31
Cr	1
Fe	0.2
W	0.8

Room temperature near normal spectral relectance data (average of three specimens) for the coated specimens are shown in figure 5. The bars denote the spread of data at a given wavelength for the three witness specimens.

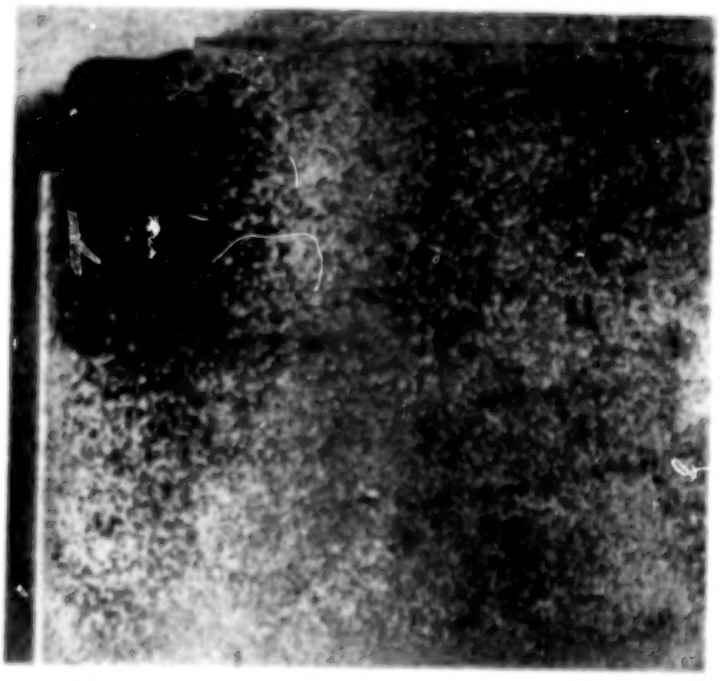

Figure 4. Visual appearance of R512E coated Cb752 Specimens.

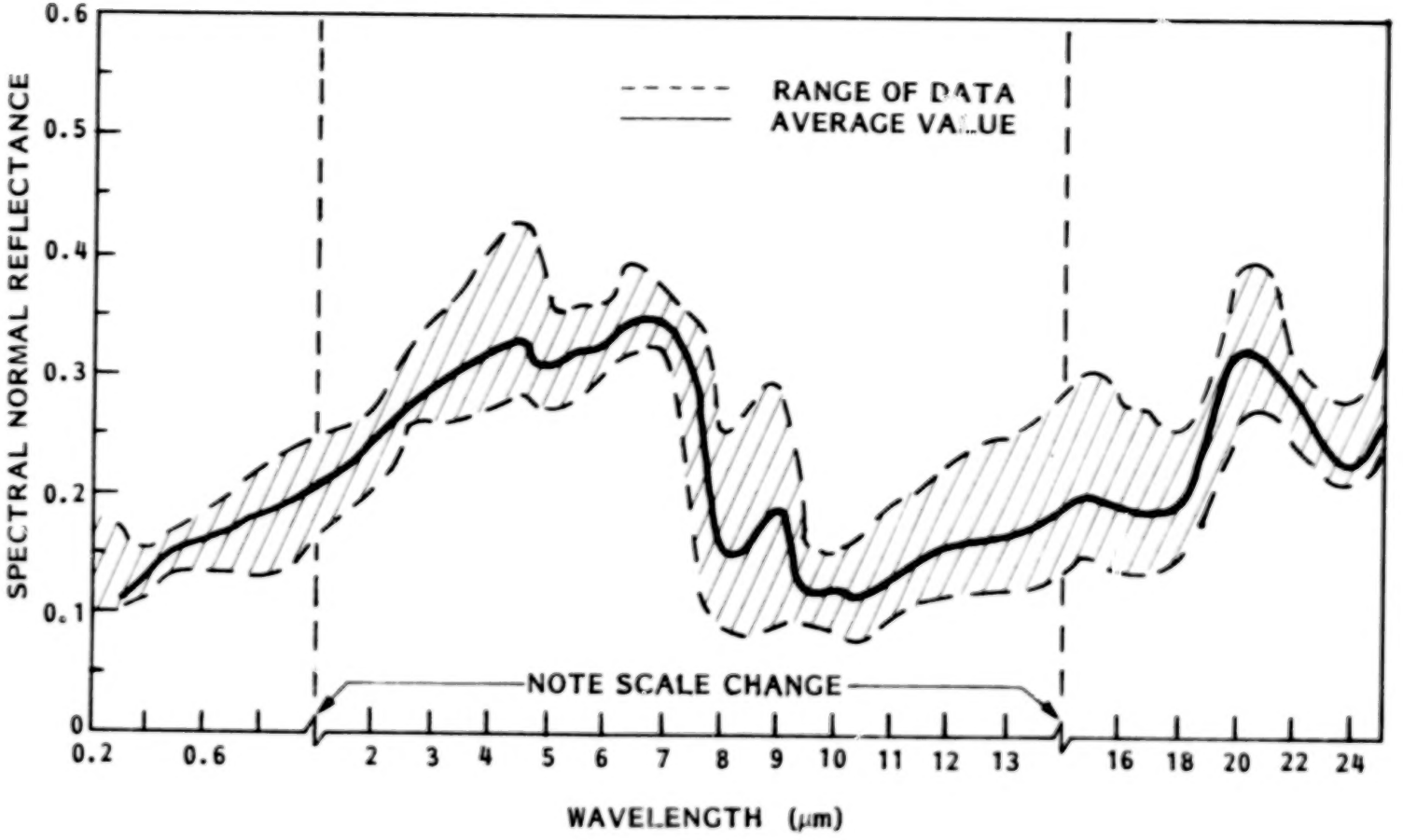

Figure 5. Room temperature (294 K) spectral normal reflectance of R512E coated Cb752 before simulated reentry testing.

BEST DOCUMENT AVAILABLE

Section 3

EXPERIMENTAL APPARATUS AND PROCEDURES

The apparatus used to expose specimens to both radiant heating and convective heating reentry simulations, perform radiative properties measurements, and analyze morphology and composition are described in this section. Convective heating exposures were done in the 1 MW supersonic arc plasma wind tunnel at the Aerotherm division of Acurex Corporation. Some of the Auger Electron Spectroscopy studies were performed at the laboratories of Charles Evans Associates and the Lawrence Berkeley Laboratory of the Unversity of California (LBL). All other facilities are located in the Lockheed Palo Alto Research Laboratories (LPARL).

3.1 SUPERSONIC ARC PLASMA WIND TUNNEL

The wind tunnel test configuration is shown in figure 6. The Acurex 1 MW constricted segmented arc plasma generator is a constant mass flowrate device using a tungsten cathode and a water cooled copper anode to transfer energy to the primary test gas (nitrogen). Oxygen gas is introduced downstream of the anode and mixed with the arc heated nitrogen in the proper ratio to simulate high enthalpy air. Equilibrium is achieved in a plenum and the resulting gases are expanded through a choked 25.4 mm diameter throat into a conical 0.203 m diameter exit nozzle. The nozzle exhausts into a 1.22 m diameter test chamber. This chamber can be continuously pumped down to a vacuum level of 25 Pa by a five-stage steam ejection system. Three water cooled stings are mounted to the chamber. The outboard and center stings held the test wedges. The third outboard sting contained either a pitot probe or a 32 mm diameter flat face calorimeter. The leading edge of each wedge was positioned 0.1 m downstream from the exit plane of the nozzle.

Water cooled 60-deg included angle wedges were used for calibration and specimen mounting. The calibration wedge was used to set tunnel conditions and verify operating parameters during exposure testing. This calibration wedge contained five pressure taps and seven Gardon type heat flux calorimeters, located as shown in figure 7. The specimen wedge (figure 8) held two samples of the same alloy, one each on opposite faces of the wedge. A high temperature rigidized silica fibrous insulation was placed underneath each specimen to provide insulation from the water cooled wedge. Two wedges were used on independent stings so that one set of materials could be exposed to a heating cycle while the other set of materials underwent a cooling cycle.

Primary instrumentation used during calibration and test runs is listed in Table 5. Data were recorded with an eight-channel Vidar data acquisition system with computer compatible magnetic tape output. An Acurex computer program reduced the tape data to a printed output of arc operating conditions, specimen thermocouple temperature, surface pyrometer temperatures, pressures, and heat fluxes.

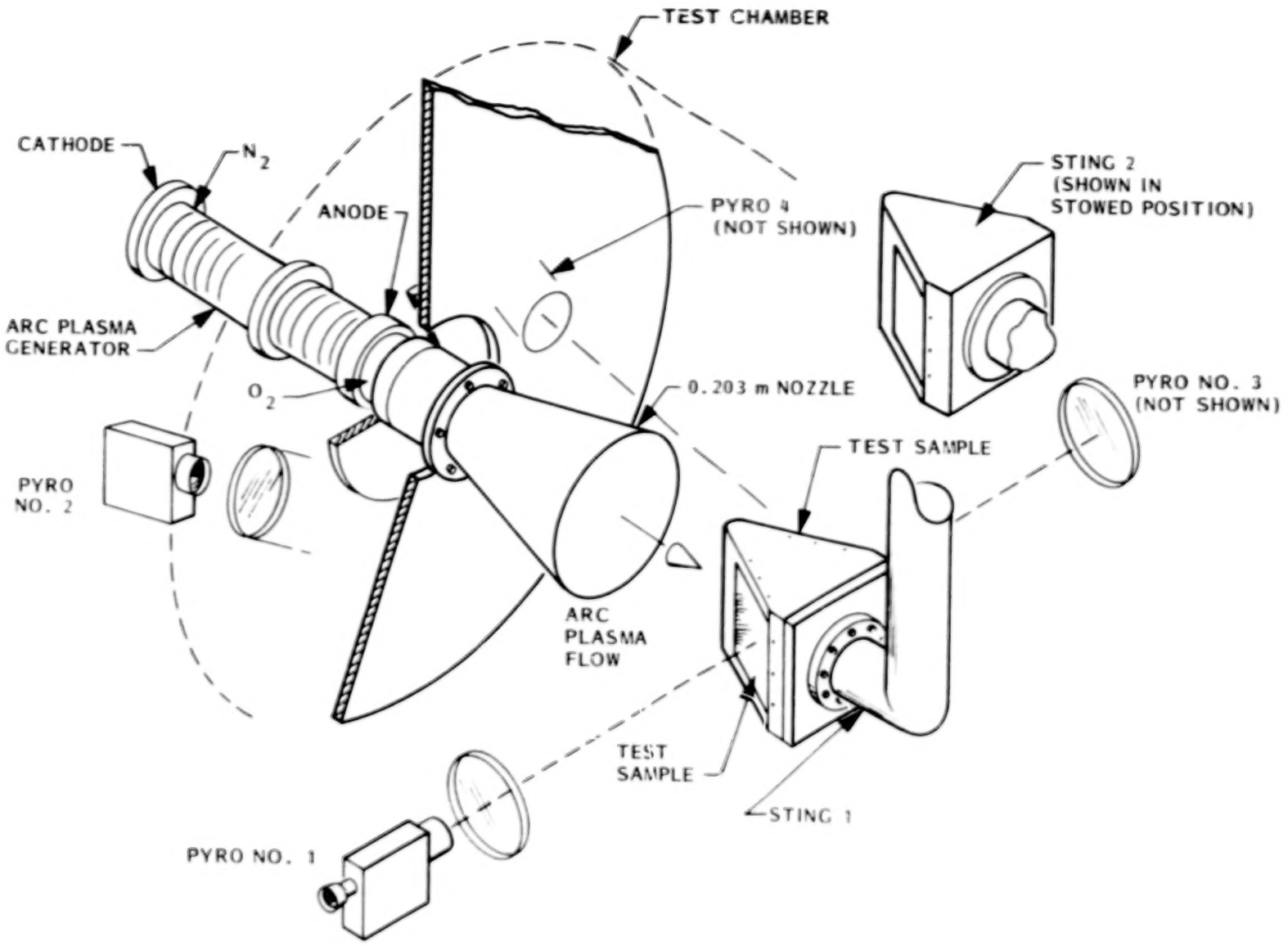

Figure 6. Schematic of Acurex 1 MW supersonic arc plasma wind tunnel.

BEST DOCUMENT AVAILABLE

13

BEST DOCUMENT AVAILABLE

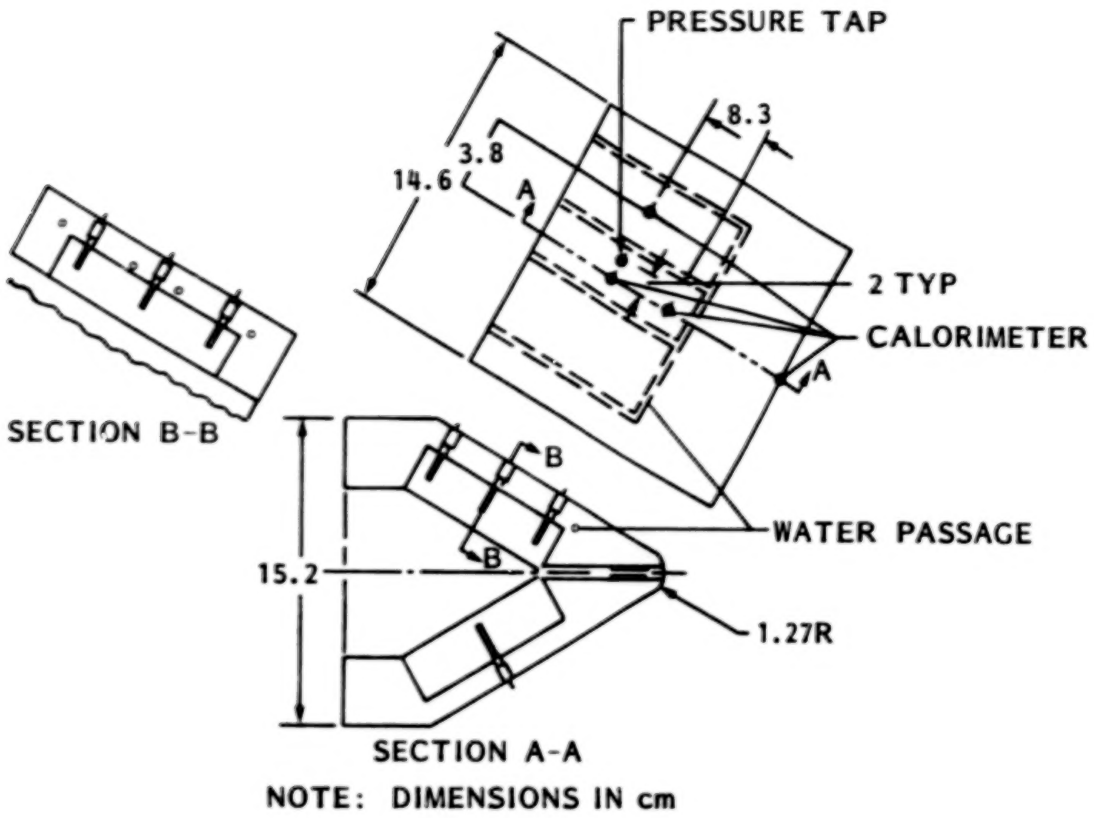

Figure 7. Acurex calibration wedge showing locations of instrumentation.

Before starting sample testing a calibration test series was run to establish the facility operating conditions that would meet the specimen test requirements for surface temperature and pressure. These requirements were 1260 K for Inconel 617 and HS188 specimens and 1590 K for the coated columbium specimens, with a surface pressure range of 300 to 600 kPa. Once the operating conditions were established, the two test wedges were alternately inserted into the flow stream for 15 min intervals of heating until the desired number of exposure cycles was completed.

The exposure conditions for the specimen tests were defined by enthalpy, pressure and heat flux corresponding to a given specimen surface temperature as achieved in this test facility. These parameters were determined from the calibration test series data (calculated enthalpy and measured pressures and heat fluxes). Then, for a specimen test, surface pressures and heat fluxes were derived on the basis of the enthalpy (calculated) and pressures (measured) during a specimen test run. Energy balance enthalpy was calculated from measurements of input power, energy loss to the cooling water and gas flowrate. Heat flux enthalpy was calculated from a catalytic surface calorimeter measurement of heat flux and a calculated heat transfer coefficient. Specimen thermcouples and the infrared pyrometers were monitored continuously during a test. The automatic optical pyrometer used to measure surface temperature spatial distributions was recorded periodically.

BEST DOCUMENT AVAILABLE

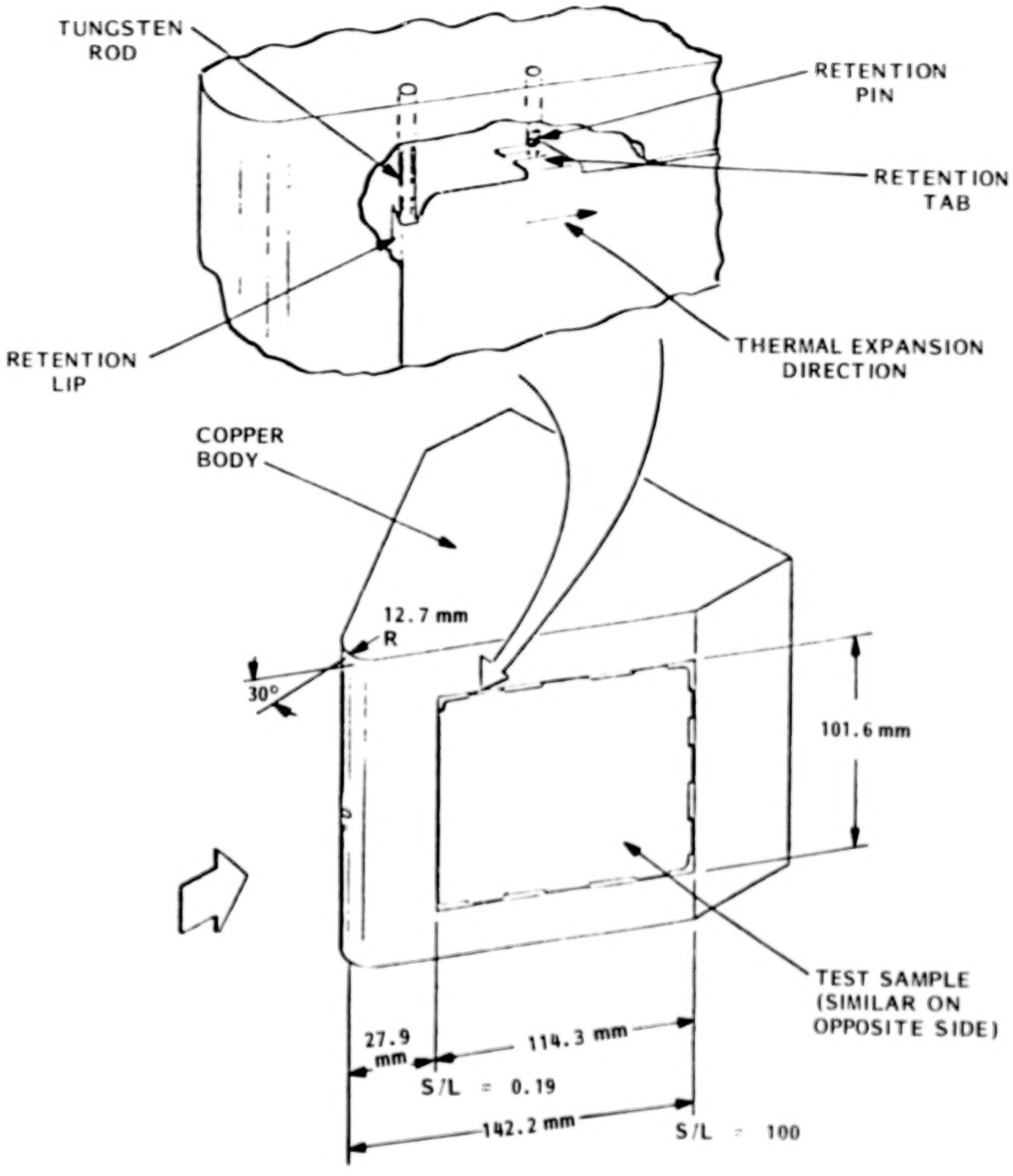

Figure 8. Configuration of sample holder for convective heating tests.

Table 5. Instrumentation For Supersonic Arc Plasma Wind Tunnel Tests

Test Parameter	Instrumentation
Arc power	0.0025 ohm current shunt and 1000:1 voltage divider
Water mass flow	Orifice plate flowmeter in main arc water return line
Water temperature rise	Differential thermopile
Gas mass flow	ASME orifice meter
Specimen backwall temperature	For the HS188 and Inconel 617 samples: Type R thermocouple with tantalum sheath (0.5 mm diameter); for the columbium samples: Type R bare thermocouple wire spot welded to columbium tab or disc bonded to rear wall with ceramic cement
Specimen surface temperature	2 each E^2T Company type TD-7B pyrometers (λ = 2.75 μm); 1 each E^2T type TD-9 pyrometer (λ = 0.9 μm); Pyro Corp. automatic optical pyrometer (λ = 0.65 μm); Pyromark disappearing filament pyrometer (λ = 0.65 μm)
Calibration model surface pressure	Pressure transducer (0 to 7 x 10^3 Pa)
Calibration model heat flux	Hy-Cal Corp. Model C-1221-A calorimeter

3.2 RADIANT HEATING APPARATUS

An inductively heated vacuum furnace, shown in figure 9, was used to conduct the cyclic temperature exposures using low velocity air at a pressure of 300 Pa. The vacuum chamber is 0.5 m diameter by 0.5 m long and is pumped by a 0.007 m^3/s mechanical vacuum pump, having a water cooled trap located in the pumping line to prevent oil backstreaming into the furnace. A cylindrical susceptor mounted in the center of the chamber is inductively heated using a microprocessor controlled induction generator. The specimens, suspended vertically within the susceptor volume, are radiatively heated by the susceptor walls.

BEST DOCUMENT AVAILABLE

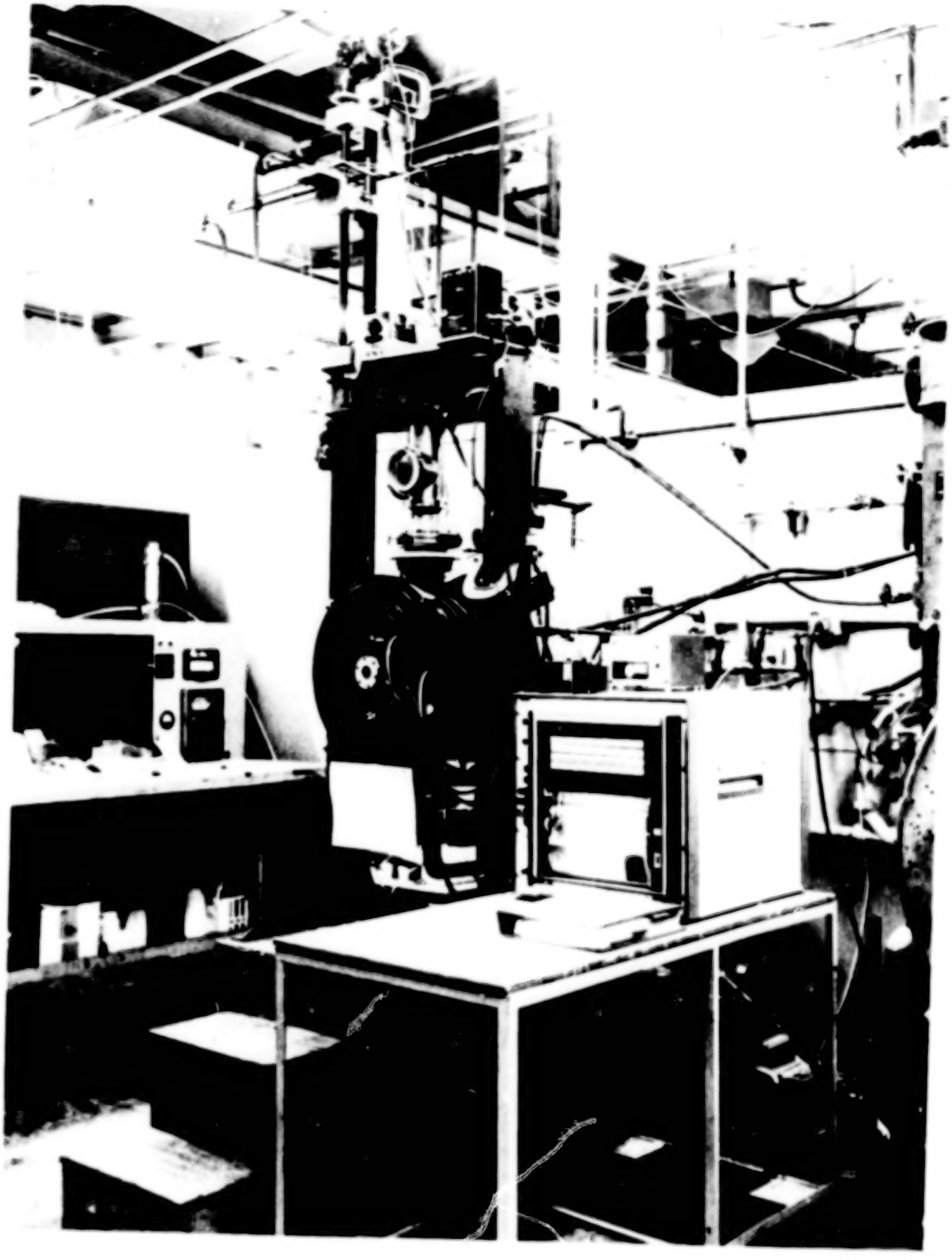

Figure 9. Radiant heating apparatus.

For the low velocity testing, the air flowing into the chamber was passed through a P_2O_5 dryer to remove water vapor. Mass flow rate of air was controlled by throttling the vacuum pumping system at a chamber pressure of 300 Pa. Velocity through the susceptor was on the order of 1 m/s.

Specimen temperature was monitored and controlled by a Type R thermocouple (3 mil diameter) spotwelded to the center of the test strip and connected to a strip chart recorder and the induction heater microprocessor, which also controls the cycle time. The chamber pressure was measured by a Bourdon tube-type gauge.

A batch of 14 strip specimens of identical material was initially placed in the furnace. Each specimen was suspended by a thin wire of Kanthal or platinum from the cooler zone of the chamber. Two specimens were instrumented with Type R themocouples for temperature monitoring. The furnace was evacuated and then brought to operating pressure with the dried air flow. A cycle was defined as a 30 min period at temperature followed by a 30 min cooling period. The time to reach test temperature was 1.5 min, after which the temperature was held constant, ±6 K, for 28.5 min. Cooling to 600 K took place during the subsequent 30 min period. The next cycle was started at this minimum temperature, and cycling was continued until 10 were completed. Three specimens were then removed for analysis, and the cycling restarted. Three specimens each were again removed after 20, 50, and 100 cycles.

3.3 EMITTANCE APPARATUS

The apparatus used to measure the high temperature emittance characteristics of the specimens is shown in figures 10 and 11. It consists of a water cooled evacuated test chamber which surrounds an electrically heated sample. The sample may be rotated in azimuth while it is viewed by an external optical transfer system. The optical system focuses an image of the center portion of the sample either on a total radiation detector or on the entrance slits of a monochromator for spectral measurements. Provision also is made to view a reference blackbody source through the same optics for absolute emittance determinations.

The vacuum chamber consists of a water cooled stainless steel bell jar which is 0.3 m in diameter and 0.36 m high. The inner surface of the chamber is coated with a low reflectance, low outgassing, flat black paint to minimize internal reflections. A potassium bromide window in the chamber wall transmits emitted energy from the sample to the external optics and the radiation detectors. A sample view port with a quartz window is also provided for visual observation of the sample and optical pyrometer temperature measurements. Vacuum feedthroughs are mounted in the base plate for access to the sample instrumentation wires. The chamber pumping system consists of a 0.10 m diameter oil diffusion pump backed with a 2.4×10^{-3} m^3/s mechanical pump with a molecular sieve trap to prevent backstreaming during the initial chamber evacuation period. A water cooled baffle and a liquid nitrogen trap are located between the diffusion pump and the chamber.

BEST DOCUMENT AVAILABLE

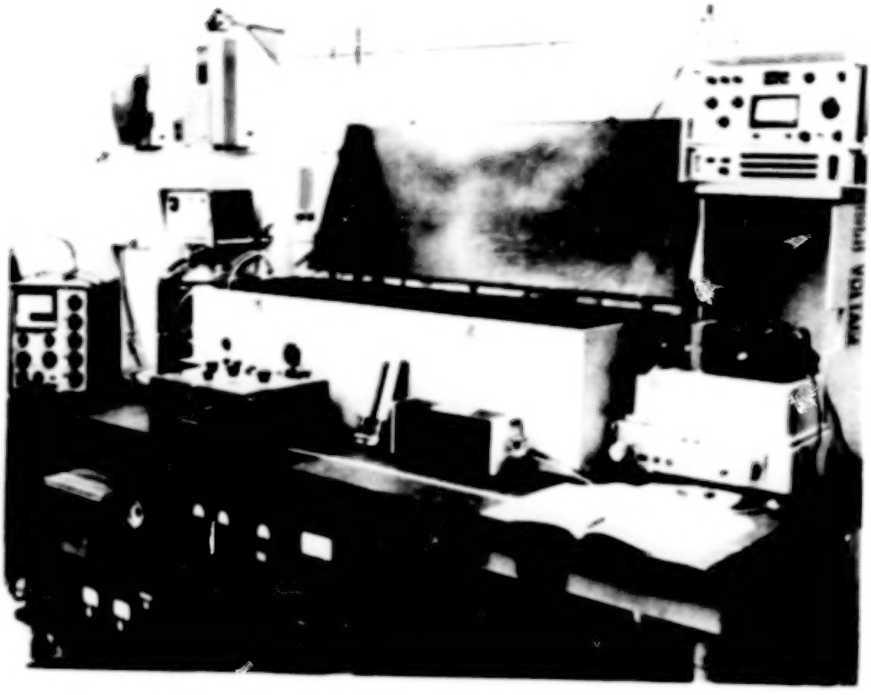

Figure 10. High temperature emittance apparatus (HTEA).

Figure 11. HTEA sample mounting.

The sample is clamped tightly between two water cooled copper electrodes (figure 11) which are displaced from the vertical axis of the chamber to eliminate reflections of sample energy into the optical path. Both electrodes pass through an insulated rotatable vacuum seal located in the bottom of the vacuum manifold. The electrodes are supported rigidly at the base plate by an insulated steel yoke which turns on a ball bearing. The sample can be rotated about its longitudinal centerline to 95 deg on either side of the normal viewing angle. Variable tension is applied to the sample by means of a bellows and spring system in series with the lower electrode. This tension adjustment accommodates the thermal expansion of the specimen and prevents bending at elevated temperatures.

Electrical power to heat the sample is supplied by a variac controlled, 10 kVA, stepdown transformer with a maximum current output of 1000 A. Specimen current is measured with a 1000 A, 100 mV current shunt. Voltage drop across the shunt is read to four place precision with a Fluke Model 803B differential ac-dc voltmeter. Chamber pressure is measured with a Baratron Type 77 gauge over the range of 1 to 1 x 10^5 Pa and with an ionization gauge for pressures less than 1 Pa.

An argon gas system is connected to the chamber to control pressure in the 10 to 1000 Pa range. The argon is supplied from a high pressure cylinder through a pressure regulator. The argon gas which is oxygen free (refer to analysis in Table 6) is passed through a molecular sieve trap and a P_2O_5 drying column to remove any residual oil and water vapor, respectively.

The optical system is shown schematically in figure 12. Radiant energy from the sample is collected and focused on either the total or the spectral energy detectors. All of the reflecting surfaces are front surface aluminized mirrors. Radiant energy emitted by the sample enters the optical system through a 38 mm diameter potassium bromide (KBr) window in the chamber wall [3]*. The window is tilted at an angle of 5 deg to the optical axis of the system to prevent interreflections between the sample and window surfaces at normal incidence. Radiant energy from the reference blackbody source [5] is directed into the same optical path as the sample energy by means of a 45 deg mirror [6] located in front of the KBr window. Energy from either source is chopped at 13 Hz [7] and collected by a 0.46 m focal length spherical mirror [8] masked to limit the collecting half angle to 2.1 x 10^{-3} sr.

Energy collected by the spherical mirror [8] is directed to the plane mirror [9] and then to the variable aperture slit [11]. At this position a real image of the sample is formed at a magnification of 1.6x, and the slit is adjusted so that it is completely filled for viewing angles up to 88 deg from the normal. After passing through the adjustable slit, the energy is either focused onto the total radiation detector [13] or is directed to fill the entrance slits of a Model 13U Perkin Elmer monochrometer [16] at a reduction

* Numbers in brackets in this section refer to the optical system components in figure 12.

Table 6. Argon Gas Analysis

Component	Mole Percent
Ar	99.951
O_2	0.001
N_2	0.042
CO_2	0.004
H_2O	<0.020
CH_4	0.000
H_2	0.0002

of 0.75x. The monochrometer is equipped with a KBr prism and a vacuum thermocouple detector [18]. Both the total and the spectral detector outputs are amplified and recorded by the Brower Laboratory Model 132 lock-in voltmeter.

For the arrangement shown in figure 12, the voltage response of the spectrometer detector is proportional to the difference in spectral radiant flux received by the detector from the sample and that received from the chopper. The response of the system with the normal to the sample plane at an angle θ to the optical axis may be expressed as (ref. 8)

$$V_s(\theta) = [\epsilon_s(\theta,\lambda,T)E_s(\lambda,T)\tau_w + \epsilon_s(\theta,\lambda,T)E_s(\lambda,T)\rho_c\rho_s\tau_w + \epsilon_c E_c(\lambda,T)\rho_s\tau_w + \epsilon_w E_w(\lambda,T) + \rho_w E_a(\lambda,T) - E_a(\lambda,T)]hF_s \quad , \quad (1)$$

where F_s is a function which describes the efficiency of the optical transfer system; h is the detector responsivity; and $\epsilon_s(\theta,\lambda,T)E_s(\lambda,T)\rho_c\rho_s\tau_w$ is an approximate term representing energy reflected by the chamber walls, which is then directed by the sample into the optical path. At $\theta = 0$, the sample plane is normal to the optical axis and the voltage response becomes

$$V_s(\theta_N) = [\epsilon_s(\theta_N,\lambda,T)E_s(\lambda,T)\tau_w + \epsilon_s(\theta_N,\lambda,T)E_s(\lambda,T)\rho_c\rho_s\tau_w + \epsilon_c E_c(\lambda,T)\rho_s\tau_w + \epsilon_w E_w(\lambda,T) + \rho_w E_a(\lambda,T) - E_a(\lambda,T)]hF_s \quad . \quad (2)$$

BEST DOCUMENT AVAILABLE

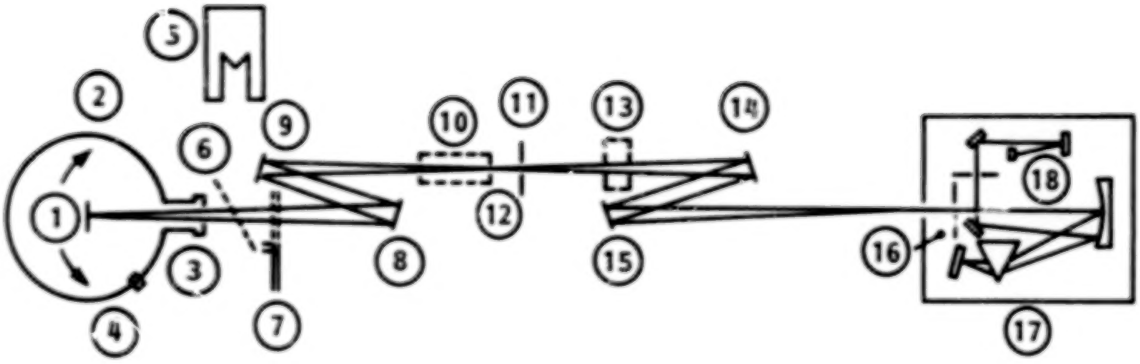

1. SAMPLE
2. VACUUM CHAMBER
3. KBr WINDOW
4. PYROMETER PORT
5. BLACKBODY
6. SELECTOR MIRROR
7. CHOPPER
8. 0.46-m FOCAL LENGTH SPHERICAL MIRROR
9. PLANE MIRROR
10. POLARIZER
11. ADJUSTABLE SLIT
12. IMAGE PLANE
13. VAC. THERMOCOUPLE - TOTAL DETECTOR
14. PLANE MIRROR
15. 0.28-m FOCAL LENGTH SPHERICAL MIRROR
16. INLET SLITS
17. MODEL 98 MONOCHROMATOR
18. VAC. THERMOCOUPLE DETECTOR

Figure 12. Schematic of optical system of HTEA.

Since the temperatures of window, chamber, and ambient environments are very nearly the same, it may be assumed that

$$E_w(\lambda,T) = E_c(\lambda,T) = E_a(\lambda,T) \quad .$$

It is also true that $\rho_c << 1$ and $\varepsilon_c \cong 1$ for reflected and emitted energy from the chamber walls. Since $\rho_w + \alpha_w + \tau_w = 1$ for the window at any given wavelength, and $\rho + \alpha = 1$ for an opaque sample, equations (1) and (2) become

$$V_s(\theta) = \varepsilon_s(\theta,\lambda,T)\tau_w [E_s(\lambda,T) - E_a(\lambda,T)]hF_s \quad , \tag{3}$$

and

$$V_s(\theta_N) = \varepsilon_s(\theta_N,\lambda,T)\tau_w [E_s(\lambda,T) - E_a(\lambda,T)]hF_s \quad , \tag{4}$$

respectively.

The voltage response of the detector when observing the blackbody reference is given by

$$V_b = [E_b(\lambda,T) - E_a(\lambda,T)]hF_s \quad . \tag{5}$$

The spectral normal emittance $\varepsilon(\theta_N,\lambda,T)$ is then determined from the ratio of signals as

$$\frac{V_s(\theta_N)}{V_b} = \frac{\varepsilon_s(\theta_N,\lambda,T)\tau_w [E_s(\lambda,T) - E_a(\lambda,T)]hF_s}{[E_b(\lambda,T) - E_a(\lambda,T)]hF_s} \quad , \tag{6}$$

and thus

$$\varepsilon_s(\theta_N,\lambda,T) = \frac{1}{\tau_w}\frac{V_s(\theta_N)}{V_b}\left[\frac{E_b(\lambda,T) - E_a(\lambda,T)}{E_s(\lambda,T) - E_a(\lambda,T)}\right] \quad . \tag{7}$$

For equal blackbody and sample temperatures

$$E_s(\lambda,T) = E_b(\lambda, T) \quad ,$$

equation (7) reduces to

$$\varepsilon_s(\theta_N,\lambda,T) = \frac{1}{\tau_w}\frac{V_s(\theta_N)}{V_b} \quad . \tag{8}$$

The spectral transmission of the KBr window, τ_w, is measured periodically for use in the computer reduction of test data.

The total directional and normal emittance is determined by placing a vacuum thermocouple detector with a KBr window at position (11) in figure 12. The detector response is proportional to the difference between energy received from the sample and that received from the chopper. Performing an analysis similar to that given above yields

$$\epsilon_s(\theta,T) = \frac{1}{w}\frac{V_s(\theta)}{V_b}\left[\frac{E_b(\lambda,T) - E_a(\lambda,T)}{E_s(\lambda,T) - E_a(\lambda,T)}\right] \quad . \tag{9}$$

For equal blackbody and sample temperatures

$$\epsilon_s(\theta,T) = \frac{1}{\tau_w}\frac{V_s(\theta)}{V_b} \quad . \tag{10}$$

The window transmission used here is that value obtained for transmitted blackbody energy at the temperature of the samples. The measured values of transmission are integrated over the blackbody spectrum to give the effective transmission for a given sample temperature.

The method for determining total hemispherical emittance $\epsilon(T)$ is similar to the methods described by Richmond and Harrison in reference 9 and by Abbott et al. in reference 10. The total hemispherical emittance for the center region of the long strip specimen is given by

$$\epsilon(T) = \frac{VI - P_L}{A\sigma_o\,(T_s^4 - T_a^4)} \quad , \tag{11}$$

where V is the voltage drop across the center of the sample, I is the current, P_L is a power loss term to account for thermal conduction losses at each end of the center portion of the sample, A is the surface area, σ is the Stefan-Boltzmann constant, T_s is the absolute temperature of the sample, and T_a is the absolute temperature of the surrounding chamber walls. Voltage drop is measured between the platinum legs of the two thermocouples located 10 mm on either side of the centerline of the sample. The P_L term is determined from the temperature gradient at the location of the two thermocouples. Estimates of the temperature gradients are obtained from inspection of graphical plots of the temperatures at the five different locations along the length of the sample strip. Except at the lowest test temperatures, both the P_L and Ta^4 terms are negligibly small. The surface area, A, is corrected for thermal expansion of the sample at each test temperature using published values for the expansion coefficients of the substrate material.

Each sample was instrumented with five 0.075 mm diameter platinum/platinum-13 percent rhodium thermocouples spotwelded to the back surface of the test strip. The thermocouple junctions were located along the

vertical centerline of the strip at 10, 20, and 30 mm above and below the midpoint of the strip (see figure 11). Care was taken to attach both wires of each junction at the same vertical location to avoid pickup of the ac-voltage gradient along the strip. Between the junctions and the vacuum feedthrough, each wire was insulated with fiberglass sleeving to prevent short circuiting (see figure 11). The leads were terminated individually in an ice bath reference junction.

After installation of the specimen in the high temperature emittance apparatus (HTEA), the chamber is evacuated to less than 1 x 10^{-4} Pa using the oil diffusion pump; this was necessary to remove any residual oxygen and water vapor prior to testing in dry argon. The chamber was then backfilled with dry argon, evacuated to 1 Pa and then backfilled to 300 Pa with dry argon prior to specimen testing. This procedure was confirmed as producing an oxygen-free environment by exposing bare strips of Inconel 617 and HS188 to the chamber environment at 1250 K for several hours. Without the initial high vacuum operation, a thin oxide layer was formed on both materials. With the initial very low pressure conditioning, no oxide layer formation was observed on either material.

Once the test pressure is established the specimen is heated to the initial test temperature. Upon temperature equilibration, a total normal emittance measurement is made followed by the spectral measurements and, lastly, a second measurement of ϵ_{TN}. Specimen power is increased to the next temperature level, and the measurement procedure repeated. This process is repeated until the maximum temperature data are obtained. For several specimens the emittance data were repeated at lower temperatures to determine if the measurement environment resulted in any radiative property changes (see section 4.2).

Upon final cooling, the chamber pressure is increased to atmospheric pressure with dry argon. The specimen is removed and packaged until subsequent reflectance measurements and/or compositional analyses are made.

3.4 REFLECTANCE APPARATUS

Spectral reflectance measurements were made at room temperature using two reflectometers. For the visible to near infrared wavelength region, 0.2 to 2.2 μm, a Cary Model 17D double beam spectrophotometer with an integrating sphere attachment was used. The specimen is located at an entrance port in the wall of the sphere and is illuminated with monochromatic energy. The energy reflected from the specimen in a near normal direction, 15 deg off normal, is collected and transferred to a photomultiplier or lead sulphide detector, depending upon the wavelength of illumination. The instrument is calibrated against a freshly evaporated first surface aluminum mirror which has been previously measured with a Gier Dunkle Model SP200 absolute directional integrating sphere reflectometer.

Spectral reflectance measurements from 1.5 to 25 μm were made using a Gier Dunkle Model 300 heated cavity reflectometer. The specimen, 24 mm diameter,

is mounted in a water cooled holder in the center of an isothermal cavity maintained at a temperature of 1050 K. Radiation from this cavity illuminates the specimen, and the reflected beam, 15 deg off normal, is directed to a prism monochrometer with vacuum thermocouple detector. This is an absolute instrument as the 100 percent level is determined by viewing a platinum foil reflector which is at cavity temperature and is placed in the sample position.

3.5 MORPHOLOGICAL AND COMPOSITIONAL ANALYSIS

Oxide and coating layer morphologies were obtained using the scanning electron microscope (SEM) and the electron microprobe (EP) operated in imaging mode. Both instruments were used for examining cross sections and the surface. Elemental analysis was done using a SEM in the electron probe configuration, the electron microprobe for point and broad area concentration measurements (including oxygen), and the Auger electron spectrometer (AES) for depth profiling and edge section point spectra. The x-ray diffractometer (XRDA) was employed for crystallographic analysis of the oxide layer. Limited secondary ion mass spectrometry (SIMS) elemental depth profiling measurements were made.

3.5.1 Imaging

Images were obtained at magnifications of 150x to 20,000x, the most useful for morphology characterization being 150 to 200x and 4000x. The Applied Research Laboratories EMX microprobe was used for some surface imaging because of the need for subsequent analysis at discrete surface points determined from the images.

Samples for analysis were cut from the test specimens using a diamond cutting wheel. They were taken at two locations on the supersonic arc plasma wind tunnel test specimens, one taken immediately downstream from the emittance specimen and the second one just upstream from the emittance specimen. These two locations were chosen because of the streamwise temperature gradient in the specimen. For the radiant heating test and the statically oxidized specimens, the sample was taken from the central region of the test specimen.

For surface imaging the specimens were unmounted. Specimens for edge examination were mounted in Bakelite and polished with Al_2O_3 compound. All surfaces to be examined were coated with a 100 to 200 Å layer of gold to reduce charging. Because of the friable nature of the oxide layers, well-defined edges corresponding to the exterior surface were not maintained. In some instances a portion of the oxide layer adhered to the Bakelite and was separated from the parent oxide.

3.5.2 Compositional Analysis

The electron microprobe was used for surface elemental analysis. Accuracy of the quantitative data is estimated to be 5 percent of the detected amount

for major elements and 25 percent for minor elements. The probe analyzed an area 0.5 to 1 μm diameter and approximately 1 μm in depth. While the spatial resolution in a plane is good for the surface features observed for these materials, the depth resolution does not permit analysis of a layer much less than 1 μm thick. The microprobe, however, does not suffer from the surface charging problems of AES or SIMS nor does the effect of irregular topography seriously degrade the analysis resolution. Analyses were made for oxygen, nickel, chromium, cobalt, iron, titanium, aluminum, molybdenum, silicon, and tungsten.

Both JOEL and PHI Auger electron spectrometers were used for elemental depth profiling and cross sectional composition studies. The JOEL instrument is owned and operated by Charles Evans Associates, and the PHI instrument is located at LPARL. Initially, the analyses were done using high areal resolution, less than 100 Å, but because of the rough surface contour and varied composition the majority of the data were obtained with a rastered beam which averages over an approximate 100 μm area. Depth resolution is 20 to 50 Å. Several analyses were also done by the Lawrence Berkeley Laboratories, University of California, using a PHI instrument for a cross check of results.

The test samples were nominally 13 mm square sections polished on one edge or surface mounted. Surfaces were coated with a few hundred angstroms of gold to provide a conductive surface to reduce charging on the oxide layer or the R512E coating which are all relatively poor electrical conductors. The quantitative nature of the results is degraded by charging, which occurred for some specimens, and the lack of standards for determining elemental yields or sensitivity factors. Bakelite mounts could not be used because of the continued outgassing which degraded instrument vacuum to a marginal operating level.

Depth profiling was done with 5 keV argon ion sputtering. In some cases, sputter crater depth was measured using a surface profilometer. The edge section samples were periodically sputtered for a few minutes to remove any oxygen or elements redeposited from a previous analysis region.

A General Electric Model XRD-5 x-ray diffractometer was employed for bulk crystallographic analysis using copper K_α radiation. The data provide an average over a nominally 25 mm^2 area and the total thickness of the oxide layer. Diffraction data were obtained on the AES and EP samples after these analyses were completed.

3.5.3 Oxide Layer Thickness

A grooving technique was found to give reliable oxide layer thickness values. A taper-like section is produced by cylindrical grinding of a small area on the surface to a depth sufficient to penetrate into the base metal. The oxide layer thickness is obtained using the geometrical relationship derived in figure 13. Photomicrographs of the grooved area show surface topography and, in some cases, base metal crystallite sizes.

BEST DOCUMENT AVAILABLE

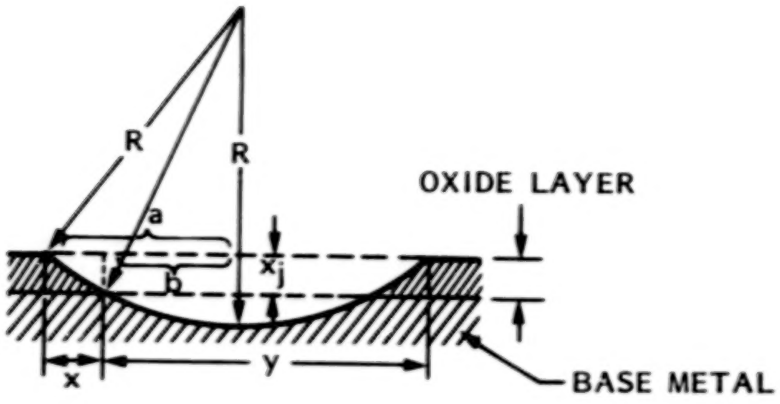

$$x = a - b,$$

$$y = a + b,$$

and

$$X_j = \sqrt{R^2 - b^2} - \sqrt{R^2 - a^2}$$

$$= R \left[\sqrt{1 - \frac{b^2}{R^2}} - \sqrt{1 - \frac{a^2}{R^2}} \right]$$

Figure 13. Schematic of oxide thickness measurement using the cylindrical grinding technique (courtesy Philtek Instruments, Philadelphia, Pennsylvania).

Section 4

EXPERIMENTAL RESULTS

Elevated temperature total and spectral normal emittance measurements were made after each simulated reentry exposure test. Room temperature spectral normal reflectance measurements were made to confirm the trends observed in the emittance data and to examine radiative properties over a broader wavelength region (0.3 to 25 μm) than achieved by the direct emittance measurements (1 to 14 μm). Compositional analysis studies were conducted to evaluate any major changes in the oxide or coating layers resulting from the exposure tests. The relation between changes in radiative properties and compositional changes was explored.

4.1 SIMULATED REENTRY EXPOSURES

Neither the convective heating nor the radiant heating simulation conditions produced a significant degradation of elevated temperature total emittance of any of the materials; however, visual appearance changes were noted in all cases after supersonic arc plasma wind tunnel testing. The reflectance data show that the appearance changes from the arc plasma testing are related to spectral changes at wavelengths shorter than 1.5 μm, and in this region the influence of spectral emittance on total emittance is negligible.

4.1.1 Supersonic Arc Plasma Wind Tunnel Tests

The nominal range of test conditions for the supersonic arc plasma wind tunnel tests is given in Table 7. The data are based upon boundary layer edge conditions calculated by Acurex using their Aerotherm Chemical Equilibrium (ACE) code (ref. 11). Test data of enthalpy, pressure, local wall heat flux, and specimen surface temperatures for each test cycle are contained in Appendix A.

Two difficulties were encountered during the arc plasma testing. Both relate to nonuniform heating and, subsequently, material temperature variations. Nonuniform heating of the specimens is the result of selecting a wedge flow test configuration. The wedge, rather than a stagnation model, was used to provide a test specimen geometry from which relatively large size emittance specimens could be cut after testing was completed. The nature of the wedge flow is such that there are streamwise and, of lesser importance as far as the emittance specimen is concerned, spanwise heating rate gradients. This results in a decreasing temperature moving downstream from the specimen leading edge. The temperature difference over the specimen streamwise dimension is on the order of 150 to 200 K for the nominal test conditions of this study. This gradient translates to a 25 to 50 K temperature nonuniformity over the area of the emittance measurement which is of minor concern. The more important consideration is that the significantly higher temperature in the leading edge zone (1) limits the test temperature in the emittance measurement region of the specimen and (2) reaction products from

Table 7. Calculated Boundary Layer Edge Conditions for Supersonic Arc Plasma Wind Tunnel Tests

Parameter	Inconel 617 and HS188 Specimens	R512E Coated Cb752 Specimens
Temperature (K)	4409 to 4419	3528 to 4261
Pressure (Pa)	219 to 267	458 to 516
Enthalpy (MJ/kg)	9.56 to 11.08	7.31 to 9.29
Entropy (kJ/kgK)	13.41 to 13.71	12.56 to 13.02
Density (kg/m^3)	1.47×10^{-4} to 1.65×10^{-4}	3.44×10^{-4} to 3.79×10^{-4}
Molecular Weight	22.64 to 23.26	23.65 to 24.28
Surface Mach Number	1.27 to 1.37	1.62 to 1.65
Surface Mass Flux (kg/m^2s)	0.262 to 0.304	0.746 to 0.757
Mol Fraction N_2	0.568 to 0.611	0.641 to 0.680
Mol Fraction N	0.005 to 0.010	0.003 to 0.048
Mol Fraction O_2	$<0.6 \times 10^{-5}$	$<1.6 \times 10^{-3}$
Mol Fraction O	0.328 to 0.337	0.308 to 0.309
Mol Fraction NO	$<2.1 \times 10^{-3}$	$<6.8 \times 10^{-3}$

the higher temperature zone may influence the material behavior in the emittance measurement region. In some instances the nonuniform heating was so severe as to produce specimen melting in the leading edge region.

For the initial testing the specimen mounting hole configuration was modified by LMSC from that originally used by Acurex for metallic specimens (ref. 6). This was done to simplify fabrication, but this change apparently led to some thermal deformations which raised the specimen leading edge above the model holder surface, i.e., a step, and this was a possible cause for the early test failures. Subsequent specimens were fabricated to the original specification, and the thermal distortions were minimized.

The probable cause of specimen failure appeared to be vacuum system pressure fluctuations which resulted in shock impingement with severe local heating causing specimen burn-through in local areas. The source of the pressure fluctuations was malfunction of the steam ejector, and overhaul of this component greatly reduced the severity of the problem.

Because of the specimen failures and the test budget limitation, a maximum exposure of 38 test cycles was achieved for each of the three materials.

The result of these test problems is that a rather large temperature uncertainty must be assigned to some exposure specimens. Appendix A contains a detailed summary of test conditions and measured temperatures for each cycle. Table 8 gives a chronology for each material, noting failures as well as successful tests. Eight Inconel 617 specimens were tested with four failures and four successful tests. Four HS188 tests were conducted with only one failure. Six coated columbium specimens were tested with no failures.

The results for the tests that were run successfully to completion are summarized in Table 9. It gives the nominal value as well as the minimum and maximum recorded values for bulk enthalpy, hot wall heat flux, and surface temperature at the position corresponding to the location of the emittance sample on the test specimen. Also any operational anomalies observed during a test are noted.

In general there was only fair agreement between boundary layer surface temperature measured radiometrically and back surface temperature measured with a thermocouple. Two reasons for the lack of correlation are (1) nonuniformity of surface temperature distribution and (2) depression of the local surface temperature by the presence of the rear surface thermocouple and thermocouple heat loss effects on the junction temperature. Figure 14 illustrates two variants of local temperature which commonly occurred during testing. Specimen leading edge is at the left of each photograph. The rear surface thermocouple location is shown by the dark area near the center of each specimen. This darkening illustrates the local surface temperature perturbation resulting from conduction along the thermocouple sheath which was spot welded to the specimen in an attempt to reduce the thermocouple heat loss due to lead wire conduction.

Initially, two radiation pyrometers were used to view the surface. The one designated as "temperature 1" of Appendix A was sighted at the thermocouple location and the one for "temperature 2" sighted approximately 25 mm upstream from the thermocouple location. After several specimen failures had occurred, a third pyrometer was sighted at the leading edge zone to continuously monitor this maximum temperature region during testing.

Ideally, the front and rear surface temperatures for the superalloys should be nearly equal as the gradient through the specimen is less than 1 K for the surface heat fluxes of these test conditions. Generally, the temperature indicated by the rear surface thermocouple was 60 to 150 K lower than the corresponding front surface temperature. This large apparent gradient is attributed to thermocouple heat loss.

BEST DOCUMENT AVAILABLE

Table 8. Wedge-Specimen Position and Cycle History of Supersonic Arc Plasma Wind Tunnel Tests

Inconel 617 Specimen History

Specimen	Wedge[a]	Cycle
		1 5 10 15 20 25 30 35 40 45 50 55
A	3F	I[b](1)---R[c](8)
AA	3F	I(16)----------R(53)
C	3N	I(1)-F[d](6)
B	3N	I(7)--F(8)
D	3N	I(9)------F(10)
BB	3N	I(16)-------F(16)
DD	3N	I(16)----------R(36)
CC	3N	I(37)----------R(53)

HS188 Specimen History

Specimen	Wedge[a]	Cycle
		1 5 10 15 20 25 30 35 40
E	2F	I(1)----------R(38)
F	2N	I(1)--R(8)
G	2N	I(9)-----F(15)
FF	2N	I(18)----------R(38)

Coated Columbium Specimen History

Specimen	Wedge[a]	1 5 10 15 20 25 30 38
7	3N	I(1)----------R(37)
8	3F	I(1)---------- R(19)
6	2F	I(1)--R(6)
5	2N	I(1)--R(6)
9	3F	I(20)------R(30)
10	3F	I(31)--R(37)

(a) 2F = wedge sting position 2, far-side specimen position
2N = wedge sting position 2, near-side specimen position
3F = wedge sting position 3, far-side specimen position
3F = wedge sting position 3, near-side specimen position
(b) I = installed on cycle ( )
(c) R = removed for analysis on cycle ( )
(d) F = failed during cycle ( )

Table 9. Summary of Supersonic Arc Plasma Wind Tunnel Tests

Material	Specimen Number	Number of Cycles	Bulk Enthalpy (MJ/kg) (a)	Hot Wall Heat Flux (kW/m^2) (a)	Specimen Temperature (K) (a)	Operational Problems During Test
Inconel 617	A	8	12.22 (12.44, 12.06)	132 (139, 127)	1268 (1300, 1247)	None
	CC	17	8.68 (9.73, 7.41)	81 (97, 66)	1257 (1265, 1250)	6 Vacuum Surges
	DD	20	9.12 (10.06, 8.34)	85 (95, 75)	1259 (1299, 1219)	None
	AA	38	9.01 (11.23, 7.41)	83 (116, 66)	1191 (1269, 1131)	6 Vacuum Surges
HS188	F	8	11.83 (12.44, 11.23)	125 (137, 116)	1283 (1317, 1256)	None
	FF	21	8.24 (10.06, 6.30)	76 (98, 55)	1259 (1285, 1249)	7 Vacuum Surges
	E	38	9.73 (12.44, 6.30)	95 (136, 51)	1206 (1300, 1062)	9 Vacuum Surges
R512E Coated Columbium 752	10	8	11.45 (12.33, 10.45)	208 (229, 187)	1447 (1490, 1413)	1 Vacuum Surge, Nozzle Failures
	9	10	10.78 (11.72, 9.12)	199 (214, 191)	1367 (1405, 1340)	3 Vacuum Surges
	7	20	9.95 (13.99, 6.41)	178 (239, 148)	1353 (1444, 1318)	5 Vacuum Surges, Nozzle Failure
	8	38	10.73 (13.99, 8.68)	190 (237, 147)	1372 (1612, 1256)	20 Vacuum Surges, Nozzle Failure

(a) Upper number is average value; numbers in parentheses are maxium and minimum values, respectively.

BEST DOCUMENT AVAILABLE

33

BEST DOCUMENT AVAILABLE

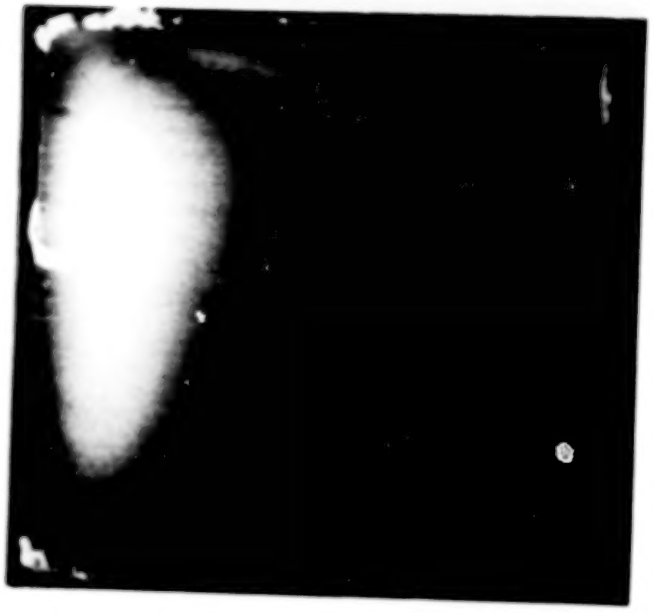

(a) Inconel Specimen AA

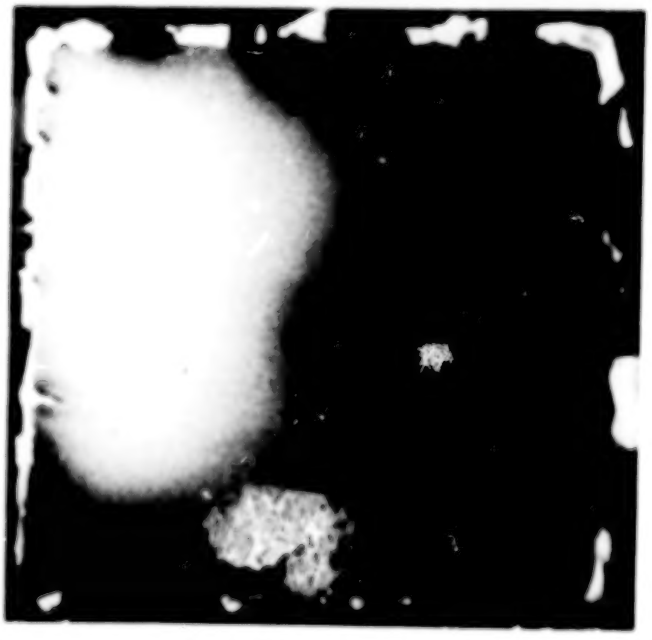

(b) HS188 Specimen E

Figure 14. Visual representation of surface temperature gradients during supersonic arc plasma wind tunnel testing.

The characteristic temperature reported for each specimen test is based on the data from pyrometers 1 and 2 (see figure 6) or the thermocouple. The rationale for this choice of temperature is the pyrometers were sighted at the emittance sample location on the test specimen and would give a representative temperature for this area. However, in several instances the corrected pyrometer temperature was well below that of the rear surface thermocouple temperature. As this is physically incorrect, it was assumed that the pyrometer was in error due to either incorrect sighting or to the correction to true temperature, i.e., an error in spectral emittance or window transmittance resulting in an erroneous true temperature correction to the measured brightness temperature. Inspection of the raw data did not lead to a conclusion as to the apparent sources of error so, in the case of low pyrometer temperature, the thermocouple temperature was used. In several instances neither temperature seemed reasonable, so the leading edge temperature was extrapolated to the emittance specimen area using the local heat flux data from the facility calibration tests.

The nominal exposure temperature for the Inconel 617 specimens is 1240 K, +60 K -100 K, for any cycle. Specimens A and DD were at a nominal temperature of 1260 to 1270 K, and Specimen AA was at a nominal temperature of 1190 K. The nominal temperature for the HS188 specimens was 1250 K. Specimen F was at a temperature of 1283 K, +34 K -27 K; Specimen FF at 1259 K, +36 K -10 K; and Specimen E at 1206 K, +94 K -142 K.

The R512E coated Cb752 specimens were exposed at temperatures considerably lower than the desired value of 1580/1590 K. The lower test temperatures were necessitated by the streamwise temperature gradient and severe vacuum surging. Because of the sporadic vacuum pressure anomalies, the leading edge temperature was reduced to 1500 K in an attempt to prevent early specimen failure. The resultant nominal test temperatures of the specimens were: Specimen 7, 1350 K, +90 K -40 K; Specimen 8, 1370 K, +240 K -116 K; and Specimen 10, 1447 K, +43 K -34 K.

Typical post-test visual appearance of each type of specimen is shown photographically in figure 15. The location of a typical failure is shown in figure 16. The Inconel 617 specimens all have a green coloration as opposed to their gray color in the statically oxidized state. The HS188 specimens darkened markedly, and the exposed surface had an exterior layer with a "soot-like" appearance. The rear surface of all specimens of both superalloys retained the gray appearance. The R512E coated Cb752 specimens darkened during exposure.

4.1.2 Radiant Heating Tests

The radiant heating test exposures produced no significant visual appearance changes in the Inconel 617 specimens. The HS188 specimens were darker after exposure, but they did not have the "soot-like" layer evident after supersonic arc plasma wind tunnel exposures. The R512E coated Cb752 specimens also darkened during the radiant heating tests.

BEST DOCUMENT AVAILABLE

(a) Inconel 617, 38 cycles

(b) HS188, 38 cycles

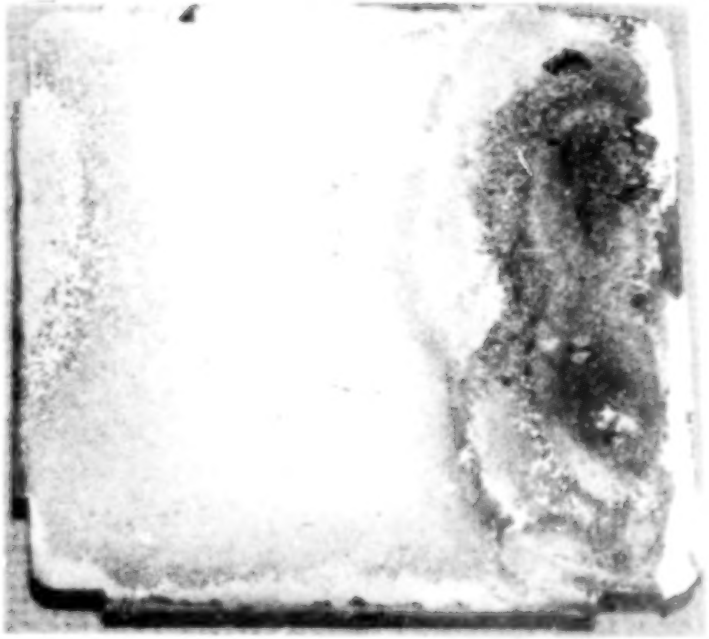

(c) R512E Coated Cb752, 38 cycles

Figure 15. Typical post-exposure appearance of supersonic arc plasma wind tunnel specimens.

BEST DOCUMENT AVAILABLE

Figure 16. Supersonic arc plasma wind tunnel specimen (HS188-G) showing a typical test failure.

Test conditions were multiple 60 min exposures to a test cycle consisting of: 1.5 min to maximum temperature, hold at maximum temperature for 28.5 min, cool for 30.0 min. Maximum temperatures were 1260 ±6 K for Inconel 617 and Haynes 188 materials and 1590 ±10 K for R512E coated Cb 752. During each cycle the specimens were exposed to slowly flowing dried air (see Section 3.2) at a pressure of 300 ±5 Pa. Triplicate specimens of each material were removed after 10, 20, 50 and 100 cycles for subsequent emittance, composition and morphology studies.

4.1.3 Sonic Velocity-Cold Air tests

A series of high velocity cold air flow tests was conducted in the HTEA in an attempt to reproduce the visual appearance and the spectral reflectance changes observed after the supersonic arc plasma wind tunnel tests of Inconel 617 specimens. The cold flow specimen was heated by passing current longitudinally through a 19 mm wide by 190 mm long strip of oxidized Inconel 617. A rectangular nozzle having an opening of 17 by 0.76 mm was located at a 45-deg angle to the surface of the specimen (figure 17). This nozzle produced a flow covering an approximate 23 by 19 mm area of the specimen. The specimen was instrumented with four platinum/platinum-rhodium thermocouples welded to the rear surface (figure 17). The spacing between thermocouples was 19 mm from T_2 to T_3 and 9.5 mm between T_1 and T_2 and between T_3 and T_4. The nozzle was centered between T_2 and T_3.

BEST DOCUMENT AVAILABLE

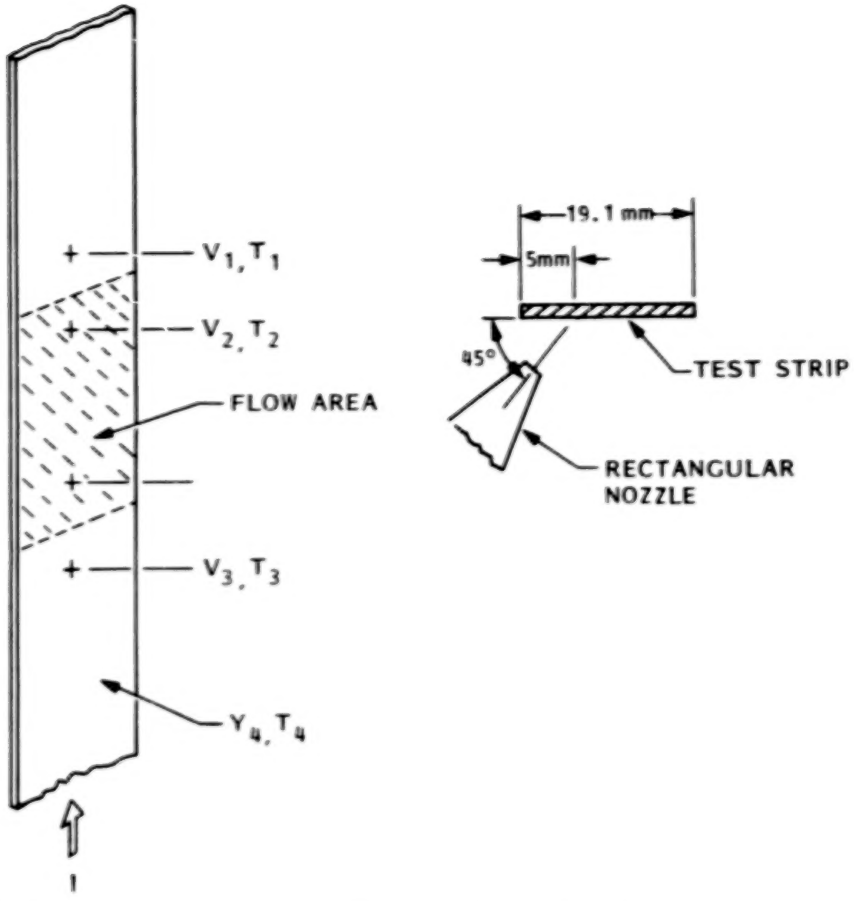

Figure 17. Schematic of sonic velocity cold air test.

The sonic velocity test used dried air which entered the flow system at a temperature of 297 K. Vacuum chamber pressure was varied to change mass flow. An initial measurement was made at a chamber pressure of 1 Pa (no flow) to obtain a calorimetric measurement of radiation loss. This was done by adjusting the current to give a temperature of 1255 K (as determined by thermocouples and an optical pyrometer viewing the front or flow surface). The current and voltage drops were measured, and the radiative power was calculated as $(V_2-V_3)I$. Total hemispherical emittance was calculated from the test data using

$$\epsilon_{TH} = \frac{(V_2 - V_3)I}{(2A_{2-3} + A_{edge})\,\sigma(T_{2-3})^4}$$

and the measured value was 0.869. This value is slightly greater than the total normal emittance of 0.85, giving a ratio of $\epsilon_{TH}/\epsilon_{TN}$ of 1.02.

Flow was then introduced through the nozzle, and the current was increased to give the same temperature as for the no-flow case. The difference in power $(V_2-V_3) \times I$ between flow and no-flow conditions was equated to the convective loss using only the flow side surface area between V_2 and V_3. A series of tests was conducted at increasing mass flow rates to

experimentally determine the best transfer coefficient as a function of chamber and nozzle pressures.

A chamber pressure of 4.6 kPa was used for two 5-h exposure periods on a specimen. This test condition gave a heat transfer coefficient of 0.17 kg/m^2-s at an oxygen mole fraction of 0.32, corresponding to the supersonic arc plasma wind tunnel conditions of 0.30 kg/m^2-s and a 0.33 mole fraction of oxygen. Neither test provided the reflectance changes observed for supersonic arc plasma wind tunnel tests. The specimen was essentially unchanged and total normal and total hemispherical emittance values remained constant.

4.2 RADIATIVE PROPERTIES

Room temperature spectral normal reflectance and elevated temperature spectral normal and total normal emittance measurements were made to characterize the radiative properties in both the initial statically oxidized (or coated) condition and after each environmental exposure test. Reflectance data were used (1) to characterize a surface without subjecting the material to elevated temperatures in an environment which may differ from that of the exposure conditions and (2) to verify uniformity of radiative properties on an extended surface or between several specimens in their initial state. All of the emittance and reflectance data of this study are tabulated in Appendix B.

4.2.1 Stability of Specimens in HTEA

Initially, an experimental investigation was conducted to determine if the pressure and gas composition of the HTEA environment would alter the radiative properties of the specimens during the elevated temperature measurement process. This was done by exposing the materials to several different atmospheres at the maximum measurement temperature and measuring spectral normal and total normal emittance as a function of time at this temperature. A total exposure period of 90 min was selected to give a factor of five times the normal time period required to perform the emittance measurements. A temperature of 1367 K, which is 100 K above the static oxidation temperature, was initially specified in the contract for exposure testing of the superalloys. This was subsequently modified to 1260 K before exposure testing was started. The coated Cb752 testing was done at 1590 K.

The stability experiment was conducted using five specimens each of the statically oxidized Inconel 617 and HS188 superalloys and two specimens of the R512E coated Cb752. For the superalloys, the test atmospheres were argon and air at 263 Pa, air at 2630 Pa, dried argon at 263 Pa, and a vacuum of $<10^{-3}$ Pa. Total normal emittance measurements were initially made at 533, 811, 1089, and 1367 K (1260 K for the dried argon test), followed by spectral normal emittance measurements as a function of time at the maximum temperature for up to 90 min at temperature. The total normal emittance measurements were then repeated for the four temperatures. The Cb752 specimens were exposed to dried argon and dried air at 263 Pa and 1590 K, and a similar emittance measurement procedure was followed.

Table 10. Spectral Normal Emittance Data for Statically Oxidized Inconel 617 After Exposures for 90 min in the HTEA at 1367 K

Wavelength (μm)	Sample 1 (263 Pa Argon)		Sample 2 (263 Pa Air)		Sample 3 (2630 Pa Air)		Sample 4 (Vacuum)	
	Initial	Final	Initial	Final	Initial	Final	Initial	Final
1.0	0.81	0.79	0.82	0.81	0.80	0.76	0.78	0.74
1.5	0.84	0.82	0.85	0.84	0.83	0.81	0.77	0.72
2	0.84	0.83	0.85	0.85	0.84	0.82	0.76	0.70
3	0.83	0.83	0.85	0.84	0.84	0.82	0.76	0.66
4	0.85	0.83	0.85	0.85	0.86	0.84	0.74	0.66
5	0.77	0.82	0.78	0.82	0.79	0.81	0.74	0.63
6	0.77	0.82	0.81	0.84	0.78	0.80	0.72	0.61
7	0.82	0.81	0.82	0.81	0.82	0.82	0.68	0.59
8	0.79	0.81	0.81	0.83	0.82	0.81	0.68	0.57
9	0.79	0.86	0.81	0.87	0.80	0.84	0.70	0.56
10	0.82	0.87	0.84	0.89	0.83	0.88	0.72	0.55
11	0.87	0.88	0.89	0.88	0.86	0.89	0.74	0.56
12	0.91	0.89	0.88	0.90	0.89	0.90	0.76	0.58
13	0.94	0.95	0.92	0.92	0.93	0.92	0.81	0.59
14	0.91	0.96	0.92	0.95	0.94	0.97	0.84	0.59

Table 11. Spectral Normal Emittance Data for Statically Oxidized HS188 After Exposures for 90 min in the HTEA

Wavelength (μm)	Sample 1 (263 Pa Argon, 1367 K)		Sample 2 (263 Pa Air, 1367 K)		Sample 3 (2633 Pa Air, 1367 K)		Sample 4 (Vacuum, 1367 K)		Sample 20 (263 Pa Dry Argon, 1260 K)[a]	
	Initial	Final	Initial	Final	Initial	Final	Initial	Final	Initial	Final
1.0	0.80	0.85	0.80	0.74	0.82	0.78	0.65	0.66	0.82	0.84
1.5	0.82	0.87	0.82	0.81	0.84	0.83	0.83	0.66	0.82	0.84
2	0.80	0.85	0.73	0.82	0.83	0.83	0.79	0.64	0.83	0.87
3	0.72	0.82	0.76	0.81	0.80	0.83	0.74	0.60	0.80	0.83
4	0.71	0.79	0.70	0.80	0.78	0.84	0.72	0.56	0.78	0.81
5	0.65	0.73	0.69	0.73	0.72	0.78	0.60	0.52	0.73	0.76
6	0.52	0.70	0.62	0.70	0.63	0.77	0.55	0.49	0.66	0.74
7	0.45	0.65	0.49	0.66	0.58	0.72	----	0.48	0.56	0.70
8	0.47	0.59	0.44	0.62	0.58	0.69	0.55	0.50	0.55	0.66
9	0.57	0.57	0.49	0.57	0.63	0.68	----	0.52	0.59	0.61
10	0.65	0.61	0.58	0.57	0.69	0.69	0.64	0.52	0.68	0.68
11	0.70	0.67	0.68	0.63	0.77	0.71	----	0.54	0.74	0.76
12	0.70	0.77	0.76	0.73	0.84	0.79	0.77	0.56	0.78	0.80
13	0.63	0.81	0.74	0.82	0.84	0.87	----	0.55	0.83	0.82
14	0.55	0.79	0.67	0.85	0.81	0.93	0.61	0.56	0.81	0.82

(a) Argon Dried in P_2O_5 Column

BEST DOCUMENT AVAILABLE

Spectral normal emittance data for 5 and 90 min at 1367 K (or 1260 K) are given in Table 10 for Inconel 617 and in Table 11 for HS188. For both materials the vacuum environment produced a strong degradation of emittance resulting from dissociation, evaporation, or reduction of one or more components of the oxide layer. Some degradation is noted even for the initial data. In the case of the Inconel 617 sample, a metallic-appearing deposit was observed on the interior surfaces of the HTEA chamber after testing in vacuum. No significant change in emittance was observed for Inconel 617 in any of the other atmospheres. The HS188 spectral data show an increase in emittance in the 3 to 14 μm region with increasing time at temperature. This may be the result of traces of water vapor in both gas atmospheres or because the test temperature of 1367 K was significantly higher than the static oxidation temperature. A subsequent test was conducted at 1260 K using a P_2O_5 drying column in the gas flow system (dried to <1 ppm H_2O), and the stability of emittance in the low pressure argon atmosphere was improved at the lower temperature (see data for specimens 1 and 20 of Table 11).

Spectral reflectance data for pre- and post-HTEA measurements in the several environments are compared with the HTEA data in figures 18 and 19 for Inconel 617 and HS188, respectively, by using the relationship $\rho_\lambda = 1 - \epsilon_\lambda$ for the HTEA values. The pretest data, shown by the solid curve on each figure, are for a separate specimen prepared at the same time as the HTEA specimen.

Except for the vacuum exposure data, the Inconel 617 post-test spectral normal reflectance data are very consistent and generally in good agreement with those for the statically oxidized condition. This agreement confirms the nonreactive nature of the HTEA environment of either dried air or argon at low pressure with the preoxidized material. In the wavelength region of 1.5 to 12 μm, the room temperature reflectance data correlate very well with the elevated temperature results indicating a negligible temperature dependency of spectral emittance. In general, the agreement between these data is within the experimental error associated with the two types of measurements.

The difference seen in the room temperature reflectance data in the 7 to 8 μm region between the statically oxidized case and the post-HTEA exposures may be the result of a small compositional change due to the additional heat treatment by HTEA exposure in a lower pressure environment. The strong disagreement between reflectance and HTEA data converted to reflectance at 13 and 14 μm is probably the result of a strong temperature dependence of the complex refractive index in this region.

Comparison of the room temperature spectral normal reflectance data with elevated temperature spectral normal emittance data for HS188 shows large differences between the values derived from the two types of measurements (figure 19). These differences are again attributed to a temperature dependence of the spectral optical constants in the measurement region of 3 to 14 μm. This broad spectral range is not surprising considering the relatively thin oxide (see section 4.3.2) which forms on this material.

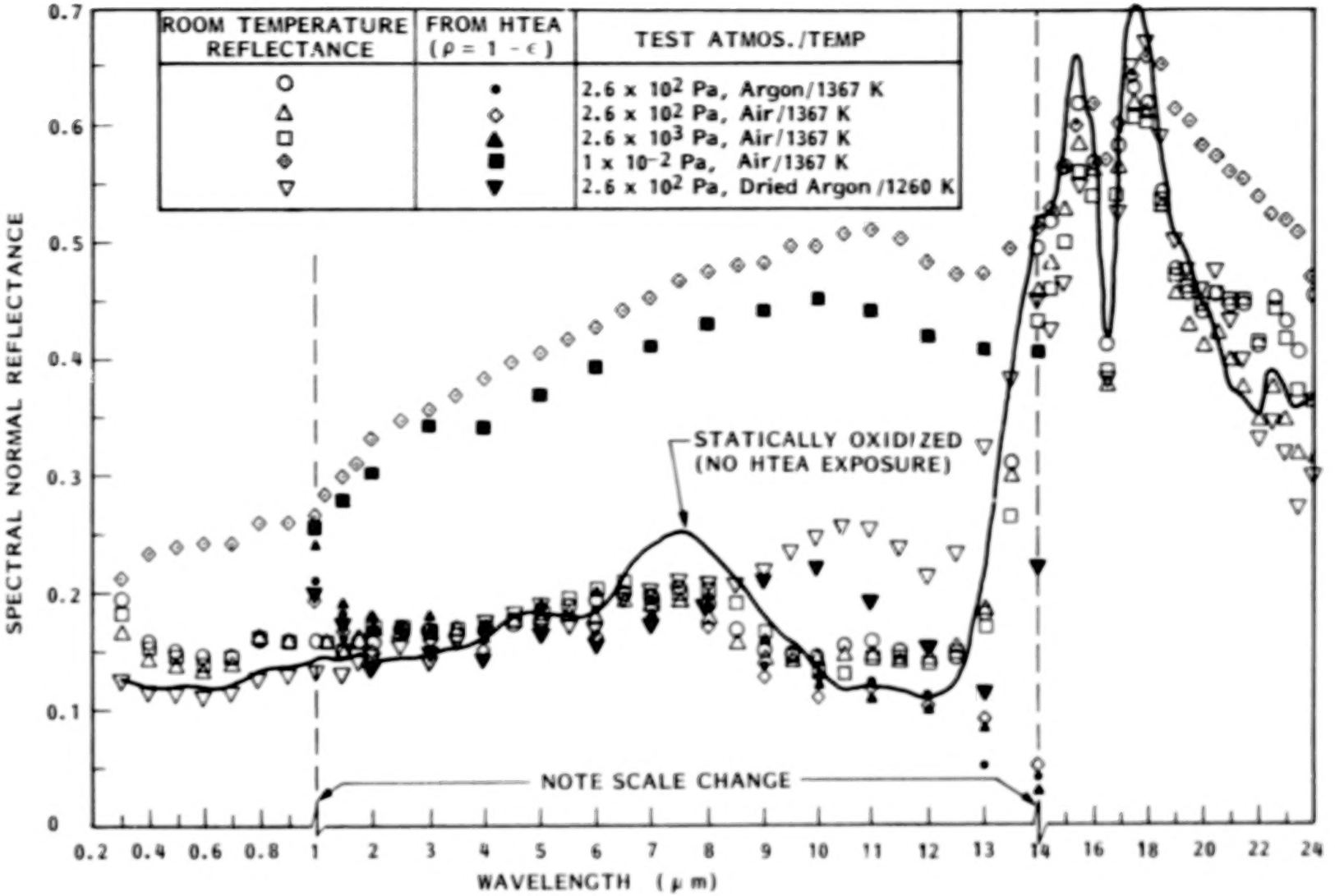
ROOM TEMPERATURE REFLECTANCE
FROM HTEA (ρ = 1 - ε)
TEST ATMOS./TEMP
2.6 x 10² Pa, Argon/1367 K
2.6 x 10² Pa, Air/1367 K
2.6 x 10³ Pa, Air/1367 K
1 x 10⁻² Pa, Air/1367 K
2.6 x 10² Pa, Dried Argon/1260 K
STATICALLY OXIDIZED (NO HTEA EXPOSURE)
NOTE SCALE CHANGE
SPECTRAL NORMAL REFLECTANCE
WAVELENGTH (μm)
0
0.1
0.2
0.3
0.4
0.5
0.6
0.7
0.2 0.4 0.6 0.8 1 2 3 4 5 6 7 8 9 10 11 12 13 14 16 18 20 22 24

Figure 18. Comparison of room temperature spectral reflectance data for statically oxidized Inconel 617 with reflectance computed from elevated temperature spectral emittance data.

BEST DOCUMENT AVAILABLE

BEST DOCUMENT AVAILABLE

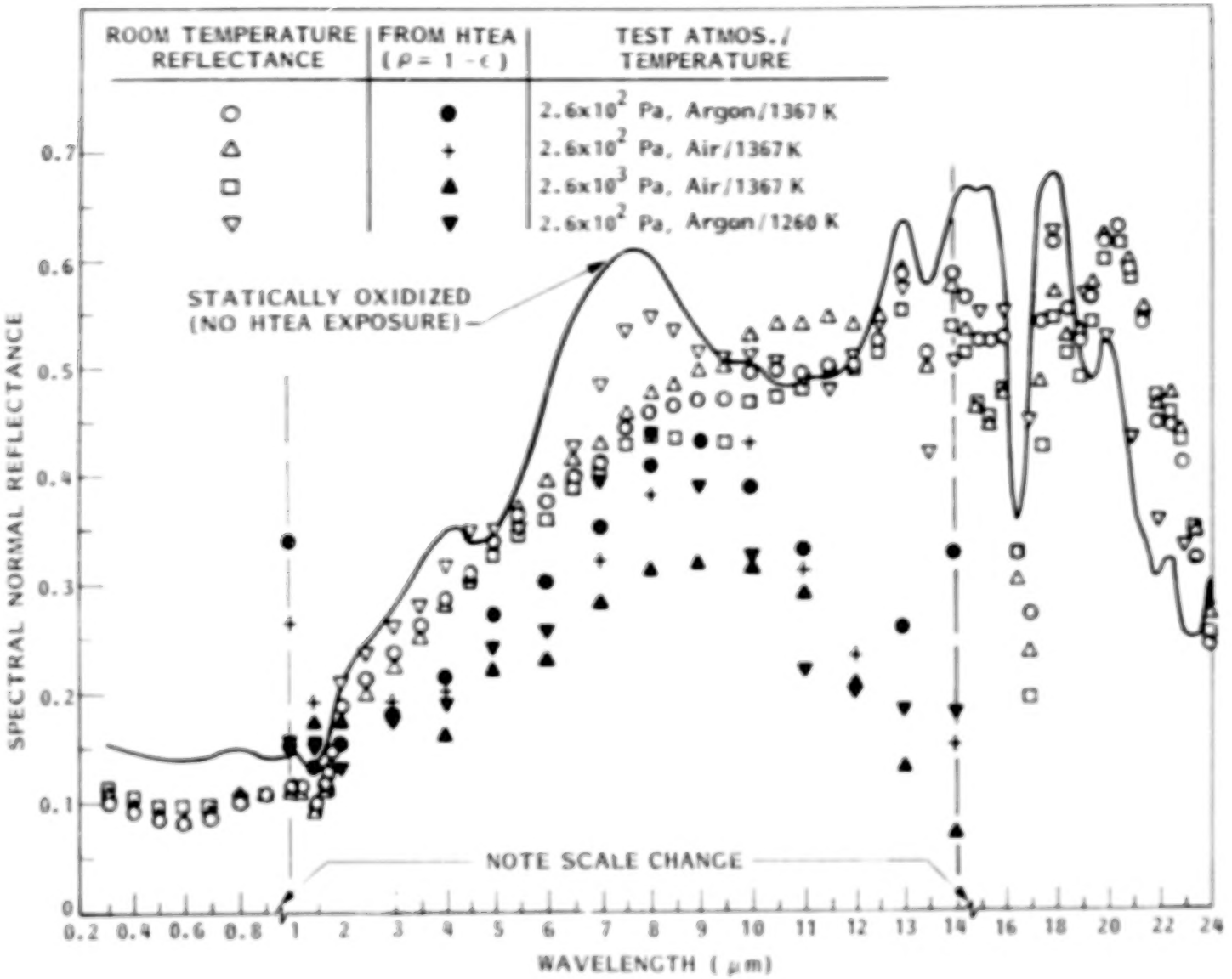

Figure 19. Comparison of room temperature spectral reflectance data for statically oxidized HS188 with reflectance computed from elevated temperature spectral emittance data.

The stability of the statically oxidized HS188 in the HTEA test environment is only fair at 1367 K in any of the test atmospheres. Based upon the spectral changes of 0.05 to 0.20 seen over the 90-min period for the 1367 K case, one could expect a 0.01 to 0.03 change during a normal HTEA test duration of 15 min. At the lower test temperature of 1260 K the differences between initial and final spectral emittance data are reduced by a factor of two, and during a typical test duration of 15 min the change would be 0.02 or less. Large differences are seen between oxidized and post-HTEA test spectral reflectance data in the 6 to 8.5 μm wavelength region. This is probably the result of a compositional change from the additional low pressure heat treatment.

Total normal emittance of statically oxidized Inconel 617 and HS188 as a function of temperature and time at maximum temperature in the HTEA are shown in Table 12 for the several gas atmospheres. Emittance was measured at successively increasing temperatures to the maximum temperature, which was then maintained for 90 min. The temperature was then decreased and emittance measurements were repeated. Total test time was 120 min. The data for Inconel 617 show good stability in the dried argon environment at 1260 K. The data for the other environments show a small increase in total normal emittance on the cooling cycle. The HS188 data show an increase in emittance with time in the non-dried gases at 1367 K. For the dried argon environment at 1260 K the stability is quite good. The presence of a very small amount of water vapor may be the cause of the observed changes for the 1367 K cases, or they may be due to an enhanced oxidation resulting from cobalt vapor at temperatures above 1335 K (ref. 12). For Inconel 617 the effect of the HTEA environment on total normal emittance is less than 0.01; for HS188 this effect is less than 0.02.

Testing the R512E coated columbium 752 material in an argon atmosphere at a pressure of 263 Pa and at 1589 K resulted in a significant degradation of the emittance from dissociation of the coating, as evidenced by a white-appearing deposit on the HTEA chamber surfaces after testing. Measurements made in air at 263 Pa showed no significant change in spectral or total emittance during the exposure period as shown in Table 13. A comparison of room temperature spectral reflectance data for pre- and post-HTEA exposure in air and argon at 263 Pa is given in figure 20. Little difference in reflectance in the 0.3 to 4.0 μm region is observed between air and argon environments. However, at wavelengths between 5 and 25 μm, the reflectance of the specimen tested in argon increases significantly (0.1 to 0.4 reflectance units) over that for the air environment specimen. These reflectance changes correlate well with the high-temperature emittance changes measured in an argon atmosphere. Because of the good stability observed in the air atmosphere, all subsequent measurements on the R512E coated specimens were done in dried air at 263 Pa pressure.

4.2.2 Inconel 617 Simulated Reentry Tests

Neither the supersonic arc plasma wind tunnel tests nor the radiant heating tests resulted in a degradation of the elevated temperature total

Table 12. Change in Total Normal Emittance of Statically Oxidized Inconel 617 and HS188 After 90 min Exposures at 1260 K and 1367 K in Several Types of Atmosphere in the HTEA

Inconel 617

Temperature (K)	Atmosphere 263 Pa Argon	263 Pa Dried Argon	263 Pa Air	2630 Pa Air
533	0.71	----	0.72	0.72
811	0.82	0.82	0.83	0.82
1089	0.80	0.83	0.80	0.83
1260	----	0.84	----	----
1367	0.83	----	0.83	0.83
1367	0.84	----	0.84	0.83
1260	----	0.84	----	----
1089	0.79	0.83	0.81	0.85
811	0.85	0.83	0.84	0.85
533	0.76	----	0.75	0.75

HS188

Temperature (K)	Atmosphere 263 Pa Argon	263 Pa Dried Argon	263 Pa Air	2630 Pa Air
533	0.49	----	0.47	0.50
811	0.66	0.67	0.65	0.68
1089	0.73	0.79	0.74	0.76
1260	----	0.80	----	----
1367	0.73	----	0.75	0.79
1367	0.77	----	0.82	0.82
1260	----	0.81	----	----
1089	0.73	0.77	0.79	0.77
811	0.72	0.68	0.71	0.76
533	0.54	----	0.53	0.58

Table 13. Change in Spectral Normal and Total Normal Emittance of R512E Coated Cb752 in Dried Air and Argon Atmospheres After 90 min Exposures at 1590 K in the HTEA

	Sample 2 (263 Pa Dried Air)		Sample 1 (263 Pa Dried Argon)	
Wavelength (μm)	Initial	Final	Initial	Final
1.0	0.66	0.68	0.69	0.68
1.5	0.72	0.72	0.74	0.72
2	0.73	0.72	0.76	0.72
3	0.76	0.74	0.77	0.73
4	0.77	0.77	0.75	0.72
5	0.76	0.77	0.77	0.70
6	0.78	0.79	0.81	0.68
7	0.78	0.79	0.85	0.64
8	0.91	0.92	0.92	0.61
9	0.92	0.90	0.88	0.55
10	0.91	0.92	0.91	0.52
11	0.91	0.92	0.86	0.50
12	0.89	0.89	0.87	0.48
13	0.89	0.90	0.90	0.47
14	0.89	0.89	0.89	0.46
ϵ_{TN}	0.79	0.79	0.80	0.70

normal emittance of Inconel 617. At 1260 K, for example, total normal emittance was 0.85 in the statically oxidized state, and it increased to 0.91 with multiple exposure in the supersonic wind tunnel tests and to 0.88 in the radiant heating tests. Significant differences were observed in the spectral reflectance data for the two types of reentry tests at wavelengths less than 1 μm and greater than 14 μm. While these differences may be indicative of compositional changes, they occur in wavelength regions which have little influence on total emittance at the higher temperatures.

The increase in total normal emittance with type of test and number of test cycles is summarized in Table 14. These data show good stability of total emittance for both types of test for the exposure times investigated. The radiant heating test results show an increase in total normal emittance of 0.03 up to 20 cycles (10 h at temperature), and no further change occurred to 100 cycles or 50 h at temperature. The supersonic arc plasma wind tunnel

BEST DOCUMENT AVAILABLE

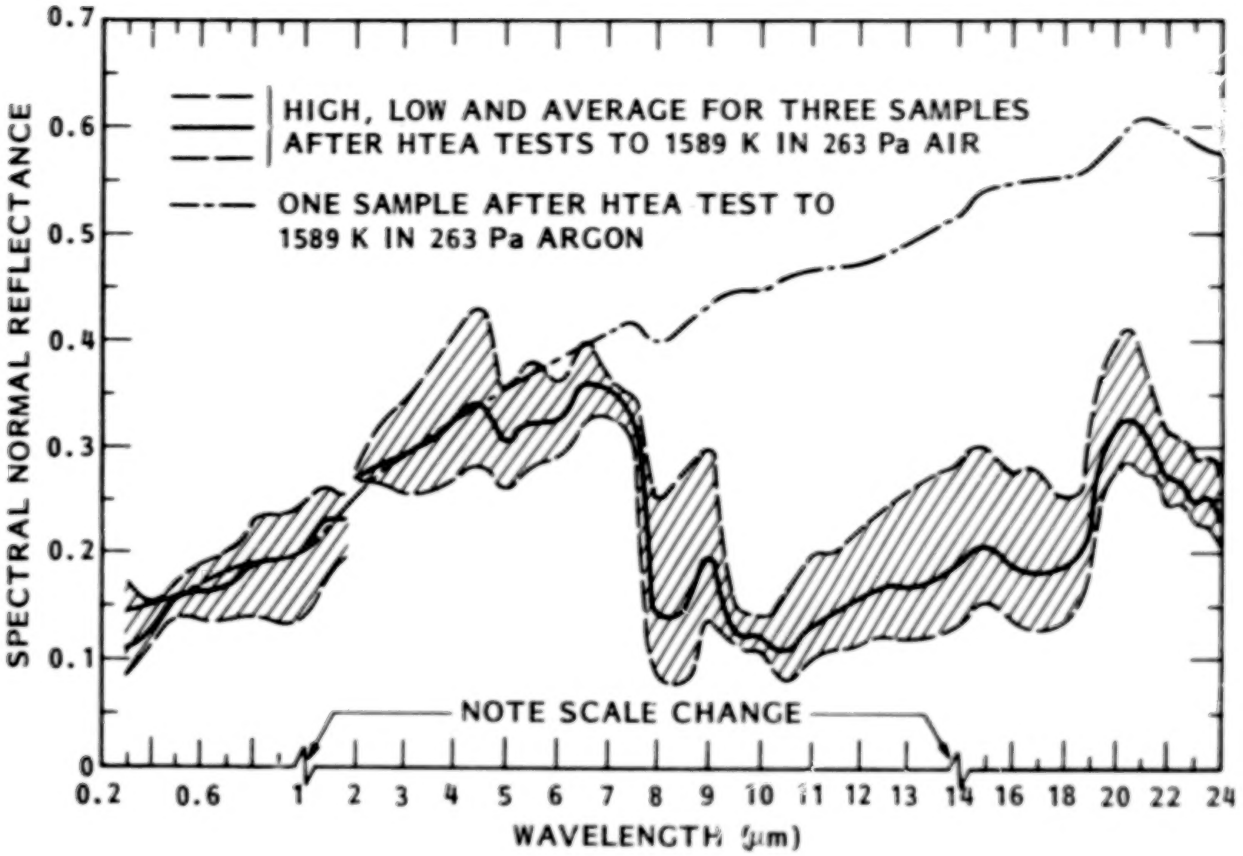

Figure 20. Comparison of pre- and post-HTEA test room temperature spectral reflectance data for R512E coated columbium 752.

testing resulted in an increase in total normal emittance from 0.85 initially to 0.91 after 20 cycles (5 h at temperature). For the 38-cycle test total normal emittance was 0.87, but there are insufficient data to conclude whether this lower value is the result of a longer exposure time or of variables in the test conditions. This specimen was tested during a period when chamber pressure fluctuations were observed, and it may have been exposed to short periods at significantly higher temperatures.

The repeatability of the elevated temperature spectral normal emittance data for triplicate specimen sets from each radiant heating test was good as shown by the data in Table B-2. In general, the spread in data at any wavelength was 0.03 or less, which is within the overlapping bands of maximum experimental uncertainty for any single data point. The total normal emittance of Inconel 617 as a function of radiant heating cycles at 1260 K is:

Number of Cycles	ε_{TN}
10	$0.86^{+0.02}_{-0.01}$
20	0.88 ± 0.00
50	$0.88^{+0.00}_{-0.01}$
100	0.88 ± 0.00

Figure 21 illustrates the modest temperature dependence of total normal emittance of statically oxidized Inconel 167, both before and after simulated earth reentry tests, in the temperature range of 800 to 1260 K. This is due to the relatively gray spectral emittance and the small observed change in spectral emittance with temperature over the wavelength region of 2 to 12 μm (c.f. Figures 22, 23, 24 and 25).

The effect of temperature on the spectral normal emittance of Inconel 617 is illustrated in figures 22 through 24 for statically oxidized (no reentry exposure) and supersonic arc plasma wind tunnel test and radiant heating test specimens. Spectral normal emittance increases slightly, typically on the order of 0.02 to 0.04, over the temperature range of 800 to 1260 K in the wavelength interval of 2 to 12 μm. At 13 and 14 μm a significantly greater temperature dependence of spectral emittance is observed. The change in spectral emittance with temperature is nearly the same for the statically oxidized and the reentry simulation test specimens over the wavelength interval of 2 to 12 μm.

BEST DOCUMENT AVAILABLE

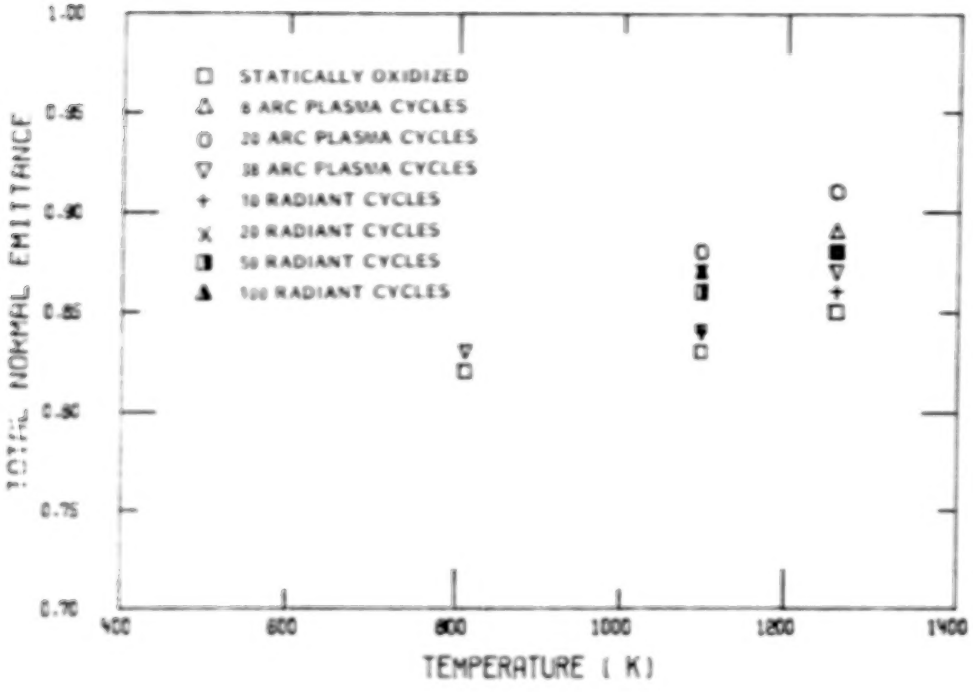

Figure 21. Total normal emittance of Inconel 617 as a function of temperature for the statically oxidized and reentry simulation test specimens.

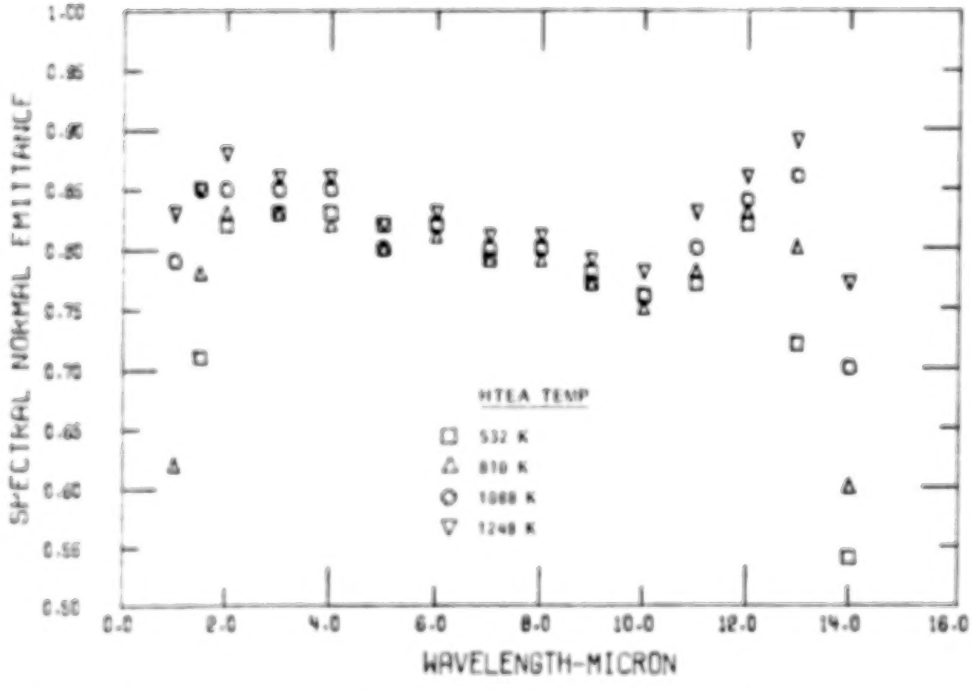

Figure 22. Spectral normal emittance of statically oxidized Inconel 617 as a function of temperature.

BEST DOCUMENT AVAILABLE

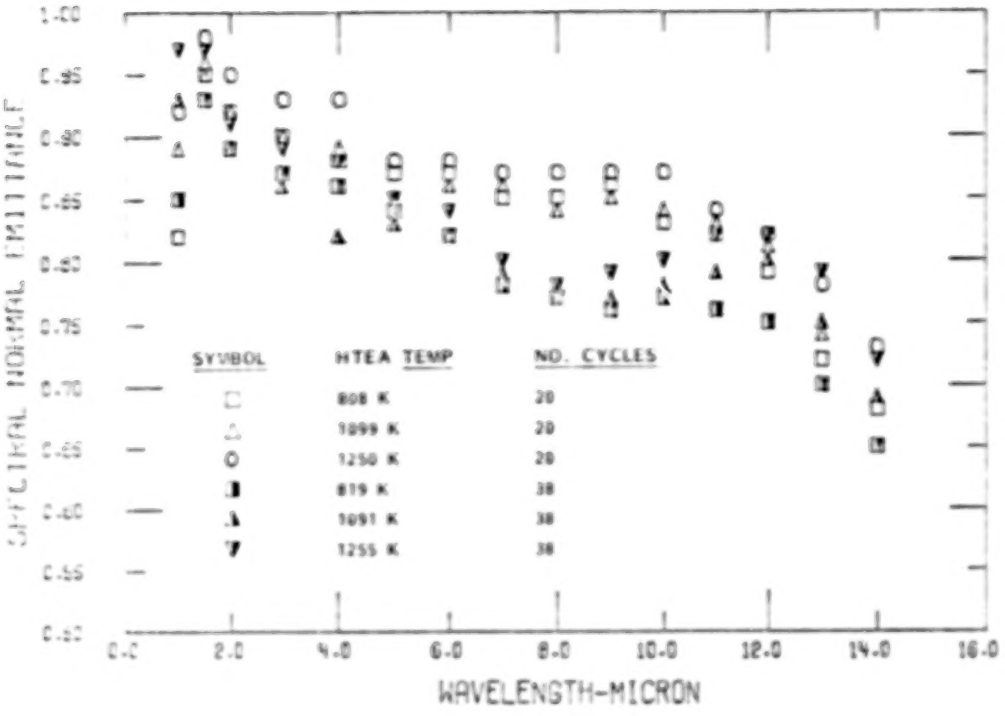

Figure 23. Spectral Normal emittance of Inconel 617 as a function of temperature for 20 and 38 cycle supersonic arc plasma wind tunnel tests.

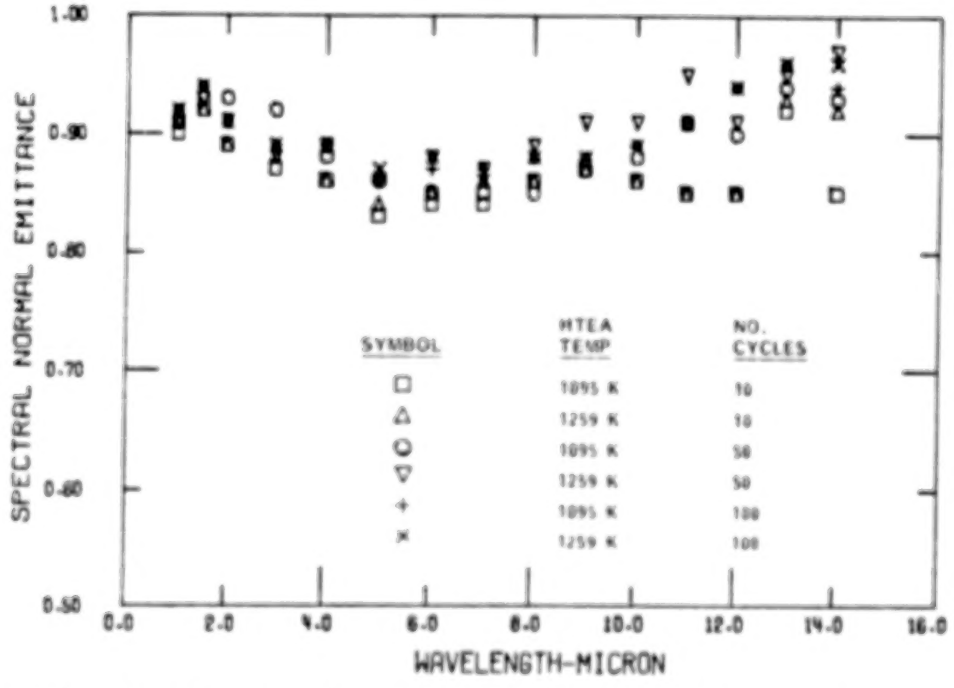

Figure 24. Spectral normal emittance of Inconel 617 as a function of of temperature for 10, 50, and 100 cycle radiant heating tests.

Table 14 Total Normal Emittance of Statically Oxidized Inconel 617 After Simulated Reentry Tests

Number of Cycles	Time at Temperature (h)	ϵ_{TN} at Two Temperatures			
		Radiant		Arc Plasma	
		1095 K	1260 K	1095 K	1260 K
0	0[a]	0.83	0.85	0.83	0.85
8	2	----	----	----	0.89
20	5	----	----	0.88	0.91
10	5	0.84	0.86	----	----
38	9.5	----	----	0.84	0.87
20	10	0.87	0.88	----	----
50	25	0.86	0.88	----	----
100	50	0.87	0.88	----	----

[a] Initial statically oxidized values

A very strong temperature effect is seen in the emittance data in the 12 to 14 μm region for the radiant heating test specimens, as is shown in figure 25(a), where the spectral normal emittance at 300 K is calculated as $\epsilon_\lambda = (1 - \rho_\lambda)$. The temperature dependence is greater than that for the supersonic arc plasma wind tunnel test specimens shown in figure 25(b). This difference may be the result of a compositional or crystallographic change in the oxide layer in the wind tunnel exposure environment as discussed in Section 4.3.1.

The 13-μm wavelength is at the beginning of the rather broad band reflectance structure seen in the spectral reflectance data of figure 18 for the statically oxidized specimens. This structure is similar to that seen from the Reststrahlen effect where vibrational frequencies of ions in a crystalline lattice give rise to enhanced reflectance for an absorbing material. The doublet structure is somewhat similar in appearance to that observed for quartz in the 9 to 12 μm wavelength region. Data for Cr_2O_3 were not found in the literature, but the Reststrahlen spectra for CoO, NiO, and TiO_2 are in the wavelength region of 12 to 30 μm, with maximum reflectances occurring at 26.6, 21.3, and 15.6 μm respectively.

BEST DOCUMENT AVAILABLE

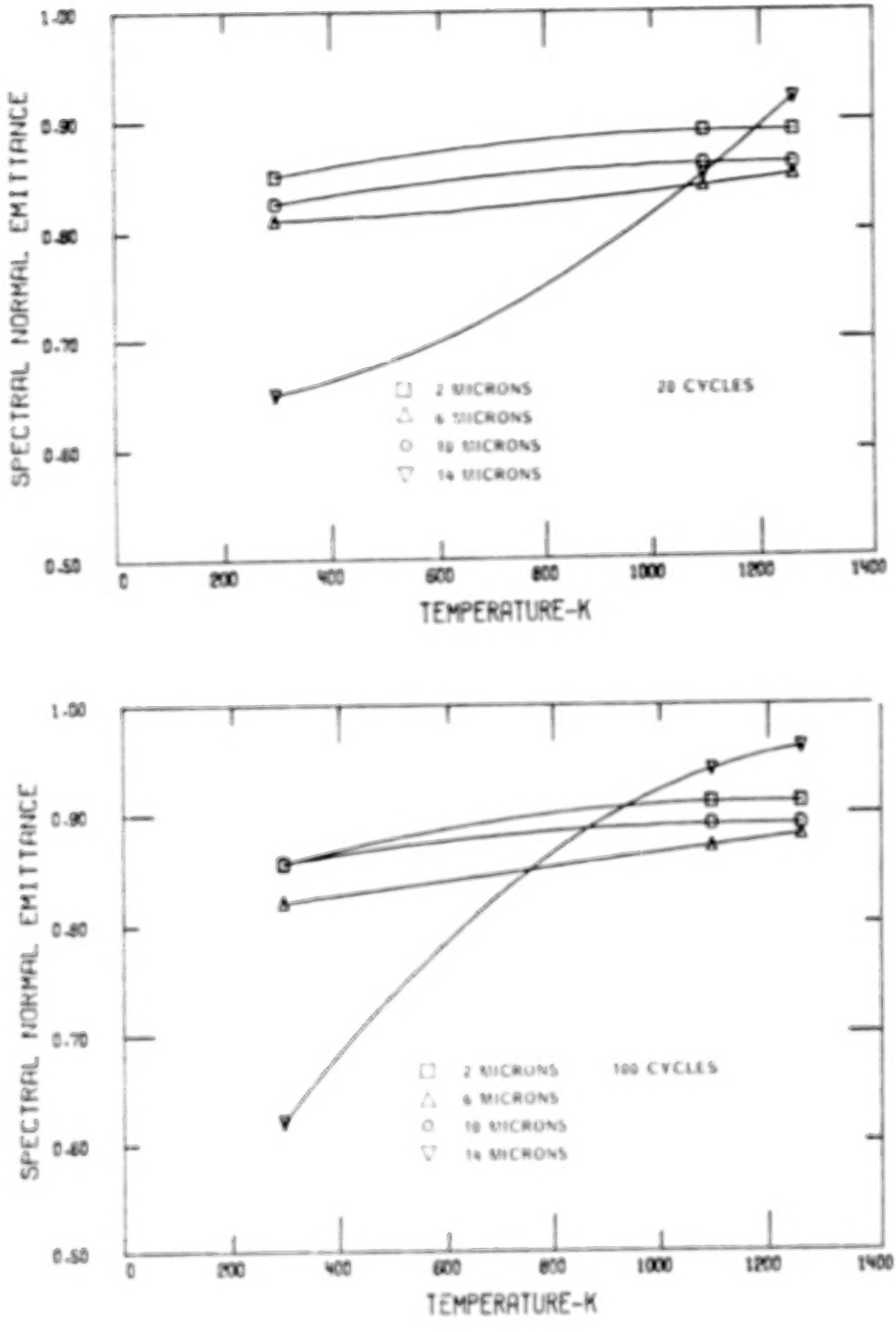

(a) Radiant heating test specimens

Figure 25. Temperature dependence of spectral normal emittance of Inconel 617 after simulated reentry tests.

BEST DOCUMENT AVAILABLE

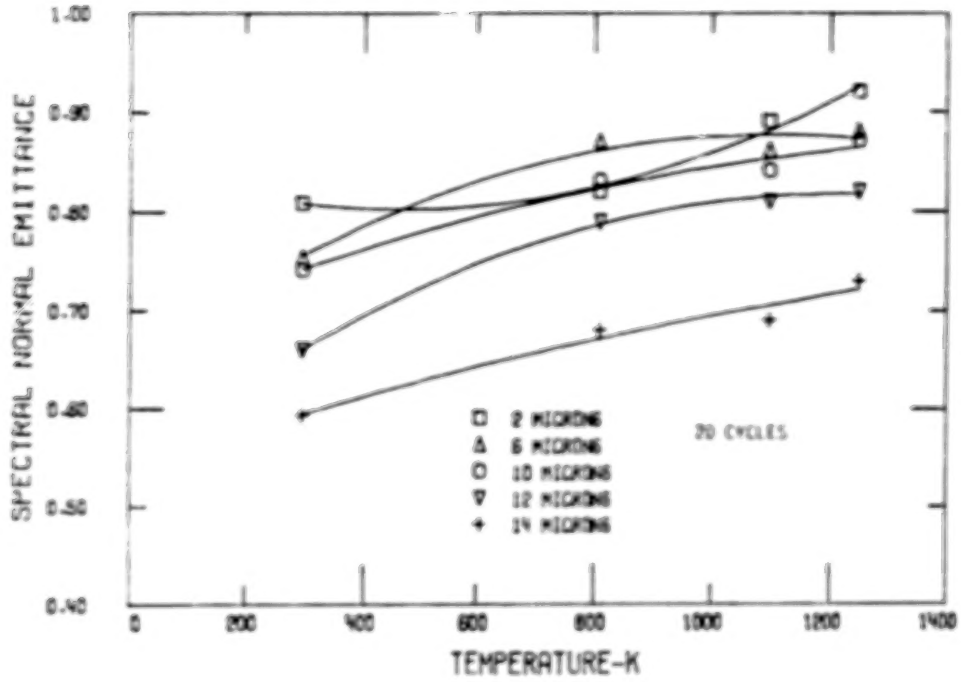

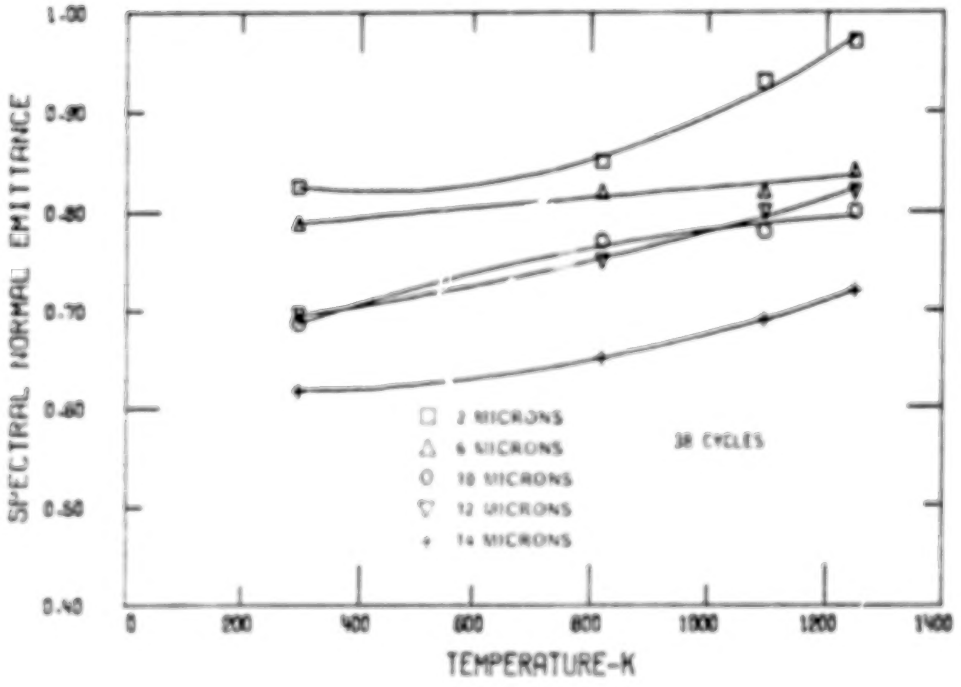

(b) Supersonic plasma wind tunnel test specimens

Figure 25 (Cont.)

The enhancement of reflection in absorbing media corresponds to frequencies near which the complex refractive index changes significantly with wavelength, and the Fresnel reflection (internal) becomes large, reducing the radiant energy to a narrower band. If either the real or imaginary parts of the refractive index become very large, the reflection coefficient approaches unity. For absorbing media such as Cr_2O_3, NiO, etc., the shift in vibrational frequency with temperature leads to a change in spectral absorption index, thereby depressing the strength of the reflection coefficient and increasing the emittance value.

Room temperature normal spectral reflectance data for the radiant heating test and supersonic arc plasma wind tunnel test specimens are shown in figures 26 and 27, respectively. Reflectance measurements were made after the HTEA emittance measurements were completed. The reflectance data for Cr_2O_3 plasma sprayed to a thickness of 75 to 100 μm on a tantalum substrate is shown in figure 28. Data for arc plasma wind tunnel test specimens show a large variation (1) with number of test cycles and (2) with respect to the statically oxidized data. The increase in reflectance over the statically oxidized case between 9 and 12 μm and the decrease in reflectance from 13 to 24 μm is the result of compositional change (see Section 4.3).

The structure of the reflectance spectra (see figures 26 to 28) is similar for all cases, but the amplitudes vary with exposure condition and duration. The eight cycle supersonic arc plasma wind tunnel test specimen shows the smallest reflectance amplitudes which then increase as the number of exposure cycles is increased. Higher reflectance values than for plasma sprayed Cr_2O_3 are seen for the statically oxidized specimen. This may be the result of the mixed oxide composition of the statically grown oxide or lattice variations introduced by melting and their rapid solidification in the plasma sprayed coating case. Since the peaks are not shifted between the thermal oxide and the plasma sprayed specimen, one would not expect lattice variations to be significant, and the amplitude differences are due either to thickness or mixed oxide effects.

Comparing the several exposure conditions, the reflectance decreases significantly between zero and 8 supersonic arc plasma wind tunnel exposures then increases at 20 and 38 cycles. The radiant heat tests initially decrease the reflectance peaks, and then they remain relatively constant with further exposure. The change in wavelength of the major amplitude peak from 16 to 14 μm for the 8 and 20 cycle supersonic arc plasma wind tunnel specimens may be the result of depletion of Cr_2O_3 or the formation of a spinel in at least the exterior portion of the oxide layer during initial testing with an increase on subsequent exposure to this environment. The radiant exposure specimens exhibit spectra similar to the statically oxidized case suggesting a predominantly Cr_2O_3 system.

The change in spectral emittance measured at 1260 K, with number and type of exposure cycles, is shown in figure 29. The supersonic arc plasma wind tunnel test for 8 cycles resulted in an increase in emittance throughout the 1.0 to 14 μm band. Between 8 and 20 cycles a smaller increase in emittance

BEST DOCUMENT AVAILABLE

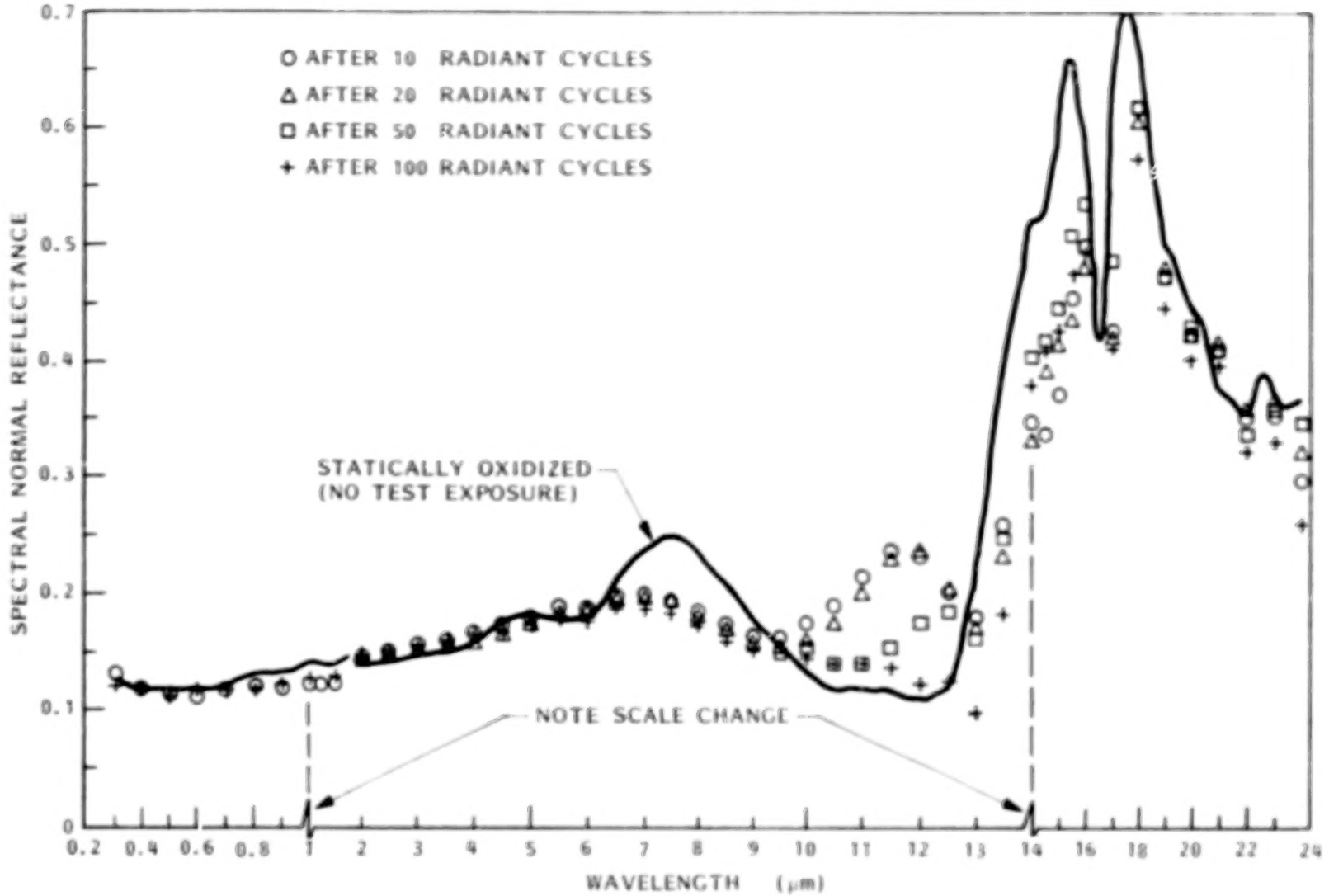

Figure 26. Room temperature (294 K) spectral normal reflectance of statically oxidized Inconel 617 after radiant heating tests and measurement in the HTEA.

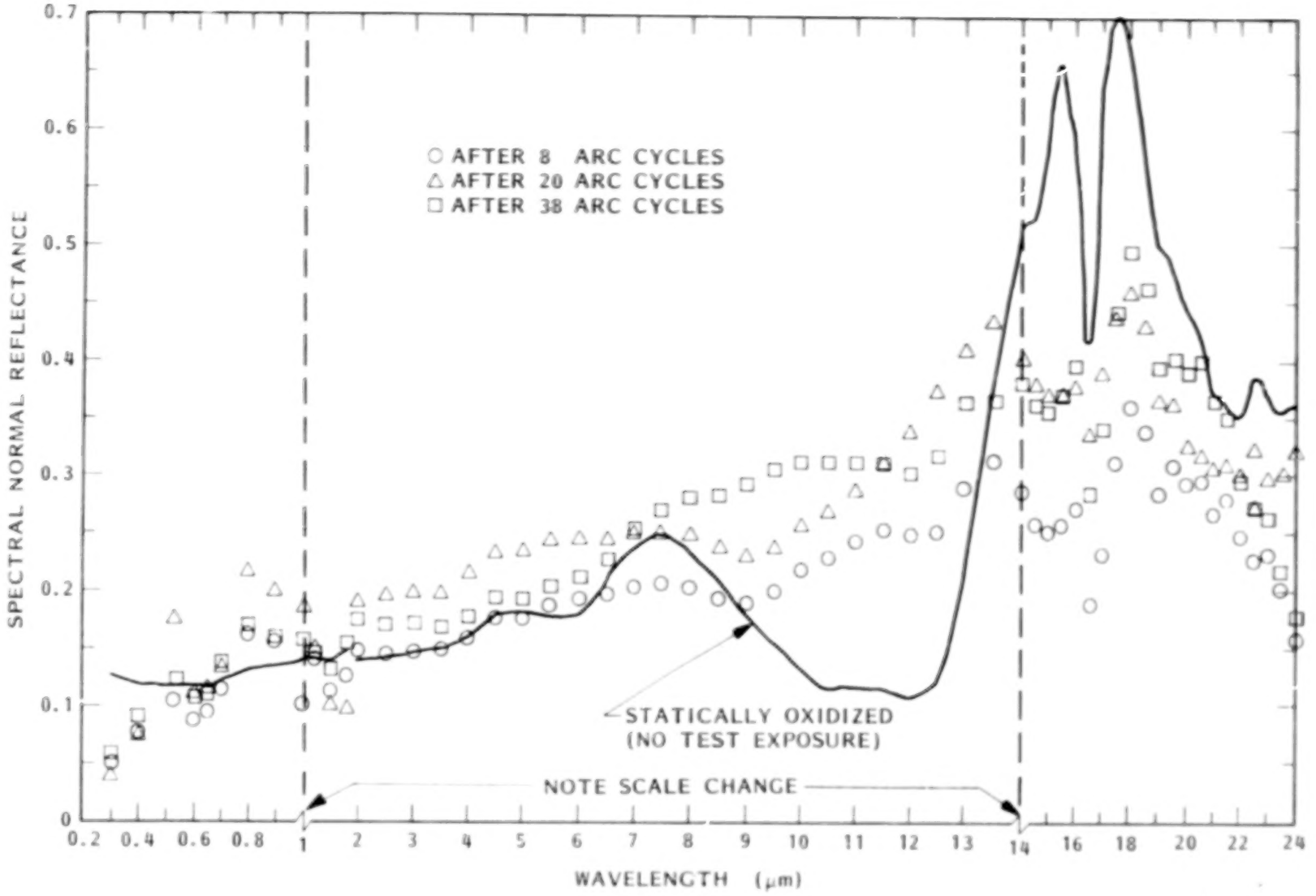

Figure 27. Room temperature (294 K) spectral normal reflectance of statically oxidized Inconel 617 after supersonic arc plasma wind tunnel tests and measurement in the HTEA.

BEST DOCUMENT AVAILABLE

BEST DOCUMENT AVAILABLE

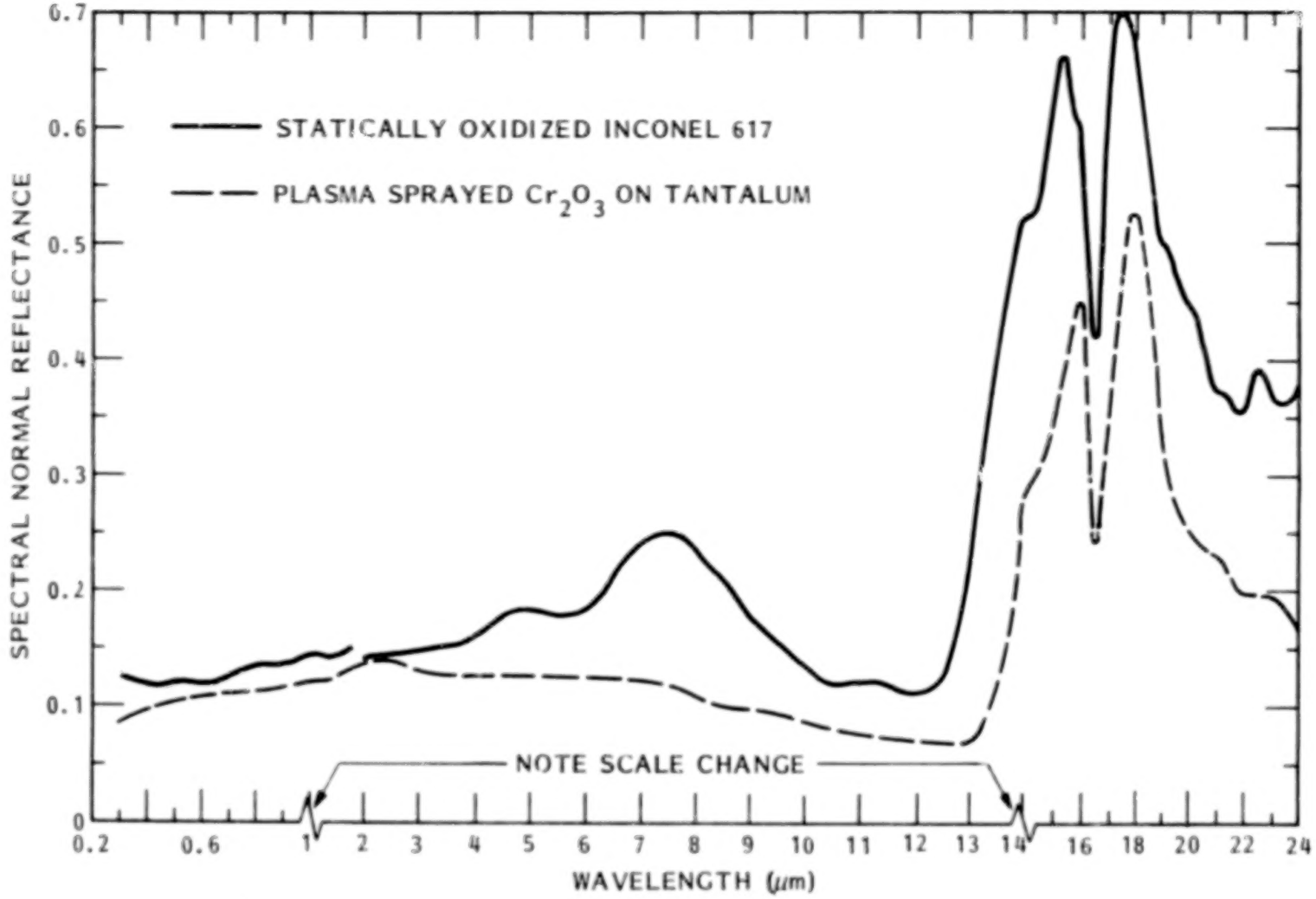

Figure 28. Room temperature (294 K) spectral normal reflectance of statically oxidized Inconel 617 and plasma sprayed Cr_2O_3

58

BEST DOCUMENT AVAILABLE

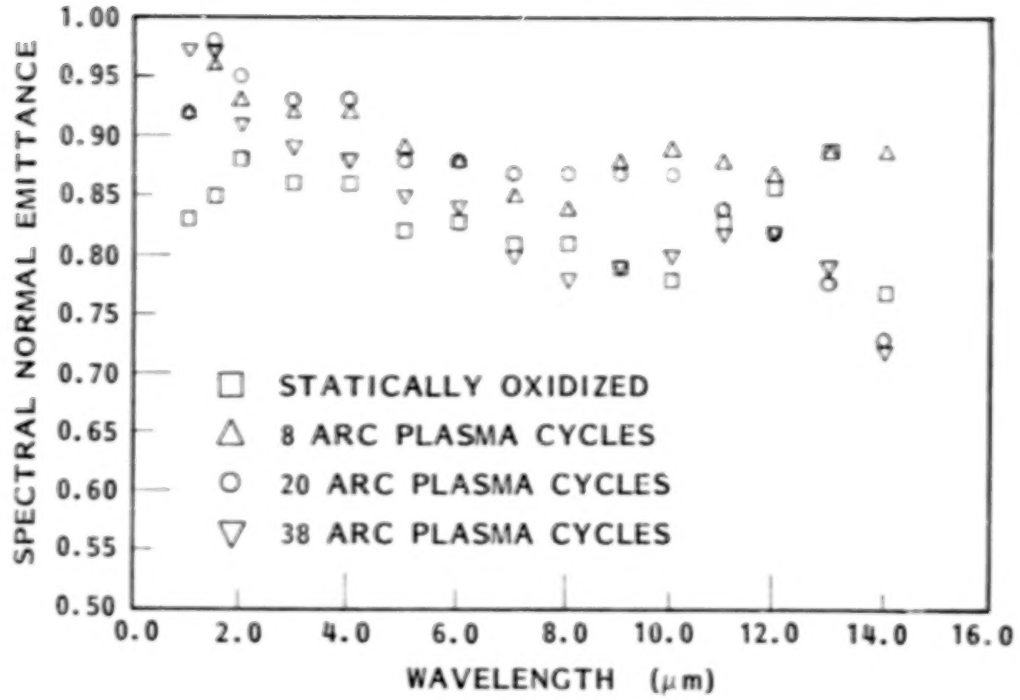

(a) Supersonic-arc plasma wind tunnel tests

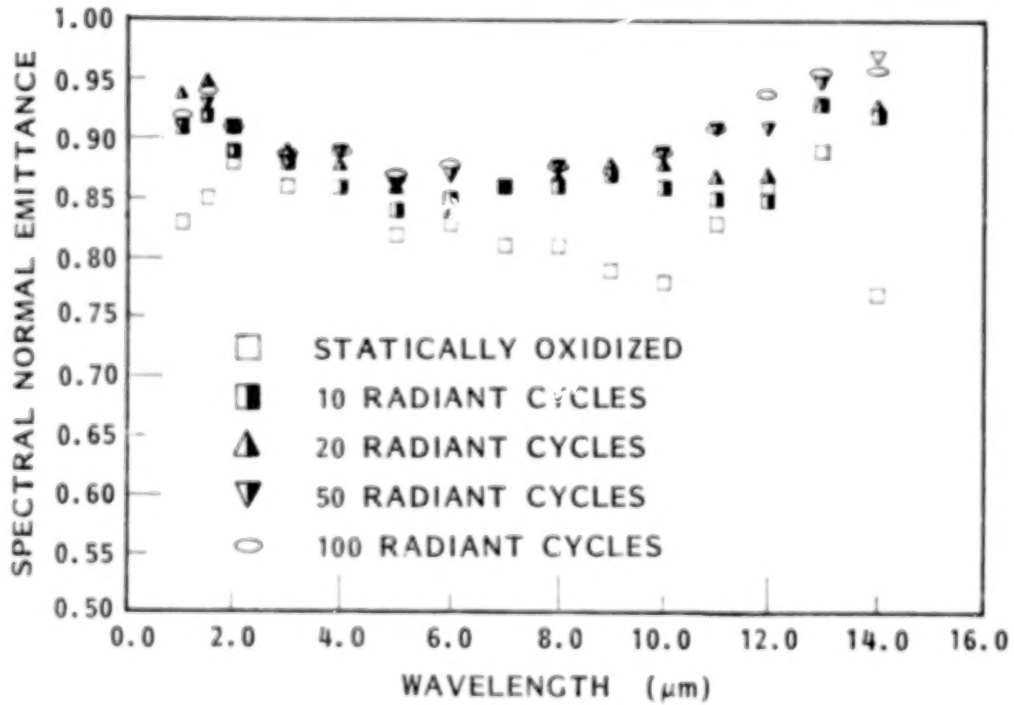

(b) Radiant heating tests

Figure 29. Spectral normal emittance of statically oxidized Inconel 617 at 1260 K after simulated reentry tests.

emittance is seen over the band of 1.5 to 8 μm, and a decrease is seen in the 8 to 14 μm band, with the greatest changes occurring at 13 and 14 μm. After 38 cycles a small decrease in emittance is observed at almost all wavelengths. This type of change again could suggest a cyclic oxidation process occurring in the supersonic arc plasma wind tunnel environment which is not seen in the radiant environment because of either different species being formed in the oxide layer or a large difference in reaction time for species and/or layer thickness changes between the two types of exposure.

In general, the values of total normal emittance computed from the elevated temperature spectral normal emittance data are in excellent agreement with the directly measured total normal emittance data. This agreement is shown in Table 15. Total hemispherical and total directional emittance data for a single statically oxidized Inconel 617 specimen are shown in Table 16. Integration of the directional data over 2π steradians gives at total hemispherical emittance of 0.82 at 1260 K, compared with the directly measured total hemispherical value of 0.85 The measured ratio of total hemispherical to total normal emittance is greater than the analytical prediction for dielectric optically smooth surfaces (ref. 8), but it is consistent with data in the literature (ref. 7) for oxidized superalloys. Integration of the directional data over 2π steradians gives a ratio closer to the analytical prediction.

Two additional supersonic arc plasma wind tunnel tests were performed by NASA/Langley Research Center personnel using their 100 kW facility (ref. 6). The test specimens, nominally 2.5 cm diameter disks, were tested for 8 h in a stagnation model at a surface temperature of 1260 K. The purpose of this test series was an attempt to (1) study the effects of oxygen dissociation on the stability of the oxide layer on Inconel 617 and (2) to compare any differences between stagnation and wedge flow. One test was to be conducted at a supersonic Mach number with low free stream enthalpy so that the oxygen in the boundary layer was essentially the molecular species. A second supersonic Mach number test was to be conducted at high enthalpy so that the oxygen was totally dissociated.

The low enthalpy test was run with supersonic flow at a bulk enthalpy of 3.6 MJ/kg or approximately one-third of the bulk enthalpy for the wedge flow tests. The flow field for the high enthalpy test was probably not supersonic, and the bulk enthalpy was not known to any reasonable degree of accuracy. Because of subsonic flow the bulk enthalpy could not be calculated from the heat transfer-pressure relationship. The arc energy balance gave a bulk enthalpy of 5.3 MJ/kg, which was estimated to be 20 to 30 percent below the correct value.

Both test conditions produced specimens having significantly different surface visual apperances from those after either the wedge model supersonic arc plasma wind tunnel tests or the radiant heating tests. The surface of the specimen exposed to the high enthalpy condition, specimen 617-2, was primarily yellow in color as opposed to the green-gray coloration after the wedge tests or the gray color after the radiant tests. The surface of low enthalpy test specimen 617-3 was a yellow-brown color.

Table 15. Comparison of Directly Measured Total Normal Emittance With Total Normal Emittance Calculated by Integration of Spectral Normal Emittance Data for Statically Oxidized Inconel 617

	Total Normal Emittance	
Temperature (K)	Calculated From Spectral Data	Measured Directly
533	0.76	0.79
811	0.80	0.82
1089	0.83	0.83
1255	0.84	0.85
1367	0.84	0.84

Table 16. Total Hemispherical Emittance and Total Directional Emittance of Statically Oxidized Inconel 617

Total Hemispherical Emittance, ϵ_{TH}		Total Directional Emittance, $\epsilon_{T\theta}$ at 1260 K	
Temperature (K)	ϵ_{TH}	Angle θ Off Normal (deg)	$\epsilon_{T\theta}$
		0	0.835
811	0.82	21	0.830
		42	0.822
1089	0.84	51	0.813
		60	0.791
1260	0.85	69	0.743
		78	0.628

The arc plasma wind tunnel test spectral normal emittance data are shown in figure 30 together with room temperature spectral normal reflectance data, plotted as emittance ($\epsilon_\lambda = 1 - \rho_\lambda$). Specimen 617-2 [figure 30(a)] changed significantly during the initial 800 K test in the HTEA as shown by the differences between initial reflectance data and the 800 K emittance data as well as between initial and post-HTEA reflectance data from 0.3 to 2.2 μm, as shown in figure 31. The post-HTEA reflectance values are in good agreement with the elevated temperature spectral emittance data for the low enthalpy specimen 617-3. The reflectance and emittance data for this specimen are also in good agreement over the 1 to 14 μm region, figure 30(b).

The exposure condition in the Langley arc plasma wind tunnel may have produced a significantly different oxide layer composition from the Acurex wedge flow tests. This is supported by the major differences in reflectance data between specimens tested in the two facilities. Comparing the room temperature spectral reflectance data of figure 31 with those in figure 27 the spectra in the 12 to 24 μm wavelength region are totally different. The Cr_2O_3 type spectra are absent for the 617-2 and 617-3 specimens. Compositional differences probably exist between 617-2 and 617-3 because of the much higher reflectance exhibited by 617-2 in the 0.6 to 3 μm region.

Total normal emittance as a function of temperature for the specimens 617-2 and 617-3 is as follows:

	ϵ_{TN}	
Temperature (K)	617-2 (high enthalpy)	617-3 (low enthalpy)
810	0.88	0.88
1095	0.88	0.87
1260	0.83 - 0.88	0.85 - 0.86

Although both the visual appearance and the spectral reflectance data in certain wavelength regions differ considerably from those of the wedge model tests and the radiant heating tests, the elevated temperature total normal emittance of the oxidized Inconel 617 is relatively insensitive to exposure conditions. Also, it remains above 0.80 for all test conditions.

BEST DOCUMENT AVAILABLE

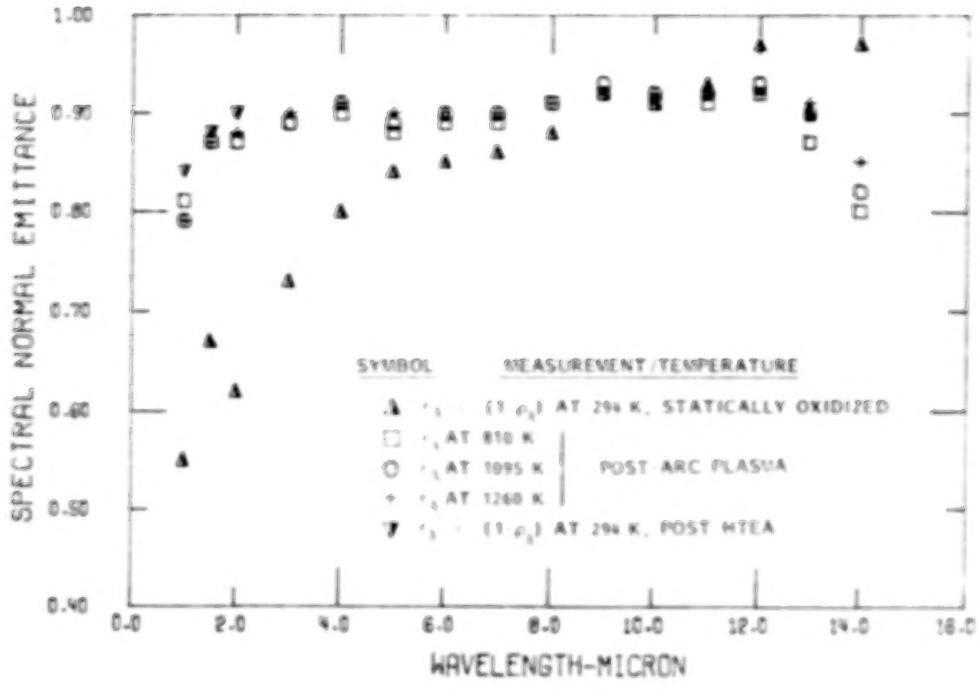

(a) Specimen 617-2

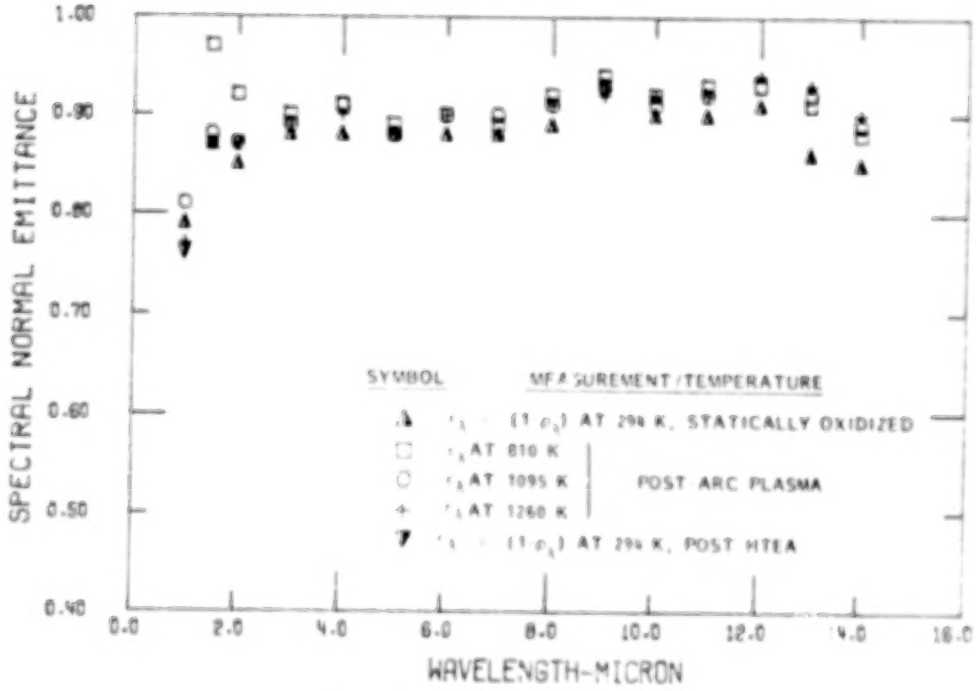

(b) Specimen 617-3

Figure 30. Spectral normal emittance of statically oxidized Inconel specimens 617-2 and 617-3 after arc plasma wind tunnel testing, stagnation flow.

BEST DOCUMENT AVAILABLE

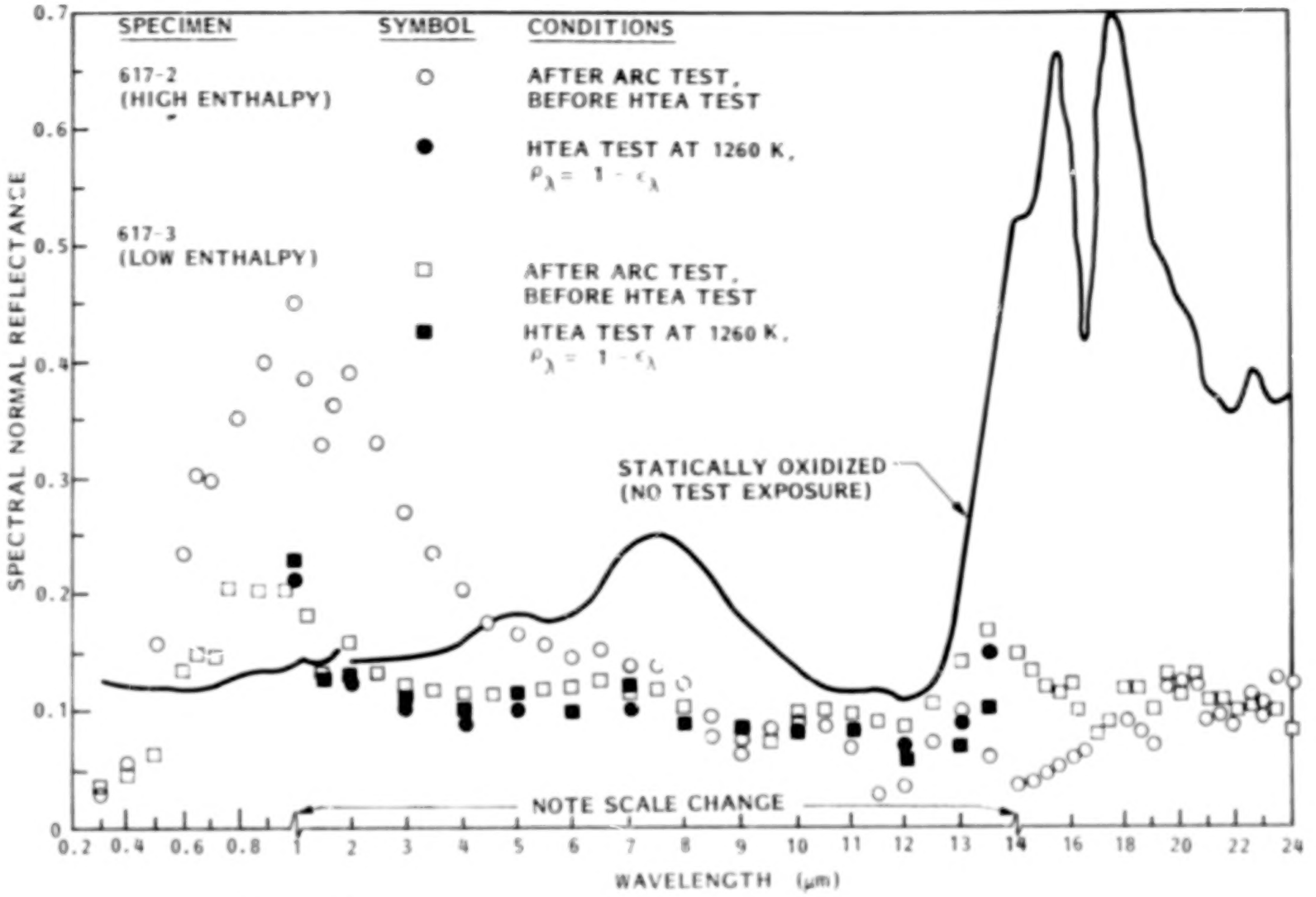

Figure 31. Room temperature (294 K) spectral normal reflectance of statically oxidized Inconel 617 specimens before and after testing in an arc plasma wind tunnel, stagnation model.

4.2.3 HS188 Simulated Reentry Tests

The elevated temperature total normal emittance of the statically oxidized HS188 specimens did not significantly change with exposure time in either the supersonic arc plasma wind tunnel tests or the radiant heating tests. At 1260 K the total normal emittance of the statically oxidized material was 0.81. After the supersonic arc plasma wind tunnel exposures, total normal emittance was 0.79 to 0.83, and after the radiant heating exposures it ranged from 0.78 to 0.86. The variation of total normal emittance with exposure type and number of cycles is summarized in Table 17. These data suggest a trend of the emittance initially decreasing with exposure and then increasing with further exposure for both environments. This can be seen from figure 32 where a change in emittance from zero exposure time is plotted as a function of exposure time. The rate of change is less for the radiant environment, which is reasonable considering the more energetic nature of the arc plasma flow.

Temperature dependence of total normal emittance is shown in figure 33. The temperature dependence decreases with increasing number of test cycles because of the increase in spectral emittance in the 1 to 4 μm wavelength region. Although total normal emittance measurements were not made as a function of temperature for the radiant heating test specimens, a similar decrease in the initial temperature dependence would again be expected because of the increase in spectral emittance observed at the shorter wavelength.

A comparison of spectral normal emittance at 1260 K for the statically oxidized, supersonic arc plasma wind tunnel tests, and radiant heating tests is shown in figure 34. Both types of reentry simulation tests initially result in a decrease in spectral emittance from the statically oxidized value in the 2 to 10 μm wavelength region. Spectral emittance then increases for longer exposure time. The results from the 20 cycle supersonic arc plasma wind tunnel test and the 10 and 20 cycle radiant heating tests show a decrease in spectral emittance. After 38 supersonic arc plasma wind tunnel test cycles and 50 and 100 radiant heating test cycles spectral emittance has increased to greater than the statically oxidized values. These data are consistent with the observed trends in total normal emittance. In the 12 to 14 μm wavelength region all reentry simulation tests decreased the spectral emittance from the statically oxidized values.

The shifts in spectral characteristics may be indicative of compositional changes in the oxide layer formed by both environments. However, the compositional changes may vary between the two types of test environments because of the differences seen in the reflectance spectra in the 12 to 14 μm region for the two types of conditions. One difference may be a chromium oxide increase in the surface layer for arc plasma exposure specimens because of the decrease in emittance at 13 and 14 μm (see figure 28 for Cr_2O_3). The statically oxidized condition may be represented by the radiative properties of a cobalt-nickel oxide(s) composition with some chromium oxide. During arc plasma exposure this layer becomes chromium oxide (or spinel) rich with a sacrifice of cobalt and/or nickel oxides. The temperature dependence of spectral emittance at 12 and 14 μm is more pronounced for the statically oxidized specimen than for the supersonic arc plasma test specimen (see figures 35 and 36).

BEST DOCUMENT AVAILABLE

Table 17. Total Normal Emittance of Statically Oxidized HS188 at 1260 K as a Function of Exposure in Supersonic Arc Plasma Wind Tunnel and Radiant Heating Tests

Number of Cycles	Time at Temperature (h)	ϵ_{TN} at 1260 K	
		Radiant	Arc Plasma
0	0	0.81	0.81
8	2	----	0.79
10	5	0.78	----
20	5	----	0.81
20	10	0.78	----
38	9.5	----	0.83
50	25	0.80	----
100	50	0.86	----

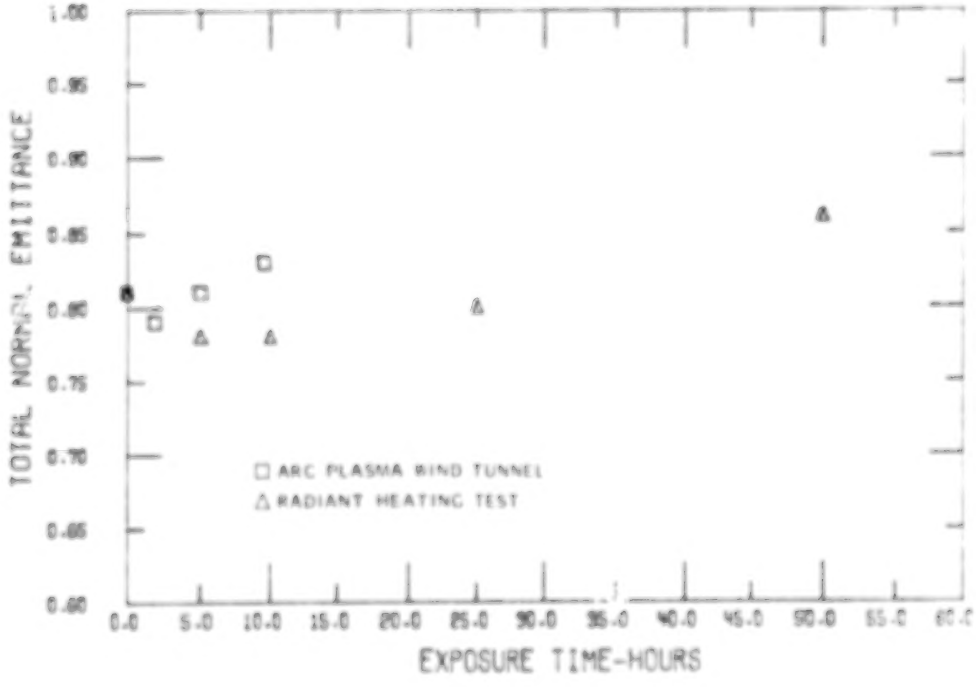

Figure 32. Change in total normal emittance of statically oxidized HS188 at 1260 K with exposure time in supersonic arc plasma wind tunnel and radiant heating tests.

BEST DOCUMENT AVAILABLE

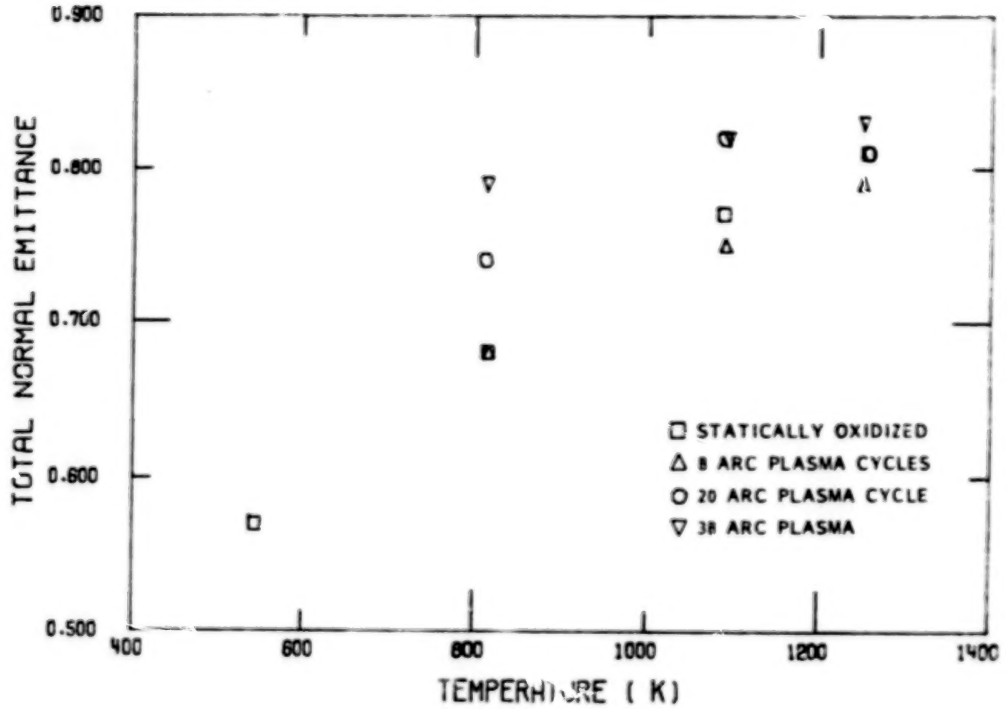

Figure 33. Temperature dependence of total normal emittance of statically oxidized HS188 after supersonic arc plasma wind tunnel tests.

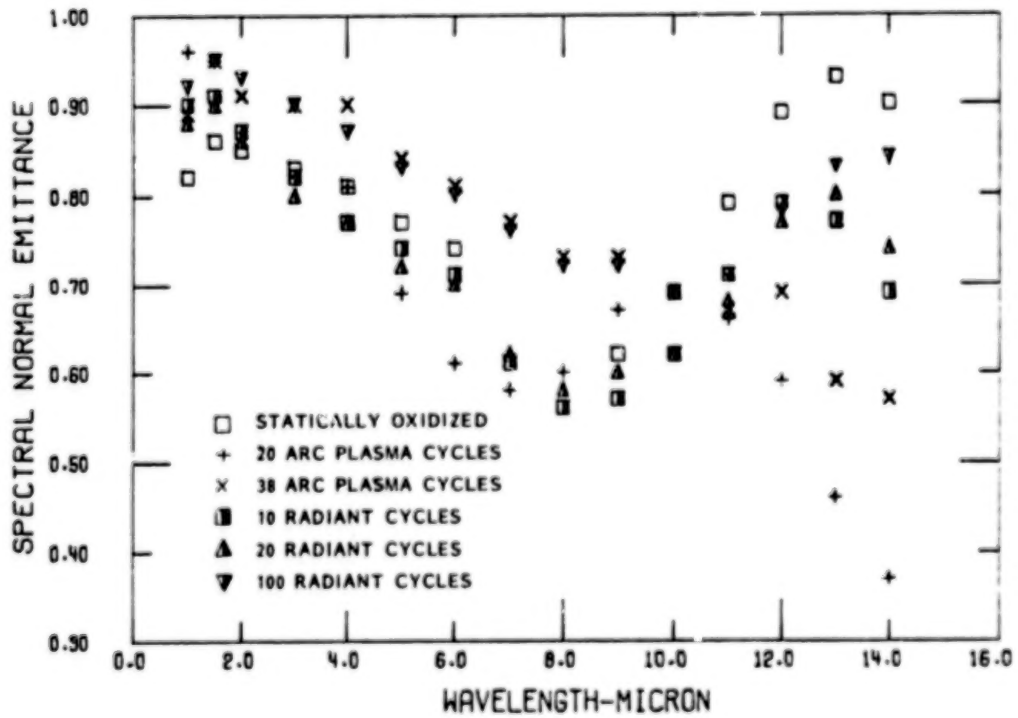

Figure 34. Spectral normal emittance of statically oxidized HS188 at 1260 K before and after supersonic arc plasma wind tunnel and radiant heating tests.

Room temperature spectral normal reflectance data for the reentry test specimens are presented in figures 37 and 38 for arc plasma and radiant heating tests, respectively. These data are consistent with the emittance values and follow the same trends seen in the change in spectral emittance with exposure.

4.2.4 R512E Coated Cb752 Simulated Reentry Tests

Both the supersonic arc plasma wind tunnel and the radiant heating tests produced a small increase in total normal emittance at elevated temperatures as shown in Table 18. Measurements were made on three specimens prior to any exposure testing, and the resultant values of total emittance were 0.80 ± 0.01 at 1260 K and 0.81 ± 0.02 at 1590 K. These data establish a baseline of initial sample-to-sample variation from which the reentry test results may be evaluated. Both types of reentry test produced an increase of 0.02 to 0.04 in total normal emittance. The 0.87 value for emittance for the 8 cycle supersonic arc plasma specimen (specimen 10) may be the result of aluminum contamination of the specimen surface. A nozzle burn-through occurred during the last exposure cycle of the test sequence. The nozzle material was aluminum, and the elemental analysis studies (see Section 4.3.3) showed significant amounts of aluminum on the surface of the coating.

In the as coated condition the total normal emittance is essentially independent of temperature. After the first 8 supersonic arc plasma wind tunnel cycles the total normal emittance shows a significant increase with a moderate increase in temperature. After 20 cycles this trend reverses and then, after 38 cycles, the temperature dependence is again positive. This changing sign of the temperature dependence of total normal emittance is consistent with the spectral normal emittance data. The total normal emittance data for the radiant heating tests show a positive temperature dependence for all number of test cycles. At 1260 K the total normal emittance decreases after 10 cycles and then increases with increasing number of cycles. The initial decrease is not observed in the data at 1590 K.

Spectral normal emittance at 1260 and 1590 K is shown in figures 39 through 42. No trend in temperature dependence of spectral normal emittance is seen from the data for the as coated specimens (figures 39 and 40). From integration of the spectral normal emittance data at 1260 and 1590 K the total normal emittance is independent of temperature over this temperature range, which is consistent with the directly measured total normal emittance data (Table 18). Spectral normal emittance data at 1260 and 1590 K for the reentry test specimens are shown in figures 41 and 42, respectively. Again, no general trends of temperature dependence of spectral emittance are evident.

BEST DOCUMENT AVAILABLE

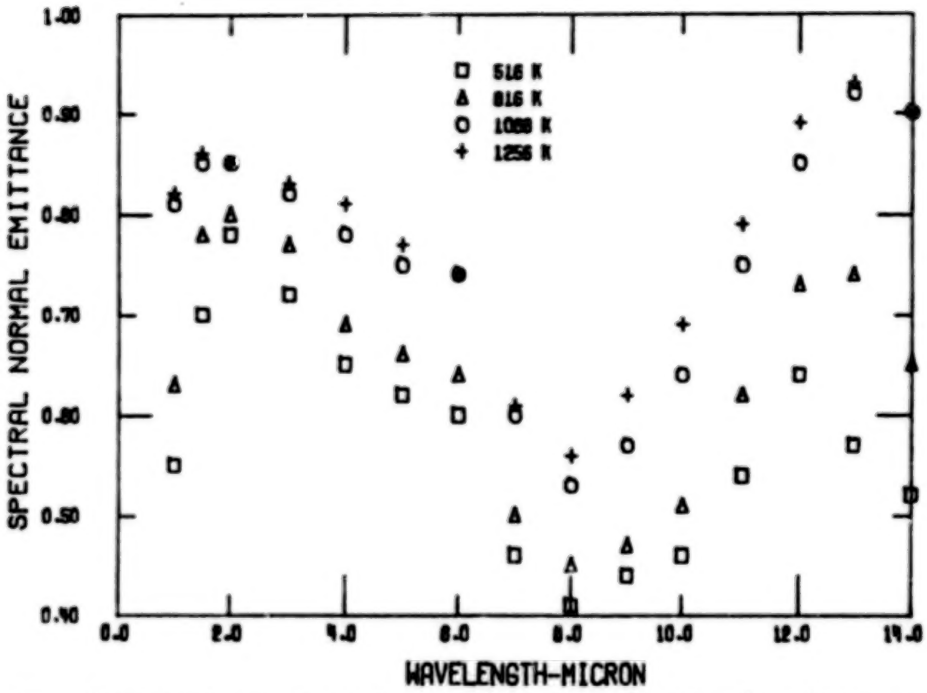

Figure 35. Temperature dependence of spectral normal emittance of statically oxidized HS188.

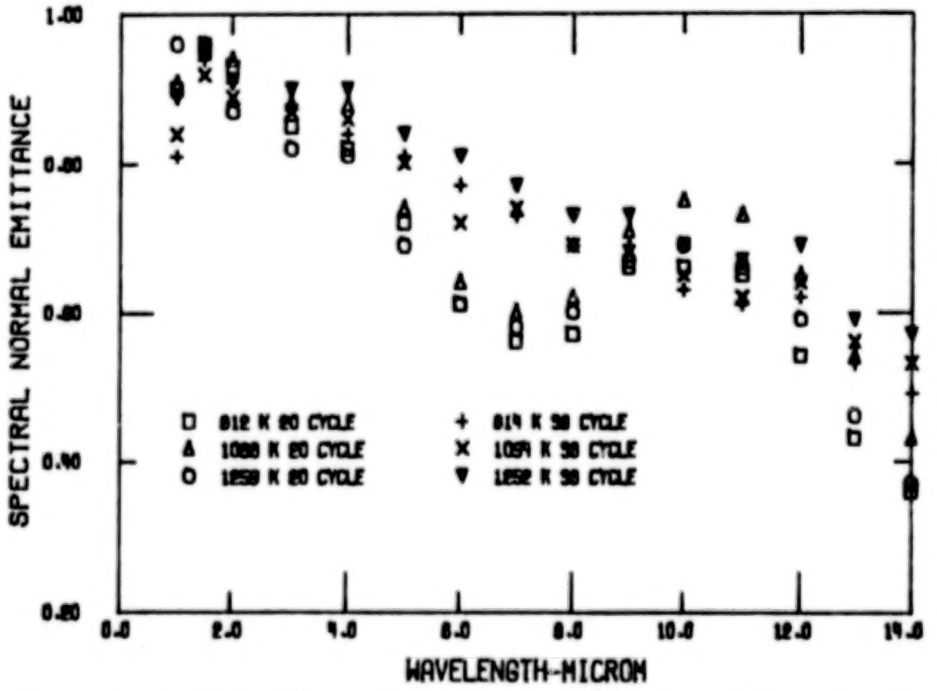

Figure 36. Temperature dependence of spectral normal emittance of statically oxidized HS188 after supersonic arc plasma wind tunnel tests.

BEST DOCUMENT AVAILABLE

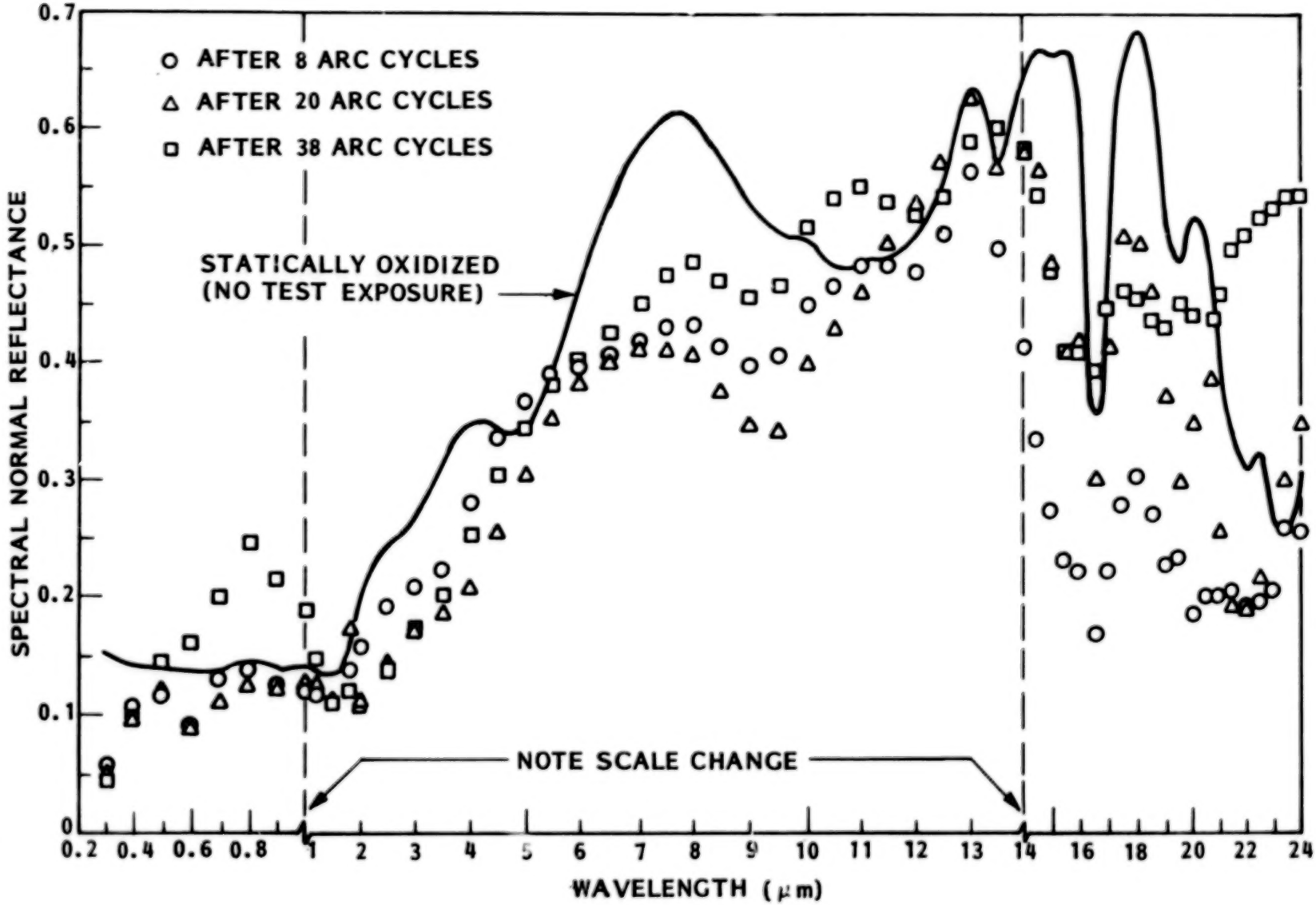

Figure 37. Room temperature (294 K) spectral normal reflectance of statically oxidized HS188 after supersonic arc plasma wind tunnel tests.

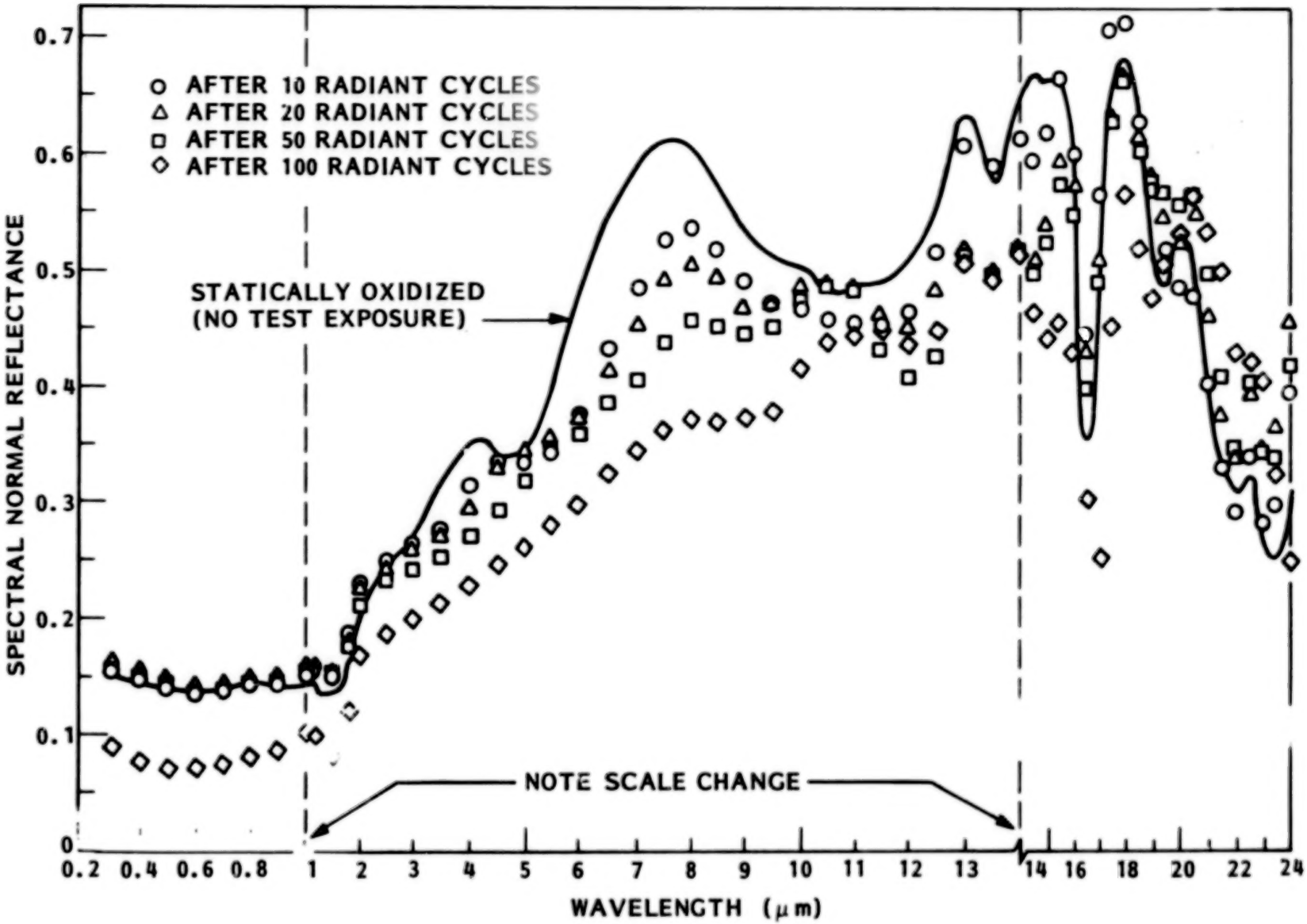

Figure 38. Room temperature (294 K) spectral normal reflectance of statically oxidized HS188 after radiant heating tests.

BEST DOCUMENT AVAILABLE

Table 18. Total Normal Emittance of R512E Coated Columbium 752 as a Function of Type of Simulated Reentry Test and Number of Test Cycles

Number of Cycles	Time at Temperature (h)	ε_{TN} at Two HTEA Temperatures			
		Radiant Test		Arc-Plasma Test	
		1260 K	1590 K	1260 K	1590 K
0	0	0.80	0.82	0.80	0.81
8	2	----	----	0.82	0.87
20	5	----	----	0.86	0.83
10	5	0.75	0.81	----	----
38	9.5	----	----	0.80	0.84
20	10	0.79	0.86	----	----
50	25	0.85	0.87	----	----

The room temperature spectral reflectance data in the post-reentry and HTEA tests are shown in figure 43. The reflectance data for both supersonic arc plasma wind tunnel and radiant heating tests are quite similar. Both test environments decrease reflectance for wavelengths of 1 μm or less and increase reflectance in the 1.5 to 3 μm region.

4.3 MORPHOLOGY, COMPOSITION, AND STRUCTURE

The thermal radiative properties of engineering materials are dependent upon the surface morphology (or topography) and the chemical and physical (or structural) characteristics of the material. In many cases the effects of surface topography, chemistry, and physical state may equal or exceed the influence of the intrinsic optical properties of the bulk material. Although the effects of these real surface conditions on radiative properties are not clearly understood, the analyses of morphology, composition, and structure provide some insight into the behavior of the thermal radiative properties after testing under several environmental exposure conditions.

BEST DOCUMENT AVAILABLE

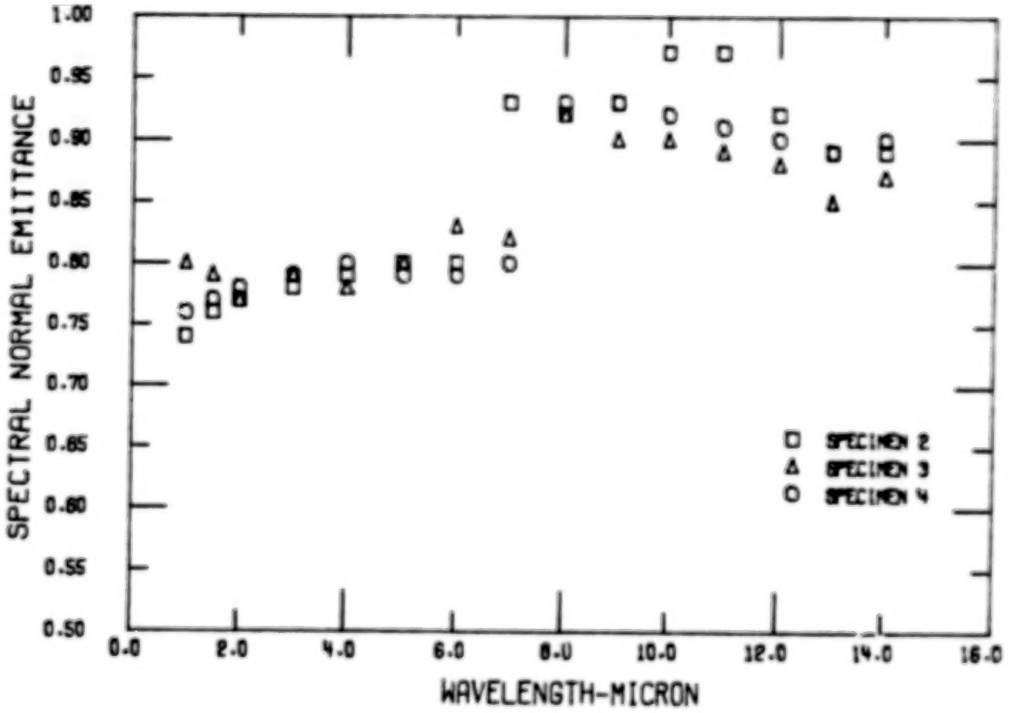

Figure 39. Spectral normal emittance of R512E coated Cb752 at 1260 K, no simulated reentry exposure.

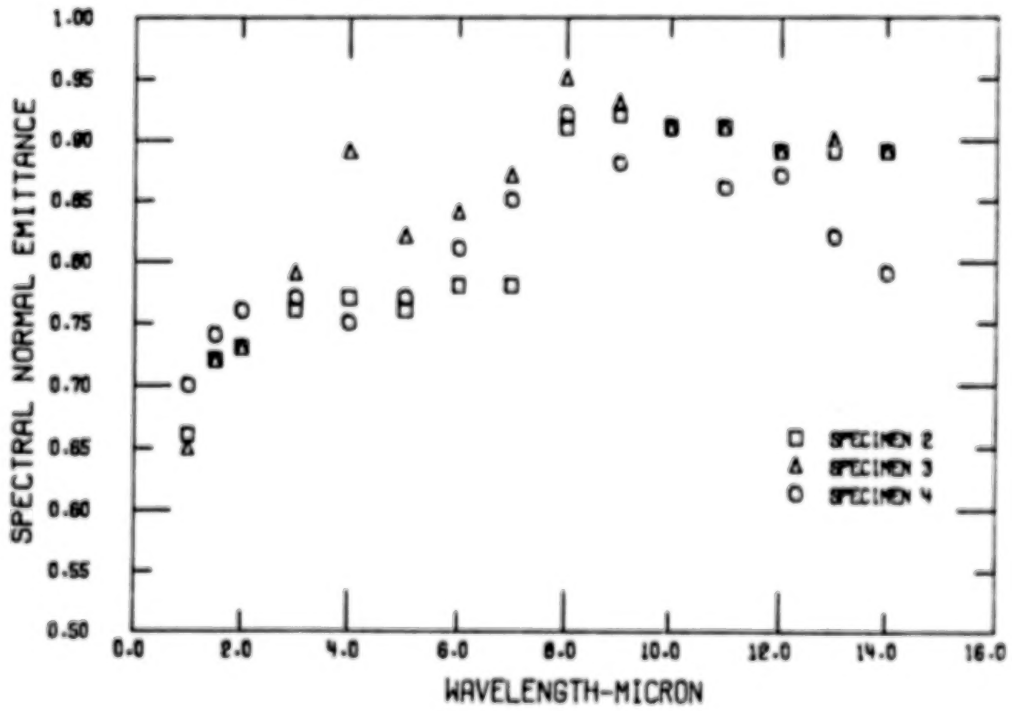

Figure 40. Spectral normal emittance of R512E coated Cb752 at 1590 K, no simulated reentry exposure.

BEST DOCUMENT AVAILABLE

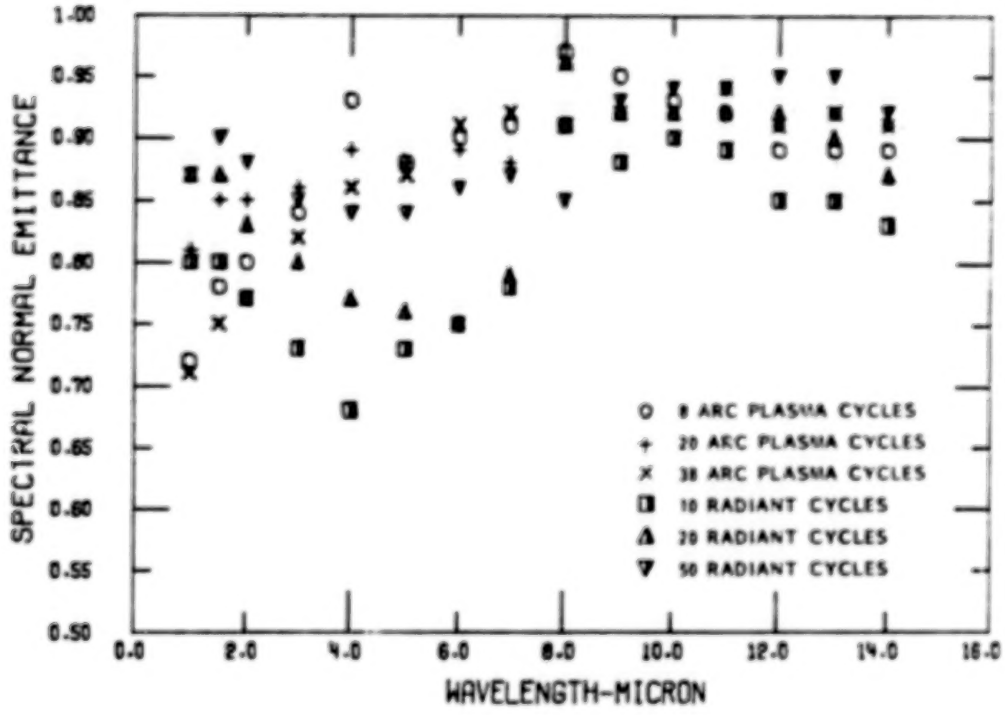

Figure 41. Spectral normal emittance of R512E coated Cb752 at 1260 K after supersonic arc plasma wind tunnel and radiant heating tests.

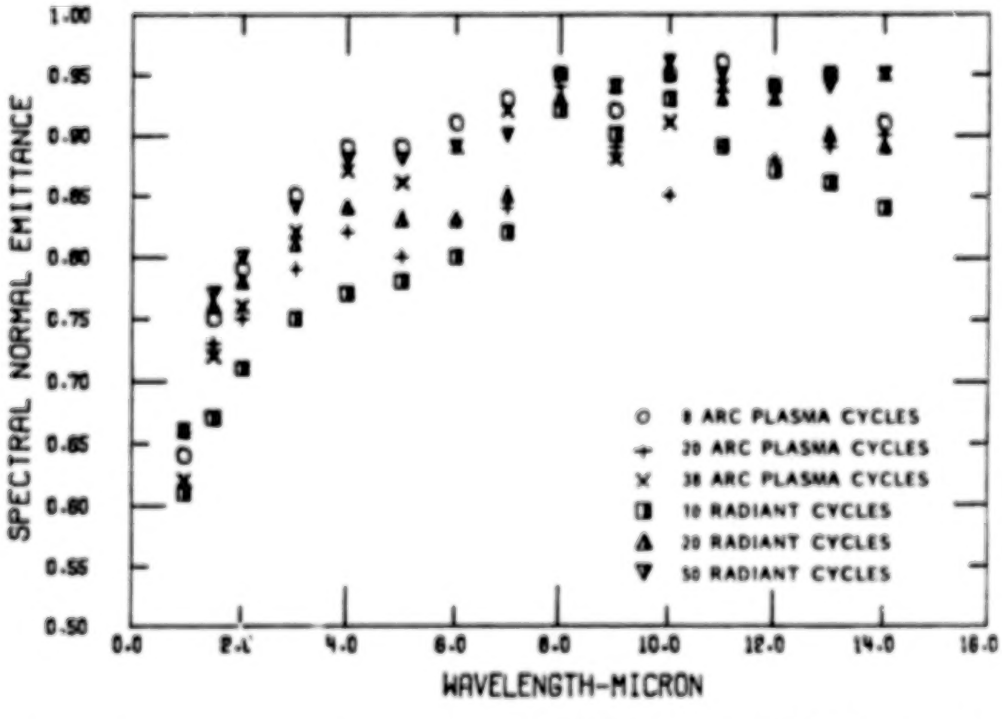

Figure 42. Spectral normal emittance of R512E coated Cb752 at 1590 K after supersonic arc plasma wind tunnel and radiant heating tests.

BEST DOCUMENT AVAILABLE

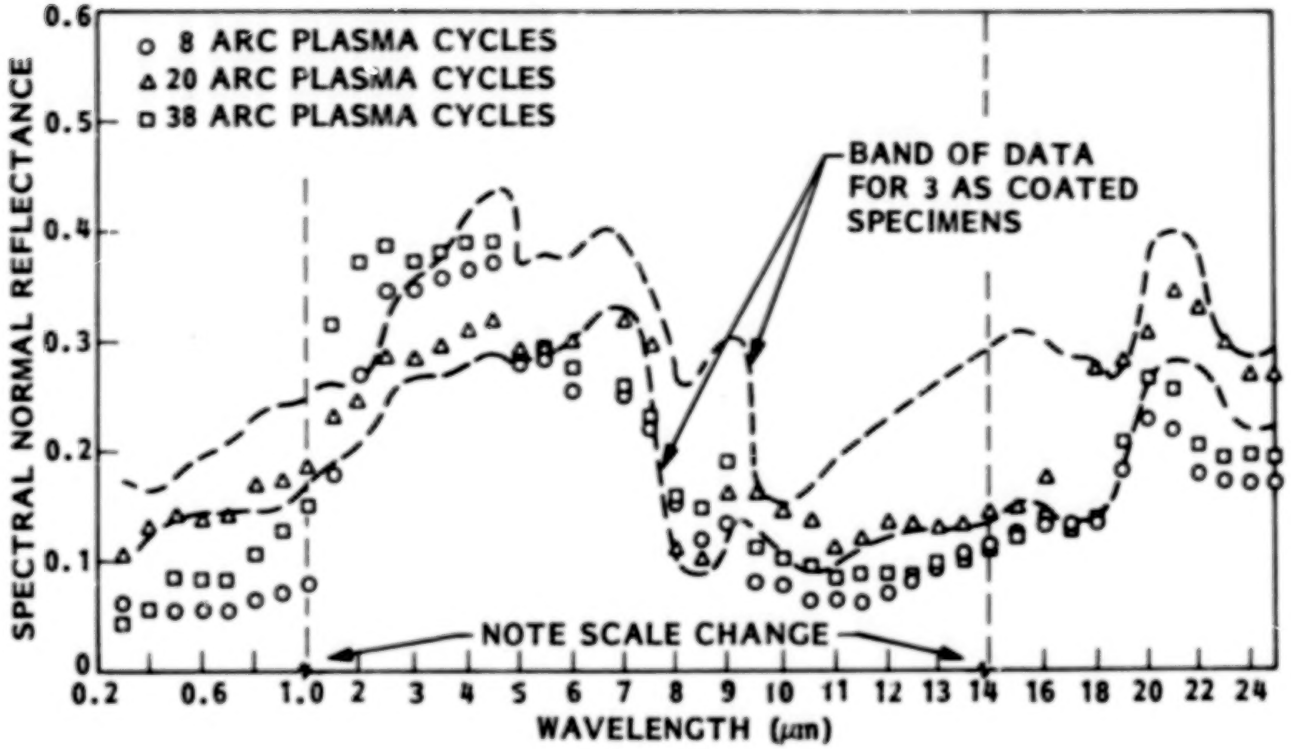
8 ARC PLASMA CYCLES
20 ARC PLASMA CYCLES
38 ARC PLASMA CYCLES
BAND OF DATA FOR 3 AS COATED SPECIMENS
NOTE SCALE CHANGE
SPECTRAL NORMAL REFLECTANCE
WAVELENGTH (μm)

(a) Supersonic arc plasma wind tunnel tests

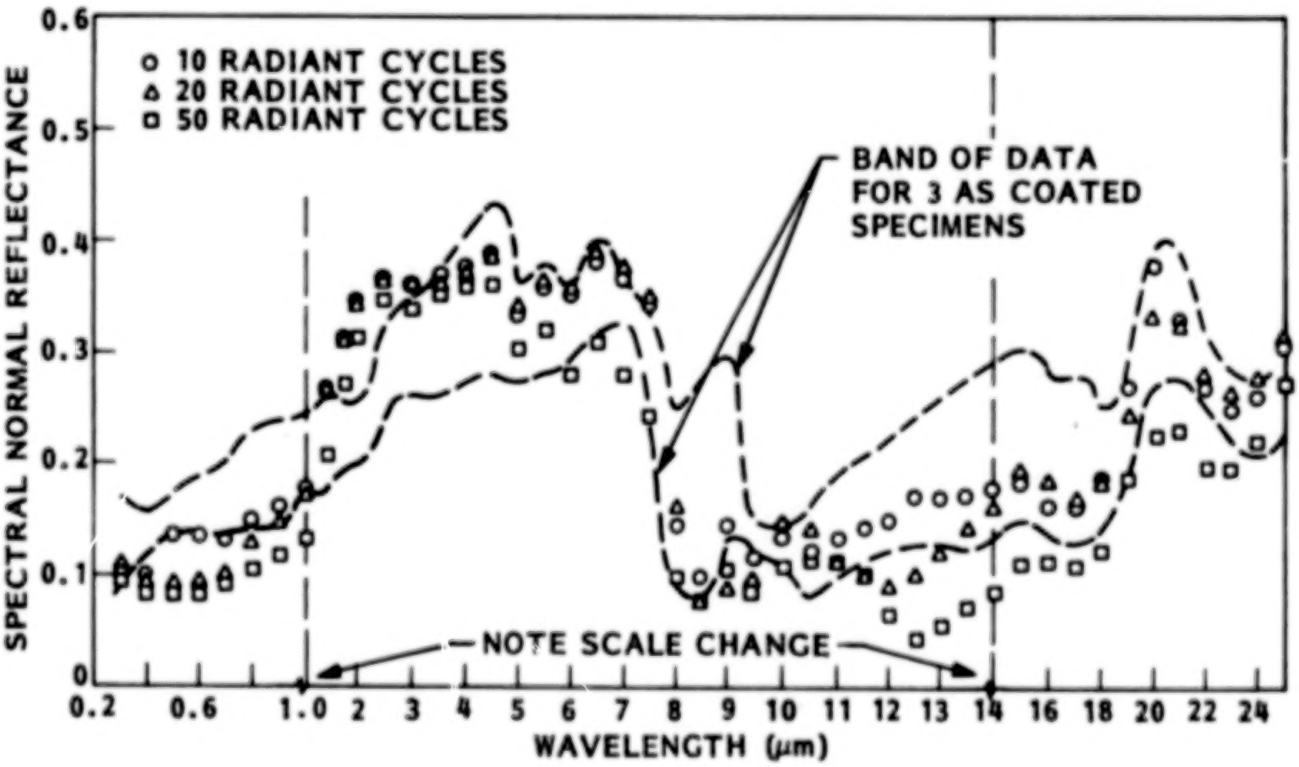

(b) HTEA tests

Figure 43. Room temperature (294 K) spectral normal reflectance of R512E coated Cb752 after reentry and HTEA testing.

Studies of the changes in surface morphology, composition, and structure resulting from the supersonic arc plasma wind tunnel and radiant heat tests were conducted using the following analysis techniques:

1. Morphology - Scanning Electron Microscope (SEM)

2. Composition - Auger Electron Spectroscopy (AES)
   - Electron Microprobe (EP)
   Secondary Ion Mass Spectrometry (SIMS)

3. Structure - X-Ray Diffraction Analysis (XRDA)

Some morphological data were also obtained during AES and EP measurements by using these instruments in their imaging modes. Conversely, the SEM was used to provide qualitative elemental compositional analyses of surfaces and cross sections through the specimens, during morphological examinations. Oxide layer thickness measurements were made using a cylindrical grinding technique which in effect gives a taper section having approximately a 50 times thickness magnification. Surface roughness of the oxides and sputtered crater depths (AES and SIMS) were measured using a DEKTAK profilometer.

4.3.1 Inconel 617

Morphology. The surface topography of the unoxidized Inconel 617 is shown in figure 44. This is typical of the appearance under microscopic examination of the bare metal after cleaning and prior to static oxidation, and it shows a fine roughness pattern superimposed on a much coarser ridge-like structure. The coarse structure has a peak-to-peak spacing on the order of 10 to 20 μm and the fine structure of 0.5 to 1 μm. A fairly thick oxide layer (on the order of 500 Å) is present on the bare metal as evidenced by a 3 weight percent oxygen concentration from an EP quantitative analysis of the surface composition.

The surface topography of the Inconel 617 after static oxidation is shown in figure 45 at three magnifications. The lowest magnification image (figure 45a) shows a macroscopic waviness pattern, with a directional orientation running diagnonally across the photograph, which is probably due to the rolling pattern in the base metal. The finer ridge-like structure is random in orientation and has a nominal peak to peak spacing of 10 to 20 μm, similar to that seen on the bare metal and typical of the base metal grain size. At the intermediate magnification (figure 45b) the surface is composed of the ridge structures tens of microns long with a finer granular phase interspersed between them. A 5000x magnification of a selected area of figure 45b is shown in figure 45c, and it is seen that the granules are in fact well formed crystalline appearing structures with dimensions of 1 to 4 μm. The areas between the crystalline bodies are relatively smooth and appear to be large agglomerates of submicron size particles. Results of a qualitative analysis (by EP) on the regions shown by the locations designated as 1 and 2 of figure 45c are given in Table 19. Analysis of location 1 shows

BEST DOCUMENT AVAILABLE

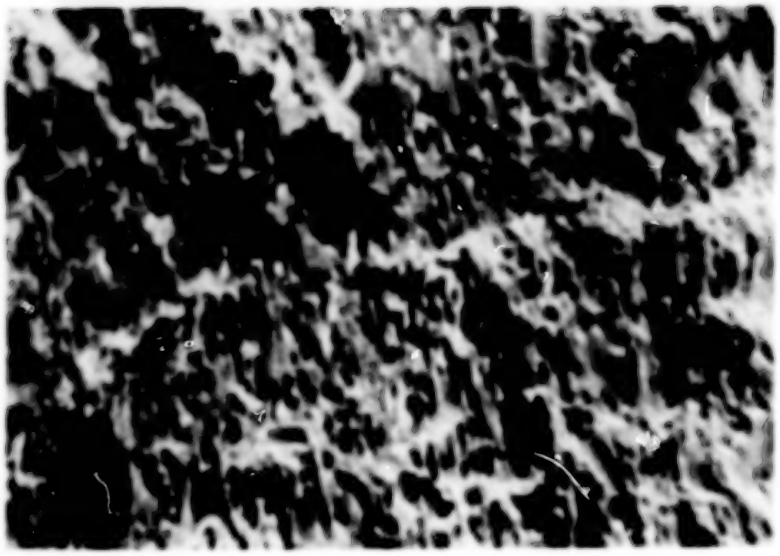

Figure 44. Surface of Inconel 617 before static oxidation at 2000x.

strong chromium and nickel intensities with a moderate cobalt intensity, whereas location 2 is predominately chromium with a moderate amount of iron.

A taper section of the statically oxidized Inconel 617, obtained by the cylindrical grinding technique (see Section 3.5.3) is shown in figure 46 at two magnifications. Figure 46a at 50x is used to get the dimensional information necessary for the measurements of oxide layer thickness. The 200x magnification shows the base metal grain boundary size. The very dark areas within the oxide layer (gray zone) are not voids within the layer but rather artifacts from the roughness characterictics of the exterior surface. The taper section is a plane at a nominal 1-deg angle with the surface, and the intersection of this plane with valleys in the surface topography produces the apparent void feature. Similarly, the gray areas within the bright appearing base metal are indicative of the roughness of the oxide layer-base metal interface. The depth of the centerline of the grind area below the nominal oxide surface is 6 to 7 μm. The grain boundary dimensions for the base metal are 10 to 25 μm. An estimate of the exterior surface macroscopic roughness from the apparent void locations is 3 μm peak-to-peak. The surface macro-roughness as determined by the DEKTAK profilometer is 2.8 μm peak-to-peak with a characteristic wavelength of 40 to 70 μm.

BLANK PAGE

BLANK PAGE

BLANK PAGE

BEST DOCUMENT AVAILABLE

(a) 165x

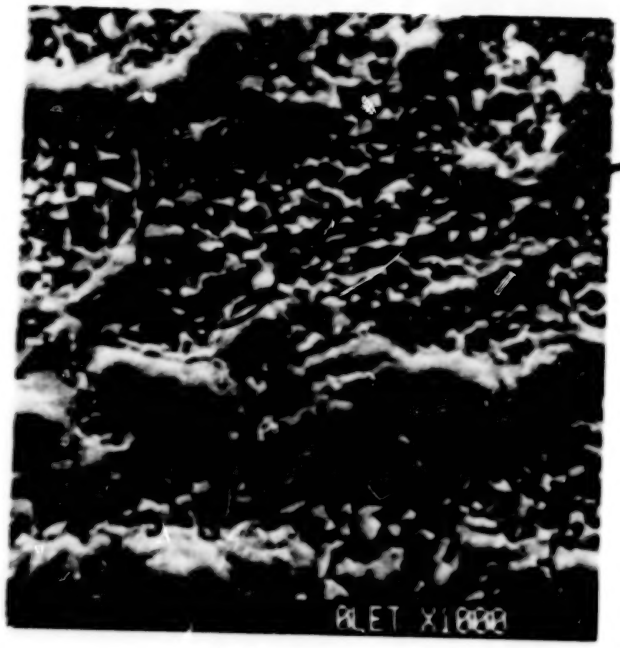

(b) 1000x

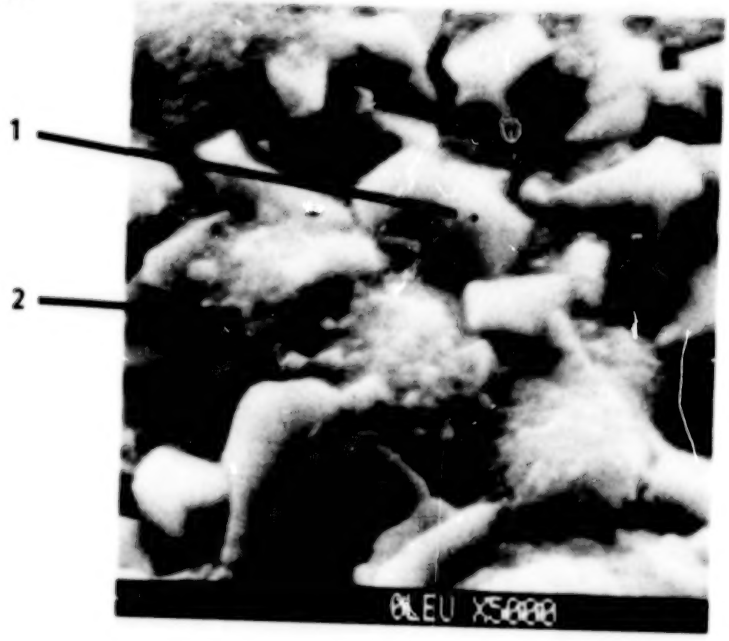

(c) 5000x

Figure 45. Surface of statically oxidized Inconel 617.

BEST DOCUMENT AVAILABLE

(a) 50x

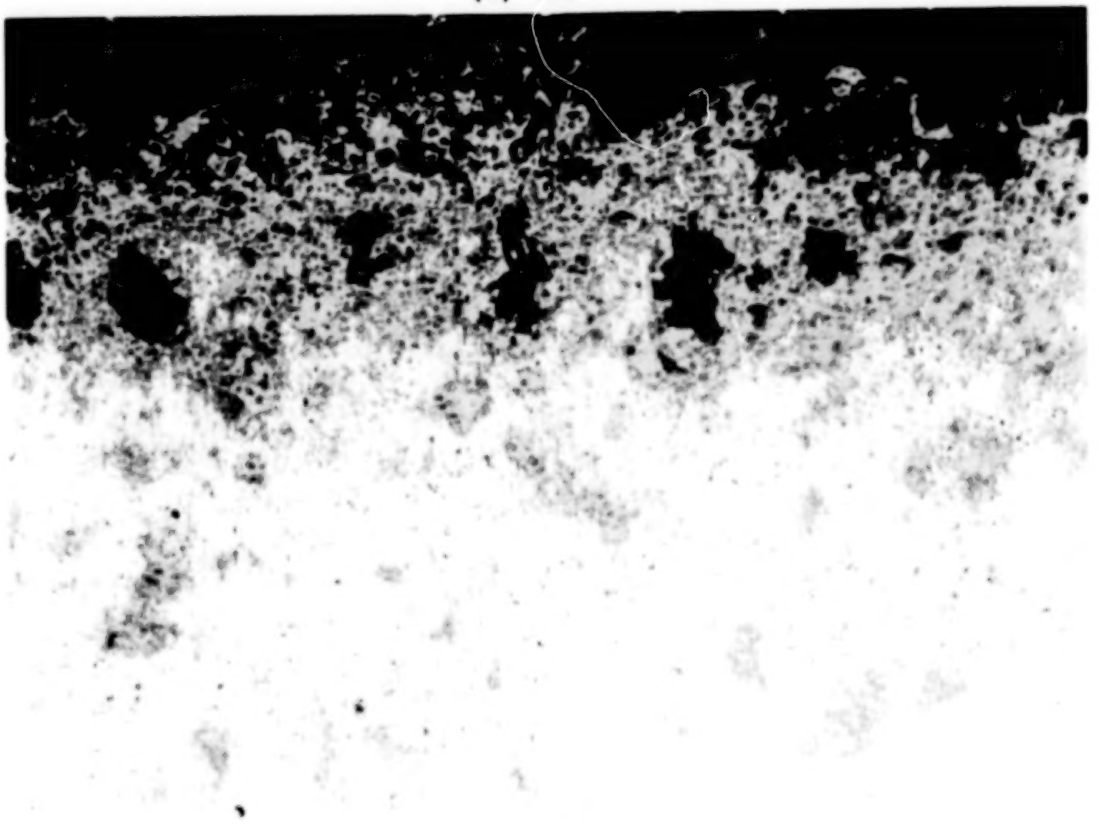

(b) 200x

Figure 46. Photomicrographs of cylindrical grinding region on surface of statically oxidized Inconel 617.

Table 19. Relative Line Intensities for Electron Microprobe Analysis of Surface of Statically Oxidized Inconel 617

Element	Location 1*	Location 2*
Cr	S	ES
Ni	S	W
Co	M	W
Ti	T	W
Al	T	T
Si	ND	ND
Fe	W	M
Mo	ND	ND

ES = extra strong, S = strong, M = moderate, W = weak, T = trace, ND = not detected

*Refers to areas denoted in figure 45c.

After exposure to eight test cycles in the supersonic arc plasma wind tunnel the crystalline appearing nature of the surfaces of the statically oxidized Inconel 617 has become less apparent. The color of the boundary layer surface of the specimen has gone from gray (statically oxidized) to an overall green color with several small brown to yellow areas. The rear surface reamined gray.

At low magnification, the surface exposed to the boundary layer (figures 47a and c) does not have the clearly defined features seen for the statically oxidized material (c.f. figure 45a) and appears to have a somewhat porous texture with numerous raised scalelike patches. At higher magnification (figures 47b and d) little clearly defined structure is seen. The angular granules seen in the statically oxidized surface (c.f. figure 45b) now have a flocculent appearance with very few well defined structure still present. Also, the ridge-like lattice pattern has blended into the diffuse background structure.

The rear surface of this 8 cycle specimen shows some of the ridge-like structure of the statically oxidized material (c.f. figures 45a and d and 48c) in some areas. At higher magnification the surface topography is quite different from the boundary layer flow surface (c.f. figures 47b and d and 48b and d) in that small nodules appear to be uniformly distributed over the entire surface. These nodules are 5 to 15 μm across, and they may be growing from the smaller crystalline shapes observed in figure 45c.

BEST DOCUMENT AVAILABLE

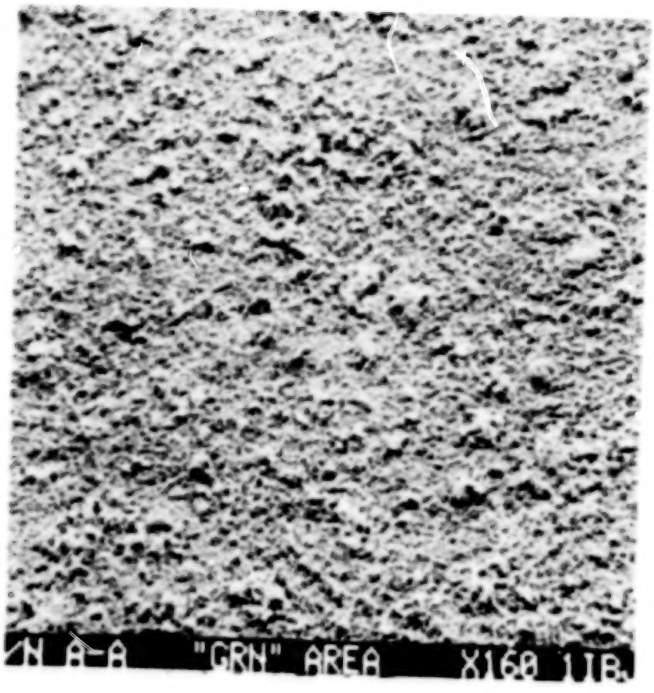

(a)

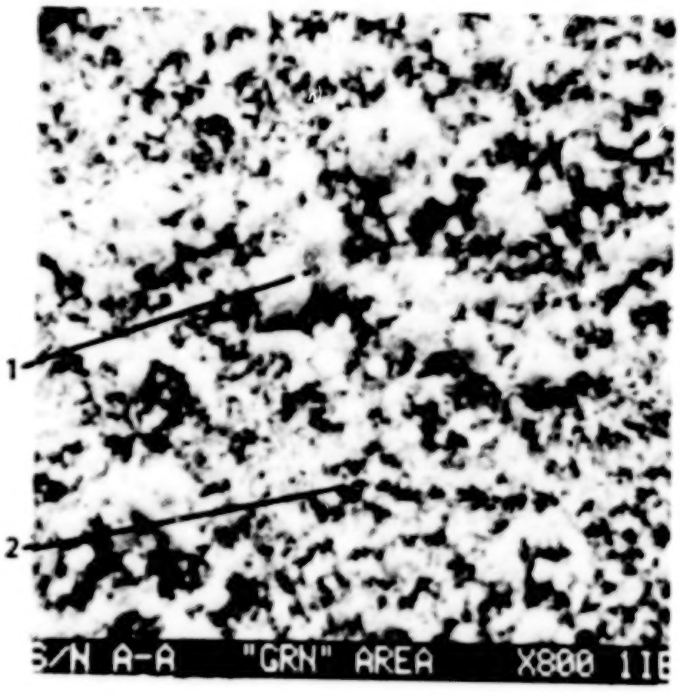

(b)

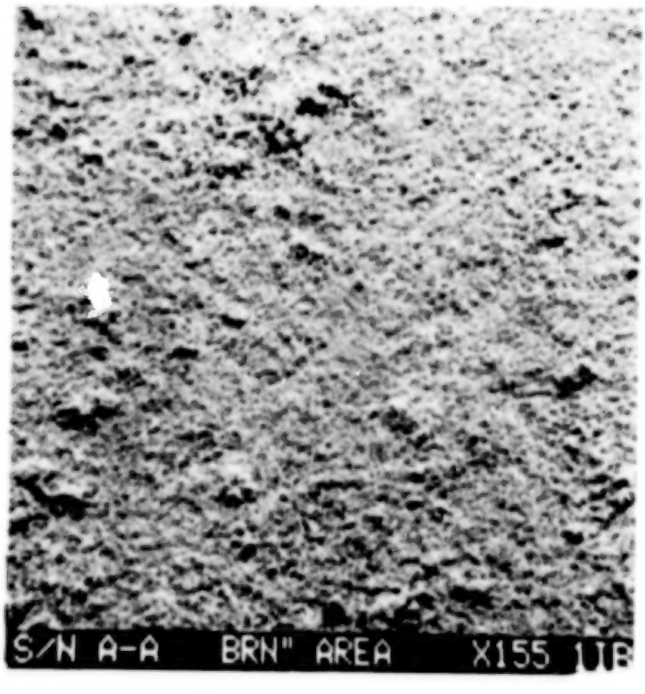

(c)

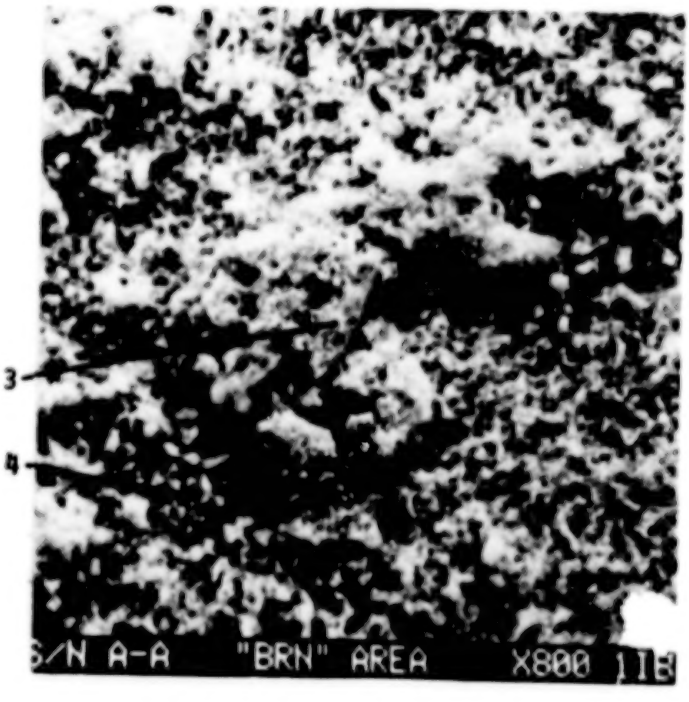

(d)

Figure 47. Boundary layer surface of statically oxidized Inconel 617 after 8 cycles in supersonic arc plasma wind tunnel.

BEST DOCUMENT AVAILABLE

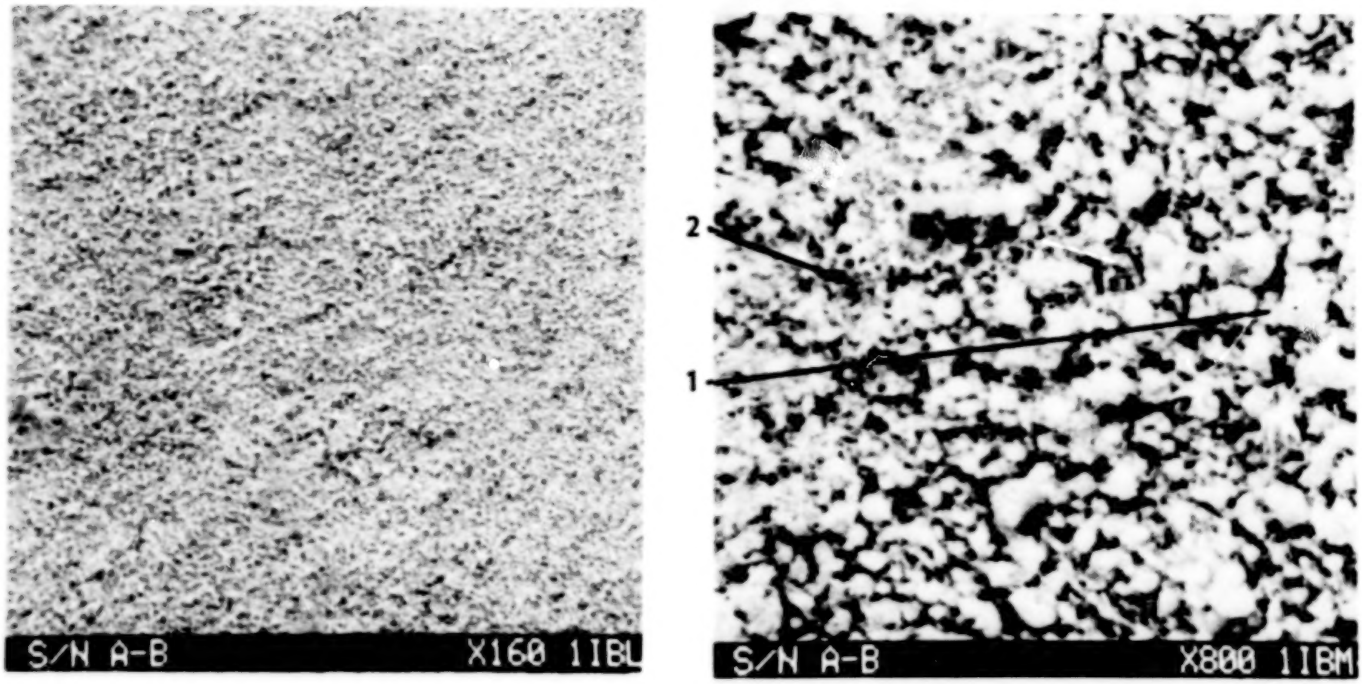

(a) (b)

Region 1

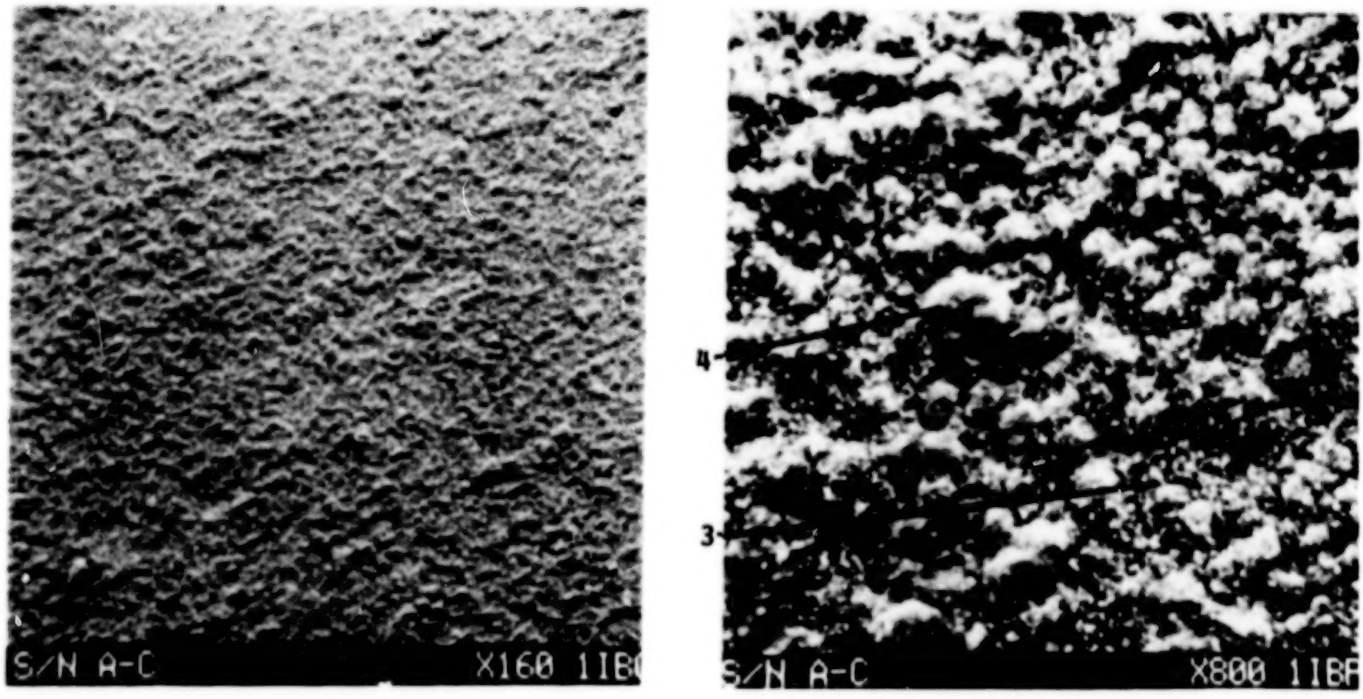

(c) (d)

Region 2

Figure 48. Rear surface of statically oxidized Inconel 617 after 8 cycles in supersonic arc plasma wind tunnel.

Qualitative EP analysis results for the eight regions shown on figures 47 and 48 are given in Table 20. It should be cautioned that these results, and those in Table 19, are qualitative from the standpoint that the composition of the surface features may be influenced by that of the sublayer because of the EP analysis depth of 1 μm. This becomes more important as the size of the surface feature in question becomes smaller than 1 μm.

The large granule, at location 1 of figure 47b, is similar in composition to the granule at location 1 in figure 45 except for the strong intensity of titanium and the weak intensity of cobalt. Silicon and molybdenum were not detected in the analysis of the statically oxidized surface because of low instrumental gain. The oxide at locations 2 and 4 of figure 47 consist predominantly of chromium and are similar to the oxide at location 2 of the statically oxidized surface shown in figure 45. The platelet-like feature identified at location 3 of figure 47d is essentially of nickel composition. The nodule-like areas on the rear surface, location 1 and 4 of figure 48, show strong intensities for chromium and nickel and in the case of location 1, titanium. The oxide at locations 2 and 3 of figure 48 consist predominantly of chromium with moderate amounts of nickel.

After a 20 cycle exposure in the supersonic arc plasma wind tunnel the boundary layer surface of the Inconel 617 specimen has a more diffuse appearance than the statically oxidized surface, and the particulate nature of the surface seen after the 8 cycle test is less distinct (c.f. figures 47 and 49). The rear surface morphology for the 20 cycle specimen is similar to the 8 cycle specimen (figure 48).

Figure 50 shows the appearance of both boundary layer and rear surfaces of the statically oxidized Inconel 617 specimen after 38 cycles in the supersonic arc plasma wind tunnel. The boundary layer surface (figures 50a and b) shows what appears to be the start of the growth of clusters of porous lumps similar to those reported in references 13 and 14. The rear surface of the specimen has a scale-like appearance and is composed of crystalline particles (see figures 50c and d) whose features are similar to those of the statically oxidized specimen (c.f. figures 45b and 50d).

Photomicrographs of the cylindrical grinding areas on both surfaces of the 38 cycle specimen are shown in figure 51. In contrast to the irregularities seen in the statically oxidized case (figure 46), both surfaces appear more uniform and the oxide-bare metal and the oxide-air interfaces appear to have a reduced macro-roughness (i.e., neither apparent voids within the oxide layer nor numerous gray areas in the base metal). The change in oxide layer appearance suggests that the supersonic arc plasma wind tunnel testing resulted in the formation of a different oxide layer from that initially formed during static oxidation. Base metal grain size has not changed significantly from that observed for the statically oxidized specimen (c.f. figures 46 and 51).

Table 20. Relative Line Intensities for Electron Microprobe Analysis of Boundary Layer and Rear Surfaces of Statically Oxidized Inconel 617 Specimen After 8 Supersonic Arc Plasma Wind Tunnel Cycles

	Boundary Layer Surface				Rear Surface			
	Green Region		Brown Region		Region 1		Region 2	
Element	(1)*	(2)	(3)	(4)	(1)	(2)	(3)	(4)
Cr	S	ES	W	ES	S	ES	ES	S
Ni	S	W	ES	W	S	M	M	S
Co	W	W	W	W	W	W	M	M
Ti	S	W	W	W	S	W	M	T
Al	T	W	W	W	M	T	W	T
Si	T	W	W	W	T	T	T	T
Fe	W	T	W	W	W	W	T	T
Mo	T	T	T	T	T	T	T	T

ES = extra strong, S = strong, M = medium, W = weak, T = trace.

*Number in parentheses denotes location on figures 47 or 48.

Figures 52 and 53 show the topographic characteristics of the surface of specimens 617-2 and 617-3 that were in contact with the boundary layer during the stagnation flow tests in the Langley arc plasma wind tunnel. The low enthalpy, supersonic flow test (specimen 617-2) produced a nodular appearing surface as seen in figure 52. All these micrographs are from the central or stagnation region, but are typical of the appearance of the total surface of this specimen. The test of specimen 617-3 (high enthalpy and probably subsonic flow) also produced a nodular appearing surface in the central region (c.f. figures 53a and b). However, near the edge of the specimens the surface was smoother and more platelet-like (see figures 53c and d), somewhat similar to the surface topographical characteristics of the rear surface of the 38 cycle wedge flow test specimen (figures 50c and d).

Cross sectional views of the three supersonic arc plasma wind tunnel specimens are shown in figure 54. The images of figures 54b and c were made using back scattered electrons to enhance the appearance of the grain boundary

BEST DOCUMENT AVAILABLE

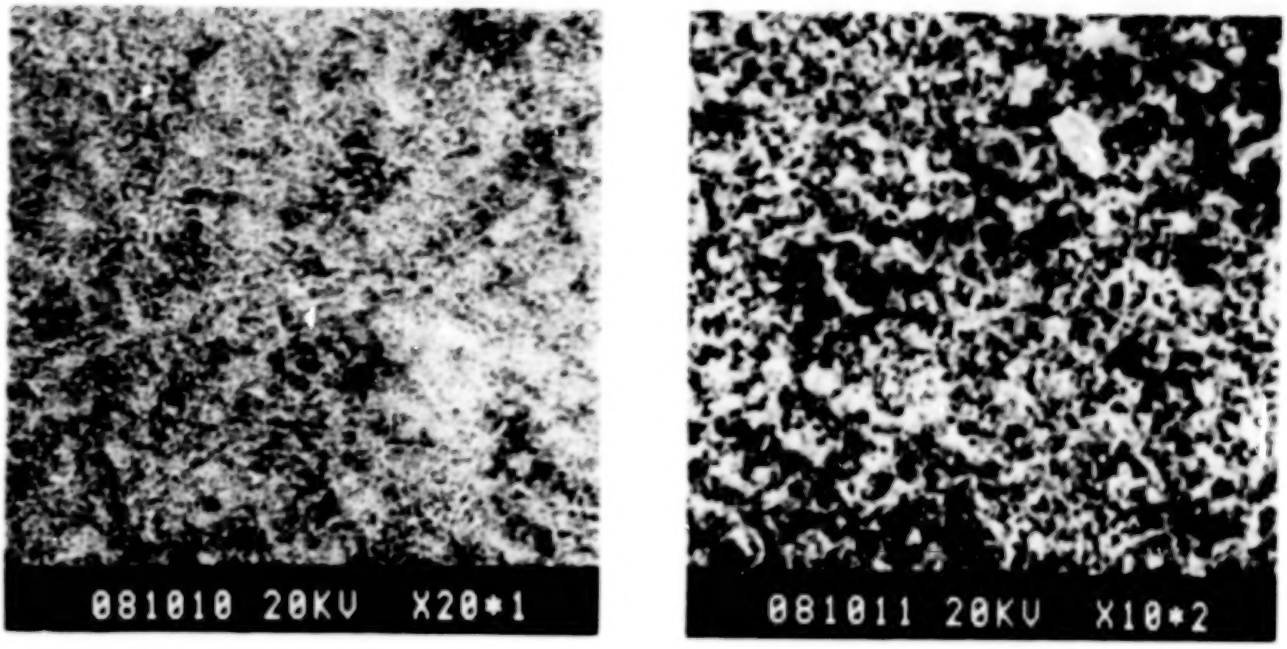

(a) 100x (b) 1000x

Figure 49. Boundary layer surface of statically oxidized Inconel 617 after 20 cycles in supersonic arc plasma wind tunnel.

and oxide-base metal interface. In figure 54a the oxide layer can still be seen as the gray layer to the right of the bright appearing base metal layer. By changing contrast the oxide layer is not seen (figure 54c) and only the base metal is shown in the image.

The radiant heating tests did not produce the changes in surface appearance that were seen in the supersonic arc plasma wind tunnel test results. The surfaces of the radiant test specimens generally showed some crystalline or faceted structure similar to that of the statically oxidized specimens (figure 45). The surface topography for the 100 cycle radiant heating test specimen also appears similar to that of the rear surface of the supersonic arc plasma wind tunnel test specimens (c.f. figures 50c and d and 55).

Total specimen thickness and oxide layer thickness data are summarized in Table 21. It must be noted that these are post-test total thickness data and

BEST DOCUMENT AVAILABLE

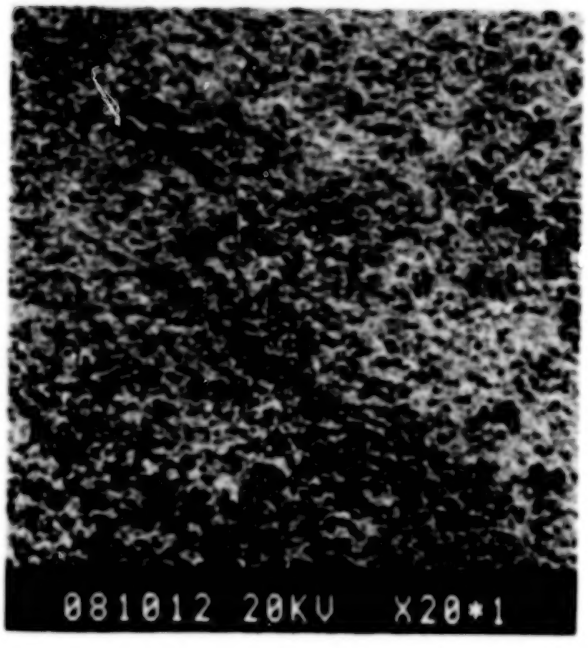

(a)

(b)

Boundary layer surface

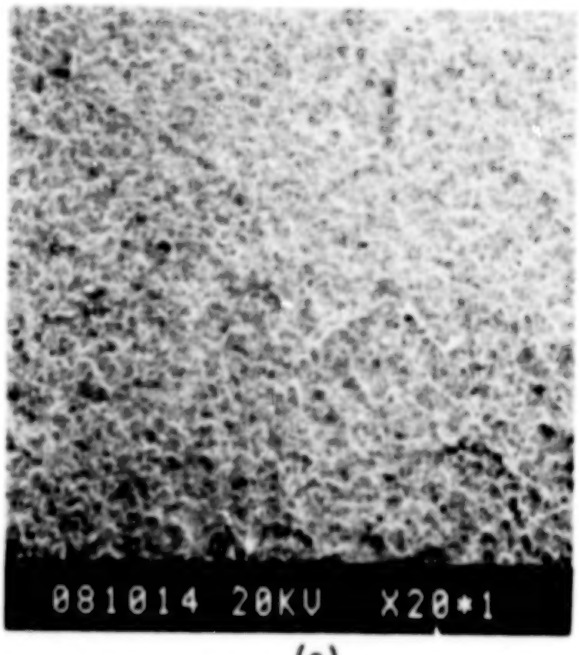

(c)

(d)

Rear Surface

Figure 50. Boundary layer and rear surfaces of statically oxidized Inconel 617 after 38 cycles in supersonic arc plasma wind tunnel.

BEST DOCUMENT AVAILABLE

(a) Boundary layer surface 63x

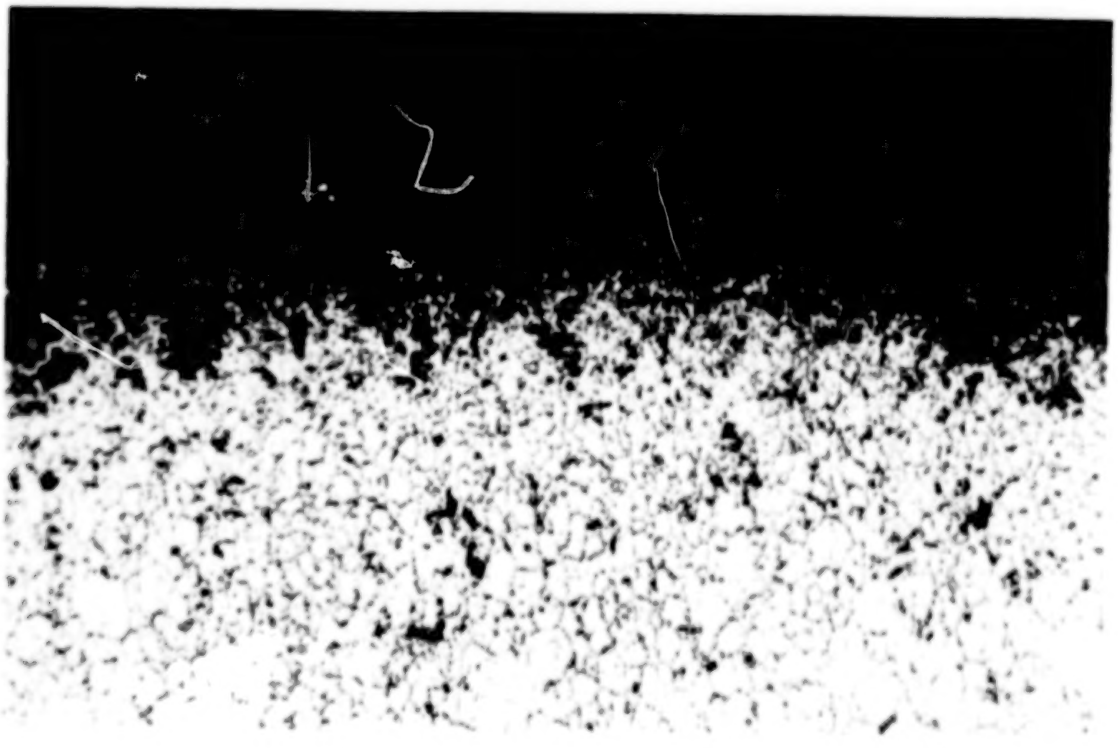

(b) Boundary layer surface 200x

Figure 51. Photomicrographs of cylindrical grinding regions on surfaces of statically oxidized Inconel 617 after 38 cycles in supersonic arc plasma wind tunnel.

BEST DOCUMENT AVAILABLE

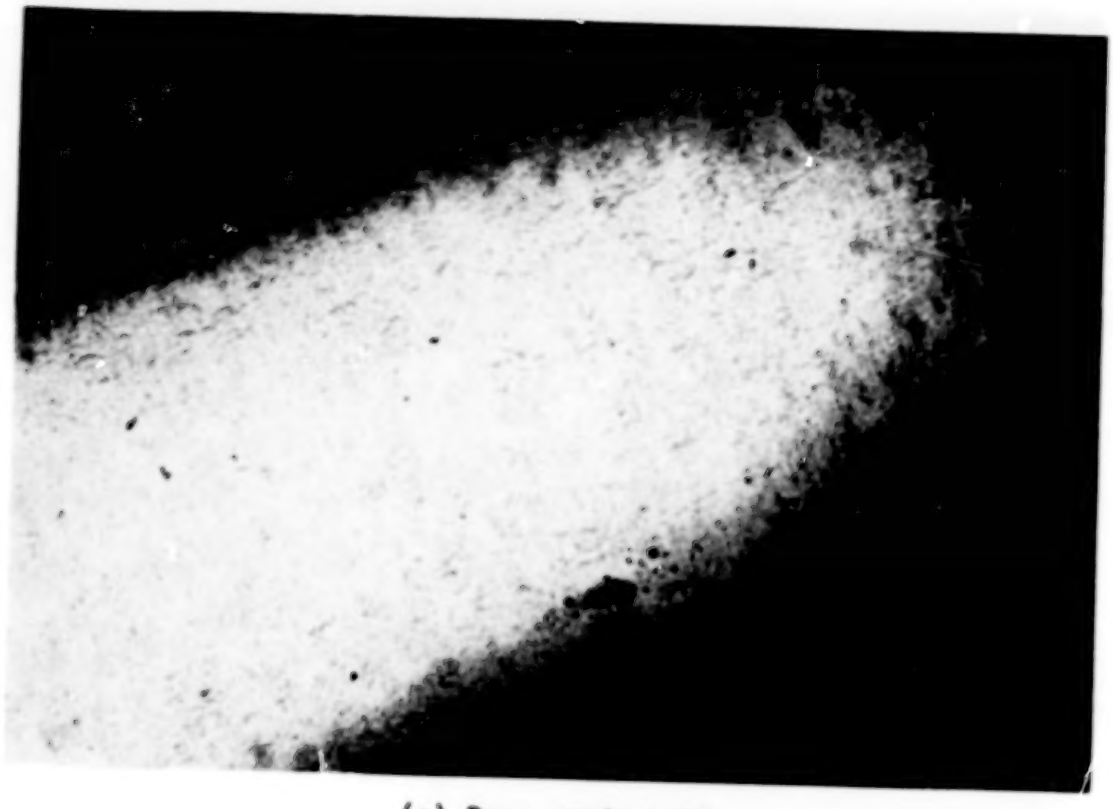

(c) Rear surface 63x

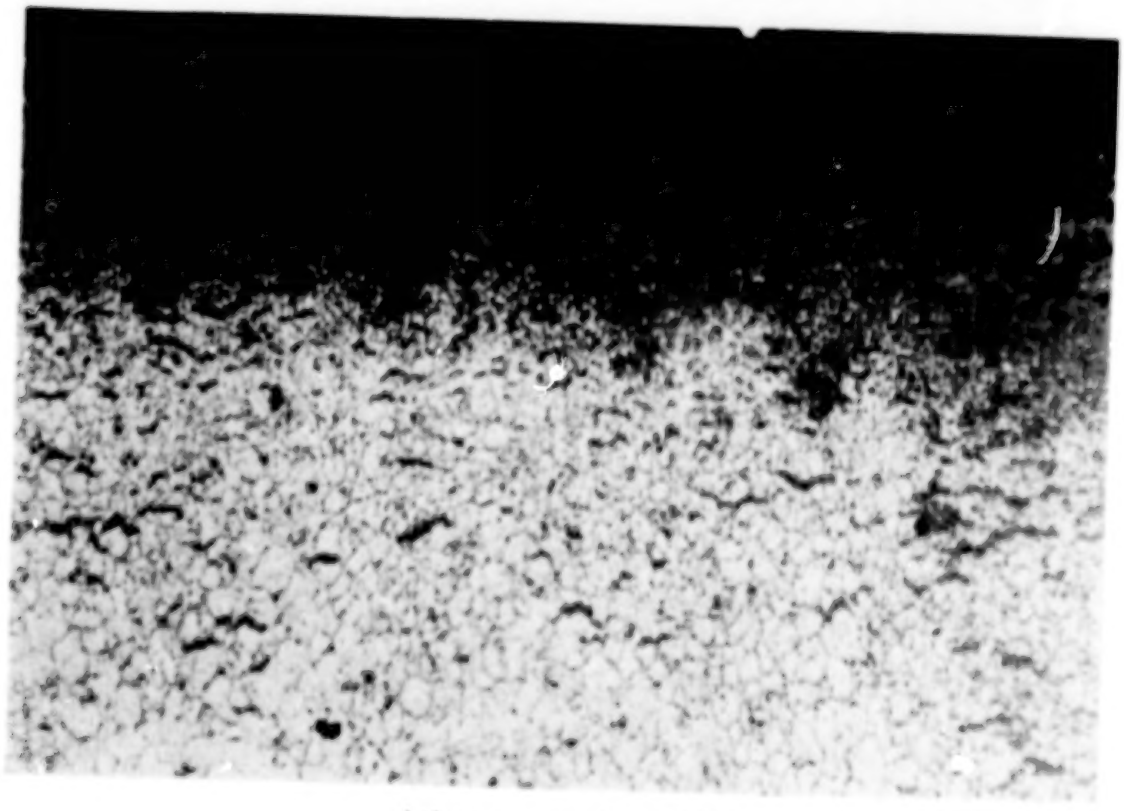

(d) Rear surface 200x

Fig. 51 (Cont.)

BEST DOCUMENT AVAILABLE

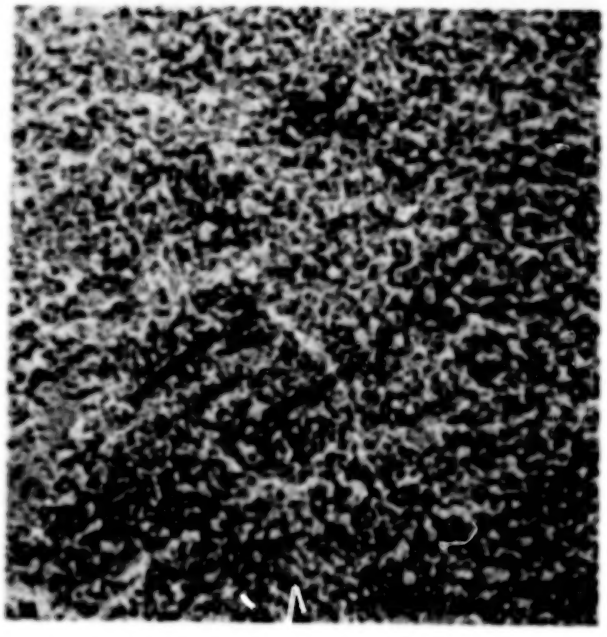

(a) 200x

(b) Location 1, 750x

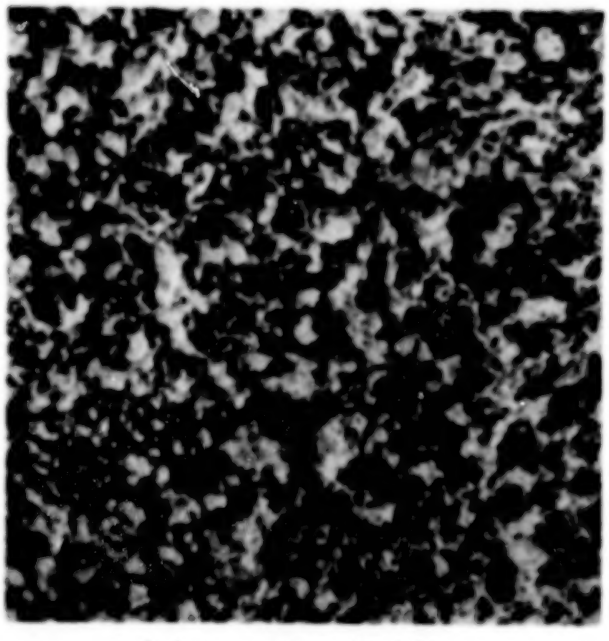

(c) Location 2, 750x

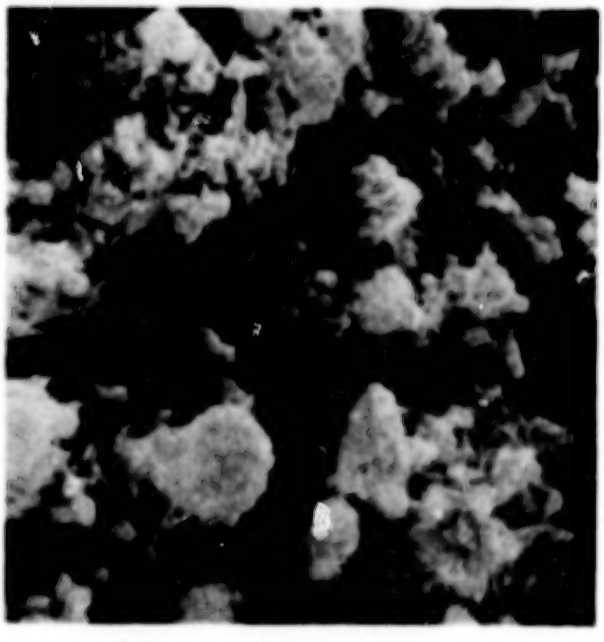

(d) Location 1, 4000x

Figure 52. Boundary layer surface of statically oxidized Inconel 617 after 8 h at 1260 K in supersonic arc plasma wind tunnel, stagnation model low enthalpy test (specimen 617-2).

BEST DOCUMENT AVAILABLE

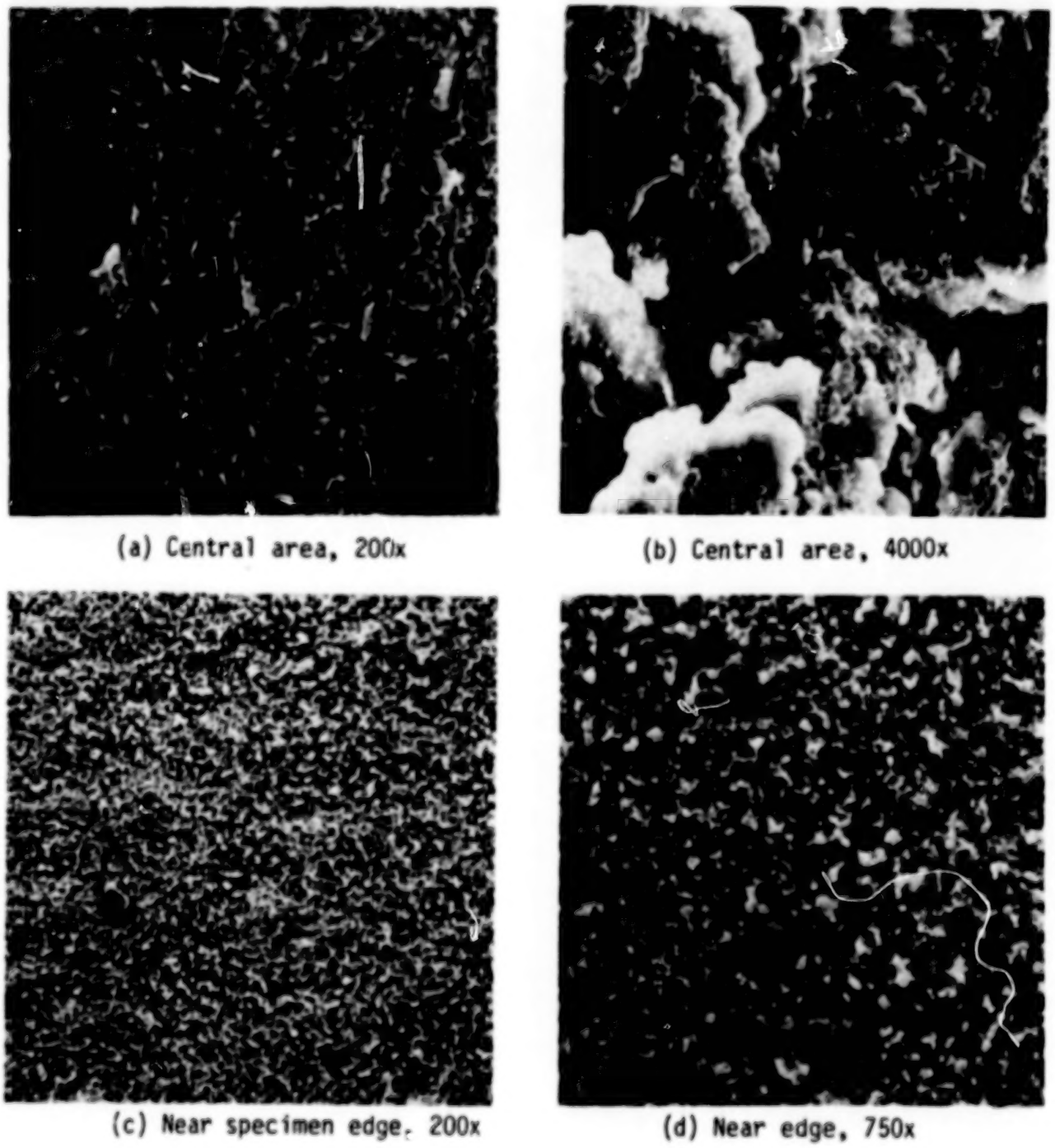

(a) Central area, 200x

(b) Central area, 4000x

(c) Near specimen edge, 200x

(d) Near edge, 750x

Figure 53. Boundary layer surface of statically oxidized Inconel 617 after 8 h at 1260 K in arc plasma wind tunnel, stagnation model high enthalpy test (specimen 617-3).

BEST DOCUMENT AVAILABLE

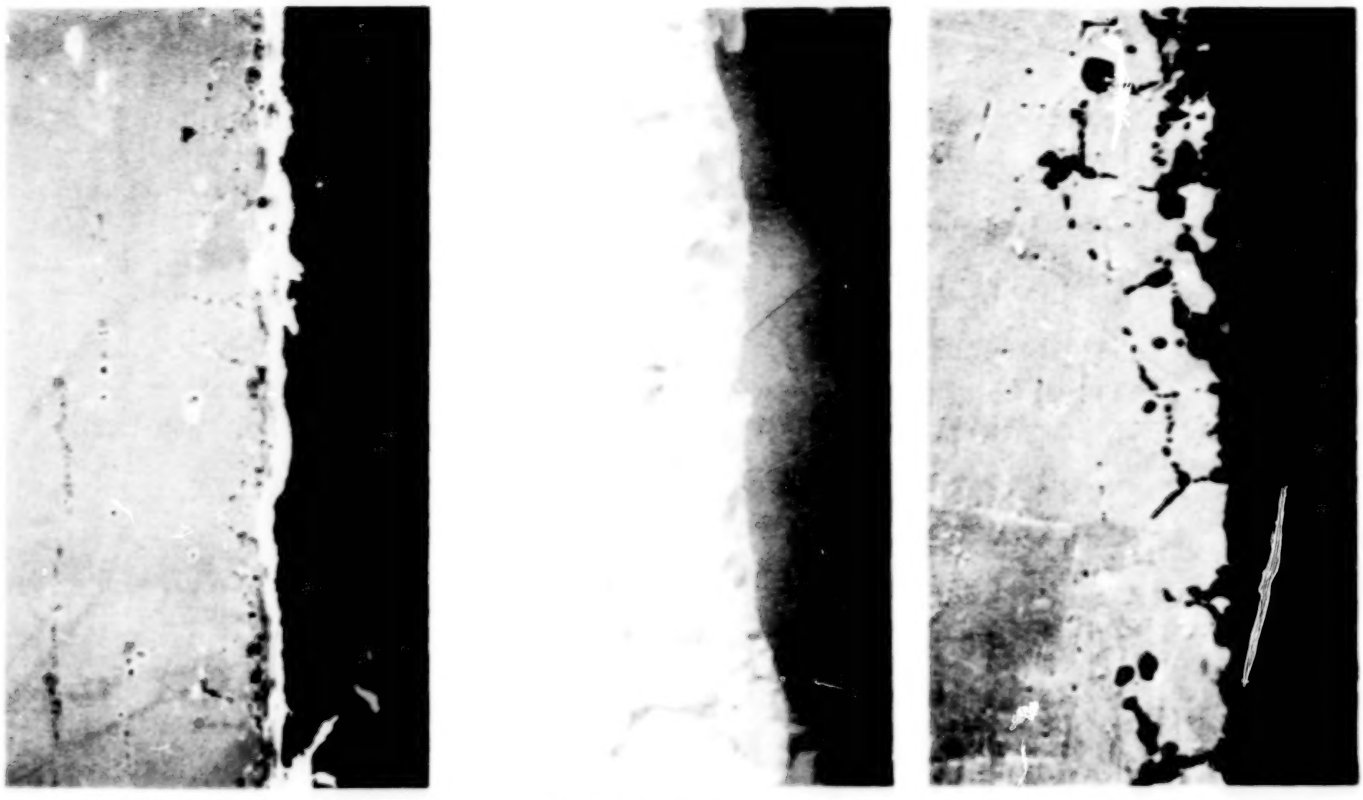

(a) 8 cycle, 500x (b) 20 cycle, 1000x (c) 38 cycle, 1000x

Figure 54. Cross section photomicrographs of supersonic arc plasma wind tunnel test specimens.

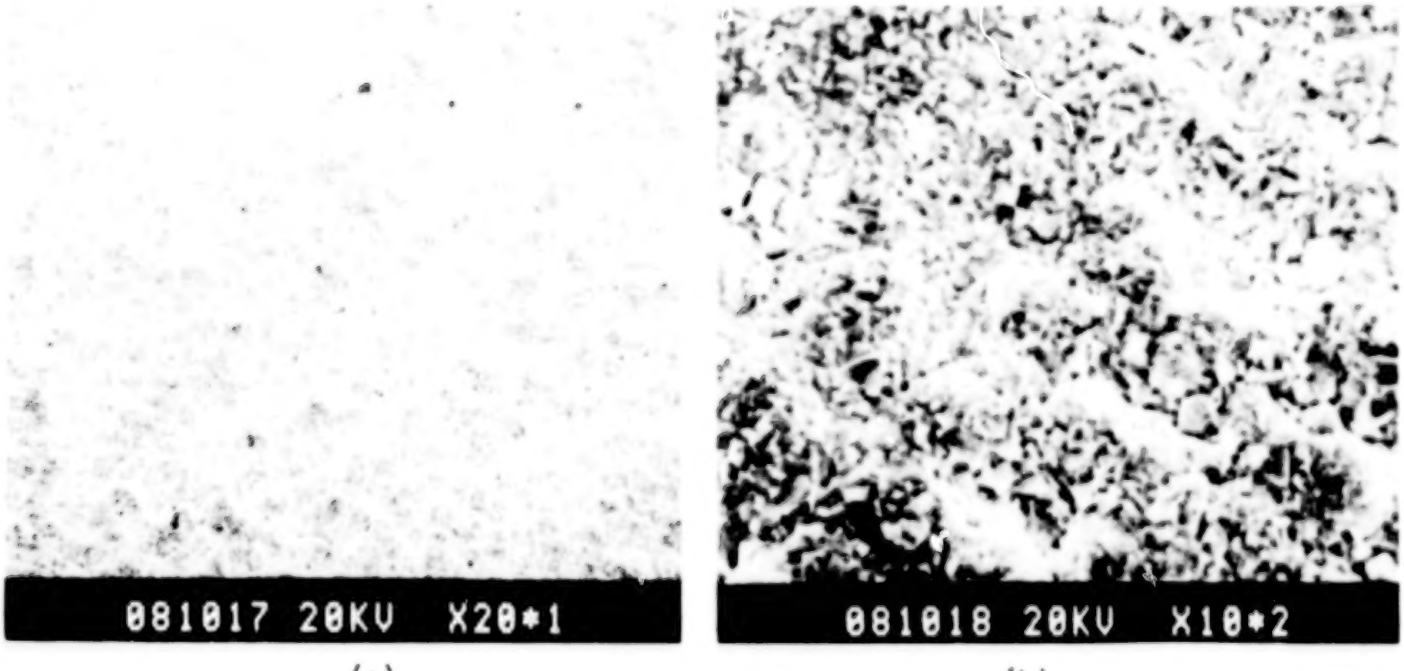

(a) (b)

Figure 55. Surface of statically oxidized Inconel 617 after 100 radiant heating cycles.

that there are no pre-test data for a direct comparision of thickness at a specific location on the arc plasma wind tunnel or radiant heating test specimens. Two columns are shown for total thickness because it was necessary to procure a second lot of Inconel 617 in order to prepare additional supersonic arc plasma wind tunnel specimens to replace those lost during initial test malfunctions. This second lot of material was slightly thicker than the initial material.

The total thickness values reported in Table 21 are the arithmetic mean (average) of a series of individual measurements on either a single specimen, in the case of supersonic arc plasma wind tunnel tests, or triplicate specimens for all others. Thickness measurements were made with a micrometer at four points bounding the area from which emittance measurements were made. Maximum uncertainty in the reported total thickness values is 0.003 mm.

Oxide thickness measurements were derived from measurements made on the cylindrical grinding section, and the values reported are the average of three measurements made on a single groove. For the statically oxidized condition two specimens were examined and both results are given in Table 21. Two areas of the single 38 cycle supersonic arc plasma wind tunnel test specimen were measured giving the results shown in Table 21. With the exception of the statically oxidized specimens, the oxide layer thickness data are estimated to have a maximum uncertainty of ±0.2 μm. The large surface irregularities in the statically oxidized specimen give rise to an uncertainty in oxide thickness of ±0.5 μm.

In view of the limited data no conclusions can be made as to overall specimen thickness changes with exposure time or type. The variations in total thickness which were observed for each specimen mask any thickness changes. The data do show, however, that no major (i.e. < 20 μm) increase or decrease in thickness resulted from the testing. Because of the uncertainty in total specimen thickness values (3 to 5 μm) obtained on the statically oxidized material, exposure to the radiant heating test conditions did not result in a significant change in total thickness of the material. There is an apparent increase in total thickness as a result of the supersonic arc plasma wind tunnel testing when comparing the 20 and 38 cycle data with those for the 1 and 2 cycle tests and the statically oxidized material. These data, however, are inconsistent with the oxide thickness measurements which show a decrease in oxide layer thickness on the boundary layer surface and no change on the rear surface of these specimens (8, 20, and 38 cycles). The observed total thickness increase in Table 21 is simply the result of material thickness variations for the "as fabricated" specimens. In summary, (1) the static oxidation procedure resulted in an oxide layer 3 to 4 μm thick; (2) the supersonic arc plasma testing resulted in an oxide layer 2 to 3 μm thick, and the thickness did not significantly change between 8 and 38 test cycles; (3) up to 50 h of exposure in the radiant heating test did not significantly alter the thickness of the statically formed oxide layer.

BEST DOCUMENT AVAILABLE

Table 21. Overall Thickness and Oxide Layer Thickness Data for Inconel 617 Specimens

Simulated Reentry Exposure Test	Overall Specimen Thickness (mm)[a]		Oxide Layer Thickness (μm)
	Heat XX01A4UK	Heat XX04A8UK	
None, Bare Metal	0.787 ±0.010	0.850 ±0.015	--
None, Statically Oxidized	0.796 ±0.006	0.868 +0.011 -0.007	4.0, 3.2[b] (oxide layer very irregular in cross section)
Supersonic Arc Plasma Wind Tunnel, 1 Cycle	0.799 ±0.002	--	--
Supersonic Arc Plasma Wind Tunnel, 2 Cycles	0.798 +0.003 -0.002	--	--
Supersonic Arc Plasma Wind Tunnel, 6 Cycles	0.806 +0.002 -0.001	--	--
Supersonic Arc Plasma Wind Tunnel, 8 Cycles	0.812 ±0.010	--	F[c], 2.6 R[c], 3.3
Supersonic Arc Plasma Wind Tunnel, 20 Cycles	--	0.847 ± 0.008	F, 2.2 R, 3.0
Supersonic Arc Plasma Wind Tunnel, 38 Cycles	0.810 +0.003 -0.004	--	F, 2.3, 2.3[d] R, 3.3, 3.1[d]
Radiant Heating, 10 Cycles	0.803 +0.005 -0.003	--	--
Radiant Heating, 20 Cycles	0.800 ±0.003	--	3.3
Radiant Heating, 50 Cycles	0.803 ±0.003	--	2.9
Radiant Heating, 100 Cycles	0.804 ±0.004	--	--

(a) With the exception of the supersonic arc plasma wind tunnel tests the values reported are for triplicate specimens, four thickness measurements were made on each specimen in the area for emittance measurements. Uncertainty in thickness measurements is ± 0.003 mm.
(b) Second number is for the second heat number base metal.
(c) F denotes boundary layer surface and R is rear surface.
(d) For two locations on single 38 cycle specimen.

Composition. Quantitative elemental analyses were obtained from electron microprobe analysis of the surfaces of a statically oxidized and the 8 cycle supersonic arc plasma wind tunnel test specimens to aid in the interpretation of the AES results. The results of the EP studies are given below.

	Oxide Composition (Atomic Percent)		
	Statically	8 Cycles	
Element	Oxidized	F^+	R^+
O	52.8	49.4	51.9
Cr	30.9	42.0	34.4
Ni	10.2	3.1	8.7
Co	2.3	1.0	1.4
Ti	2.2	2.4	2.2
Fe	1.0	0.7	0.9
Mn	0.6	0.6	0.5
Mo	0.06	0.05	0

+ Denotes boundary layer, F, and rear surface, R, of specimen

AES sensitivity factors were derived for the oxide layer using the above concentrations together with the elemental intensities observed in the AES spectrometer. For the base metal region the data of Table 2 were used to compute the elemental sensitivities for these particular compositions. The EP analyses was assumed to integrate composition over a 1 μm depth from the surface of the specimen. Using this calibration technique, the accuracy of the AES data for quantitatively determining the concentration of an element in a complex mixed oxide layer is estimated to be ±30 percent of the value for concentrations of 20 atomic percent or greater, and a factor of 2 to 3 for smaller concentrations.

Because of the irregular surface topography seen in the SEM studies, the AES analysis was done by rastering an area approximately 1 mm by 1.5 mm. Surface charging effects required operating with a low beam current (60 nA at 10 keV and 100 nA at 5 keV) for the argon ion sputtering. This resulted in very long analysis times because of the low sputter rate, which was on the order of 300 angstroms per minute.

An AES depth profile for statically oxidized Inconel 617 is shown in figure 56. Emphasizing the semiquantitative nature of the AES data, it is

BEST DOCUMENT AVAILABLE

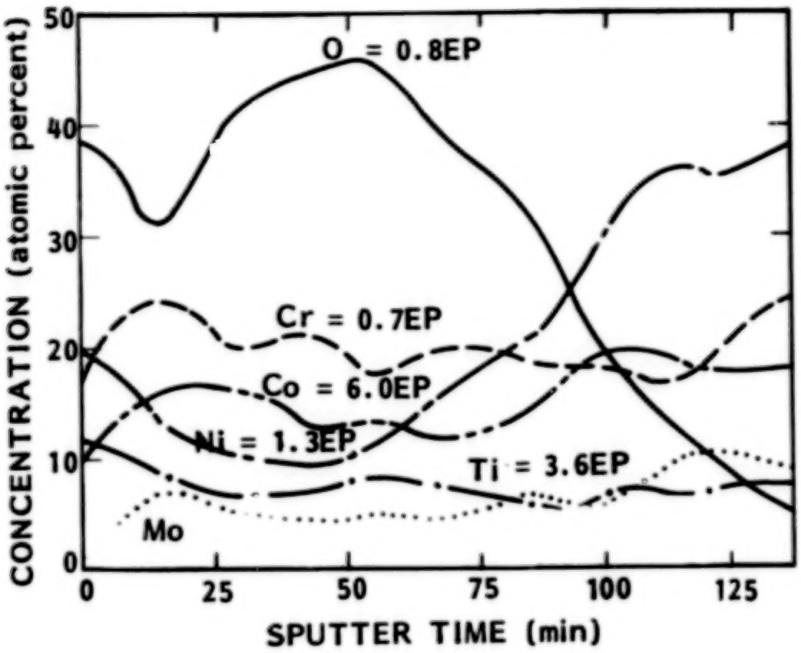

Figure 56. AES depth profile of statically oxidized Inconel 617.

noted that the oxygen concentration is approximately 0.8 of the EP derived value, chromium is 0.7 of the EP value, and the AES data for cobalt and titanium are 4 to 6 times those for the EP data. Although the absolute accuracy is poor, the relative distributions of an element within a single specimen and between specimens are believed to be considerably more accurate.

Figure 56 shows a relatively uniform chromium (with some depletion at the surface) and cobalt distribution through the bulk of the oxide layer; the oxide-base metal interface is in the region of 100 to 140 min on the abscissa. Nickel concentration, however, drops with increasing depth in the oxide. The surface layer has nearly equal concentrations of chromium and nickel, 20 atomic percent, and 10 to 11 atomic percent each of cobalt and titanium. Oxide layer thickness appears to be roughly equivalent to 100 min of sputtering time. Recalling the irregular surface and interface contours of the statically oxidized material (figure 46) it is expected this interface would extend for 30 to 40 min in the time domain.

A surface profilometer (DEKTAK) trace of the sputtered crater and the oxide surface in the vicinity of the crater revealed (1) an average crater depth of 4.3 μm with a peak-to-peak roughness at the bottom of the crater of 2 μm, (2) a crater width of 0.8 by 1.4 mm (from two orthogonal traces), and (3) an oxide surface roughness of 2.8 μm peak-to-peak. In view of the crater bottom roughness the location of an oxide-base metal interface is poorly defined and the accuracy of the concentration gradient information is compromised. The measured crater depth at the termination of sputtering corresponds to an overall sputtering rate of approximately 5 Å per second.

AES data showed that testing in the radiant heating apparatus did not appreciably influence concentration profiles in the oxide as can be seen in figure 57 for the 20 radiant heating cycle test data. The bulk oxide composition measured after 20 to 30 minutes of sputtering is similar to the statically oxidized specimen data. Similar results also are observed for 10 and 100 cycles of radiant heating (figures C-7 and C-9 of Appendix C). A substantial oxygen decrease is seen during the initial sputtering for the 100 radiant cycle specimen (figure C-9), which is probably an artifact of the analysis due to increased surface roughness (as seen from the DEKTAK data) or a more discontinuous scale-like outer layer.

Profilometer traces were made on the sputtered craters for the 10, 20, and 100 radiant heating test specimens to verify sputtering rates. In all cases the average rate computed from crater mean depth divided by total sputtering time was 4.9 to 5.7 Å per second. Crater bottom surface roughness was 2 to 3 μm peak-to-peak, which is consistent with the observation for the statically oxidized specimen. Surface roughness measurements made in areas immediately adjacent to the craters gave peak-to-peak roughness values of 3.0 μm for 10 radiant test cycles, 2.4 μm for 20 radiant test cycles, and 5 μm for 100 radiant test cycles.

AES depth profiles for the statically oxidized Inconel 617 after 8 cycles in the supersonic arc plasma wind tunnel are shown in figures 58 and 59 for boundary layer and rear surfaces of the specimen, respectively. On the boundary surface (figure 58) the nickel and cobalt follow each other closely. The oxide surface has nearly equal amounts of nickel, chromium, and cobalt. The rear surface of this specimen shows a nickel rich surface layer and concentration profiles of nickel, chromium, and cobalt which are similar to the statically oxidized and radiant heating results (c.f. figures 57 and 59).

Figures 60 and 61 show the AES depth profile results for the specimens tested for 38 cycles in the supersonic arc plasma wind tunnel. The boundary layer surface profile (figure 60) shows a higher nickel concentration than was seen for the 8 cycles specimen, but a similar nickel-cobalt behavior is evident; i.e., nickel and cobalt concentrations vary in the same manner in the oxide layer. After the first oxide layer sputtering period of 350 min (figure 60a), a second depth profile was done for an additional 470 min (figure 60b) starting at the bottom of the initial sputter crater. This profile was done to examine the elemental distributions in the base metal.

BEST DOCUMENT AVAILABLE

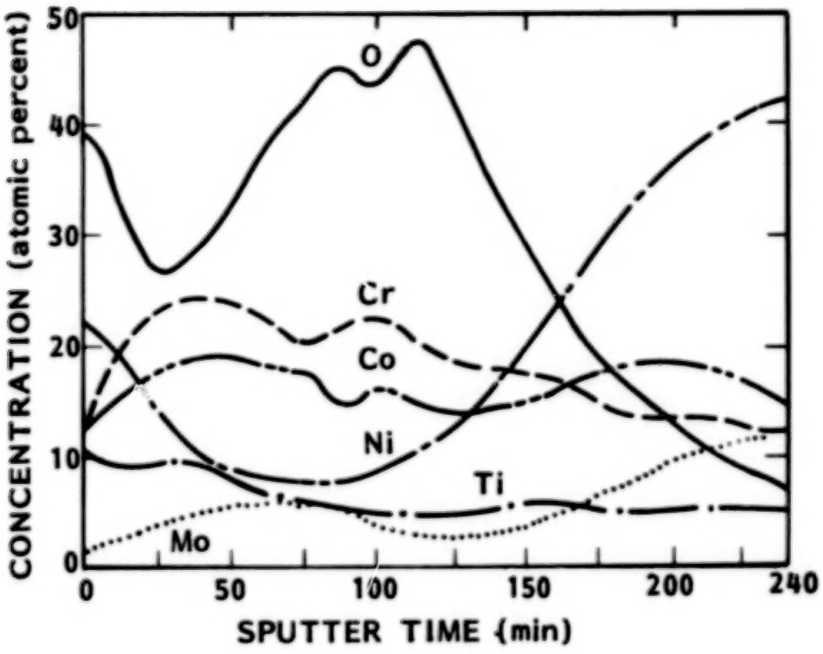

Figure 57. AES depth profile of statically oxidized Inconel 617 after 20 radiant heating test cycles.

The results show a chromium depletion in the vicinity of the oxide-metal interface, with the chromium increasing to the bulk value as one proceeds away from the interface into the base metal.

The rear surface of this 38 cycle specimen (see figure 61) shows a very high nickel concentration at the exterior surface with high cobalt and low chromium percentages. After the initial sputtering period chromium rises very strongly and nickel shows a corresponding decrease.

Figure 62 shows the average concentration of chromium, cobalt, nickel, and titanium in the oxide layers of Inconel 617 specimens as a function of reentry test conditions. These data were obtained from the AES depth profiles for the exterior surface and for two depths into the oxide from its surface. The depths are 25 and 50 percent of the oxide thickness, and the compositions are the average over each thickness. Thickness determination was based upon the sputter time required for oxygen concentration to decrease to 10 percent; e.g., for the statically oxidized specimen (figure 56), the oxide layer thickness was taken as 120 min, and the 25 and 50 percent values are the average compositions (in atomic percent) from 0 to 30 and 0 to 60 min, respectively. The surface composition is included since changes in a thin layer at the surface may correlate with the visual appearance and short

BEST DOCUMENT AVAILABLE

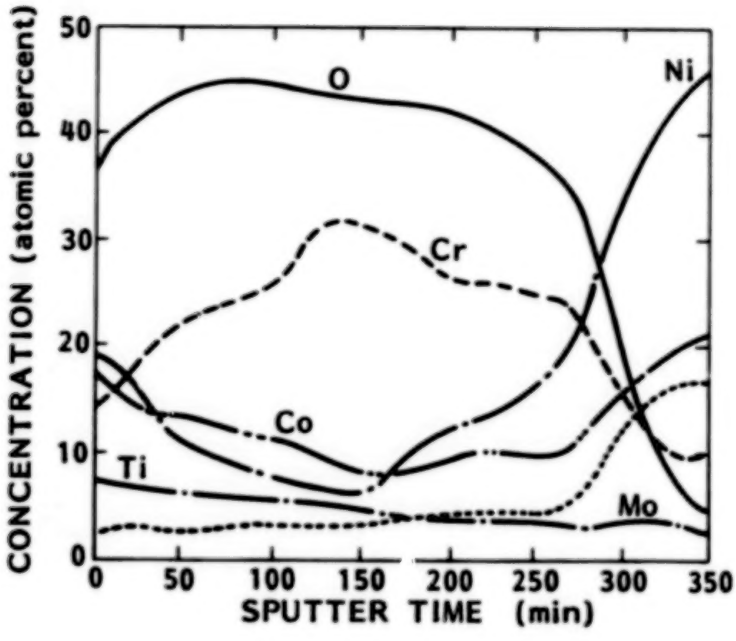

Figure 58. AES depth profile of boundary layer surface of statically oxidized Inconel 617 after 8 supersonic arc plasma wind tunnel test cycles.

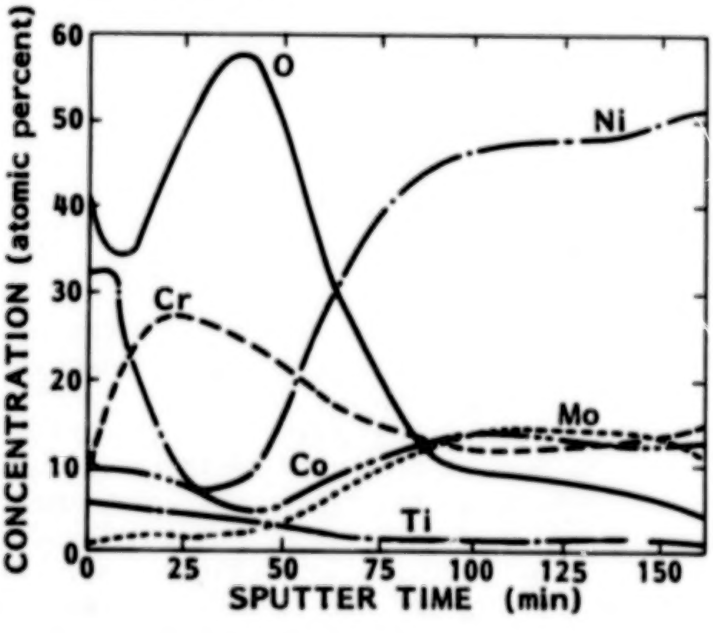

Figure 59. AES depth profile of rear surface of statically oxidized Inconel 617 after 8 supersonic arc plasma wind tunnel test cycles.

BEST DOCUMENT AVAILABLE

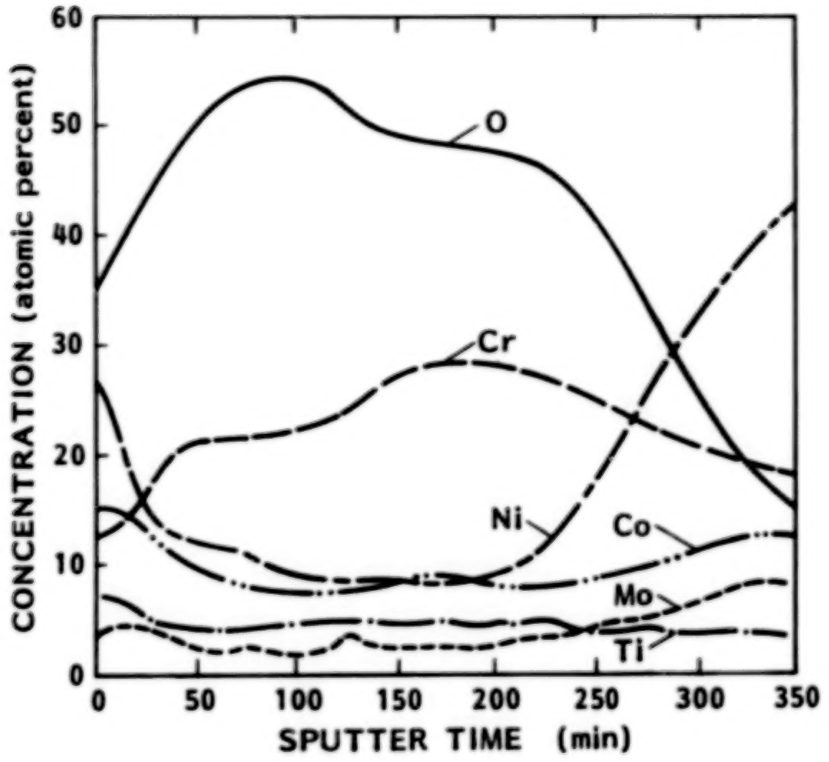

(a) First 350 min of sputtering

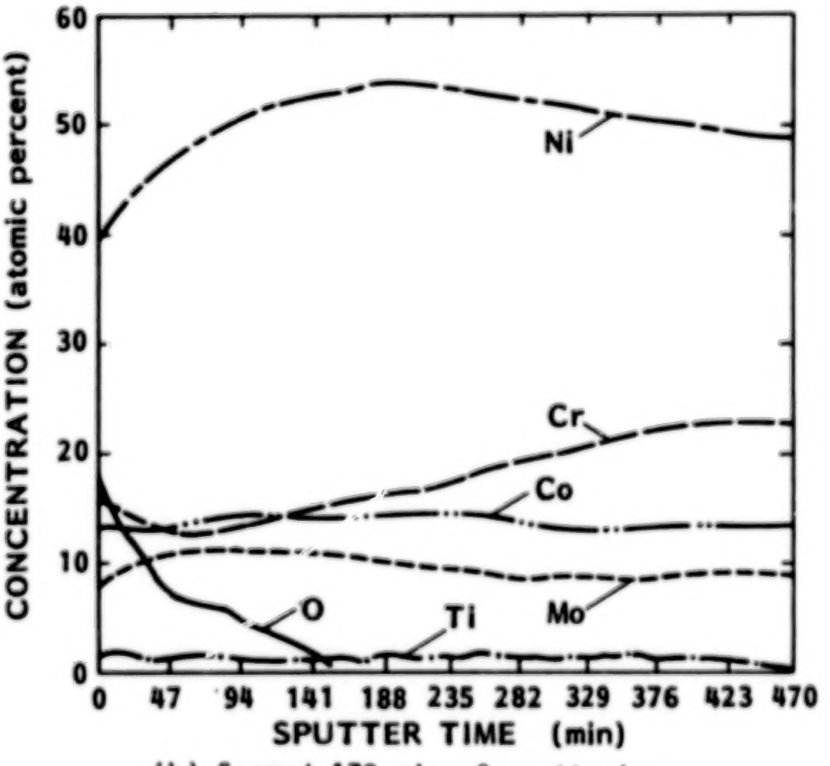

(b) Second 470 min of sputtering

Figure 60. AES depth profile of boundary layer surface of statically oxidized Inconel 617 after 38 supersonic arc plasma wind tunnel test cycles.

BEST DOCUMENT AVAILABLE

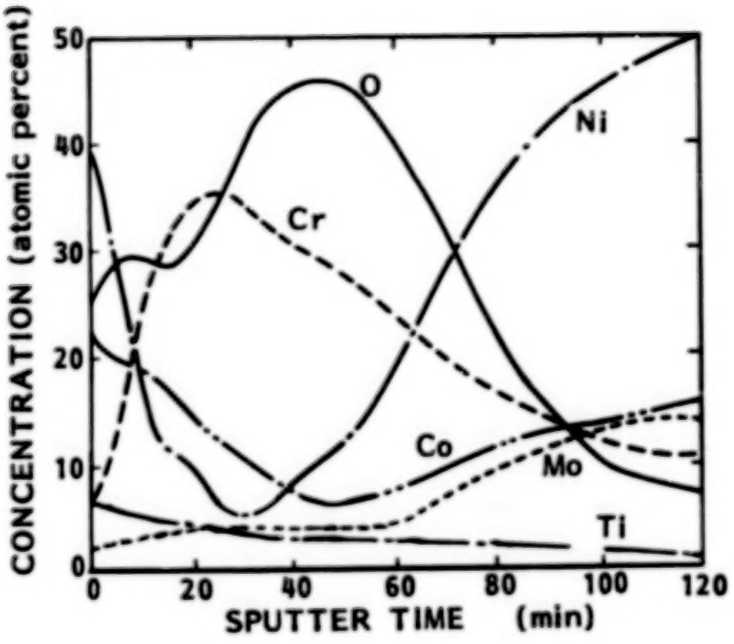

Figure 61. AES depth profile of rear surface of statically oxidized Inconel 617 after 38 supersonic arc plasma wind tunnel test cycles.

wavelength spectral normal reflectance differences seen after supersonic arc plasma wind tunnel tests. The 25 and 50 percent values can be compared with the EP and x-ray diffraction data which are more representative of the bulk oxide characteristics.

In all cases, the surface composition data (figure 62a) show nickel as having the highest concentration. For the statically oxidized specimen there is almost as much chromium as nickel, but after reentry tests the trend is for increasing nickel and decreasing chromium. Titanium is present in much higher concentrations than would be expected on the basis of the EP data. The cobalt-nickel ratio is nearly unity for the statically oxidized, the 10 and 20 radiant heating cycle test, and the boundary layer surface of the 38 cycle supersonic arc plasma wind tunnel test specimens. Both surfaces of the 8 cycle supersonic arc plasma wind tunnel test specimen and the rear surface of the 38 cycle specimen show a cobalt-nickel ratio of 2 or greater.

The average elemental composition data for the outer 25 percent of the oxide layer (figure 62b) show chromium as a major element in comparable concentrations in all cases. Cobalt shows the most variability with reentry testing. Titanium remains relatively high in concentration and generally follows the surface results (c.f. figures 62a and b). The 50 percent

BEST DOCUMENT AVAILABLE

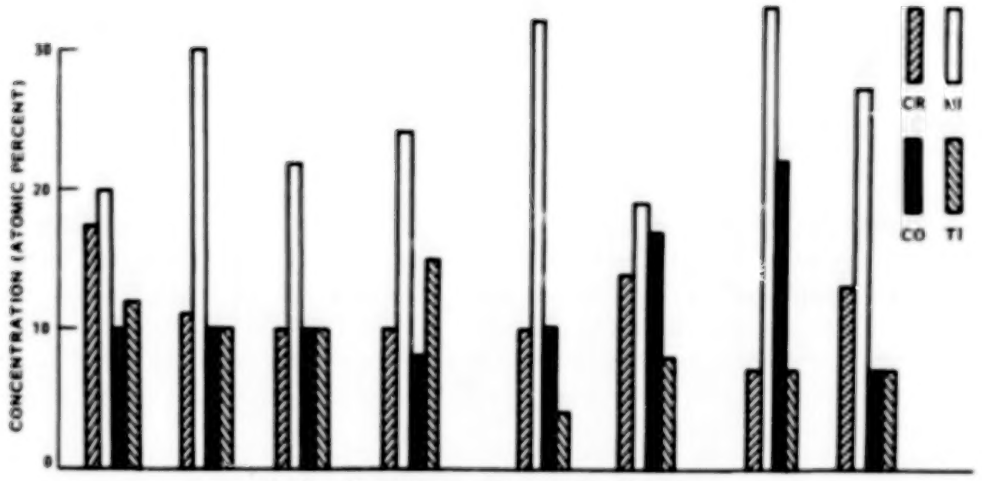

(a) Surface of oxide layer

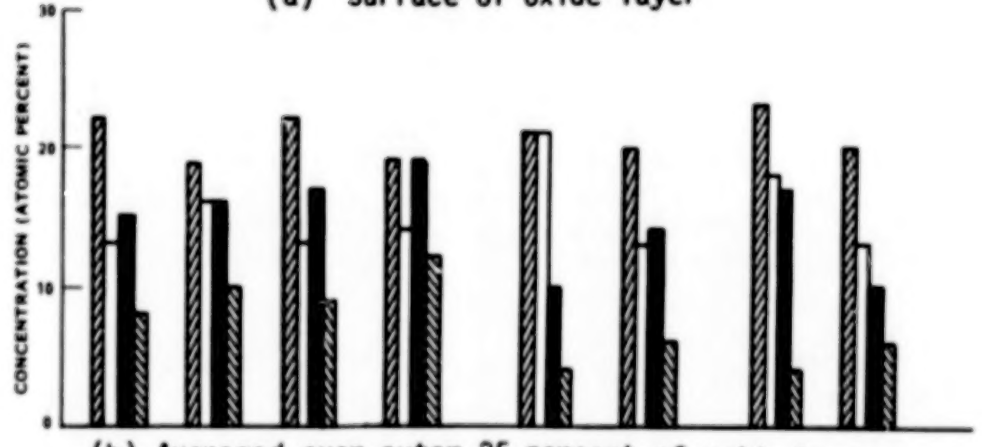

(b) Averaged over outer 25 percent of oxide layer

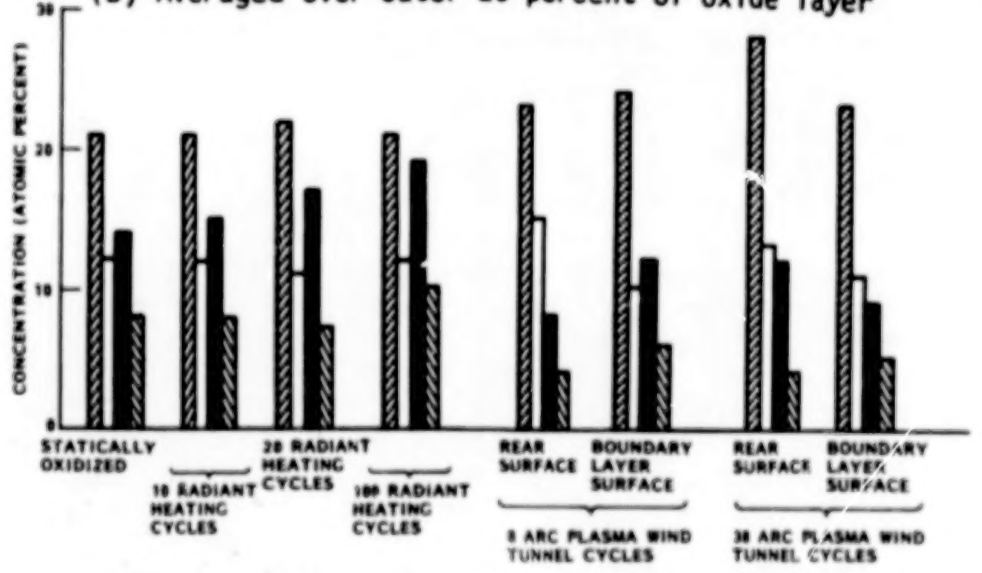

(c) Averaged over outer 50 percent of oxide layer

Figure 62. Inconel 617 oxide layer chromium, cobalt, nickel, and titanium concentrations as a function of reentry test condition.

thickness averaged data (figure 62c) show a small increase in percentages of chromium over those for the 25 percent thickness. Nickel content is decreased from that observed for the 25 percent thickness and surface data. Also, cobalt is lower than the corresponding 25 percent thickness averaged values for the supersonic arc plasma wind tunnel test specimens.

On a quantitative basis the AES results do not agree with the EP data in that the percentage of chromium from the AES results is on average only 0.7 times that reported using the EP. Nickel concentrations derived from the AES are on the order of twice those determined with the EP. Cobalt and titanium concentrations are much greater using the AES. As was emphasized previously these disagreements arise from the semiquantitative nature of the AES in converting electron intensities to atomic concentrations using imprecise sensitivity factors.

SIMS measurements were made on only two specimens, viz., the statically oxidized, and the 38 cycle supersonic arc plasma wind tunnel test specimens. These data are qualitative, but were obtained to verify the trends in elemental concentration gradients observed in the AES data. In order to increase the sputtering rate to an acceptable level (approximately 500 Å per minute), a 5 keV O^+ ion beam was used and, consequently, no oxygen analysis could be made. The SIMS profiles (figure 63) support the AES data showing the general trends of the chromium, nickel, and cobalt concentration gradients, and a high titanium concentration at the surface decreasing into the base metal.

Structure. Results of the x-ray diffraction analyses of the Inconel 617 specimens are given in Table 22. The data are qualitative as they are given in a coarse scale of the amount of a specific crystallographic phase present; i.e., major, minor, trace, or not detectable. These rankings are derived from line intensities which were not compared with standards containing known quantitites of the mixed phases. These analysis results are for the total thickness of the oxide layers. No crystallographic depth profile data were obtained by sectioning, etc.

Only three distinct crystallographic phases were detected; Cr_2O_3, (CoNi)O, and $(CoNi)Cr_2O_4$. (CoNi)O represents the cubic mixed oxide which forms a continuous solid solution between CoO and NiO. Similarly, $(CoNi)Cr_2O_4$ represents the cubic spinel which forms a continuous solid solution between $CoCr_2O_4$ and $NiCr_2O_4$. In both the mixed oxide and the spinel cases the x-ray diffraction data were not sufficiently precise to determine the relative amounts of nickel and cobalt in each of these compounds. Comments are made on the degree of crystallographic orientation for the (CoNi)O phase on the basis of the intensity of the [200] reflection. No orientation was observed for the other phases which were detected.

Cr_2O_3 is a major phase in all specimens examined, regardless of type or duration of testing. For the statically oxidized Inconel 617, (CoNi)O is

BEST DOCUMENT AVAILABLE

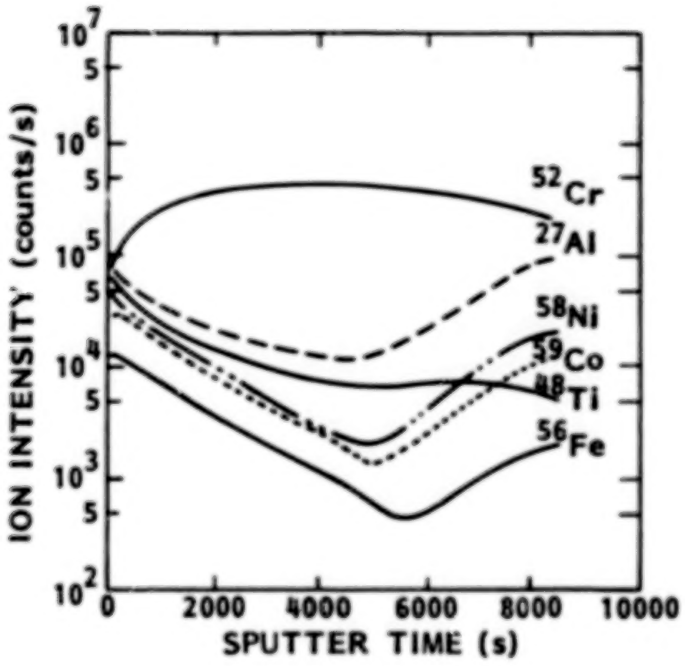

(a) As prepared

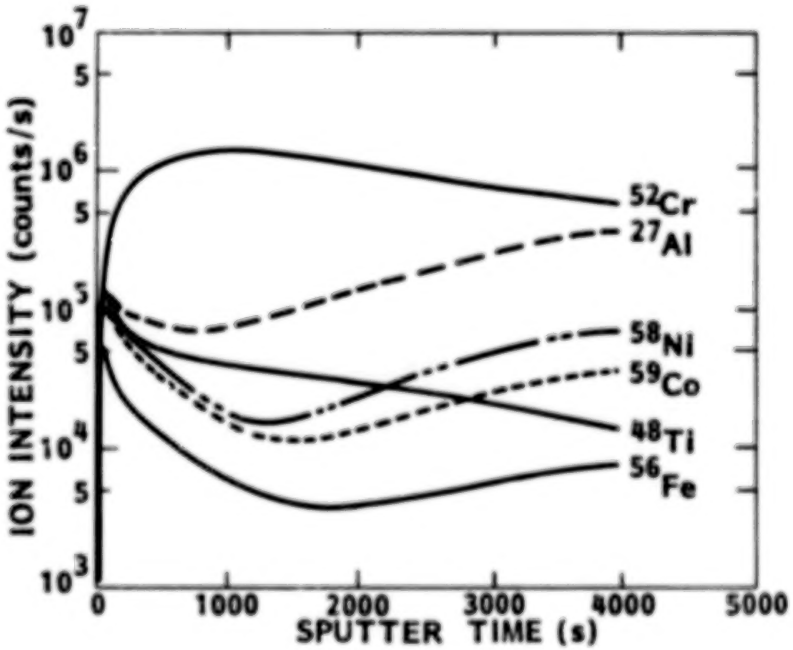

(b) Boundary layer surface after 38 supersonic arc plasma wind tunnel test cycles

Figure 63 SIMS depth profile of statically oxidized Inconel 617.

Table 22. X-ray Diffraction Analysis of Inconel 617 Specimens

Simulated Reentry Exposure Test		Crystallographic Phase		
		Cr_2O_3	(CoNi)O	$(CoNi)Cr_2O_4$
None, Statically Oxidized		M	M[b]	Tr
Supersonic Arc Plasma	F	M	Tr	ND
Wind Tunnel, 8 cycles[a]	R	M	Mr-M	Tr-Mr
Supersonic Arc Plasma	F	M	Mr[c]	Tr-Mr
Wind Tunnel, 20 cycles[a]	R	M	Tr-Mr[c]	Tr-Mr
Supersonic Arc Plasma	F	M	Tr[c]	Tr-Mr
Wind Tunnel, 38 cycles[a]	R	M	Mr-M[c]	Tr-Mr
Radiant Heating, 10 cycles		M	Mr[c]	Tr-Mr
Radiant Heating, 20 cycles		M	Tr-Mr[c]	Tr-Mr
Radiant Heating, 100 cycles		M	Tr	Mr-M

M = Major, Mr = Minor, Tr = Trace, ND = not detected

(a) F denotes boundary layer surface, R denotes rear surface for supersonic arc plasma wind tunnel test specimens

(b) Strongly oriented

(c) Some orientation

also a major phase and $(CoNi)Cr_2O_4$ is present as a trace amount. The (CoNi)O is strongly oriented crystallographically.

After the radiant heating tests, Cr_2O_3 remains a major phase, (CoNi)O decreases with increasing number of test cycles to a trace amount after 100 radiant heating cycles, and $(CoNi)Cr_2O_4$ increases to a minor-major amount present. The terminology of trace-minor and minor-major is used to describe cases in which the measured x-ray intensities fell in the region between clearly defined levels. The decrease in (CoNi)O was nearly monotonic with increasing number of test cycles, the amount of this phase changing from major for the statically oxidized specimen to trace after 100 radiant heating test cycles. The level of crystallographic orientation also decreases from strongly oriented for the statically oxidized specimen to weakly oriented after 10 and 20 radiant heating test cycles to no detectable orientation after 100 cycles. The amount of $(CoNi)Cr_2O_4$ increases with the number of radiant heating cycles from a trace amount at 0 cycle to minor-major after 100 cycles.

After testing in the supersonic arc plasma wind tunnel the amount of (CoNi)O present in the rear surface of the test specimen decreases with increasing number of test cycles to 8 and 20 cycles, then increases between 20 and 38 test cycles. No crystallographic orientation of the (CoNi)O phase was observed after 8 test cycles, but then a weak orientation was seen after 20 and 38 test cycles. The $(CoNi)Cr_2O_4$ phase increases from a trace amount for the statically oxidized specimen to trace-minor after 8 test cycles and then remains constant for 20 and 38 test cycles.

The boundary layer surfaces of these specimens show a different behavior than that of the rear surfaces with respect to (CoNi)O and $(CoNi)Cr_2O_4$ in that there is a sharp decrease in the amount of these phases present after 8 test cycles. Then the (CoNi)O increases at 20 cycles, but decreases again at 38 cycles. The $(CoNi)Cr_2O_4$ is not detected at 8 cycles, and then it rises to trace-minor for 20 and 38 cycles.

Data Summary. The bulk oxide layer formed by the static oxidation procedure used in this study is composed primarily of Cr_2O_3 and the mixed cobalt-nickel oxide (otherwise referred to as mixed metal oxide), (CoNi)O, with smaller amounts of the spinel, $(CoNi)Cr_2O_4$. This composition is obtained from the x-ray diffraction analyses. The strongly oriented nature of the x-ray diffraction pattern for the (CoNi)O phase shows that it is present in single crystal form.

The SEM images of the surface together with the EP analysis identified two principal features. They are smooth regions consisting almost wholly of chromium, and crystalline appearing bodies rich in nickel with some cobalt. Chromium also was detected strongly in the EP analysis of the lumps; it may derive, however, from the underlying or surrounding material.

The EP analysis of the bulk oxide indicates that about four times as much nickel as cobalt is present. The AES and SIMS data show that the nickel concentration drops off with depth; i.e., much of the nickel is concentrated near the surface of the oxide. Conversely, the chromium concentration rises rapidly with depth to a roughly constant value.

The data summarized above can be interpreted in a consistent manner to derive the following description of the statically formed oxide. It consists of a Cr_2O_3 matrix in which are imbedded crystallites of (CoNi)O. The preponderance of nickel over cobalt indicates that the mixed metal oxide is almost pure NiO. The size of the crystallites (1 to 4 μm) is comparable to the layer thickness. It is likely therefore that they are oriented by contact with the subsurface metal. In view of the trace amounts of spinel detected by XRDA it is not possible to locate its position in the oxide layer.

Surfaces of the radiant test specimens and those of the rear of the supersonic arc plasma exposed specimens generally showed some crystalline or faceted structure similar to that of the statically oxidized specimens. Boundary layer surfaces have an apparent porous texture, with poorly defined lumps 1 to 5 μm in size. EP measurements on both surfaces of the supersonic arc plasma exposed specimens are similar to those obtained on the static oxide; i.e., featureless areas consist predominantly of chromium and the lumps contain substantial amounts of nickel. Since the XRDA measurements show that there is still oriented (CoNi)O present and very little spinel the lumps are probably the mixed metal oxide.

Cr_2O_3 is the major phase detected in all oxides formed after radiant heating or supersonic arc plasma wind tunnel tests. This was determined by x-ray diffraction analyses and confirmed by AES measurements. The x-ray diffraction analysis show a decrease in the mixed metal oxide phase and a pronounced increase in the spinel phase with increasing number of radiant cycles.

A small change in oxide layer thickness occurred during supersonic arc plasma wind tunnel testing on the specimen surfaces exposed to the boundary layer flow, from a statically oxidized thickness of 3.2 - 4 μm to 2.2 - 2.6 μm after testing. The oxide layer thicknesses on the rear surfaces of these arc plasma test specimens was relatively constant at 3.0 to 3.3 μm. This range of oxide layer thicknesses observed for the rear surfaces is similar to that measured on the radiant heating test specimens, 2.9 to 3.3 μm.

4.3.2 Haynes 188

Morphology. A low magnification SEM image of the statically oxidized Haynes 188 alloy (HS188) is shown in figure 64a. The surface morphology has the appearance of a grain boundary pattern as was also the case for statically oxidized Inconel 617 (figure 45). Higher magnification images of the surface oxide from the SEM are shown in figures 64b through 64d. The entire surface is covered with well defined crystallite shaped features. Two distinct types

BEST DOCUMENT AVAILABLE

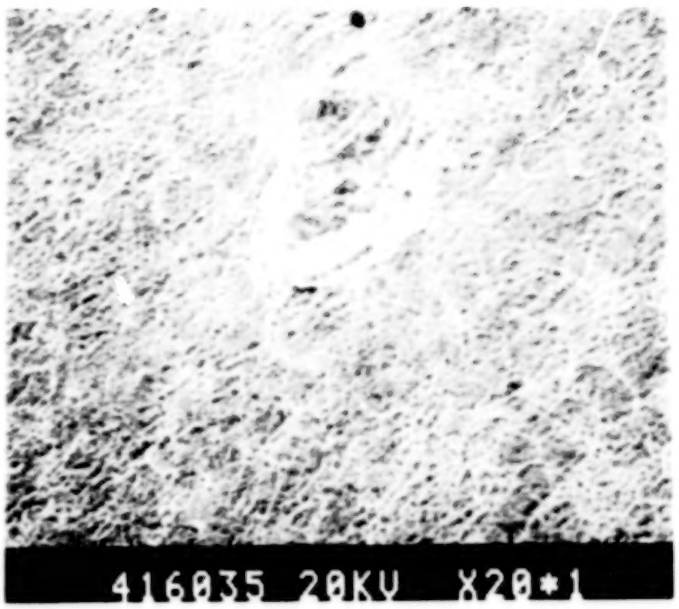

(a) 200x

(b) 1000x

(c) 4000x

(d) 10,000x

Figure 64. Surface topography of statically oxidized HS188.

are present, one is 1 to 2 μm in size, and the other is multifaceted, about 0.3 μm in size.

Photomicrographs of the taper sections produced by the cylindrical grinding method (see Section 3.5.3) are shown in figure 65. The oxide layer appears considerably more uniform than was seen for the statically oxidized Inconel 617 (c.f. figures 46a and 65a). Grain size in the base metal (figure 65b) is in the 30 to 50 μm range.

The appearance of the specimens of statically oxidized HS188 after 8, 20 and 38 cycles of supersonic arc plasma wind tunnel tests all appear very similar. Figures 66 and 67 show SEM images of the boundary layer surface of HS188 after supersonic arc plasma wind tunnel tests of 8 and 38 cycles, respectively. No strong indication of grain boundary structure is evident. The surface has a structureless or flocculent appearance. The crystalline features of the thermal oxide are no longer present.

The rear surfaces of the 8 and 38 cycle test specimens are shown in figures 68 and 69, respectively. At the low magnification (200x), it can be seen that the surfaces are weakly ridged; i.e., the grain boundary structure is not as clearly defined as for the statically oxidized sample (c.f. figure 64a). At higher magnification (4000x) the surface is seen to be covered with granules of comparable size to those seen in figure 64c, but they are somewhat rounded. In fact, after 38 supersonic arc plasma wind tunnel test cycles (see figure 69b), the particles appear to have interdiffused to the stage of losing their individual identities.

The surface morphology of the specimens exposed to the radiant heating tests (see figure 70 for 20 radiant heating cycles) is similar to that of the rear surfaces of the supersonic arc plasma wind tunnel test specimens, i.e., a crystalline like structure, but with rounding of corners and apparent fusion of adjacent particles. The 20 and 50 cycle radiant heating test specimens appear very similar to the SEM images of the rear surface of the 38 cycle supersonic arc plasma wind tunnel specimen (figure 69). After 100 radiant test cycles the individual particles are all interdiffused into a continuous, ridge-like structure.

Photomicrographs of the cylindrical grinding areas on both surfaces of the 38 cycle supersonic arc plasma wind tunnel test specimen are shown in figure 71. The appearance of the oxide layer on the rear surface of the specimen (figures 71a and b) is quite similar to that for the statically oxidized specimen (figure 65) in that the layer is of uniform thickness with a relatively smooth oxide-metal interface zone. Conversely, the boundary layer surface is more irregular at the oxide metal interface and the oxide layer is somewhat discontinuous in appearance. The grain size in the base metal (figure 71d) is 40 to 50 μm which is the same as that in the statically oxidized material.

BEST DOCUMENT AVAILABLE

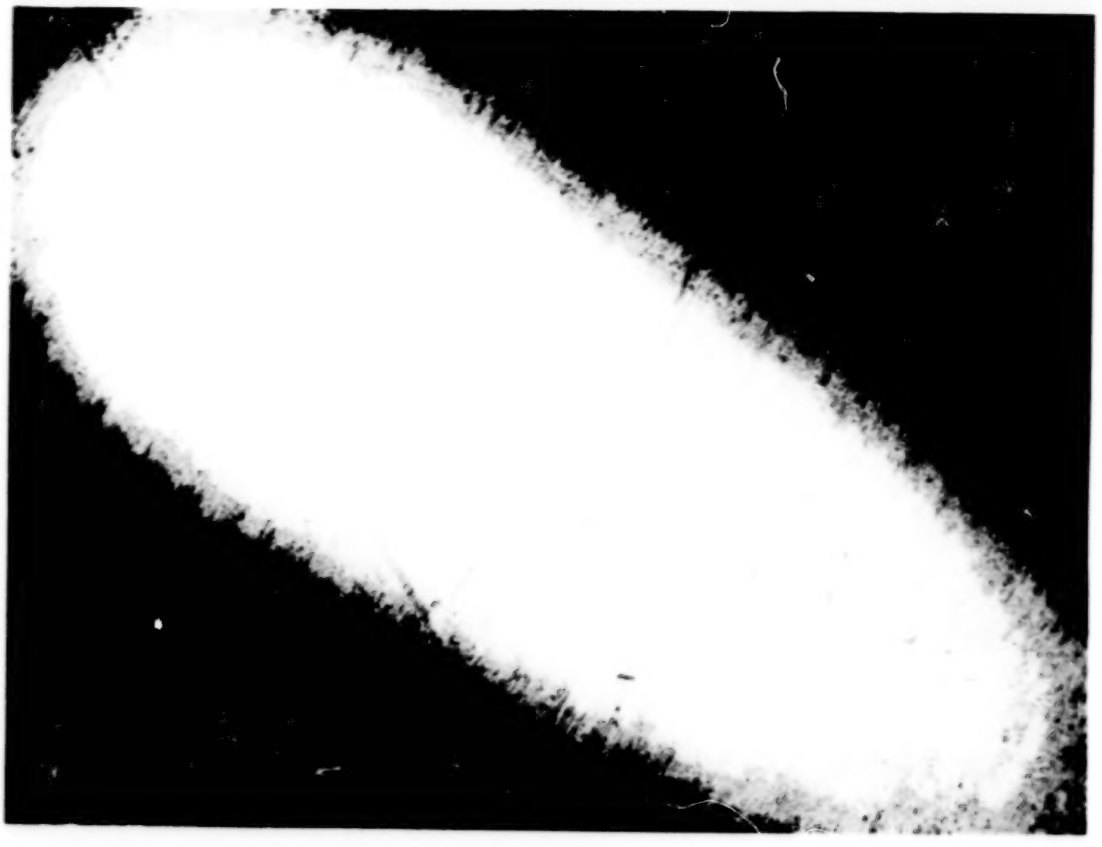

(a) 63x

(b) 200x

Figure 65. Photomicrographs of the cylindrical grinding region on the surface of statically oxidized HS188.

BEST DOCUMENT AVAILABLE

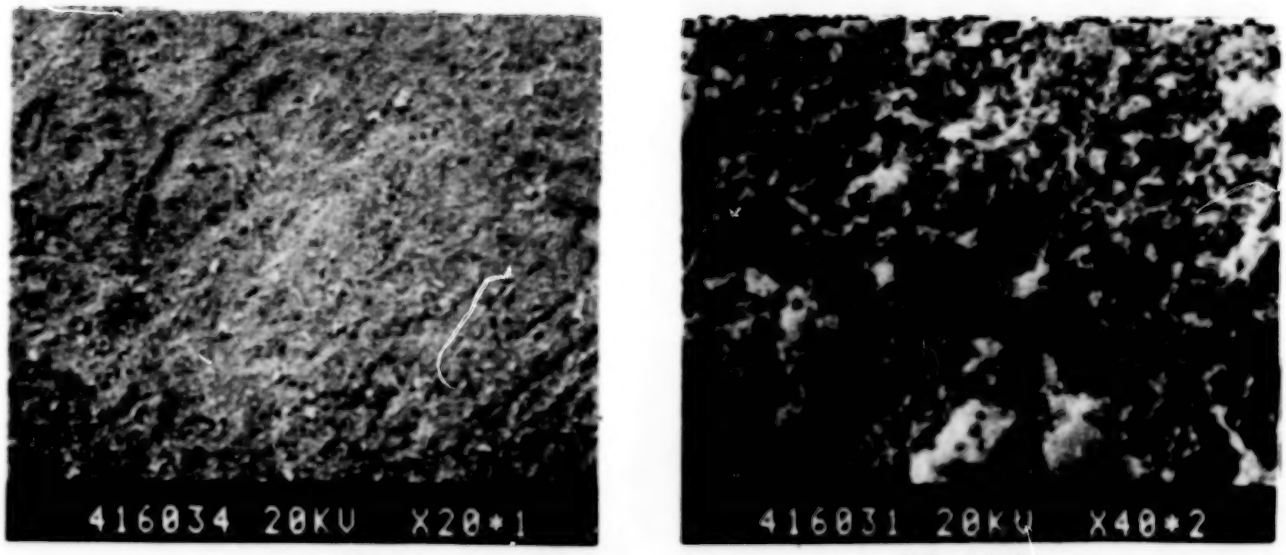

(a) 200x (b) 4000x

Figure 66. Boundary layer surface of statically oxidized HS188 after 8 cycles in supersonic arc plasma wind tunnel.

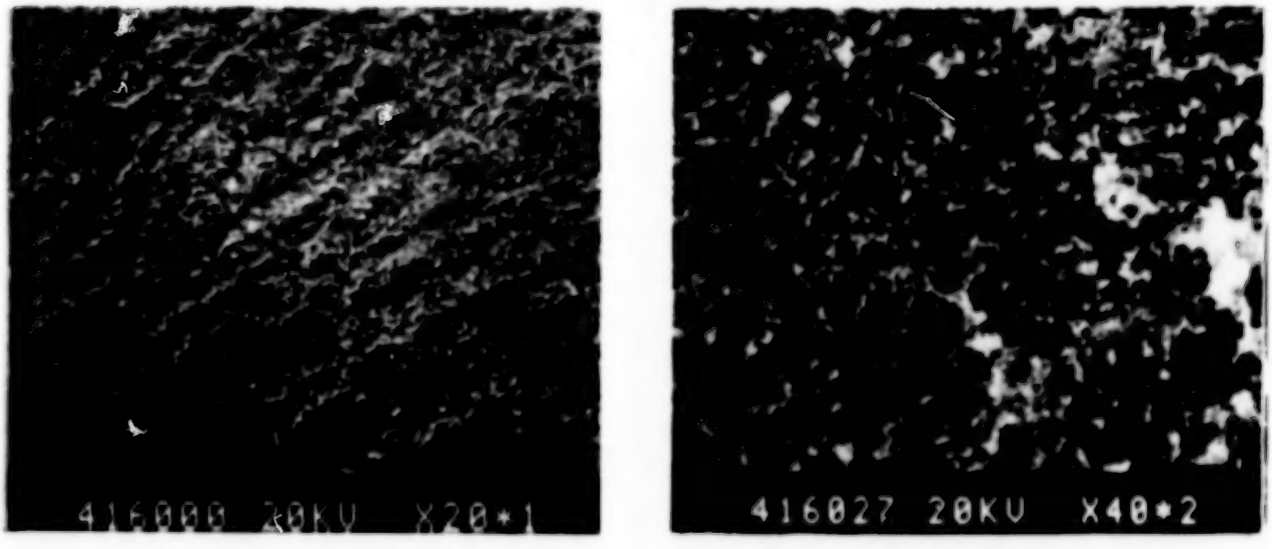

(a) 200x (b) 4000x

Figure 67. Boundary layer surface of statically oxidized HS188 after 38 cycles in supersonic arc plasma wind tunnel.

BEST DOCUMENT AVAILABLE

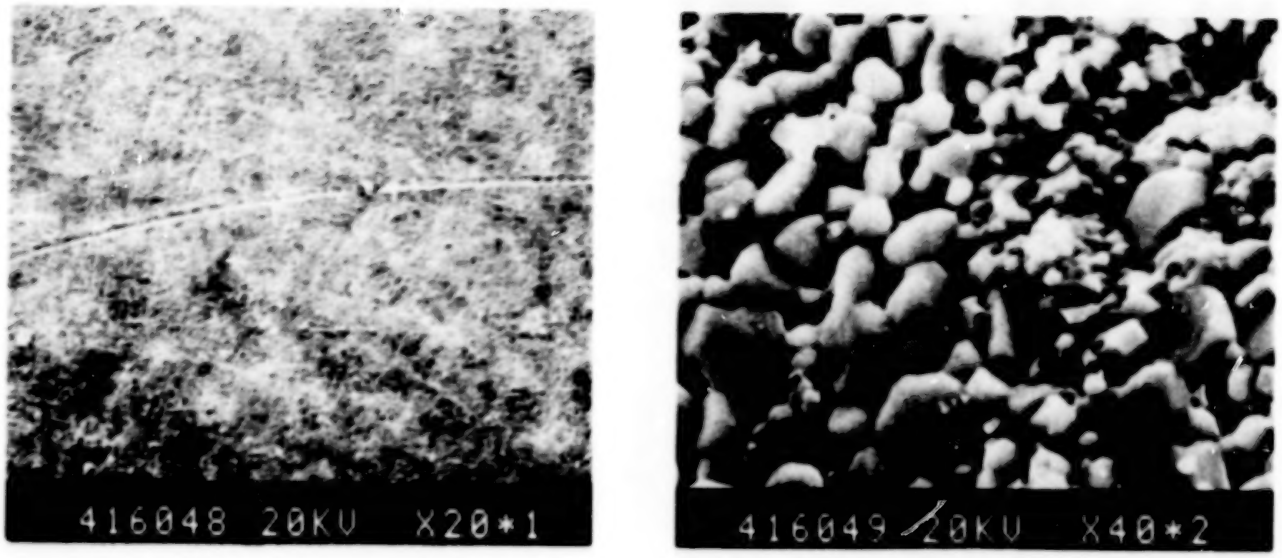

(a) 200x (b) 4000x

Figure 68. Rear surface of statically oxidized HS188 after 8 cycles in supersonic arc plasma wind tunnel.

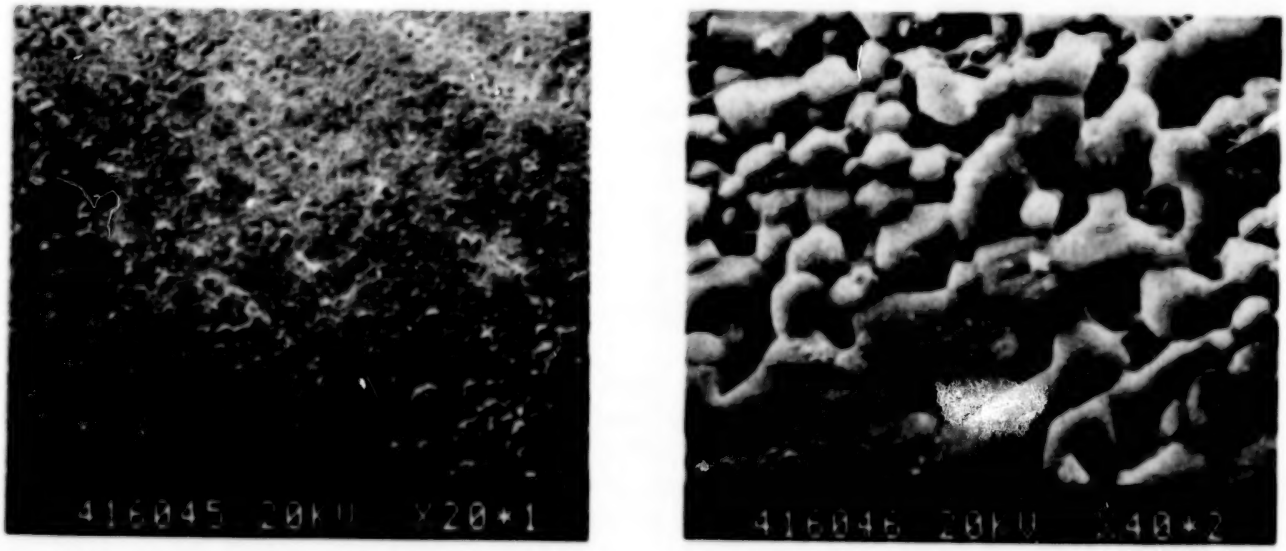

(a) 200x (b) 4000x

Figure 69. Rear surface of statically oxidized HS188 after 38 cycles in supersonic arc plasma wind tunnel.

BEST DOCUMENT AVAILABLE

Figure 70. Surface of statically oxidized HS188 after 20 radiant heating test cycles (1000 x).

Oxide layer and specimen overall thickness measurements were made on the test specimens, and the results are given in Table 23. The first of two columns under the overall Specimen Thickness heading are for the HS188 alloy initially procured for test specimen preparation and the second for additional test specimens for the supersonic arc plasma wind tunnel. Overall thickness data show that no significant change was induced by the reentry testing. All measurements fall within the bare metal sheet thickness range. Oxide layer thickness increased during the initial 8 test cycles in the supersonic arc plasma wind tunnel, then decreased to nearly the statically oxidized thickness after 38 cycles. The radiant heating test produced an initial increase in oxide layer thickness (10 cycles) and then a decrease to a sightly greater thickness than for the statically oxidized case.

Composition. Electron microprobe analyses were done to (1) give quantitative elemental composition of the oxide surface and (2) qualitative compositions of characteristic surface features observed during morphological examinations. The EP analysis covered an area typically 1 μm in diameter by 1 μm in depth. The AES was used primarily to measure elemental profile distributions through the oxide layers by a sputtering technique using a rastered 5 keV argon ion beam to analyze an area approximately 1 by 1.5 mm. Because of the charging effects with the HS188 specimens the beam current was very low, 100 nA or less.

BEST DOCUMENT AVAILABLE

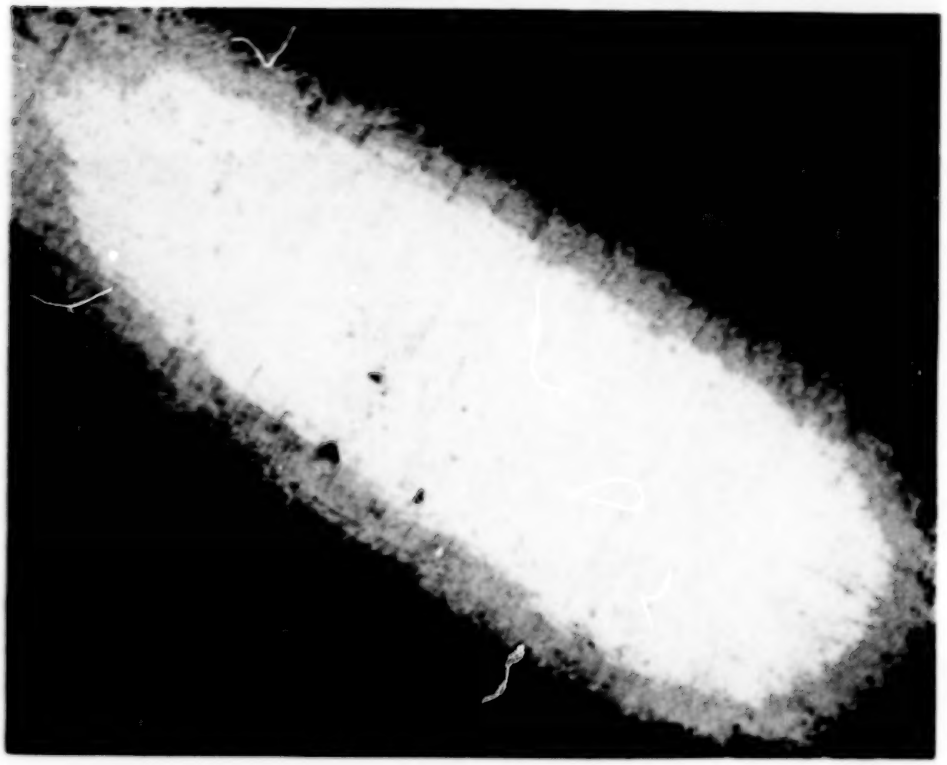

(a) Rear surface, 63x

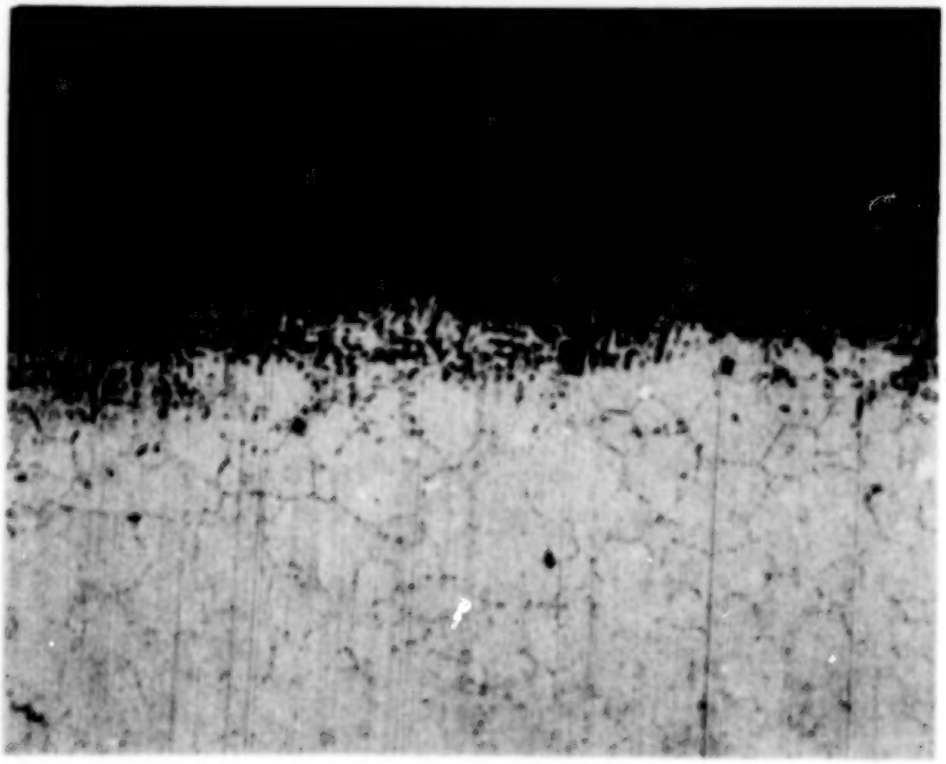

(b) Rear surface, 200x

Figure 71. Photomicrographs of the cylindrical grinding areas on both surfaces of the HS188 38 cycle supersonic arc plasma wind tunnel test specimen.

BEST DOCUMENT AVAILABLE

(c) Boundary layer surface, 80x

(d) Boundary layer surface, 200x

Fig. 71. (Cont.)

BEST DOCUMENT AVAILABLE

Table 23. Overall Thickness and Oxide Layer Thickness Data for H188 Specimens

Simulated Reentry Exposure Test	Overall Specimen Thickness (mm)[a]		Oxide Layer Thickness (μm)
	Initial Purchase	Second Purchase	
None, Bare Metal	1.016 -1.041	0.889 -0.914	--
None, Statically Oxidized[b]	1.035 ±1.003	0.888 +0.008 -0.007	1.5 - 1.7
Supersonic Arc Plasma Wind Tunnel, 7 Cycles[c]	1.041 +0.005 -0.004	--	--
Supersonic Arc Plasma Wind Tunnel, 8 Cycles[c]	1.036 +0.001	--	F[d], 2.9 R[d], 2.6
Supersonic Arc Plasma Wind Tunnel, 20 Cycles[c]		0.895 ±0.001	--
Supersonic Arc Plasma Wind Tunnel, 38 Cycles[c]	1.041 +0.005 -0.006	--	F, 1.6 R, 1.8
Radiant Heating, 10 Cycles[b]	1.040 +0.007 -0.006	--	2.5
Radiant Heating, 20 Cycles[b]	1.033 +0.005 -0.008	--	2.1
Radiant Heating, 50 Cycles[b]	1.034 +0.005 -0.008	--	1.5
Radiant Heating, 100 Cycles[b]	1.038 +0.003 -0.004	--	2.0

(a) Measurement Uncertainty = ±0.0025 mm
(b) Triplicate specimens, 4 measurements on each in central 25 mm by 50 mm region of strip.
(c) Single specimen, 5 measurements in vicinity of emittance specimen.
(d) F denotes boundary layer surface; R is rear surface.

SIMS measurements were made on several specimens to examine both major and minor element distribution profiles. In the measurements a 5 keV O^+ ion beam is focused onto the sample. Surface atoms are ejected or sputtered and the charged ions collected in a mass analyzer. For the data reported herein, the oxygen beam was rastered over an area of 60 by 100 μm, and the surface eroded at approximately 500 Å per minute. Continuous analysis of the ejected ions gives a profile of the elements in the oxide. Normally 30 to 40 min of sputtering was sufficient to sputter completely through the oxide to the metal. Major elements in the oxide, e.g., chromium, were detected using a Faraday cup. Minor elements, e.g., tungsten, were detected using an electron multiplier.

In view of the inhomogeneous nature of the oxides under study it was not possible to use the AES or SIMS techniques in a rigorously quantitative fashion. However, both techniques are useful for gaining insight into the semiquantitative profiles of the individual elements through the oxides.

Typical regions of the surface of the statically oxidized HS188 were analyzed for elemental composition in the EP. The results are given in Table 24 for the features or locations shown in figures 72 and 73.

Locations 2 and 3 of figure 72b, showed spectral intensities very similar to those seen in the metal. On the other hand, the small crystallite in the same figure (location 4) is considerably enriched in chromium and depleted of nickel. The well defined crystalline region of figure 72a shows a substantial enrichment of cobalt and nickel and a large drop in chromium, compared to the concentrations in the metal. Figure 73 shows two analysis locations for the

Table 24. Relative Line Intensities for Electron Microprobe Analysis of HS188 Specimens.

	Statically Oxidized (see figure 72)				Statically Oxidized Plus 38 Supersonic Arc Plasma Wind Tunnel Cycles, Boundary Layer Surface (see figure 73)	
Element	(1)	(2)	(3)	(4)	(1)	(2)
Co	ES	S	S	S	S	ES
Cr	S	S	S	ES	S	M
Ni	S	S	S	W	M	M
Mn	M	M	M	S	W	W
Fe	W	W	W	W	W	W
W	W	T	W	T	M	W

ES = extra strong, S = strong, M = medium, W = weak, T = trace.
Numbers in parentheses denotes locations on figures 72 and 73.

BEST DOCUMENT AVAILABLE

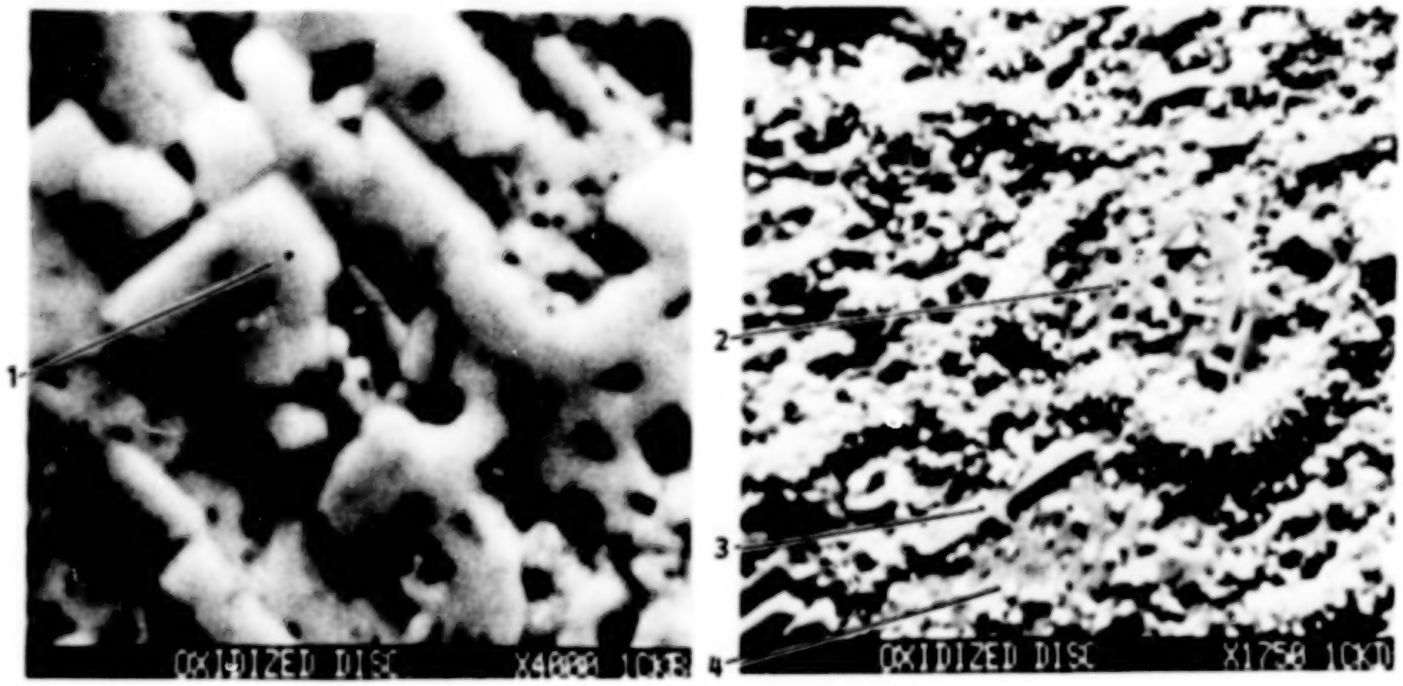

(a) (b)

Figure 72. EP analysis locations for the statically oxidized HS188 specimen.

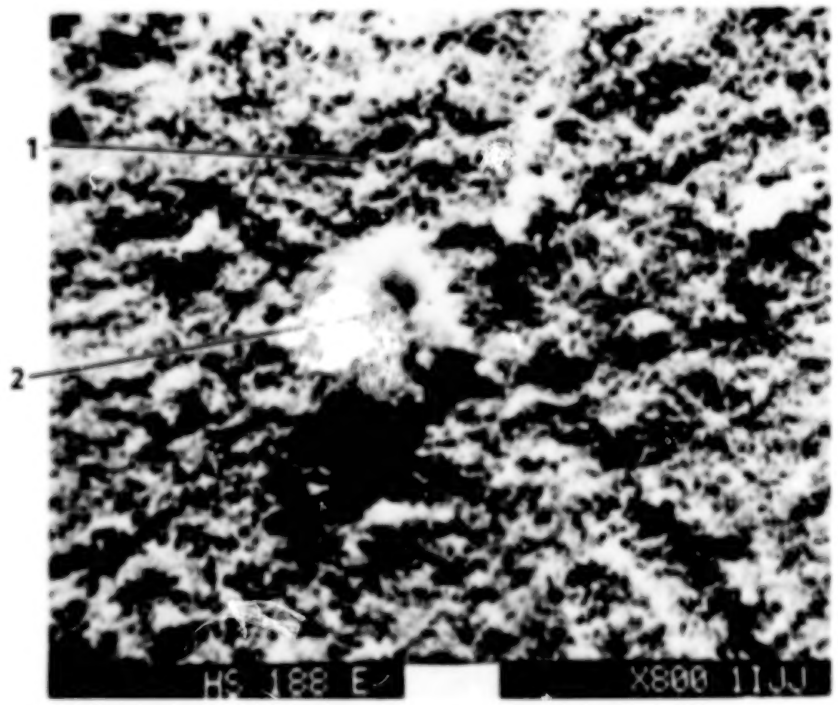

Figure 73. EP analysis locations for boundary layer surface of the HS188 38 cycle supersonic arc plasma wind tunnel test specimen.

boundary layer surface of the 38 cycle supersonic arc plasma wind tunnel test specimen. These results (Table 24) show a reduction of nickel and chromium from that seen for the statically oxidized condition.

Quantitative elemental surface analyses of the oxide layers on statically oxidized, 100 cycle radiant-heating test, and 38 cycle supersonic arc plasma wind tunnel test specimens are given in Table 25. These results are estimated to have an accuracy of 5 percent of the reported value based upon the standards used for the elemental quantification. In comparison with the statically grown oxide, both radiant heating and supersonic arc plasma wind tunnel tests reduced the concentration of cobalt and increased the concentration of chromium present in the oxide surface layer. The supersonic arc plasma wind tunnel tests also significantly decreased the nickel and manganese concentrations while increasing the percentage of silicon and tungsten.

SIMS derived profiles for the statically oxidized sample are shown in figure 74. Cobalt and nickel profiles track each other quite closely. Their concentrations are high at the surface, then drop significantly in the oxide, before increasing to the metal values. Conversely, the chromium concentration increases from the surface of the oxide to a maximum value roughly coincident with the minima in the cobalt and nickel values. Minority elements such as manganese, aluminum, silicon, molybdenum, lanthanum, and tungsten also were profiled as seen in figure 74.

The 10 and 100 radiant heating test cycle samples were profiled also using SIMS. The 100 radiant cycle oxide elemental profiles were almost identical with those of the static oxide. The 10 radiant cycle sample, however, showed a smaller variation in cobalt and nickel

Table 25. Quantitative EP Analysis of HS188 Oxide Layers

	Concentration (atomic percent)		
Element	Statically Oxidized	After 100 Cycles Radiant Test	After 38 Cycles Supersonic Arc Plasma Wind Tunnel Test
O	44.2	47.1	43.1
Co	29.4	22.6	24.6
Cr	12.2	16.4	21.5
Ni	7.4	7.1	4.5
Fe	1.1	1.2	1.5
Mn	5.0	4.8	1.2
W	0.2	0.4	0.8
Si	0.1	0.4	1.7

BEST DOCUMENT AVAILABLE

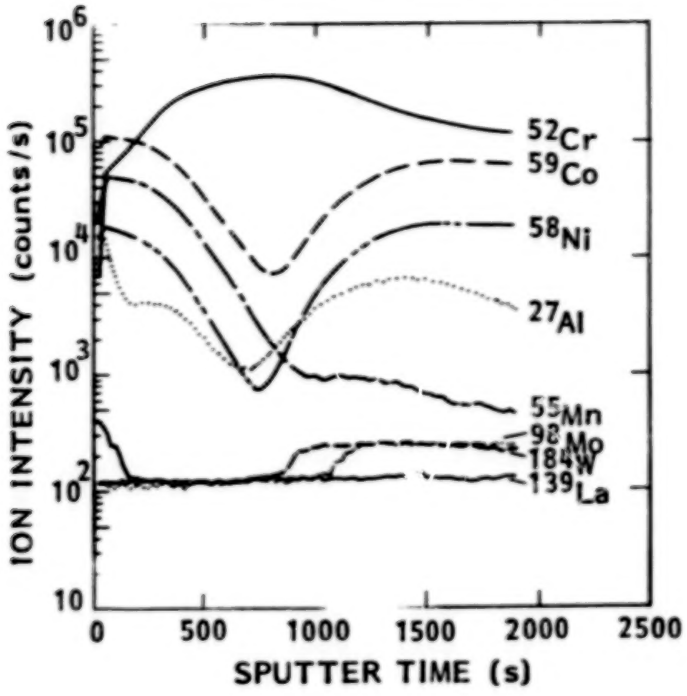

Figure 74. SIMS depth profiles of statically oxidized HS188.

concentrations (20 to 50 percent) than seen (1 to 1.5 orders of magnitude) in the 100 cycle specimen. Also, the chrominum concentration increase with depth was smaller for this specimen.

Elemental depth profiles, as intensity versus sputter time, obtained from the AES are shown in figures 75 through 78 for the statically oxidized and the supersonic arc plasma wind tunnel specimens. For the statically oxidized material (figure 75) nickel and cobalt concentrations are at a maximum near the surface of the oxide and decrease in the same manner with increasing distance into the oxide. Chromium on the other hand increases with depth into the oxide. After testing in the supersonic arc plasma wind tunnel certain trends are observed on the boundary layer surface as exposure time increases. After the 8 cycle test the cobalt and nickel concentrations decrease less rapidly with depth and chromium increases more slowly (see figure 76a). As the number of test cycles is increased to 20, the cobalt and nickel concentrations rise with increasing depth and the chromium concentration rapidly reaches a constant value (figure 77). The 38 test cycle specimen shows a similar behavior to the 20 cycle specimen except that the cobalt concentration rises very rapidly in the surface region of the oxide layer (c.f. figures 77 and 78a).

BEST DOCUMENT AVAILABLE

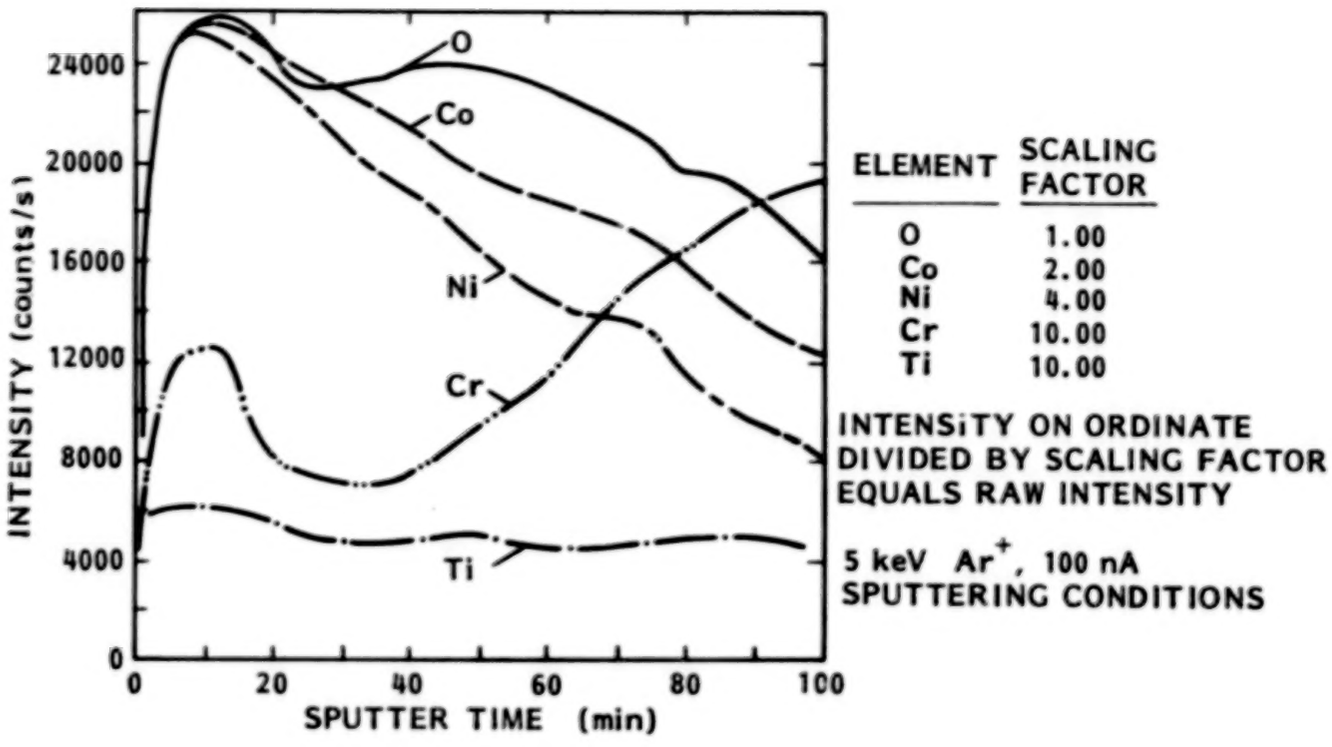

Figure 75. AES depth profile of statically oxidized HS188 (note scaling factors).

The rear surfaces of the supersonic arc plasma wind tunnel test specimens are very similar in elemental depth variations to those of the statically oxidized specimen (c.f. figures 76b and 78b with 75). The similarity in compositional profiles was also observed for the only radiant heating test specimen examined in the AES, specimen 11, after 20 test cycles.

Concentration profiles using SIMS were obtained for specimens from the 8, 20 and 38 cycle supersonic arc plasma wind tunnel tests (see figures 79 through 81). Each set of SIMS profiles appears very similar, showing little variation in the cobalt and nickel concentration through the oxide and a monotonically increasing chromium concentration. Minor element concentrations, except for lanthanum and manganese, vary little with depth.

A DEKTAK profilometer was used to measure the cross-sectional details of the crater formed in the 8 cycle supersonic arc plasma wind tunnel test specimen after oxygen ion sputtering during the SIMS measurements. The crater had an average depth of 1.5 μm but a variation in the bottom topography of as much as half this amount. Clearly an elemental concentration profile obtained on the HS188 oxides must be treated as semiquantitative at best.

BEST DOCUMENT AVAILABLE

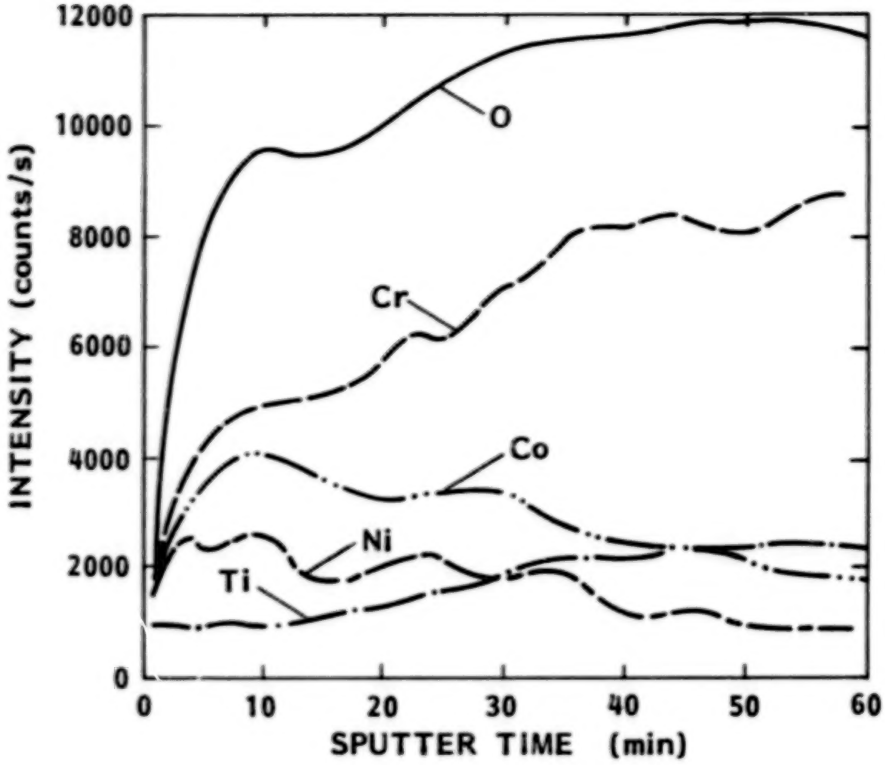

ELEMENT	SCALING FACTOR
O	1.00
Co	5.00
Ni	5.00
Cr	5.00
Ti	5.00

5 keV Ar^+, 100 nA
SPUTTERING CONDITIONS

(a) Boundary layer surface

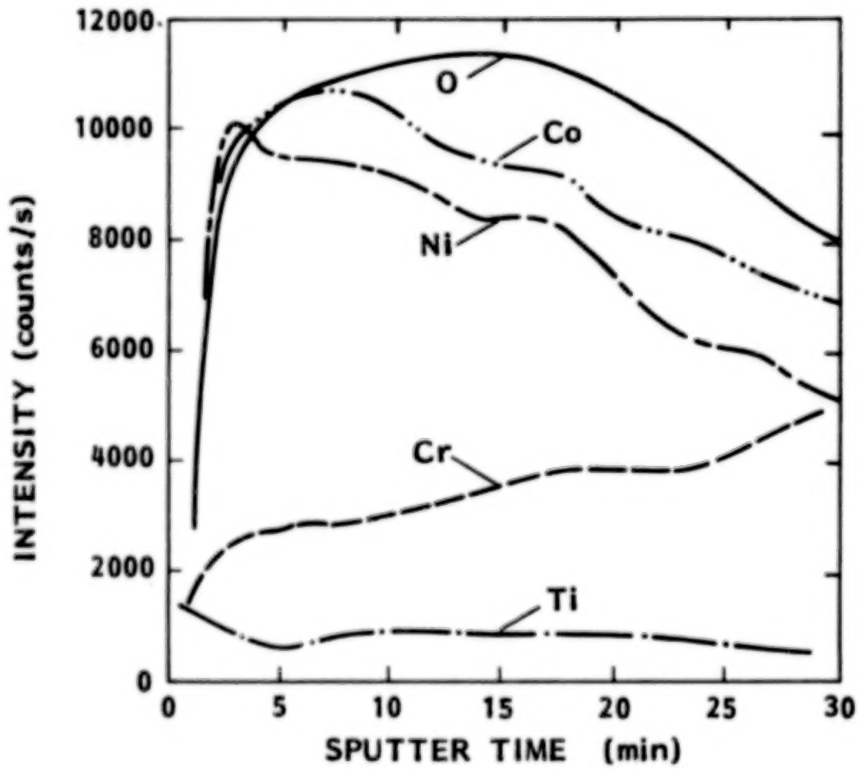

ELEMENT	SCALING FACTOR
O	1.00
Co	5.00
Ni	5.00
Cr	5.00
Ti	5.00

5 keV Ar^+, 100 nA
SPUTTERING CONDITIONS

(b) Rear surface

Figure 76. AES depth profiles of the HS188 8 cycle supersonic arc plasma wind tunnel test specimen.

BEST DOCUMENT AVAILABLE

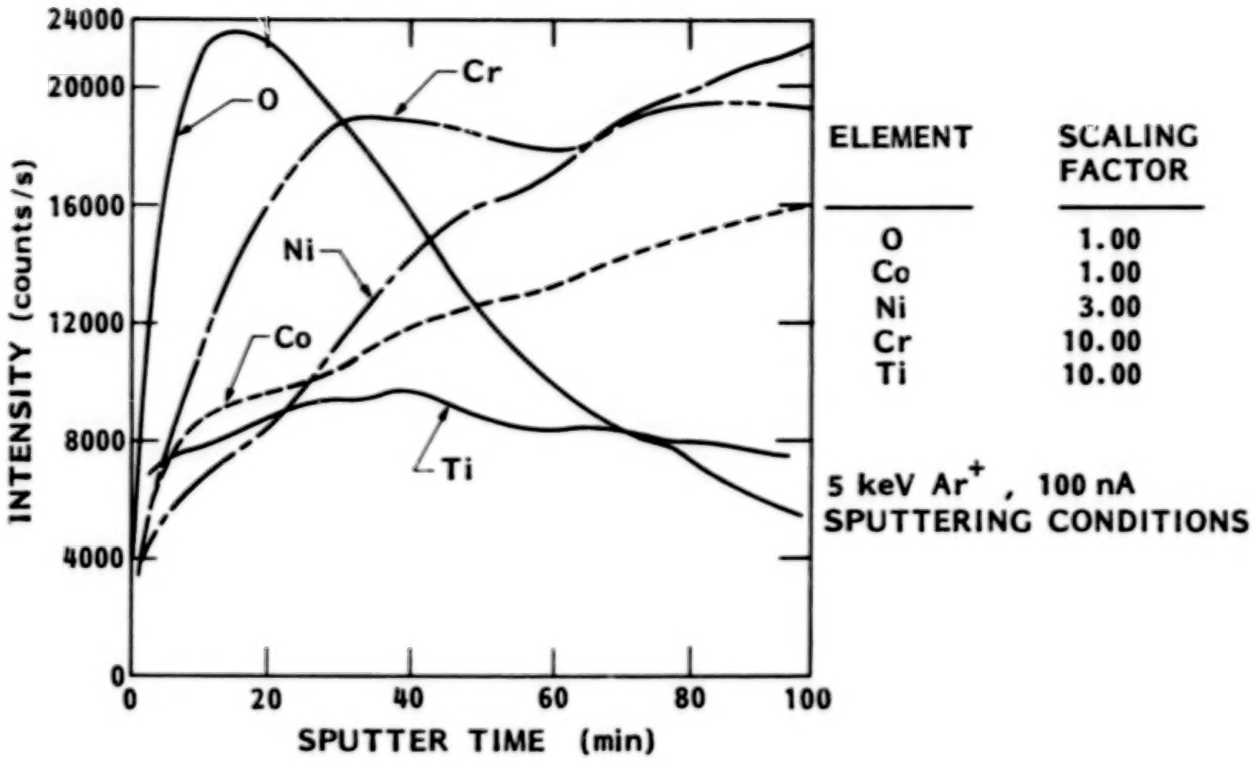

Figure 77. AES depth profile of the HS188 20 cycle supersonic arc plasma wind tunnel test specimen, boundary layer surface.

Structure. The x-ray diffraction analysis data for the HS188 specimens resulted in the detection of only three distinct crystallographic phases, (see Table 26). In all cases but two, Cr_2O_3 was identified as the major phase. The two other phases present, and ranging in concentration from trace to major were the spinel $(CoNi)Cr_2O_4$ and the mixed oxide of cobalt and nickel (CoNi)O.

The diffraction data for the spinel are not sufficiently accurate (low signal to noise ratio) to distinguish between $CoCr_2O_4$ (a_o = 8.306 Å) and $NiCr_2O_4$ (a_o = 8.330 Å). In all probability the spinel phase is mixed and also contains additional trace elements such as manganese and iron.

There is a 2 percent difference in the lattice parameters of CoO (a_o = 4.26 Å) and NiO (a_o = 4.17 Å). As these two compounds form a continuous solid solution with lattice parameters proportional to the CoO/NiO ratio a lattice parameter measurement should give an indication of this ratio for the test specimens. Several HS188 specimens were chosen for more detailed x-ray analysis. The lattice parameter values for the mixed metal oxide were plotted versus the Taylor-Sinclair (ref. 15) function, $1/2 \cos^2 \theta(\theta^{-1} + \text{cosec } \theta)$. The intercept of the least square fit to the data for 2θ = 180 deg gives the CoO/NiO ratio (see figure 82).

BEST DOCUMENT AVAILABLE

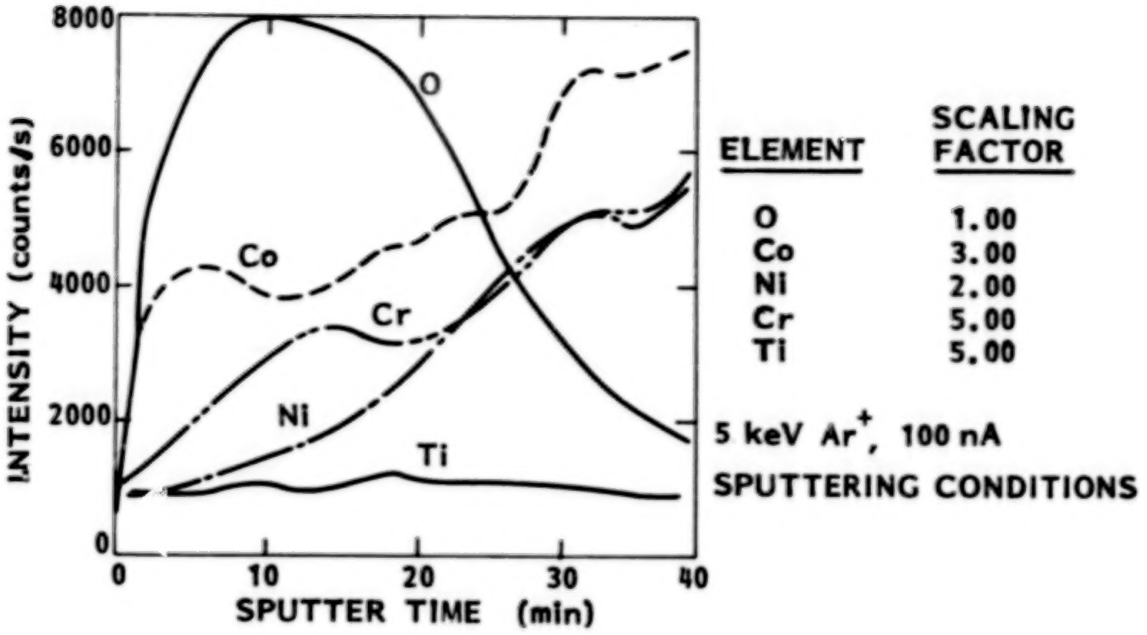

(a) Boundary layer surface

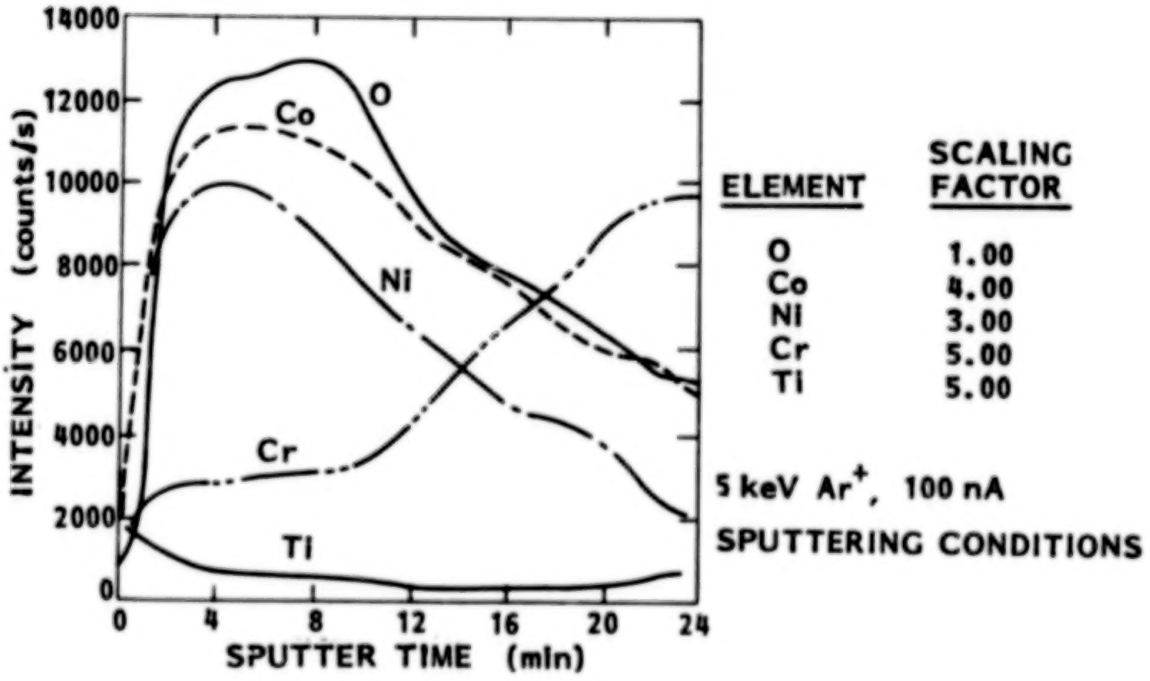

(b) Rear surface

Figure 78. AES depth profiles of the HS188 38 cycle supersonic arc plasma wind tunnel test specimen.

BEST DOCUMENT AVAILABLE

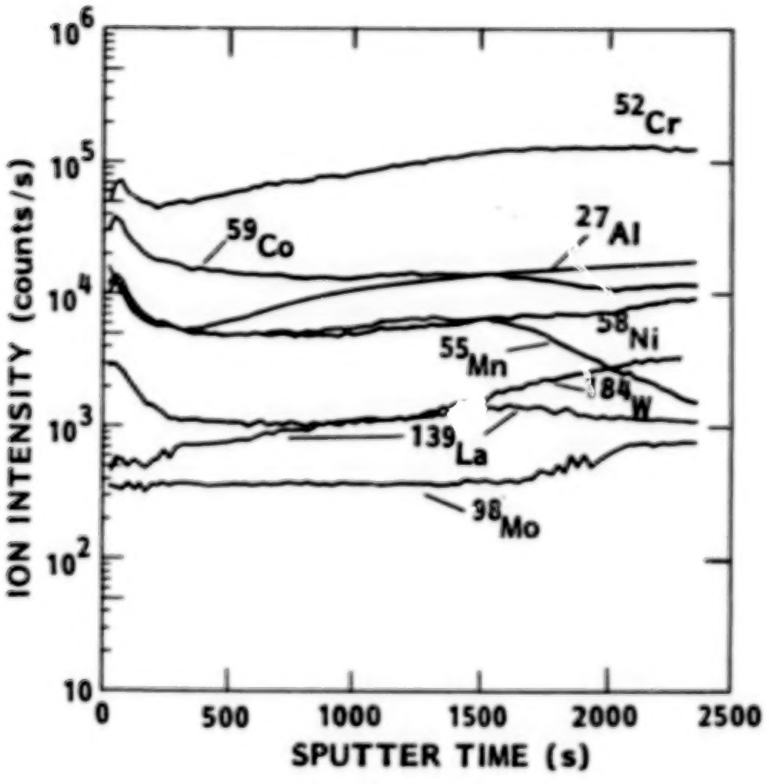

Figure 79. SIMS depth profile of the HS188 8 cycle supersonic arc plasma wind tunnel test specimen, boundary layer surface.

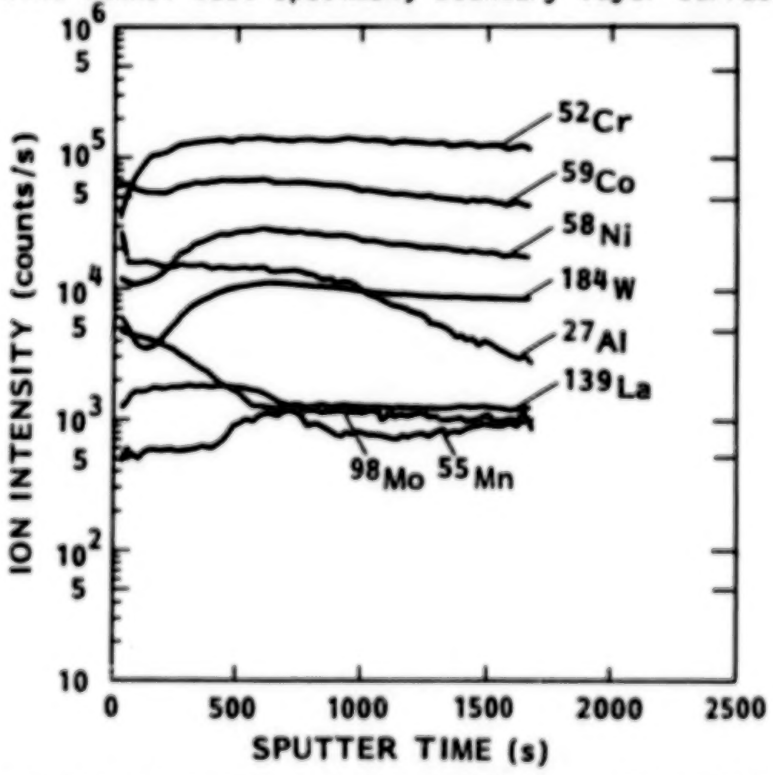

Figure 80. SIMS depth profile of the HS188 20 cycle supersonic arc plasma wind tunnel test specimen, boundary layer surface.

BEST DOCUMENT AVAILABLE

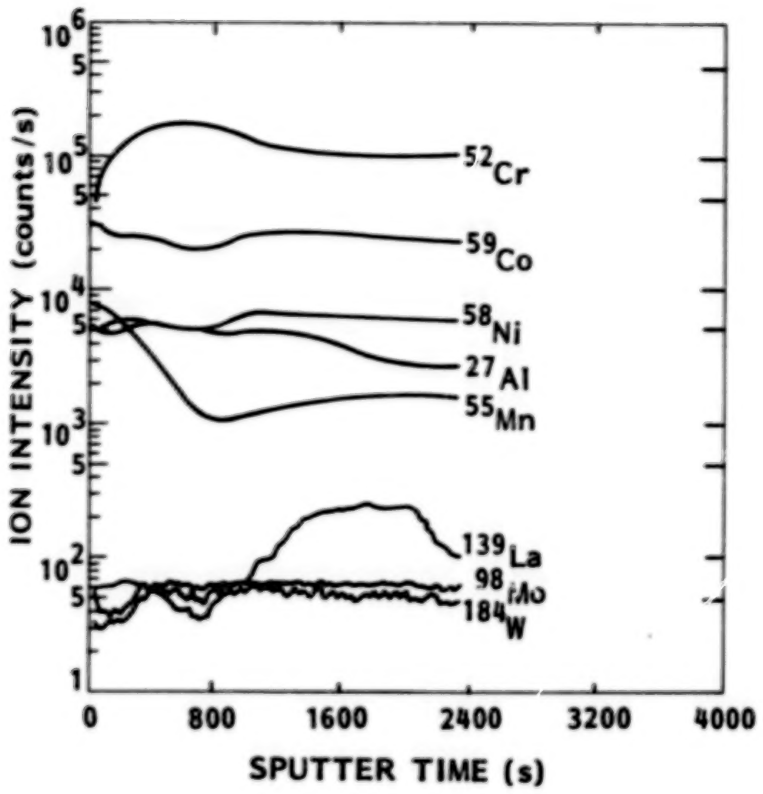

Figure 81. SIMS depth profile of the HS188 38 cycle supersonic arc plasma wind tunnel test specimen, boundary layer surface.

The CoO component of the mixed metal oxide in the statically oxidized specimen and of the rear surfaces of the supersonic arc plasma wind tunnel test specimens lies in the range of 55 to 60 percent. The boundary layer surfaces of these specimens, however, have substantially lower CoO/NiO ratios, viz., 20 to 30 percent CoO.

The [200] reflection for the mixed metal oxide in some samples was found to be very pronounced, indicating that the samples are oriented. It was possible to observe this effect only in those oxides where the (CoNi)O phase was present in substantial amounts, i.e., as a major or minor constituent.

Data Summary. The SEM images (see figure 64) showed that two types of crystallites were observed on the surface of the statically oxidized material. Those larger than 1 μm in size were rich in cobalt and nickel, and the small ones (~0.3 μm) were rich in chromium and cobalt and deficient in nickel. The x-ray diffraction data indicate that the phase rich in cobalt and nickel is the mixed oxide $(Co_{0.6}\ Ni_{0.4})O$. It gives rise to an oriented x-ray diffraction pattern which is likely to originate from large single crystals.

BEST DOCUMENT AVAILABLE

Table 26. X-ray Diffraction Analysis of HS188 Specimens

Simulated Reentry Exposure Test		Crystallographic Phase		
		Cr_2O_3	(CoNi)O	$(CoNi)Cr_2O_4$
None, Statically Oxidized		M	Mr[b]	Mr
Supersonic Arc Plasma	F	M	Tr-Mr	M
Wind Tunnel, 8 cycles[a]	R	Mr	M[c]	Mr
Supersonic Arc Plasma	F	M	M	Tr-Mr
Wind Tunnel, 20 cycles[a]	R	M	M	Tr-Mr
Supersonic Arc Plasma	F	M	Tr-Mr	M
Wind Tunnel, 38 cycles[a]	R	Mr	M[c]	Mr
Radiant Heating, 10 cycles		M	Tr-Mr	Tr-Mr
Radiant Heating, 20 cycles		M	M[b]	Mr
Radiant Heating, 100 cycles		Mr	Mr-M[b]	M

M = Major, Mr = Minor, Tr = Trace

(a) F denotes boundary layer surface, R denotes rear surface for supersonic arc plasma wind tunnel test specimens

(b) Strongly oriented

(c) Some orientation

BEST DOCUMENT AVAILABLE

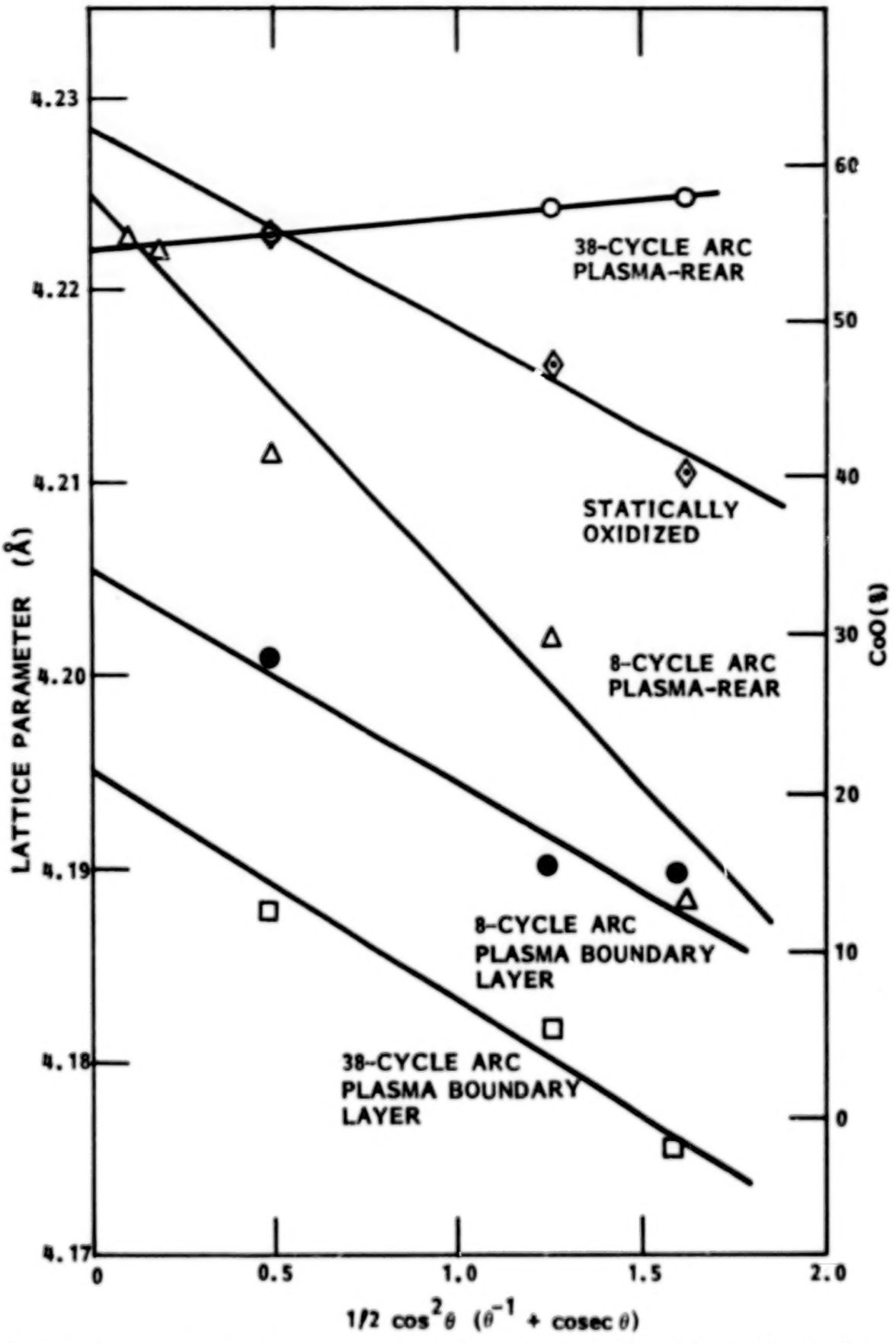

Figure 82. Determination of the cobalt oxide/nickel oxide ratio in the HS188 mixed metal oxide phase using the Taylor-Sinclair function method.

The EP analysis of the statically oxidized surface indicated that it contained much more cobalt than nickel (see Table 25). Thus cobalt that is not bound up in the large crystallites is present in the small granules. Their composition is consistent with the spinel structure, and such an interpretation would account for the lack of orientation seen in the spinel x-ray diffraction data. A large number of 0.3 μm granules (even though they may be individually single crystals) are likely to be randomly oriented. The large mixed metal oxide crystallites, however, could be oriented by subsurface contact with the metal.

Despite the presence of cobalt and nickel containing crystallites the major phase in the statically oxidized material is Cr_2O_3. When taken with the AES and SIMS data, which show high nickel and cobalt concentrations near the surface and maximum chromium concentration below the surface, the following picture emerges.

The static oxide consists of a surface region almost completely covered in crystallites of mixed metal oxide and spinel. These account for much of the nickel and cobalt in the oxide. The crystallites in turn are imbedded in a layer of mostly Cr_2O_3 which extends to the interface with the metal.

The x-ray diffraction data for the radiant heating test samples indicate that the relative concentrations of the three crystallographic phases change as a function of exposure time. Far reaching changes do take place; e.g., after 100 cycles most of the chromium is bound up in spinel form, caused possibly by substantial interdiffusion of Cr_2O_3 and the mixed metal oxide.

The supersonic arc plasma wind tunnel tests result in almost complete homogenization of the elemental constituents in the oxide. Both SIMS and AES give concentration profiles which are only weakly dependent on depth. The EP detects the presence of the major elements in roughly the concentration found in the metal, and the SEM images show a surface where all crystal and grain boundary effects are absent. The x-ray diffraction data indicate that as exposure time is increased the relative concentrations of spinel and mixed oxide change dramatically although Cr_2O_3 remains the dominant phase at all time.

The rear surface SEM images (see figures 68 and 69) showed loss of individuality in the crystallite structures as a function of exposure time. This can be ascribed to interdiffusion of the various crystallites or granules. The dominance of the mixed metal oxide, as well as thickness and morphological changes indicate, however, that the rear surface oxide layer does not remain unaffected with increasing supersonic arc plasma wind tunnel exposure.

4.3.3 R512E Coated Cb752

SEM images of the surface of the R512E coating are shown in figures 83 through 86 for the as prepared and supersonic arc plasma wind tunnel test

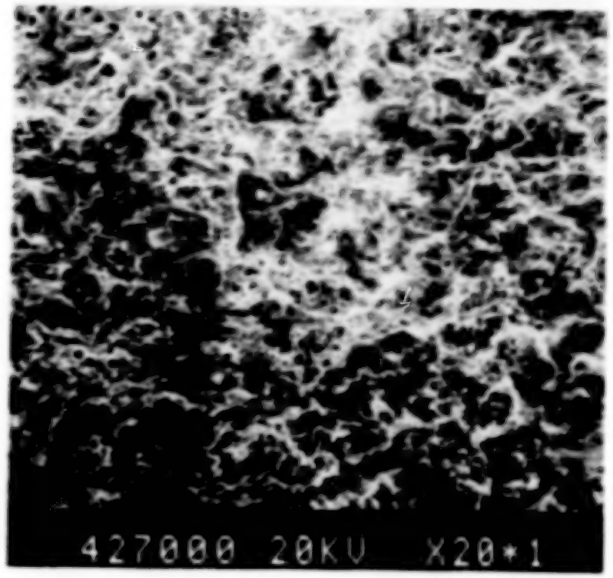

(a) 200x

(b) 1000x

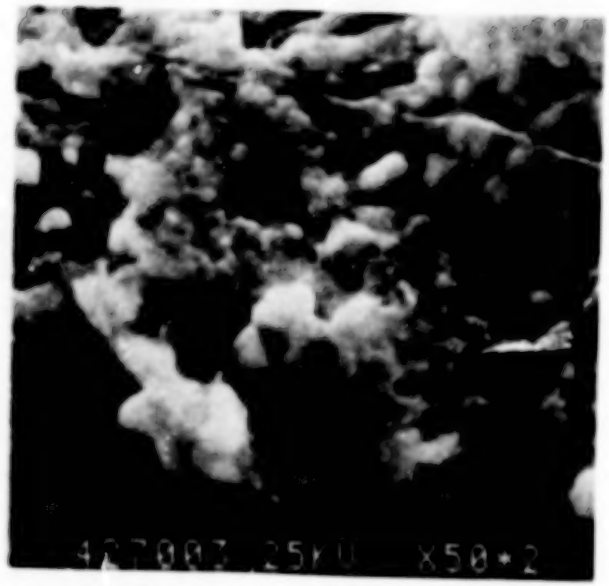

(c) 5000x

Figure 83. SEM images of the surface of KBI2E coated CD752 (as prepared).

BEST DOCUMENT AVAILABLE

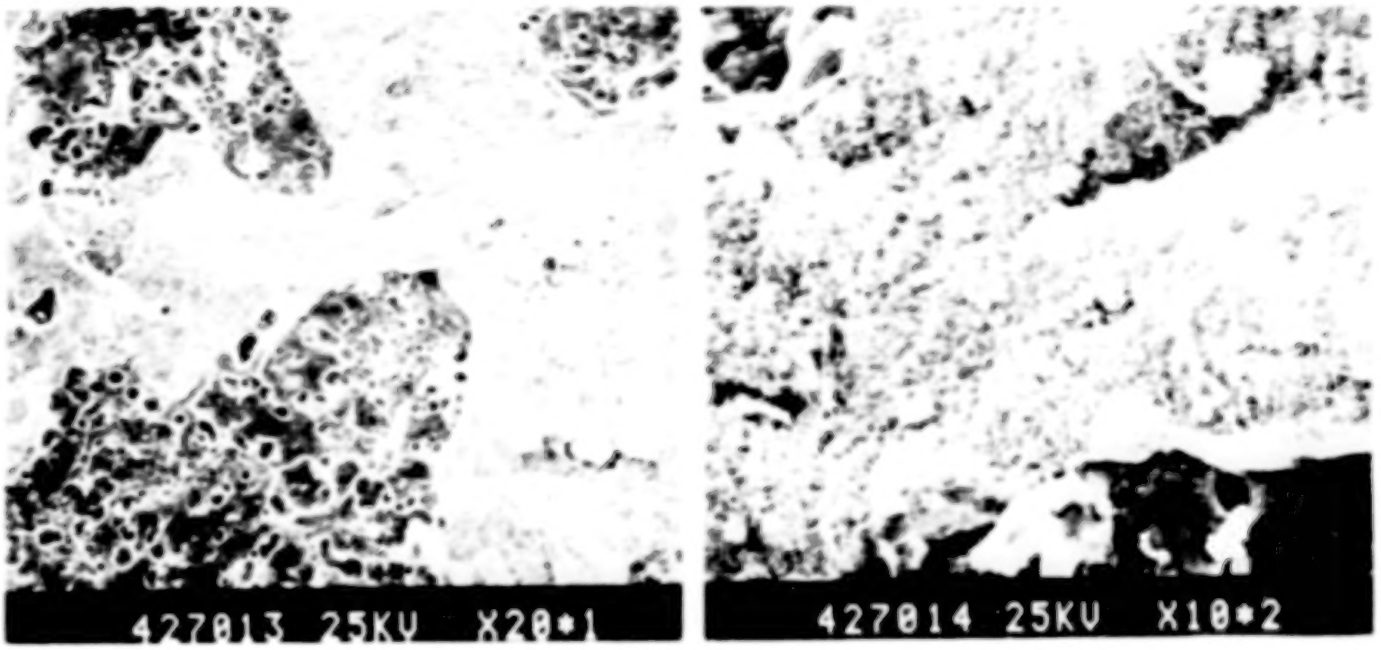

(a) 200x (b) 1000x

Figure 84. SEM images of boundary layer surface of R512E coated Cb752 after 8 cycles in supersonic arc plasma wind tunnel.

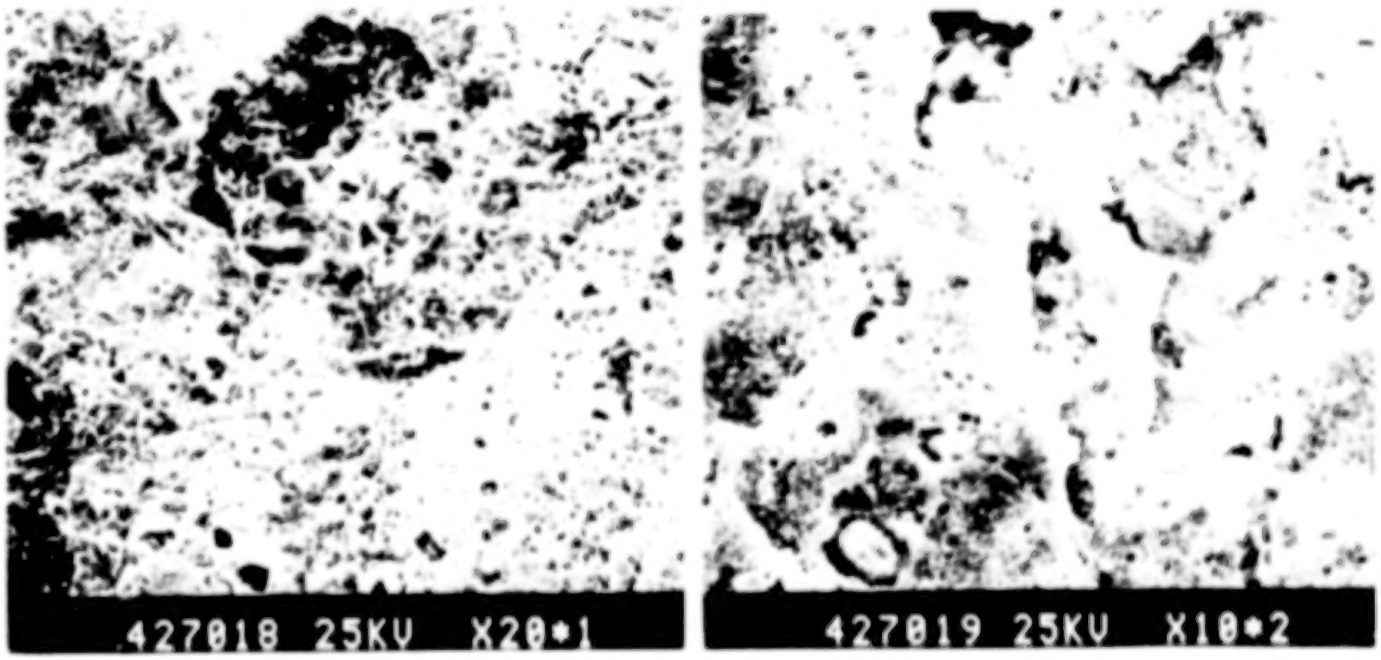

(a) 200x (b) 1000x

Figure 85. SEM images of the boundary layer surface of R512E coated Cb752 after 20 test cycles in supersonic arc plasma wind tunnel.

BLANK PAGE

BLANK PAGE

BLANK PAGE

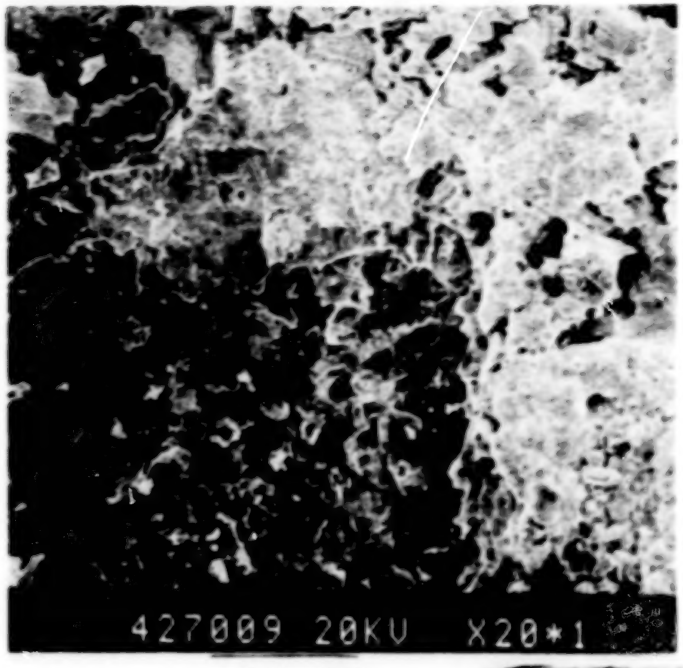

(a) 200x

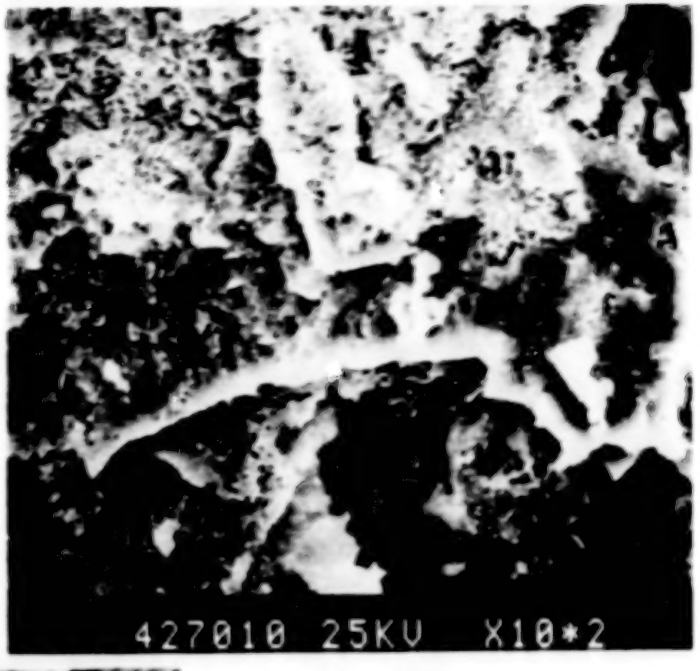

(b) 1000x

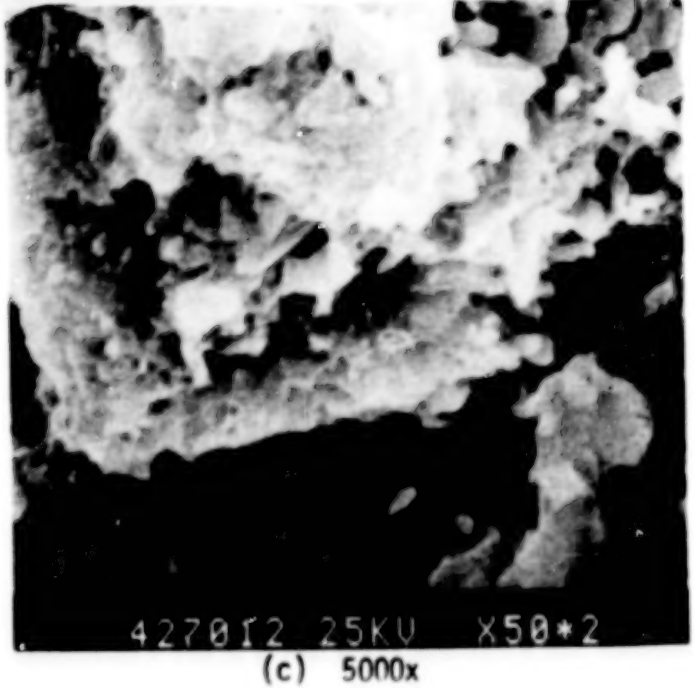

(c) 5000x

Figure 86. SEM Images of the boundary layer surface of R512E coated Cb752 after 38 test cycles in supersonic arc plasma wind tunnel.

BEST DOCUMENT AVAILABLE

131

exposed specimens. Little change in surface topography with number of test cycles is seen. The surface remains rough and glass-like. It has the appearance of a fused platelet or layered structure. The platelet-like character becomes more pronounced as the number of supersonic arc plasma wind tunnel test cycles increases. No fractures or fissures were observed on the surfaces of any specimen.

Overall specimen thickness measurements for the radiant heating and supersonic arc plasma wind tunnel tests are summarized in Table 27. No significant difference in thickness is observed between the as prepared specimens and those after testing in the two reentry simulation test types.

Surface elemental analysis data for the three supersonic arc plasma wind tunnel test specimens are summarized in Table 28. No attempt was made to quantify these data, and they are presented as intensities in each case. Two silicon auger electron peak structures were used to differentiate between silicon as the oxide SiO_2 and silicon in the silicide $CbSi_2$. The peak characteristics are shifted for the oxide form whereas they are unaffected for the silicide form. Similarly, two columbium peaks were used in an attempt to discriminate between the oxide and the silicide. The 168 eV peak is used to evaluate the oxide. The 198 eV peak is used to define metal assuming the pure metal and silicide behave in a similar fashion. Cb_2O_3 and Cb with 2 percent oxygen were used as calibration standards.

For the 8 test cycle specimen 10, the boundary layer surface is composed primarily of aluminum and oxygen with small amounts of silicon and columbium. The aluminum is probably Al_2O_3 deposited on the surface when a nozzle burn-through occurred during the last exposure cycle of this test sequence. The rear side of the specimen, however, shows a mixed silicon and columbium oxide layer, and no detectable aluminum. The major fraction of silicon appears to be as an oxide form. After 30 min of sputtering, to approximately 0.2 μm depth, the total columbium content is greater, but SiO_2 remains strong.

The 20 test cycle specimen 7 was analyzed at three depths, approximately 0.01, 0.5, and 1 μm, to examine changes in SiO_2 concentration. At the surface the layer is basically SiO_2 with a small amount of a columbium oxide plus the silicide. At the 0.5 μm depth, the SiO_2 is reduced markedly and both the columbium and oxygen increase together. After 120 min of sputtering, nominally 1 μm depth, silicon is principally in the silicide form, but the silicon and columbium oxides are still detectable. From these data it appears that the SiO_2 extends to a depth of 1 to 2 μm, and this layer is a mixture of columbium silicides and oxides in a SiO_2 glass-like matrix.

Results of the analysis of specimen 8 (38 test cycles) at 60 min and approximately 1 μm depth, are similar to those for specimen 7 (20 test cycles). It does not appear that the supersonic arc plasma wind tunnel tests produced any significant compositional changes in the surface. Specimen 7 might contain more silicide at the 60 min point based on the intensities of

Table 27. Overall Thickness Data for R512E Coated Cb752 Specimens

Simulated Reentry Exposure Test	Overall[a] Thickness (mm)
None, Base Metal	0.508 ±0.010
None, Coated Specimen	0.610 ±0.025
Supersonic Arc Plasma Wind Tunnel, 8 Cycles	0.622 +0.023 −0.028
Supersonic Arc Plasma Wind Tunnel, 20 Cycles	0.638 +0.007 −0.011
Supersonic Arc Plasma Wind Tunnel, 38 Cycles	0.610 +0.005 −0.006
Radiant Heating, 10 Cycles	0.623 +0.032 −0.021
Radiant Heating, 20 Cycles	0.634 +0.014 −0.005
Radiant Heating, 50 Cycles	0.647 +0.008 −0.021

(a) Single specimen only for each exposure test condition, four thickness measurements made on each specimen in area of emittance measurements. Uncertainty in thickness measurement is ±0.003 mm.

the silicon metal peaks. However, this must be considered in the light of the uncertainties in the reproducibility of the depth versus sputtering time relationship.

An alternative way of treating the data presented in Table 28, albeit to reach the same conclusions as those above, is by examining intensity ratios. For instance, the ratio of Cb_{168}/Cb_{198} gives an indication of the oxygen-metal ratio for columbium. As is seen from the last two lines of Table 29 the Cb_{168}/Cb_{198} ratio is 3.03 for the oxide of columbium and

Table 28. Elemental Surface Analyses of R512E Coated Cb752 After Supersonic Arc Plasma Wind Tunnel Tests

Specimen (Number of Supersonic Arc Plasma Wind Tunnel Test Cycles)	AES Sputter Time (min)	Intensity - Counts						
		Silicon			Columbian (a)			
		As SiO_2	As Metal	Total	Cb_{168}	Cb_{198}	Oxygen	Aluminum
7(20)	1	11,316	ND	635	2240	779	6606	ND
	60	2010	774	2217	4213	1547	11,958	ND
	120	778	8511	2109	5281	2051	6698	ND
8(38)	60	2094	D	1506	2653	961	11,796	ND
10(8)	0	2565	ND	2035	452	ND	29,084	11,908
	0 R	2461	ND	2727	2656	881	23,747	ND
	30 R	2359	ND	2170	3161	1149	11,991	ND
Cb_2O_3	--	ND	<500	ND	6874	2270	20,184	ND
Cb + 2%O	--	ND	638	ND	15,832	8657	376	ND

ND = not detected, D = detected but not quantifiable, R = rear side of specimen

(a) Subscript is line energy, eV

134

Table 29. AES Intensity Ratios for R512E Coated Cb752 (See Table 28)

Specimen (Number of Test Cycles)	AES Sputter Time (min)	Ratios(a)		
		$\frac{Cb_{168}}{Cb_{198}}$	$\frac{Cb_{168}}{O_{510}}$	$\frac{Si_{Total}}{O_{510}}$
7(20)	1	2.88	0.339	0.096
	60	2.72	0.352	0.185
	120	2.58	0.788	0.315
8(38)	60	2.76	0.225	0.128
10(8)	0	--	0.016	0.070
	0 R	3.02	0.112	0.115
	30 R	2.75	0.264	0.181
Cb_2O_3	--	3.03	0.341	--
Cb + 2%O	--	1.83	42.11	--

(a) Subscript is line energy, eV.

decreases to 1.83 for nearly pure metal in the presence of a small amount of oxygen. Clearly, the smaller the value of this ratio, the more metallic-like (silicide) is the material. Consequently, one may obtain an approximate composition using this and other ratios. For Specimen 7, the columbium ratio decreases with depth while the Cb_{168}/O_{510} increases; i.e., the silicide concentration increases at the expense of SiO_2 and columbium oxide.

Section 5

DISCUSSION AND RECOMMENDATIONS

Total normal emittance at elevated temperatures of the three candidate heat shield materials showed excellent stability with reentry testing in both supersonic arc plasma wind tunnel and radiant heating apparatus tests. Exactness of flow field simulation, i.e., supersonic hot boundary layer or quiesent air flow, had no appreciable effect on the stability of total normal emittance at elevated temperature. The two types of reentry test produced morphological compositional, and crystallographic changes in the statically oxidized superalloys. These changes, however, had only a minor effect on the thermal radiative properties of the oxide layers in the wavelength region (1 to 12 μm), which controls total normal emittance in the temperature range of 1100 to 1300 K.

The results of the thermal radiative properties and morphological, compositional, and crystallographic studies are discussed in Sections 5.1 and 5.2, respectively. Recommendations for future studies are summarized in Section 5.3.

5.1 THERMAL RADIATIVE PROPERTIES

The formulation of an exact theoretical model for the thermal radiative properties of a large surface roughness layer contiguous with a rough substrate and composed of several different elements making up three separate crystallographic phases is not a tractable problem. Some general comparisons, however, can be drawn from the classical theories for spectral reflectance and emittance. In drawing these comparisons we will separate the problem into two regions; (1) the coating layer, or a thickness element of that layer, is optically very thick so that the substrate or adjacent layer can be ignored and (2) a multilayer case in which the optical constants of all elements must be considered. Certain wavelength regions of the statically oxidized superalloys fall into this latter case, whereas, the R512E coating may be considerd to be in the former, providing we exclude the surface silicon/columbium oxide thickness element.

Consider first a layer of material having optical constants n and k and thickness t on a substrate of infinite optical thickness, and having optical thickness and optical constants n_1 and k_1, where all optical constants are spectrally dependent. Temperature dependence will be discussed later. For a layer radiating into air or vacuum, the normal reflectance can be written as

$$R = \frac{(a_1^2 + b_1^2)e^{2\beta} + (a_2^2 + b_2^2)e^{-2\beta} + 2(a_1a_2 + b_1b_2)\cos 2\alpha}{e^{2\beta} + (a_1^2 + b_1^2)(a_2^2 + b_2^2)e^{-2\beta} + 2(a_1a_2 - b_1b_2)\cos 2\alpha}$$

$$\frac{+ 2(a_1 b_2 - a_2 b_1) \sin 2\alpha}{+ 2(a_1 b_2 + a_2 b_1) \sin 2\alpha} \qquad (12)$$

where

$$a_1 = \frac{1-n^2 - k^2}{(1+n)^2 + k^2} \quad , \qquad a_2 = \frac{n^2 - n_1^2 + k^2 - k_1^2}{(n+n_1)^2 + (k+k_1)^2} \quad ,$$

$$b_1 = \frac{2k}{(1+n)^2 + k^2} \quad , \qquad b_2 = \frac{2(n\,k_1 - n_1\,k)}{(n+n_1)^2 + (k+k_1)^2} \quad ,$$

$$\alpha = 2\pi nt/\lambda \quad , \qquad \text{and} \qquad \beta = 2\pi kt/\lambda \quad .$$

This equation is valid for a homogenous optically smooth layer of singular optical constants and does not include effects from mixed phases/compositions, defect or boundary scattering, and surface roughness, all of which influence phase relationships and subsequent reflectance minima and maxima.

As an example of the application of this equation to an oxide layer on a superalloy substrate, let us compute the reflectance for statically oxidized Inconel 617, a nominally 3.5 μm thick oxide layer. No optical constants data were found in the literature for either the mixed oxide or the alloy. However, making the assumption that the optical constants of the oxide layer are $n = 1.5$ and $k < 0.01$ from 2 to 10 μm and n_λ and k_λ can be computed from the base metal (unoxidized) reflectance data, several spectral reflectance values are computed for the statically oxidized Inconel 617. Values of n and k for Cr_2O_3 at room temperature from 12.5 to 50 μm are shown in figure 87. At 12.5 μm, $n \approx 1$ and k approaches zero. This is consistent with the optical constants for many metal oxides (i.e., aluminum, titanium, magnesium, etc.); from 0 to 10 μm, n and k are generally less than 1.5, and less than 0.01, respectively.

The n_1 and k_1 values for the substrate are computed from the base metal spectral normal reflectance data making the assumption $n_1 = k_1$, which is a reasonable approximation for metals in the 2 to 10 μm wavelength region. This computation gives $n_1 = k_1 = 5.2$ at 2 μm increasing to $n_1 = k_1 = 13.3$ at 10 μm. Substituting these values of n, n_1, k, and k_1 into equation (12) gives spectral normal reflectances of 0.19 at 2 μm, 0.18 at 5 μm and 0.18 at 10 μm, all of which are in reasonable agreement with the measured reflectance values.

From figure 87 it is seen that n and k of Cr_2O_3 vary strongly with wavelength in the 15 to 25 μm region. When k and/or n are large, the substrate properties can be neglected as a first approximation, since either

BEST DOCUMENT AVAILABLE

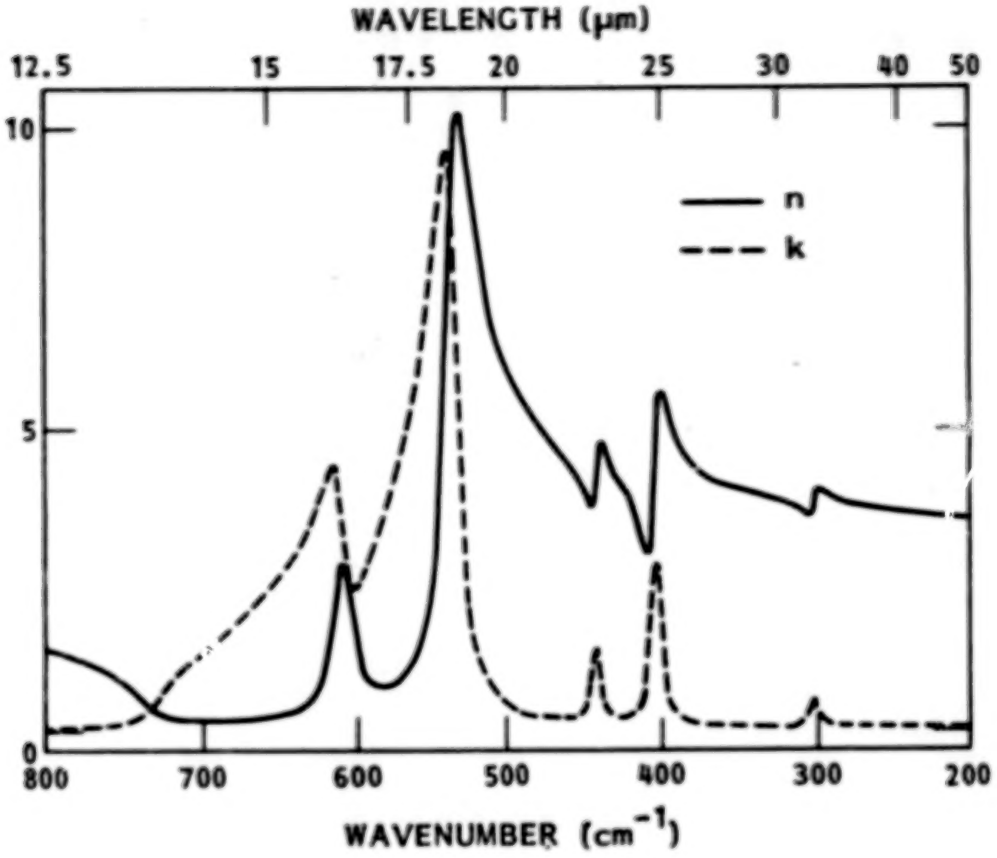

Figure 87. Calculated optical constants for Cr_2O_3 (from ref. 16).

absorption is very large for the 3.5 μm thickness or internal reflection is large for large values of n. Equation (12) can then be reduced to

$$R = 1 - \frac{4n}{(n+1)^2 + k^2} \tag{13}$$

With the n and k values of figure 87, room temperature spectral normal reflectances from 12 to 25 μm were computed using equation (13). The results are shown in figure 88 together with experimental values for statically oxidized Inconel 617 and HS188. The calculated values are in surprisingly good agreement with the Inconel 617 data for both the frequencies of the minima and maxima as well as the amplitudes. From this, one might conclude that (1) the Cr_2O_3 controls the radiative properties or (2) the optical properties of Cr_2O_3 and (CoNi)O, and to a lesser extent the spinel, are nearly equal.

Agreement of the data with the calculation for HS188 is poor for amplitudes at wavelengths less than 14 μm, but it is good for frequency or wavelength at which minima and maxima occur. The poor correlation for amplitude may be the result of other oxides dispersed within the overall matrix such that a mixed phase optical constants model is required to get improved computational accuracy.

BEST DOCUMENT AVAILABLE

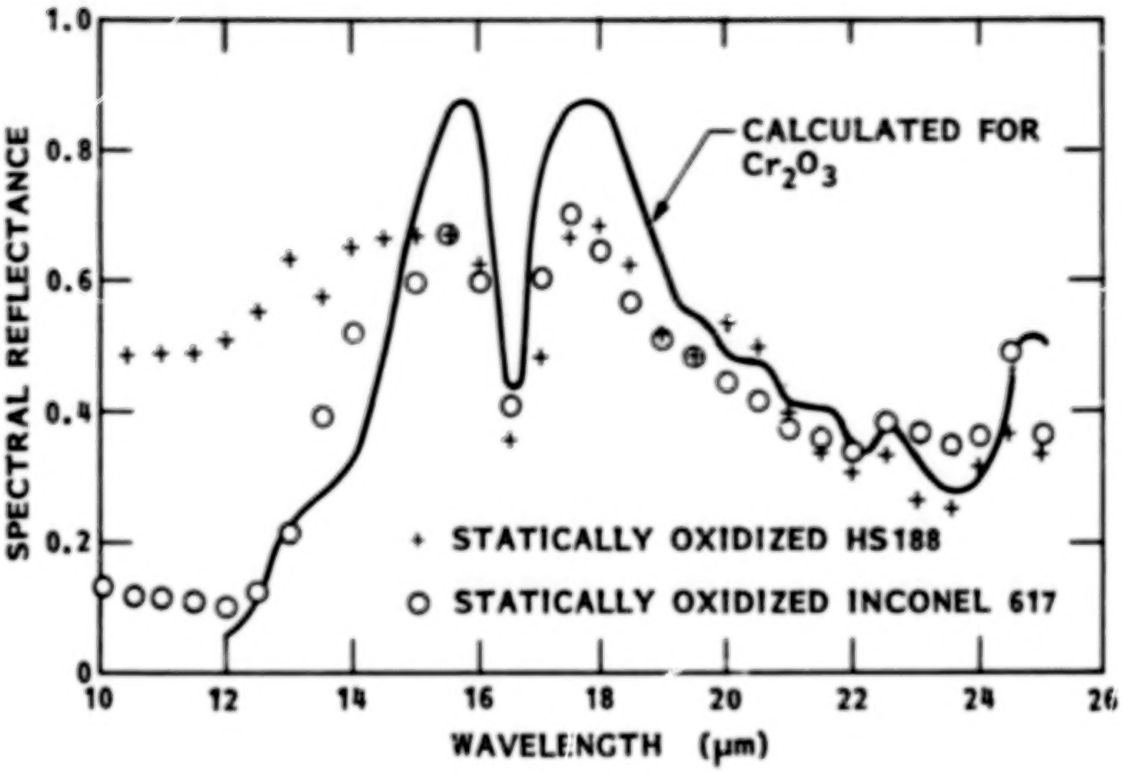

Figure 88. Comparison of spectral reflectance calculated for Cr_2O_3 (from optical constants) with data measured for statically oxidized Inconel 617 and HS188.

The temperature dependence of spectral emittance observed in the 12 to 14 μm wavelength region, where ϵ_λ increases with increasing temperature, may be the result of an increase in n with temperature. For example, if n at 14 μm increased from 0.9 to 1.5 in going from 300 to 1260 K, the reflectance would decrease from 0.32 to 0.17. If k decreases with increasing temperature, a similar decrease in spectral normal reflectance, or increase in spectral normal emittance, is seen.

5.2 OXIDE LAYERS ON INCONEL 617 AND HS188

Several important parallels can be drawn between the oxide layers on Inconel 617 and HS188 metals. The x-ray diffraction analysis showed that in almost all cases Cr_2O_3 was present as a major phase. Spinel compounds such as $(CoNi)Cr_2O_4$ were detected in typically trace or minor amounts, and

variable quantities of (CoNi)O were observed. No other compounds were of sufficiently high concentration to be detectable.

The statically formed oxides of both metals showed a polycrystalline ridge pattern as revealed in SEM images of the surface. The EP data from the oxides indicated that chromium dominated the ridge structures whereas nickel and cobalt were more prevalent in the discrete crystallites.

Morphological observations of the supersonic arc plasma wind tunnel boundary layer surfaces again showed the similarity between the behavior of the two statically oxidized metals. The surfaces had an essentially amorphous appearance, with few if any crystalline structures visible. Elemental composition measurements showed a strong chromium and nickel presence in Inconel 617 and also strong cobalt in HS188 oxides.

It appears that there is a considerable evidence to support the hypothesis that the static oxidation mechanisms for Inconel 617 and HS188 are similar. It has been shown that the thermal oxidation of high nickel chrome alloys takes place preferentially at grain boundaries on the surface of the material (refs. 13 and 14). In this case, chromium diffuses to the surface via grain boundaries and dislocations and is then oxidized. Thus, ridges of predominantly Cr_2O_3 grow on the alloy surface. Regions between the ridges oxidize more slowly and form mixed oxides of both nickel and chromium. These oxides may be crystallographically oriented since they grow on the faces of individual substrate crystallites.

The SEM imaging data for the thermal oxides of Inconel 617 and HS188 agree qualitatively with this model. Ridges are observed with a surface pattern typical of grain boundaries. The electron microprobe shows that these ridges are chromium rich, and the crystallite oxide-rich regions which are found mostly between the ridges contain both chromium and nickel, and also cobalt in the HS188 case.

Further support for this model comes from other investigations. T. Shikama et al. (ref. 17) recently studied the high temperature oxidation of Inconel 617 by radiant heating over the temperature range 923 to 1273 K in a flowing gas mixture having relatively high oxidizing potential (80 H_2/15 CO/5 CO_2) and obtained a Cr_2O_3 scale containing TiO_2, with an internal oxidation layer of Al_2O_3. No scale compositional data were presented for oxidation periods less than 200 h. These results obtained with Inconel 617 are not contradictory to the present data. A NiO phase was not formed, since it would be reduced by the reactant gas mixture to metallic nickel. It is known that TiO_2 is a component of the outer regions of the oxide layer in the present study also, since it was observed at a weak level in the featureless surface of the oxide and at medium to strong levels on selected areas in the EP analyses.

It has also been shown previously (ref. 18) with nickel-chromium alloys (0 to 10 weight percent chromium) that as oxygen partial pressure is reduced

(H_2/H_2O mixtures), chromium is preferentially oxidized at 1073 to 1523 K and appears as Cr_2O_3 on the metal with no significant internal oxidation occurring. Oxidation in air produces, on the other hand, a layer of mixed NiO and $NiCr_2O_4$, with a pure NiO layer at the oxide layer/air interface and an inner oxidation zone containing Cr_2O_3 particles imbedded in a nickel matrix, produced by oxygen diffusion into the alloy. These results are similar to those obtained in the present work for the statically oxidized layer since the AES data indicate that the surface region is nickel-rich, and major amounts of (CoNi)O and Cr_2O_3 phases were identified by x-ray diffraction analyses. Hence, an oxidation model similar to that proposed by Moreau and Bernard (ref. 18) would fit the present results.

A very similar model, which does not involve the spinel, was proposed by Tenney et al. (ref. 13) for TDNiCr alloy in both static and high-speed flowing air environments at 1373 and 1473 K. Upon thermal cycling, the thermodynamically less stable $NiCr_2O_4$ phase largely disappears with the formation of additional Cr_2O_3 and NiO.

When the statically formed oxide surface is exposed to the supersonic arc plasma wind tunnel environment, the oxidation mechanism is modified by the presence of a relatively high partial pressure of atomic oxygen. This rapidly oxidizes Cr_2O_3 to CrO_3, which volatilizes at the test temperatures. This Cr_2O_3 oxidation/volatilization tends to open up grain boundaries near the surface, which increases the diffusion rate of atomic oxygen to the inner oxidation zone along these opened grain boundary paths.

Thermodynamically, the introduction of atomic oxygen at a pressure Po may be considered as equivalent to a virtual pressure of molecular oxygen Po_2. At typical experimental values of 1260 K and Po = 10^1 Pa, Po_2 = 10^8 Pa. This enhancement of the chemical potential of oxygen in the gas phase will (1) favor the formation of higher oxides, as seen by the reduction in (CoNi)O content at the boundary layer surfaces of supersonic arc plasma wind tunnel test specimens and (2) change the defect concentration at the oxide/gas interface. Atomic oxygen is removed at the oxide/gas interface by (a) the oxidation reaction itself and (b) the competing reaction of atomic recombination (ref. 19). Kinetic reaction with atomic oxygen is not thermally activated; initially all atoms that reach the reaction surface will not react. The rate determining step in normal oxidation is molecular association; hence, atomic oxygen acts to increase the oxidation rate (ref. 20).

5.3 RECOMMENDATIONS

The results of this investigation point to two areas for additional study to resolve the questions of environmental stability and the thermal radiative properties of statically formed mixed metal oxide layers. These areas are discussed briefly in the following paragraphs.

5.3.1 Environmental Stability

Because of a possible trend towards a cyclic oxidation behavior in the supersonic arc plasma wind tunnel tests, additional cyclic exposures should be conducted covering both shorter and longer cycle times (i.e., 1, 2, 50, and 100 test cycles). Because of the differences in visual appearance and the spectral normal reflectance data for statically oxidized Inconel 617 between stagnation and wedge model tests in the supersonic arc plasma wind tunnel, the additional cyclic exposure tests should be duplicated for both flow conditions. Effects of dissociated versus molecular oxygen on oxidation behavior of the statically oxidized materials should be investigated in the supersonic flow regime.

5.3.2 Thermal Radiative Properties

Optical constant data should be obtained as a function of wavelength and temperature for single and mixed oxide layers. Polished chromium and nickel metals would be oxidized to obtain a range of oxide thicknesses, and then optical constants determined from elevated temperature emittance data. Next, polished chromium-nickel and chromium- nickel-cobalt alloys would be oxidized and optical constants measured. Finally, the data from the present study should be further analyzed to develop bulk layer optical constants and the results correlated with the data for specific species to develop a model more applicable to the mixed layer situation.

Section 6

CONCLUSIONS

The results of this study show that the high-temperature emittance of statically oxidized Inconel 617 and Haynes 188 (HS188) superalloys and R512E coated Cb752 is not degraded by multiple exposures to simulated earth reentry conditions. Total normal emittance values remain at or above 0.80, within the experimental uncertainty of the measurement, after multiple simulated reentry tests. The principal conclusions from this research are:

- At the maximum test temperature of 1260 K total normal emittance of statically oxidized Inconel 617 and HS188 remains greater than 0.80 after 38 exposures of 15 min each in a supersonic arc plasma wind tunnel or 100 exposures of 15 min each in a radiant heated low-pressure slowly flowing air test facility. Similar results were observed for R512E coated Cb752 for a 1590 K test temperature.

- No oxide or coating layer failures were observed for any test condition. A slight thinning of the oxide layer on the surface of Inconel 617 specimens which was exposed to the flow was observed during supersonic arc plasma wind tunnel testing. For HS188, the oxide layer thickness increased during initial cycling and then decreased slightly with further testing in both simulation facilities.

- The oxide layers on both Inconel 617 and HS188 consisted of a major phase of Cr_2O_3 with mixed metal oxide, (CoNi)O and spinel, (CoNi) Cr_2O_4 phases present. Both types of simulated earth reentry exposures produced changes in the ratios of these phases, but they remained present after all test conditions. Surface morphology changes were observed in conjunction with the crystallographic changes. Initially the surfaces had a sharply defined crystalline appearance, whereas after exposures the appearance was a much less well defined surface with smaller typological features.

- The changes in crystallography under supersonic arc wind tunnel test conditions appear to be cyclic in nature with regard to the mixed metal oxide to spinel ratio.

- Although the total emittance data are similar for both supersonic arc plasma wind tunnel and radiant heating test environments, the crystallographic and spectral emittance data suggest some differences in material performance between these two types of test facilities. The former is a more reactive environment because of the presence of dissociated oxygen, and as such the compositional and crystallographic changes may occur at a much faster rate than in the radiant heating test environment.

Section 7

REFERENCES

1. Jackson, L. Robert; and Dixon, Sidney C.: A Design Assessment of Multiwall, Metallic Stand-Off, and RSI Reusable Thermal Protection Systems Including Space Shuttle Applications. NASA TM-81780, 1980.

2. Taylor, Allan H.; and Jackson, Robert L.: Thermostructural Analyses of Structural Concepts for Hypersonic Cruise Vehicles. AIAA Paper No. 80-0407, Pasadena, California, January 1980.

3. Deveikis, W. D.; Miserentino, R.; Weinstein, I.; and Shideler, J. L.: Aerothermal Performance and Structural Integrity of a Rene 41 Thermal Protection System at Mach 6.6. NASA TN D-7943, 1975.

4. Sawyer, J. W.: Aerothermal and Structural Performance of a Cobalt-Base Superalloy Thermal Protection System at Mach 6.6. NASA TN D-8415, 1977.

5. Black, W. E.: Summary Report for Evaluation of Coated Columbium Alloy Heat Shields for Space Shuttle Thermal Protection Systems Applications. NASA CR-2824, 1977.

6. Schaffer, John W.; et al.: Analytical and Experimental Evaluation of Flowing Air Test Conditions for Selected Metallics in a Shuttle TPS Application. NASA CR-2531, 1975.

7. Cunnington, G. R.; Funai, A. I.; and Cassady, P. E.: Development of Techniques and Associated Instrumentation for High Temperature Emissivity Measurements. LMSC-D352380 (Contract NAS8-26304), Lockheed Missiles & Space Co., Inc., June 1973. (Available as NASA CR-124423.)

8. Rolling, R. E.; and Funai, A. I.: Investigation of the Effect of the Surface Conditions on the Radiant Properties of Metals. Air Force Materials Laboratory Technical Report AFML-TR-64-363, Part II, April 1967.

9. Richmond, J. C.; and Harrison, W. N.: Equipment and Procedures for Evaluation of Total Hemispherical Emittance. Ceramic Bull., Vol. 39, 1960.

10. Abbott, G. L.; Alvares, N. J.; and Parker, W. J.: Total Normal and Total Hemispherical Emittance of Polished Metals. WADD Tech Rep 61-94, U.S. Air Force, Nov. 1961.

11. Aerotherm Chemical Equilibrium Users Manual - ACE 1981, Acurex Report UM-81-11/ATD, Acurex Corp., August 1981.

12. Gulbransen, E. A.; and Meier, G. H.: Thermochemical Stability Diagrams for Condensed Phases and Volatility Diagrams for Volatile Species Over Condensed Phases in Twenty Metal-Sulphur-Oxygen Systems Between 1150 and 1450 K. U. S. Dept. of Energy, DOE/FE/13547-01, May 1980.

13. Tenney, D.R., ; Young, C.T.; and Herring, H.W.: Oxidation Behavior of TD-NiCr in a Dynamic High Temperature Environment. Metallurgical Trans., Vol. 5, May 1974.

14. Young, C.T.; Tenney, D.R.; and Herring, H.W.: Dynamic Oxidation Behavior of TD-NiCr Alloy with Different Surface Pretreatments. Metallurgical Trans. A, Vol. 6A, December 1975.

15. Taylor, A., and Sinclair, H.: On the Determination of Lattice Parameters by the Debye-Scherer Method, Proc. Phys. Soc. (London), Vol. 57, 126-135, 1945.

16. Allen, G.G.; and Swallow, G.A.: Reflectance Spectroscopy of Oxide Films, II Oxide Layers on Chromium Metal. Oxidation of Metals, Vol. 17, pp. 150-175, 1982.

17. Shikama, T.; et al.: Corrosion Behavior of Inconel 617 in Hydrogen Base Gas Mixture, Metallurgical Trans. A. Vol. 11A, pp. 1589-98, 1980.

18. Moreau, J.; and Benard, J.: The Selective Oxidation of Nickel-Chromium 1571 Alloys at High Temperature. J. Inst. Metals. Vol. 83, p. 87, 1954-55.

19. Dickens, P.G.; et al.: Oxidation of Metals and Alloys, Part 2 - Oxidation of Metals by Atomic and Molecular Oxygen. Trans. Far. Soc. Vol. 65, pp. 2235-47, 1969.

20. Clark, R. K.; Dicis, D.L.; and Lisagor, W.B.: Emittance of TD-NiCr Simulated Reentry Heating. NASA TM-78784, 1978.

APPENDIX A

EXPERIMENTAL DATA FOR SUPERSONIC ARC PLASMA WIND TUNNEL TEST PROGRAM

The test results from the supersonic arc plasma wind tunnel testing conducted at Acurex are tabulated in this Appendix. Tables A-1 through A-4 contain the data for the statically oxidized Inconel 617 samples. Data for the statically oxidized HS188 samples are contained in Tables A-5 through A-8. Tables A-9 through A-14 are for the R512E Coated Cb752 samples.

BEST DOCUMENT AVAILABLE

Table A-1. Inconel 617 Samples A and AA

Test No.	Wedge No.	Sample No.	Cycle No.	Cumulative Exposure Time (min)	Bulk Enthalpy Mj/kg	Arc Pressure kPa	Convective Heat Flux	
							Coldwall kW/m^2	Hotwall kW/m^2
3,364.01	3F	A	1	15	12.2	24.6	149	132
3,364.01	3F	A	2	30	12.3	24.3	149	132
3,364.01	3F	A	3	45	12.4	24.2	150	132
3,364.02	3F	A	4	60	12.3	24.2	149	132
3,364.02	3F	A	5	75	12.2	23.9	146	131
3,364.02	3F	A	6	84	12.1	23.6	143	127
3,365.02	3F	A	7	99	12.1	24.4	146	131
3,365.03	3F	A	8	108	12.5	24.1	151	135
3,367.01	3F	AA	16	7.5	11.3	22.8	131	116
3,368.01	3F	AA	17	22.5	9.8	21.1	103	93
3,368.02	3F	AA	18	37.5	9.9	20.8	103	94
3,368.03	3F	AA	19	52.5	9.6	20.4	103	91
3,368.04	3F	AA	20	67.5	10.0	20.6	109	95
3,368.05	3F	AA	21	82.5	10.1	20.3	109	94
3,370.01	3F	AA	22	100	9.5	21.1	104	91
3,370.02	3F	AA	23	115	9.5	20.6	102	89
3,370.03	3F	AA	24	130	9.5	20.3	102	89
3,370.04	3F	AA	25	145	9.5	20.2	102	89
3,370.05	3F	AA	26	160	9.7	20.1	103	90
3,370.06	3F	AA	27	175	9.7	20.3	104	90
3,370.07	3F	AA	28	190	8.5	18.9	87	75
3,370.08	3F	AA	29	205	8.5	18.7	86	74
3,371.01	3F	AA	30	220	8.5	18.8	87	75
3,371.02	3F	AA	31	235	8.8	19.0	91	7[illegible]
3,372.01	3F	AA	32	250	8.6	19.9	90	7[illegible]
3,372.02	3F	AA	33	265	8.7	19.8	91	7[illegible]
3,372.02	3F	AA	34	280	8.4	19.3	86	74
3,372.03	3F	AA	35	295	8.3	19.3	85	73
3,372.04	3F	AA	36	310	8.4	19.1	86	74
3,372.09	3F	AA	37	325	7.9	20.4	83	69
3,372.10	3F	AA	38	340	7.7	20.7	81	68
3,372.11	3F	AA	39	355	7.5	20.4	78	66
3,372.12	3F	AA	40	370	7.5	20.4	78	66
3,372.13	3F	AA	41	385	7.7	21.2	82	68
3,372.14	3F	AA	42	400	8.1	21.4	87	74
3,372.15	3F	AA	43	415	7.9	20.6	83	69
3,373.01	3F	AA	44	430	9.6	22.1	108	93
3,373.02	3F	AA	45	445	9.8	21.8	110	95
3,373.03	3F	AA	46	460	9.8	21.7	109	95
3,373.04	3F	AA	47	475	9.7	21.5	107	93
3,374.01	3F	AA	48	490	9.4	21.5	103	90
3,374.02	3F	AA	49	505	9.2	21.3	101	88
3,374.03	3F	AA	50	520	9.3	21.3	102	89
3,374.04	3F	AA	51	535	9.3	21.3	102	89
3,375.02	3F	AA	52	550	8.9	18.2	90	77
3,376.01	3F	AA	53	568.5	9.3	18.3	94	81

Table A-2. Inconel 617 Samples A and AA

Test No.	Wedge No.	Sample No.	Surface Temperature 1 (K)	Surface Temperature 2 (K)	Backwall Temperature (K)	Leading Edge Temp (K)	Remarks
3,364.01	3F	A	1247		1146		Surface temperature 1 TD-7BH pyro with ϵ = 0.82, near T/C zone
3,364.01	3F	A	1256		1153		
3,364.01	3F	A	1300		1188		
3,364.02	3F	A	1280		1172		
3,364.02	3F	A	1283		1175		
3,364.02	3F	A	1277		1170		Sting removed from flow at 9 min because of failure on opposite side specimen C
3,365.02	3F	A	1249		1138		Slight VAC fluctuations
3,365.03	3F	A	1249		1144		VAC fluctuations, opposite side specimen failed at 9 min, removed sample for analysis
3,367.01	3F	AA	1231	1339	1202	1458	Temperature 2 is Pyromark optical pyro, short run, sample BB failed
3,368.01	3F	AA	1217	1350	1163	1389	
3,368.02	3F	AA	1197		1141		
3,368.03	3F	AA	1131		1108		Small VAC fluctuations
3,368.04	3F	AA	1138		1117		
3,368.05	3F	AA	1269		1114		VAC pulses
3,370.01	3F	AA	1208	1275	1127	1333	Ran 2.5 min on 3,369.01, bad VAC fluctuations, reran full 15 min
3,370.02	3F	AA	1196	1172	1116	1314	Read 1264K near focus zone of TD-7BH on Pyromark
3,370.03	3F	AA	1192	1194	1110		
3,370.04	3F	AA	1211	1166	1111	1356	TD-7BH read 1075K on T/C zone, Pyromark read 1294K near TD-7 focus
3,370.05	3F	AA	1239	1153	1109	1356	
3,370.06	3F	AA	1236		1119		Slight VAC pulses
3,370.07	3F	AA	1182	1133	1109	1325	VAC fluctuation
3,370.08	3F	AA	1142		1056		
3,371.01	3F	AA	1147	1239	1101	1267	VAC fluctuations
3,371.02	3F	AA	1150		1106		Numerous VAC fluctuations
3,372.01	3F	AA	1186		1058		
3,372.02	3F	AA	1186	1111	1060	1283	
3,372.02	3F	AA	1172		1047	1267	
3,372.03	3F	AA	1168		1043		
3,372.04	3F	AA	1169	1111	1042	1261	1172K on Pyromark over TD-7 focus zone
3,372.09	3F	AA	1189		1125	1333	Slight VAC surge
3,372.10	3F	AA	1150	1111	1061	1314	Two VAC surges
3,372.11	3F	AA	1167		1108	1308	
3,372.12	3F	AA	1165		1103		VAC fluctuations
3,372.13	3F	AA	1203		1140	1342	VAC fluctuations
3,372.14	3F	AA	1184		1092		
3,372.15	3F	AA	1200		1138		VAC fluctuations
3,373.01	3F	AA	1206		1083	1328	
3,373.02	3F	AA	1194		1069	1331	
3,373.03	3F	AA	1192		1067		
3,373.04	3F	AA	1208		1128	1314	VAC surge
3,374.01	3F	AA	1206		1125		
3,374.02	3F	AA	1207		1128	1322	VAC surge
3,374.03	3F	AA	1161		1133	1322	VAC surges
3,374.04	3F	AA	1236		1139		VAC surges
3,375.02	3F	AA	1198		1067	1281	
3,376.01	3F	AA	1213		1098		Sample removed for analysis

A3

BEST DOCUMENT AVAILABLE

BEST DOCUMENT AVAILABLE

Table A-3. Inconel 617 Samples B, C, D, BB, CC and DD

Test No.	Wedge No.	Sample No.	Cycle No.	Cumulative Exposure Time (min)	Bulk Enthalpy (MJ/kg)	Arc Pressure (kPa)	Convective Heat Flux Coldwall (kW/M^2)	Convective Heat Flux Hotwall (kW/M^2)
3,364.01	3N	C	1	15	12.2	24.6	149	133
3,364.01	3N	C	2	30	12.3	24.3	149	134
3,364.01	3N	C	3	45	12.4	24.3	150	135
3,364.02	3N	C	4	60	12.3	24.3	149	134
3,364.02	3N	C	5	75	12.2	23.9	146	132
3,364.02	3N	C	6	84.9	12.1	23.6	143	127
3,365.02	3N	B	7	15	12.1	24.4	146	130
3,365.03	3N	B	8	24	12.5	23.2	151	134
3,366.01	3N	D	9	15	12.0	24.6	145	131
3,366.02	3N	D	10	29.2	12.0	24.4	145	131
3,367.01	3N	BB	16	7.5	11.3	22.8	131	116
3,368.01	3N	DD	17	15	9.8	21.2	108	95
3,368.02	3N	DD	18	30	9.9	20.8	108	95
3,368.03	3N	DD	19	45	9.6	20.4	103	91
3,368.04	3N	DD	20	60	10.0	20.6	109	96
3,368.05	3N	DD	21	75	10.1	20.3	109	96
3,370.01	3N	DD	22	92	9.5	21.1	105	92
3,370.02	3N	DD	23	107	9.5	20.6	102	90
3,370.03	3N	DD	24	122	9.5	20.3	102	90
3,370.04	3N	DD	25	137	9.5	20.2	102	90
3,370.05	3N	DD	26	152	9.6	20.1	103	91
3,370.06	3N	DD	27	167	9.7	20.3	105	92
3,370.07	3N	DD	28	182	8.5	18.9	87	76
3,370.08	3N	DD	29	197	8.4	18.7	85	75
3,371.01	3N	DD	30	212	8.5	18.7	87	76
3,371.02	3N	DD	31	227	8.8	18.8	91	78
3,372.01	3N	DD	32	242	8.6	19.9	90	77
3,372.02	3N	DD	33	257	8.7	19.8	91	78
3,372.02	3N	DD	34	272	8.4	19.3	86	77
3,372.03	3N	DD	35	287	8.3	19.2	85	75
3,372.04	3N	DD	36	302	8.4	19.0	86	75
3,372.09	3N	CC	37	15	7.9	20.4	83	70
3,372.10	3N	CC	38	30	7.7	20.7	81	68
3,372.11	3N	CC	39	45	7.5	20.4	79	66
3,372.12	3N	CC	40	60	7.5	20.4	79	66
3,372.13	3N	CC	41	75	7.6	21.2	82	69
3,372.14	3N	CC	42	90	8.1	21.4	87	75
3,372.15	3N	CC	43	105	7.9	20.6	83	70
3,373.01	3N	CC	44	120	9.6	22.1	108	94
3,373.02	3N	CC	45	135	9.8	21.8	110	96
3,373.03	3N	CC	46	150	9.8	21.7	109	95
3,373.04	3N	CC	47	165	9.7	21.5	107	93
3,374.01	3N	CC	48	180	9.4	21.4	103	90
3,374.02	3N	CC	49	195	9.2	21.3	101	90
3,374.03	3N	CC	50	210	9.3	21.3	102	89
3,374.04	3N	CC	51	225	9.3	21.3	102	89
3,375.02	3N	CC	52	240	8.9	18.2	90	81
3,376.01	3N	CC	53	258.5	9.3	18.3	94	83

Table A-4. Inconel 617 Samples B, C, D, BB, CC and DD

Test No.	Wedge No.	Sample No.	Surface Temperature 1 (K)	Surface Temperature 2 (K)	Backwall Temperature (K)	Leading Edge Temp (K)	Remarks
3,364.01	3N	C	1,221	1,289	1,258		Temperature 1 is TD-78 with ND = 5.6, temperature 2 is Pyromark pyro
3,364.01	3N	C	1,132	1,225	1,148		Uneven heat appearance to sample
3,364.01	3N	C	1,161	1,278	1,188		
3,364.02	3N	C	1,177	1,278	1,207		
3,364.02	3N	C	1,193	1,289	1,278		
3,364.02	3N	C	1,236	1,311	1,267		Sample failed at 9 min 50 sec into run
3,365.02	3N	B	1,296		1,171		
3,365.03	3N	B	1,296	1,256	1,200		Sample failed at 9 min into run
3,366.01	3N	D	1,109	1,139	1,047	1,311	VAC fluctuations
3,366.02	3N	D	1,125	1,178	1,083	1,306	Sample failed at 14 min 20 sec into run
3,367.01	3N	BB	1,207		1,261		Sample failed at 7.5 min into test
3,368.01	3N	DD	1,075		1,275	1,472	Restricted leading edge temperature to 1367K with photometric pyro, TD-78 view front port
3,368.02	3N	DD	1,091		1,299	1,476	
3,368.03	3N	DD	1,078		1,271	1,456	VAC fluctuation, slight temperature rise
3,368.04	3N	DD	1,083		1,282	1,461	
3,368.05	3N	DD	1,082		1,281	1,440	VAC fluctuations
3,370.01	3N	DD	1,069		1,284	1,450	Bad VAC fluctuation, withdrew at 2.5 min, reran full 15 min next day
3,370.02	3N	DD	1,072		1,276	1,452	
3,370.03	3N	DD	1,067		1,273	1,444	
3,370.04	3N	DD	1,067		1,270	1,440	
3,370.05	3N	DD	1,073		1,273	1,451	
3,370.06	3N	DD	1,075		1,279	1,445	VAC fluctuation
3,370.07	3N	DD	1,072		1,248	1,453	VAC fluctuation
3,370.08	3N	DD	1,056		1,219	1,450	
3,371.01	3N	DD	1,104		1,248	1,447	VAC fluctuations
3,371.02	3N	DD	1,108		1,249	1,440	VAC fluctuations , leading edge to temperature to 1561K.
3,372.01	3N	DD	1,090		1,238	1,447	
3,372.02	3N	DD	1,092	1,188	1,241	1,398	Surface temperature 2 photometric pyro on T/C zone (ε = 1.0)
3,372.02	3N	DD	1,088		1,225	1,447	
3,372.03	3N	DD	1,084		1,222	1,444	
3,372.04	3N	DD	1,086		1,221	1,446	Removed for analysis
3,372.09	3N	CC	1,139		1,156	1,451	Slight VAC surge
3,372.10	3N	CC	1,125		1,089	1,454	Two VAC surges
3,372.11	3N	CC	1,133		1,144	1,447	
3,372.12	3N	CC	1,132		1,144	1,444	VAC fluctuations
3,372.13	3N	CC	1,141		1,160	1,446	VAC fluctuations
3,372.14	3N	CC	1,132		1,109	1,454	
3,372.15	3N	CC	1,131		1,158	1,451	VAC fluctuations
3,373.01	3N	CC	1,119		1,106	1,443	
3,373.02	3N	CC	1,117		1,104	1,451	
3,373.03	3N	CC	1,119		1,103	1,451	
3,373.04	3N	CC	1,128		1,158	1,446	VAC surge
3,374.01	3N	CC	1,124		1,159	1,443	
3,374.02	3N	CC	1,127		1,158	1,444	VAC surge
3,374.03	3N	CC	1,128		1,155	1,443	VAC surges
3,374.04	3N	CC	1,139		1,160	1,445	VAC surges
3,375.02	3N	CC	1,086		1,086	1,440	
3,376.01	3N	CC	1,081		1,127	1,447	Sample removed for analysis

BEST DOCUMENT AVAILABLE

BEST DOCUMENT AVAILABLE

Table A-5. HS188 Sample E

Test No.	Wedge No.	Sample No.	Cycle No.	Cumulative Exposure Time (min)	Bulk Enthalpy (MJ/kg)	Arc Pressure (kPa)	Convective Heat Flux	
							Coldwall (kW/m^2)	Hotwall (kW/m^2)
3,364.01	2F	E	1	15	12.5	24.9	153	136
3,364.01	2F	E	2	30	12.2	24.8	149	131
3,364.01	2F	E	3	45	12.4	24.4	150	132
3,364.02	2F	E	4	60	11.5	23.7	136	120
3,364.02	2F	E	5	75	11.9	23.4	140	123
3,364.02	2F	E	6	90	11.6	23.1	136	120
3,365.01	2F	E	7	105	11.6	22.4	134	118
3,365.03	2F	E	8	120	11.3	23.3	132	116
3,366.01	2F	E	9	135	12.5	24.0	151	133
3,366.02	2F	E	10	150	11.4	23.9	136	120
3,366.02	2F	E	11	165	11.3	23.7	133	117
3,366.03	2F	E	12	180	11.2	23.4	132	116
3,366.04	2F	E	13	195	11.3	23.2	132	116
3,366.05	2F	E	14	210	11.5	22.8	133	117
3,366.06	2F	E	15	225	11.6	22.9	135	119
3,367.01	2F	E	16	240	11.3	22.7	129	113
3,367.01	2F	E	17	255	11.2	22.3	127	112
3,368.02	2F	E	18	270	9.4	20.9	102	89
3,368.03	2F	E	19	285	9.1	19.9	95	83
3,368.04	2F	E	20	300	9.8	20.5	106	92
3,368.05	2F	E	21	315	10.1	20.4	109	95
3,369.01	2F	E	22	330	10.1	21.2	111	98
3,370.02	2F	E	23	345	9.4	20.7	101	89
3,370.03	2F	E	24	360	9.2	20.1	96	83
3,370.04	2F	E	25	375	9.1	19.9	95	83
3,370.05	2F	E	26	390	9.1	19.8	93	81
3,370.06	2F	E	27	405	9.0	19.4	92	81
3,370.07	2F	E	28	420	8.8	19.4	75	66
3,370.08	2F	E	29	435	7.6	17.7	70	61
3,371.01	2F	E	30	450	7.2	18.0	75	62
3,371.02	2F	E	31	465	7.5	17.8	74	61
3,372.01	2F	E	32	480	7.5	18.9	75	62
3,372.05	2F	E	33	495	6.3	18.0	61	51
3,372.06	2F	E	34	510	6.7	20.3	68	57
3,372.07	2F	E	35	525	6.7	19.8	68	57
3,372.08	2F	E	36	540	7.3	20.5	76	63
3,372.09	2F	E	37	555	7.0	20.1	71	60
3,372.10	2F	E	38	570	7.5	20.3	78	66

BLANK PAGE

BLANK PAGE

BLANK PAGE

Table A-6. HS188 Sample E

Test No.	Wedge No.	Sample No.	Surface Temperature 1 (K)	Surface Temperature 2 (K)	Backwall Temperature (K)	Leading Edge Temp (K)	Remarks
3,364.01	2F	E	1,263		1,217		Surface temperature 1 is TD-7BH with ϵ = 0.82
3,364.01	2F	E	1,294		1,210		
3,364.01	2F	E	1,300		1,217		
3,364.02	2F	E	1,256		1,172		
3,364.02	2F	E	1,283		1,198		
3,364.02	2F	E	1,283		1,197		
3,365.01	2F	E	1,254		1,184		
3,365.03	2F	E	1,278		1,167		Noticed VAC fluctuations during test
3,366.01	2F	E	1,265		1,198	1,411	Leading edge used TD-7BH (ϵ = 0.82 on meter)
3,366.02	2F	E	1,298		1,206		
3,366.02	2F	E	1,294		1,208		
3,366.03	2F	E	1,267		1,206		
3,366.04	2F	E	1,274		1,213		
3,366.05	2F	E	1,262		1,206		
3,366.06	2F	E	1,266		1,207		
3,367.01	2F	E	1,219		1,139		
3,367.01	2F	E	1,256		1,1[illegible]		
3,368.02	2F	E	1,139	1,183	1,034	1,361	Restricted leading edge temperatures to 1367K for remainder of series (micro optical pyro)
3,368.03	2F	E	1,110	1,20[illegible]	1,007	1,353	Surface temperature 2 over or near the T/C zone, surface temperature 1 at 0.5 in. upstream of T/C zone
3,368.04	2F	E	1,156		1,097		Temperature/VAC pulse once
3,368.05	2F	E	1,201		1,106		Temperature/VAC pulses, one large, three small
3,369.01	2F	E	1,215		1,064		
3,370.02	2F	E	1,204	1,172	1,061	1,428	
3,370.03	2F	E	1,169		1,039		
3,370.04	2F	E	1,203	1,089	1,078	1,358	Surface temperature 2 over T/C spot (with micro optical pyro)
3,370.05	2F	E	1,193	1,083	1,031	1,356	
3,370.06	2F	E	1,166		1,028		
3,370.07	2F	E	1,171	1,158	1,027	1,342	
3,370.08	2F	E	1,117	1,067	1,016	1,256	Controlling to "hot spot" on W2N side, to 1367K, one VAC surge
3,371.01	2F	E	1,111	1,111	1,031		One VAC surge during test
3,371.02	2F	E	1,110		1,028	1,256	
3,372.01	2F	E	1,129		1,004		
3,372.05	2F	E	1,023		944	1,245	Volt signal missing, used manual data
3,372.06	2F	E	1,083		1,017		
3,372.07	2F	E	1,062		984		
3,372.08	2F	E	1,131		1,067		VAC surge during test
3,372.09	2F	E	1,138		1,028		
3,372.10	2F	E	1,170	1,111	1,064	1,314	Sample removed for analysis, two VAC surges during test

BEST DOCUMENT AVAILABLE

BEST DOCUMENT AVAILABLE

Table A-7. HS188 Samples F, G and FF

Test No.	Wedge No.	Sample No.	Cycle No.	Cumulative Exposure Time (min)	Bulk Enthalpy (Mj/kg)	Arc Pressure (kPa)	Convective Heat Flux Coldwall (kW/M^2)	Convective Heat Flux Hotwall (kW/M^2)
3,364.01	2N	F	1	15	12.5	24.9	153	137
3,364.01	2N	F	2	30	12.2	24.8	149	133
3,364.01	2N	F	3	45	12.5	24.4	150	134
3,364.02	2N	F	4	60	11.5	23.7	136	119
3,364.02	2N	F	5	75	11.9	23.4	140	123
3,364.02	2N	F	6	90	11.6	23.1	136	120
3,365.01	2N	F	7	105	11.6	22.4	134	118
3,365.03	2N	F	8	120	11.3	23.3	132	116
3,366.01	2N	G	9	15	12.5	24.0	151	133
3,366.02	2N	G	10	30	11.4	23.9	136	120
3,366.02	2N	G	11	45	11.3	23.7	133	117
3,366.03	2N	G	12	60	11.2	23.4	132	116
3,366.04	2N	G	13	75	11.3	23.2	132	116
3,366.05	2N	G	14	90	11.5	22.8	133	117
3,366.06	2N	G	15	104.7	11.6	22.9	135	119
3,368.02	2N	FF	18	15	9.4	20.9	102	90
3,368.03	2N	FF	19	30	9.1	19.9	95	84
3,368.04	2N	FF	20	45	9.8	20.5	106	93
3,368.05	2N	FF	21	60	10.1	20.4	109	95
3,369.01	2N	FF	22	75	10.1	21.2	111	98
3,370.02	2N	FF	23	90	9.4	20.7	101	89
3,370.03	2N	FF	24	105	9.2	20.1	96	85
3,370.04	2N	FF	25	120	9.1	19.9	96	85
3,370.05	2N	FF	26	135	9.1	19.8	95	84
3,370.06	2N	FF	27	150	9.0	19.4	93	82
3,370.07	2N	FF	28	165	8.8	19.4	92	81
3,370.08	2N	FF	29	180	7.6	17.7	75	66
3,371.01	2N	FF	30	195	7.2	18.0	70	63
3,371.02	2N	FF	31	210	7.5	17.8	74	65
3,372.01	2N	FF	32	225	7.5	18.9	75	66
3,372.05	2N	FF	33	240	6.3	18.0	61	54
3,372.06	2N	FF	34	255	6.7	20.3	68	60
3,372.07	2N	FF	35	270	6.7	19.8	68	60
3,372.08	2N	FF	36	285	7.3	20.5	76	67
3,372.09	2N	FF	37	300	7.0	20.1	71	62
3,372.10	2N	FF	38	315	7.5	20.3	78	69

Table A-8. HS188 Samples F, G and FF

Test No.	Wedge No.	Sample No.	Surface Temperature 1 (K)	Surface Temperature 2 (K)	Backwall Temperature (K)	Leading Edge Temperature (K)	Remarks
3,364.01	2N	F	1,238	1,261	1,244		Temperature 1 is TD-7B with ND = 5.6 filter, temperature 2 is Pyromark pyro (ε = 1.0)
3,364.01	2N	F	1,254	1,261	1,255		
3,364.01	2N	F	1,258	1,256	1,258		
3,364.02	2N	F	1,289	1,306	1,273		
3,364.02	2N	F	1,294	1,317	1,287		
3,364.02	2N	F	1,283	1,257	1,283		
3,365.01	2N	F	1,277	1,278	1,299		
3,365.03	2N	F	1,296	1,292	1,268		VAC fluctuations during test, removed for analysis
3,366.01	2N	G	1,254	1,292	1,297		
3,366.02	2N	G	1,248	1,294	1,273	1,483	
3,366.02	2N	G	1,222	1,278	1,241	1,478	
3,366.03	2N	G	1,286	1,319	1,269		
3,366.04	2N	G	1,293	1,289	1,280		
3,366.05	2N	G	1,281	1,278	1,278		
3,366.06	2N	G	1,266	1,267	1,266		Sample failed at 14 min 40 sec
3,368.02	2N	FF	1,050		1,175	1,478	Restrict leading edge 2,000°F TD-7B view port on front bulkhead
3,368.03	2N	FF	1,047		1,144	1,481	
3,368.04	2N	FF	1,062		1,172	1,427	VAC fluctuation
3,368.05	2N	FF	1,067		1,188	1,481	Four VAC surges
3,369.01	2N	FF	1,054		1,171	1,438	
3,370.02	2N	FF	1,049		1,168	1,447	
3,370.03	2N	FF	1,039		1,144	1,450	
3,370.04	2N	FF	1,049		1,159	1,442	
3,370.05	2N	FF	1,041		1,127	1,452	
3,370.06	2N	FF	1,044		1,139	1,447	
3,370.07	2N	FF	1,043		1,141	1,444	
3,370.08	2N	FF	1,035		1,098	1,447	VAC surge, control leading edge to ~2,000°F
3,371.01	2N	FF	1,067		1,122	1,446	VAC surge
3,371.02	2N	FF	1,072		1,124	1,450	
3,372.01	2N	FF	1,058		1,114	1,445	
3,372.05	2N	FF	1,067		1,081	1,446	
3,372.06	2N	FF	1,092		1,117	1,451	
3,372.07	2N	FF	1,089		1,105	1,448	
3,372.08	2N	FF	1,114		1,171	1,444	VAC surge
3,372.09	2N	FF	1,107		1,152	1,446	
3,372.10	2N	FF	1,126		1,162	1,445	Two VAC fluctuations, sample removed for analysis

BEST DOCUMENT AVAILABLE

BEST DOCUMENT AVAILABLE

Table A-9. R512E Coated Cb752 Samples 5, 6, 9a and 10

Test No.	Wedge No.	Sample No.	Cycle No.	Cumulative Exposure Time (min)	Bulk Enthalpy (Mj/kg)	Arc Pressure (kPa)	Convective Heat Flux	
							Coldwall (kW/m^2)	Hotwall (kW/m^2)
3,380.01	3F	6	1	2.2	9.0	74.5		
3,380.02	3F	6	1	5.9	8.9	74.3	267	
3,380.03	3F	6	2	10.1	8.7	73.2	263	
3,381.01	3F	6	3	21.6	8.6	73.9		
3,381.01	3N	5	1	11.5	7.7	73.9	530	
3,382.01	3F	6	4					
3,413.01	3N	9	20	15	11.8	62.4	238	213
3,413.02	3N	9	21	30	11.1	62.6	224	199
3,413.03	3N	9	22	45	9.1	63.1	233	208
3,413.04	3N	9	23	60	11.2	63.3	228	203
3,413.05	3N	9	24	75	11.3	63.1	228	203
3,413.05	3N	9	25	90	11.1	63.0	222	197
3,413.06	3N	9	26	105	10.9	62.9	221	196
3,413.07	3N	9	27	120	10.3	62.7	209	184
3,413.08	3N	9	28	127.5	10.9	62.8	220	195
3,413.09	3N	9	29	137.8	10.7	62.0	216	191
3,414.01	3N	10	30	15	11.0	62.6	221	195
3,414.02	3N	10	31	30	10.9	62.4	219	193
3,414.03	3N	10	32	45	10.5	62.2	212	187
3,414.04	3N	10	33	53.5	10.7	62.5	217	191
3,415.01	3N	10	34	63.3	12.1	65.2	250	221
3,415.02	3N	10	35	78.3	12.5	64.0	313	229
3,415.03	3N	10	36	93.3	12.1	64.7	249	221
3,415.04	3N	10	37	100.8	12.4	65.0	254	226

Table A-10. R512E Coated Cb752 Samples 5, 6, 9a and 10

Test No.	Wedge No.	Sample No.	Surface Temperature 1 (K)	Surface Temperature 2 (K)	Backwall Temperature (K)	Leading Edge Temp (K)	Remarks
3,380.01	3F	6	1,370	1,493	1,166	1,550	
3,380.02	3F	6	1,387	1,513	1,203	1,601	
3,380.03	3F	6	1,372	1,495	1,196	1,598	
3,381.01	3F	6	1,333	1,450	1,062	1,569	T/C may not be connected to surface,
3,381.01	3N	5	1,505	1,569	1,569	1,597	T = 1553K at ε = 0.65, T/C type 12, 1 each, cal
3,382.01	3F	6					data during surge
3,413.01	3N	9	1,358		NG	1,418	Surface temperature 1 is TD-9CH (ε = 1.0), surface temperature 2 and leading edge are automatic pyro (ε = 1.0)
3,413.02	3N	9	1,357		NG	1,414	
3,413.03	3N	9	1,352		NG	1,418	
3,413.04	3N	9	1,354		NG	1,417	
3,413.05	3N	9	1,348		NG	1,416	
3,413.05	3N	9	1,344		NG	1,415	Surge to 1478K
3,413.06	3N	9	1,351		NG	1,418	Surge to 1502K
3,413.07	3N	9	1,339		NG	1,418	
3,413.08	3N	9	1,360		NG	1,424	
3,413.09	3N	9	1,353		NG	1,417	Surge to 1517K on ℄, 1682K on LE
3,414.01	3N	10	1,376		NG	1,422	
3,414.02	3N	10	1,373	1,331	NG	1,416	
3,414.03	3N	10	1,362		NG	1,422	
3,414.04	3N	10	1,378		NG	1,428	
3,415.01	3N	10	1,450		NG	1,481	Raised LE temperature to 1478K
3,415.02	3N	10	1,424		NG	1,468	
3,415.03	3N	10	1,433		NG	1,476	
3,415.04	3N	10	1,450		NG	1,477	Large VAC surges, nozzle failure

BEST DOCUMENT AVAILABLE

Table A-11. R512E Coated Cb752 Sample 7

Test No.	Wedge No.	Sample No.	Cycle Number	Cumulative Exposure Time (min)	Bulk Enthalpy (Mj/kg)	Arc Pressure (kPa)	Convective Heat Flux	
							Coldwall (kW/m^2)	Hotwall (kW/m^2)
3,384.01	3N	7	1	15	9.6	62.9	194	170
3,384.01	3N	7	2	27.8	9.3	62.6	187	163
3,384.03	3N	7	3	40.1	9.3	63.0	187	163
3,385.01	3N	7	4	55.1	9.0	62.1	180	157
3,385.02	3N	7	5	70.1	9.2	62.4	185	161
3,385.03	3N	7	6	85.1	9.1	62.6	184	160
3,385.04	3N	7	7	100.1	9.2	64.1	188	163
3,385.05	3N	7	8	115.1	9.1	64.3	186	162
3,385.06	3N	7	9	130.1	8.7	64.0	178	153
3,385.07	3N	7	10	145.1	8.6	62.0	173	146
3,386.01	3N	7	11	160.1	10.2	62.2	205	183
3,386.02	3N	7	12	175.1	11.2	63.5	228	204
3,387.01	3N	7	13	190.1	10.6	64.0	216	192
3,387.01	3N	7	14	205.1	10.8	63.9	220	196
3,387.03	3N	7	15	230.1	10.6	62.7	213	190
3,387.04	3N	7	16	245.1	10.2	62.2	204	182
3,387.05	3N	7	17	260.1	9.9	62.0	203	180
3,387.07	3N	7	18	273	10.3	61.9	205	182
3,389.01	3N	7	19	279	11.5	62.9	233	207
3,389.01	3N	7		282.5	14.0	51.3	258	238

Table A-12. RS12E Coated Cb752 Sample 7

Test No.	Wedge No.	Sample No.	Surface Temperature 1 (K)	Surface Temperature 2 (K)	Backwall Temperature (K)	Leading Edge Temp (K)	Remarks
3,384.01	3N	7	1,?1?		978	1,429	Surface temperature 1 is TD-9GM (ε = 1.0), leading edge temperature is auto pyro
3,384.01	3N	7	1,329		1,039	1,457	Bad surges, stopped early
3,384.03	3N	7	1,312		1,046	1,419	Bad surges
3,385.01	3N	7	1,314		1,001	1,421	
3,385.02	3N	7	1,312		1,037	1,419	
3,385.03	3N	7	1,316		1,028	1,423	
3,385.04	3N	7	1,338		1,072	1,444	
3,385.05	3N	7	1,344		1,077	1,450	
3,385.06	3N	7	1,361		1,117	1,439	Surges to 1613K at LE, T/C zone to 1391K and T/C to 1138K
3,385.07	3N	7	1,361		1,079	1,450	Surges to 1661K LE, temperatures to 1370K T/C to 1122K
3,386.01	3N	7	1,307		1,038	1,419	
3,386.02	3N	7	1,337		1,086	1,417	1365K maximum temperature, T/C maximum 1111K
3,387.01	3N	7	1,331		1,054	1,441	
3,387.02	3N	7	1,325		1,053	1,436	
3,387.03	3N	7	1,320		1,052	1,418	
3,387.04	3N	7	1,309		1,033	1,417	
3,387.05	3N	7	1,290		1,012	1,423	
3,387.07	3N	7	1,317		1,029	1,422	
3,389.01	3N	7	1,416		1,099	1,413	VAC loss during test Lower ṁ to 0.0091 kg/s; nozzle failure
3,389.01	3N	7	1,259		941	1,400	Removed from sting, T/C disconnected from Columbium disc, Columbium disc was disconnected from sample.

BEST DOCUMENT AVAILABLE

Table A-13. R512E Coated Cb752 Sample 8

Test No.	Wedge No.	Sample No.	Cycle Number	Cumulative Exposure Time (min)	Bulk Enthalpy (MJ/kg)	Arc Pressure (kPa)	Convective Heat Flux	
							Coldwall (kW/M^2)	Hotwall (kW/M^2)
3,384.01	3F	8	1	15	9.57	62.9	194	173
3,384.02	3F	8	2	27.8	9.27	62.6	187	166
3,384.03	3F	8	3	40.1	9.25	63.0	187	167
3,385.01	3F	8	4	55.1	8.94	62.1	179	159
3,385.02	3F	8	5	70.1	9.17	62.4	185	162
3,385.03	3F	8	6	85.1	9.09	62.6	184	161
3,385.04	3F	8	7	100.1	9.21	64.1	188	165
3,385.05	3F	8	8	115.1	9.11	64.3	186	160
3,385.06	3F	8	9	130.1	8.69	64.0	178	152
3,385.07	3F	8	10	145.1	8.56	62.0	173	146
3,386.01	3F	8	11	160.1	10.21	62.2	206	183
3,386.02	3F	8	12	175.1	11.21	63.5	228	203
3,387.01	3F	8	13	190.1	10.55	64.0	216	192
3,387.01	3F	8	14	205.1	10.79	63.9	220	196
3,387.03	3F	8	15	230.1	10.53	62.7	213	191
3,387.04	3F	8	16	245.1	10.15	62.2	204	182
3,387.05	3F	8	17	260.1	9.84	62.0	203	181
3,387.07	3F	8	18	273	10.24	61.9	206	184
3,389.01	3F	8	19	279	11.45	63.3	233	208
3,389.01	3F	8	20	282.5	9.38	51.3	258	237
3,413.01	3F	8	21	297.5	11.79	62.4	238	212
3,413.02	3F	8	22	312.5	11.08	62.6	224	199
3,413.03	3F	8	23	327.5	11.45	63.1	233	208
3,413.04	3F	8	24	342.5	11.23	63.3	228	203
3,413.05	3F	8	25	357.5	11.26	63.1	228	203
3,413.05	3F	8	26	372.5	11.04	63.0	223	196
3,413.06	3F	8	27	387.5	10.90	62.9	221	195
3,413.07	3F	8	28	402.5	10.33	62.7	209	184
3,413.08	3F	8	29	410	10.90	62.8	220	195
3,413.09	3F	8	30	420.3	10.71	62.0	216	191
3,414.01	3F	8	31	435.3	10.95	62.6	221	196
3,414.02	3F	8	32	450.3	10.84	62.4	219	195
3,414.03	3F	8	33	465.3	10.61	62.3	212	190
3,414.04	3F	8	34	473.8	10.71	62.6	217	193
3,415.01	3F	8	35	484	12.10	65.1	250	223
3,415.02	3F	8	36	499	12.53	64.0	257	232
3,415.03	3F	8	37	514	9.77	64.7	249	223
3,415.04	3F	8	38	521.5	12.35	64.9	254	228

BEST DOCUMENT AVAILABLE

Table A-14. R512E Coated Cb752 Sample 8

Test No.	Wedge No.	Sample No.	Surface Temperature 1 (K)	Surface Temperature 2 (K)	Backwall Temperature (K)	Leading Edge Temp (K)	Centerline Surface Temp at ε = 0.79 (K)	Remarks
3,384.01	3F	8	1,170		1,092	1,456	1,222	Surface temperature 1 is TD-78H (ε = 1.0) surface temperature 2 and leading edge are Pyromark (ε = 1.0)
					1,156		1,247	
3,384.02	3F	8	1,194		1,133		1,223	Bad surges, removed early
3,384.03	3F	8	1,172		1,082	1,378	1,236	Bad surges, removed early
3,385.01	3F	8	1,183	1,217	1,113	1,372	1,269	
3,385.02	3F	8	1,209	1,260	1,109		1,266	
3,385.03	3F	8	1,211		1,159	1,411	1,322	
3,385.04	3F	8	1,259	1,256	1,172	1,444	1,336	
3,385.05	3F	8	1,278		1,233	1,456	1,612	Surges on LE to 1589K
3,385.06	3F	8	1,324	1,328	1,236		1,401	Surges on LE to 1589K
3,385.07	3F	8	1,333		1,137		1,288	
3,386.01	3F	8	1,231		1,197		1,350	
3,386.02	3F	8	1,288		1,147		1,307	
3,387.01	3F	8	1,248		1,144		1,305	
3,387.01	3F	8	1,244		1,147	1,417	1,305	
3,387.03	3F	8	1,244		1,127	1,411	1,278	
3,387.04	3F	8	1,222		1,103		1,256	
3,387.05	3F	8	1,203		1,125		1,268	
3,387.07	3F	8	1,218		1,111	1,394	1,377	
3,389.01	3F	8	1,311		1,048		1,282	VAC loss
3,389.01	3F	8	1,230					Lowered ṁ to 0.020 lb/s; nozzle failure Removed, Cb disc was disconnected from surface of sample, T/C still attached to Cb disc
							1,419	Reinstated on wedge, continue cycle
3,413.01	3F	8	1,351		NG		1,368	
3,413.02	3F	8	1,306		NG		1,361	
3,413.03	3F	8	1,299		NG		1,384	Photographs taken during testing
3,413.04	3F	8	1,319		NG			VAC surge at 11-1/2 min into cycle, surface temperature surges to 1378K
							1,385	3 VAC surges at 6 min, 9 min and 13-1/2 min
3,413.05	3F	8	1,319		NG			
							1,402	Several small surges
3,413.05	3F	8	1,335		NG		1,390	Realized TD-7, several vacuum surges
3,413.06	3F	8	1,324		NG		1,364	Several vaccum surges
3,413.07	3F	8	1,299		NG		1,384	Several small surges
3,413.08	3F	8	1,317		NG		1,374	Several surges, severe surge at 10-1/2 min, removed sample from flow
3,413.09	3F	8	1,311		NG			
							1,367	
3,414.01	3F	8	1,303		NG		1,336	
3,414.02	3F	8	1,273	1,317	NG	1,394	1,308	
3,414.03	3F	8	1,251		NG		1,326	
3,414.04	3F	8	1,267		NG		1,461	
3,415.01	3F	8	1,391		NG		1,392	Raised LE to 1478K
3,415.02	3F	8	1,326		NG		1,441	Several surges
3,415.03	3F	8	1,371		NG		1,457	Several severe surges
3,415.04	3F	8	1,387		NG			Burned out nozzle

BEST DOCUMENT AVAILABLE

APPENDIX B

RADIATING PROPERTIES DATA

Spectral normal (1.0 to 14.0μm) and total normal emittance data at elevated temperatures and near normal spectral reflectance (0.3 to 25.0μm) data at nominally 294K are tabulated in the Appendix. Tables B-1 through B-5 contain the data for statically oxidized Inconel 617 specimens. The data for statically oxidized HS188 are contained in Tables B-6 through B-13. Table B-14 through B-17 contain the data for the R512E coated Cb752 alloy.

BEST DOCUMENT AVAILABLE

Table B-1. Spectral and Total Normal Emittance of Statically Oxidized Inconel 617

	STATICALLY OXIDIZED				AFTER ARC PLASMA TESTS							AFTER RADIANT HEATING TESTS							
					8 CYCLE	20 CYCLE			38 CYCLE			10 CYCLE		20 CYCLE		50 CYCLE		100 CYCLE	
TEMPERATURE (K)	532	810	1088	1248	1249	809	1093	1250	819	1091	1259	1095*	1259*	1095	1259*	1095*	1259*	1095	1259*
WAVELENGTH (μm)																			
1.0	-	0.62	0.79	0.83	0.92	0.82	0.89	0.92	0.85	0.93	0.97	0.90	0.91	0.93	0.94	0.91	0.91	0.92	0.92
1.5	0.71	0.78	0.85	0.85	0.96	0.95	0.96	0.98	0.93	0.95	0.97	0.92	0.92	0.94	0.95	0.93	0.93	0.94	0.94
2.0	0.82	0.83	0.85	0.88	0.93	0.92	0.92	0.95	0.89	0.89	0.91	0.89	0.89	0.91	0.91	0.93	0.91	0.91	0.91
3.0	0.83	0.83	0.85	0.86	0.92	0.90	0.90	0.93	0.87	0.86	0.89	0.87	0.88	0.89	0.89	0.92	0.88	0.89	0.89
4.0	0.83	0.82	0.85	0.86	0.92	0.88	0.89	0.93	0.86	0.82	0.88	0.86	0.86	0.88	0.88	0.88	0.89	0.89	0.89
5.0	0.82	0.80	0.80	0.82	0.89	0.87	0.85	0.88	0.84	0.83	0.85	0.83	0.84	0.85	0.86	0.86	0.86	0.86	0.87
6.0	0.82	0.81	0.82	0.83	0.88	0.87	0.86	0.88	0.82	0.82	0.84	0.84	0.85	0.86	0.85	0.85	0.87	0.87	0.88
7.0	0.79	0.79	0.80	0.81	0.85	0.85	0.86	0.87	0.78	0.79	0.80	0.84	0.86	0.85	0.86	0.85	0.86	0.87	0.86
8.0	0.80	0.79	0.80	0.81	0.84	0.85	0.84	0.87	0.77	0.77	0.78	0.86	0.86	0.87	0.87	0.85	0.88	0.88	0.88
9.0	0.78	0.77	0.77	0.79	0.88	0.86	0.85	0.87	0.76	0.77	0.79	0.87	0.87	0.94	0.88	0.87	0.87	0.88	0.88
10.0	0.76	0.75	0.76	0.78	0.89	0.83	0.84	0.87	0.77	0.78	0.80	0.86	0.86	0.89	0.88	0.88	0.89	0.89	0.89
11.0	0.77	0.78	0.80	0.83	0.88	0.82	0.83	0.84	0.76	0.79	0.82	0.85	0.85	0.88	0.87	0.91	0.91	0.91	0.91
12.0	0.82	0.83	0.84	0.86	0.87	0.79	0.81	0.82	0.75	0.80	0.82	0.85	0.85	0.86	0.87	0.90	0.91	0.94	0.94
13.0	0.72	0.80	0.86	0.89	0.89	0.72	0.74	0.78	0.70	0.75	0.79	0.92	0.93	0.92	0.93	0.94	0.95	0.96	0.96
14.0	0.54	0.60	0.70	0.77	0.88	0.68	0.69	0.73	0.65	0.69	0.72	0.85	0.92	0.92	0.93	0.93	0.97	0.94	0.96
ϵ_{TN}	0.79	0.82	0.83	0.85	0.89	0.87	0.88	0.91	0.83	0.84	0.87	0.84	0.86	0.87	0.88	0.86	0.88	0.87	0.88

*Value shown in Table is average for three specimens

Table B-2. Near Normal Spectral Reflectance (at 298K) of Statically Oxidized Inconel 617 from 0.3 to 2.2μm.

WAVELENGTH (μm)	AS OXIDIZED*	AFTER RADIANT HEATING TESTS					AFTER ARC PLASMA TEST									8 HOURS @ LaRC	
		NUMBER OF RADIANT CYCLES					8 CYCLE			20 CYCLE			38 CYCLE			HIGH ENTHALPY	LOW ENTHALPY
		0	10	20	50	100	A	B	C	A	B	C	A	B	C		
0.3	0.128	0.130	0.128	0.137	0.130	0.122	0.118	0.047	0.048	0.128	0.027	0.040	0.187	0.045	0.060	0.477	0.032
0.4	0.119	0.130	0.117	0.122	0.120	0.119	0.112	0.090	0.077	0.122	0.070	0.075	0.155	0.087	0.091	0.056	0.043
0.5	0.119	0.130	0.114	0.121	0.119	0.117	0.116	0.130	0.105	0.120	0.130	0.175	0.150	0.109	0.123	0.158	0.062
0.6	0.118	0.127	0.108	0.115	0.111	0.113	0.112	0.117	0.089	0.119	0.098	0.112	0.150	0.108	0.108	0.235	0.135
0.65	0.113	0.129	0.112	0.116	0.113	0.114	0.113	0.122	0.095	0.120	0.100	0.117	0.150	0.110	0.110	0.300	0.148
0.7	0.121	0.130	0.117	0.120	0.118	0.116	0.115	0.145	0.115	0.123	0.113	0.135	0.150	0.122	0.140	0.298	0.149
0.8	0.133	0.132	0.120	0.129	0.127	0.122	0.127	0.220	0.162	0.130	0.177	0.217	0.162	0.160	0.170	0.350	0.210
0.9	0.135	0.130	0.118	0.127	0.125	0.121	0.130	0.217	0.157	0.123	0.170	0.200	0.169	0.163	0.160	0.397	0.205
1.0	0.141	0.130	0.119	0.129	0.131	0.128	0.137	0.207	0.103	0.130	0.167	0.186	0.175	0.163	0.158	0.448	0.205
1.1	0.144	0.131	0.120	0.130	0.135	0.130	0.140	0.192	0.150	0.132	0.153	0.170	0.176	0.160	0.155	0.423	0.196
1.2	0.142	0.131	0.120	0.130	0.135	0.130	0.140	0.170	0.140	0.132	0.135	0.150	0.177	0.155	0.148	0.383	0.180
1.3	0.140	0.131	0.119	0.128	0.132	0.130	0.137	0.145	0.126	0.130	0.112	0.126	0.178	0.142	0.135	0.340	0.160
1.4	0.140	0.132	0.120	0.129	0.132	0.130	0.136	0.136	0.121	0.131	0.108	0.115	0.180	0.140	0.134	0.331	0.146
1.5	0.139	0.131	0.120	0.128	0.130	0.129	0.136	0.128	0.115	0.130	0.100	0.102	0.180	0.140	0.132	0.325	0.130
1.6	0.140	0.132	0.121	0.128	0.130	0.129	0.133	0.124	0.112	0.130	0.100	0.097	0.182	0.140	0.132	0.340	0.125
1.7	0.145	0.137	0.127	0.130	0.131	0.131	0.140	0.132	0.120	0.130	0.107	0.096	0.187	0.154	0.148	0.360	0.130
1.8	0.150	0.138	0.129	0.132	0.136	0.133	0.148	0.140	0.127	0.132	0.116	0.098	0.192	0.162	0.155	0.373	0.145
1.9	--	0.140	0.131	0.136	0.138	0.135	--	0.142	--	0.130	0.120	--	--	0.167	--	0.373	0.150
2.0	--	0.138	0.130	0.132	0.136	0.133	--	0.137	--	0.128	0.115	--	--	0.164	--	0.354	0.142
2.1	--	0.140	0.132	0.137	0.138	0.137	--	0.134	--	0.130	0.116	--	--	0.167	--	0.347	0.138
2.2	--	0.144	0.138	0.139	0.140	0.140	--	0.135	--	0.130	0.120	--	--	0.169	--	0.345	0.134

*Average of 8 specimens before testing. Note: A = before test, B = after test, C = after HTEA test

BEST DOCUMENT AVAILABLE

BEST DOCUMENT AVAILABLE

Table B-3. Near Normal Spectral Reflectance (at 294K) of Statically Oxidized Inconel 617 from 2.0 to 25μm

WAVELENGTH (μm)	STATICALLY OXIDIZED	AFTER ARC PLASMA EXPOSURE			8 Hours @ LaRC		AFTER RADIANT HEATING TESTS			
		8 CYCLE	20 CYCLE	38 CYCLE	High ΔH	Low ΔH	10 CYCLE	20 CYCLE	50 CYCLE	100 CYCLE
2.0	0.140	0.148	0.192	0.175	0.390	0.159	0.145	0.141	0.146	0.146
2.5	0.143	0.144	0.197	0.171	0.323	0.133	0.153	0.143	0.149	0.152
3.0	0.147	0.148	0.199	0.173	0.270	0.121	0.157	0.152	0.151	0.156
3.5	0.149	0.149	0.199	0.169	0.234	0.117	0.160	0.155	0.151	0.153
4.0	0.160	0.160	0.216	0.179	0.201	0.115	0.167	0.162	0.156	0.162
4.5	0.181	0.177	0.235	0.196	0.178	0.115	0.174	0.169	0.162	0.168
5.0	0.183	0.177	0.236	0.194	0.162	0.115	0.178	0.174	0.165	0.169
5.5	0.180	0.189	0.246	0.205	0.155	0.118	0.188	0.183	0.173	0.177
6.0	0.181	0.194	0.246	0.212	0.144	0.117	0.187	0.184	0.173	0.178
6.5	0.216	0.198	0.246	0.229	0.150	0.125	0.199	0.196	0.183	0.186
7.0	0.238	0.205	0.252	0.256	0.136	0.117	0.194	0.195	0.182	0.186
7.5	0.251	0.207	0.253	0.272	0.136	0.119	0.191	0.194	0.179	0.183
8.0	0.237	0.205	0.250	0.283	0.121	0.104	0.180	0.181	0.170	0.172
8.5	0.210	0.194	0.238	0.284	0.095	0.078	0.167	0.165	0.158	0.159
9.0	0.180	0.191	0.232	0.293	0.076	0.063	0.162	0.155	0.155	0.150
9.5	0.156	0.200	0.240	0.306	0.080	0.075	0.165	0.156	0.156	0.148
10.0	0.133	0.219	0.259	0.313	0.091	0.097	0.175	0.163	0.151	0.143
10.5	0.113	0.230	0.271	0.313	0.086	0.097	0.192	0.176	0.142	0.142
11.0	0.118	0.245	0.288	0.314	0.069	0.095	0.215	0.203	0.141	0.141
11.5	0.116	0.254	0.312	0.312	0.026	0.090	0.238	0.234	0.155	0.136
12.0	0.108	0.250	0.340	0.304	0.037	0.089	0.232	0.235	0.175	0.1[illegible]
12.5	0.121	0.254	0.376	0.320	0.072	0.106	0.202	0.205	0.188	0.121
13.0	0.220	0.291	0.413	0.365	0.098	0.142	0.173	0.172	0.159	0.097
13.5	0.383	0.315	0.436	0.366	0.058	0.169	0.260	0.237	0.249	0.179
14.0	0.522	0.288	0.403	0.383	0.032	0.150	0.346	0.335	0.404	0.380
14.5	0.525	0.260	0.382	0.364	0.040	0.135	0.335	0.343	0.416	0.411
15.0	0.539	0.254	0.372	0.357	0.046	0.120	0.369	0.368	0.446	0.427
15.5	0.660	0.260	0.372	0.374	0.054	0.116	0.452	0.436	0.516	0.475
16.0	0.600	0.273	0.380	0.398	0.060	0.123	0.505	0.485	0.539	0.497
16.5	0.420	0.190	0.338	0.287	0.064	0.096	0.331	0.337	0.382	0.341
17.0	0.618	0.234	0.393	0.343	0.080	0.077	0.424	0.421	0.489	0.412
17.5	0.702	0.314	0.440	0.447	0.092	0.090	0.560	0.549	0.584	0.525
18.0	0.677	0.363	0.463	0.498	0.090	0.113	0.620	0.610	0.615	0.571
18.5	0.583	0.342	0.435	0.466	0.079	0.118	0.566	0.565	0.556	0.524
19.0	0.507	0.287	0.369	0.397	0.068	0.100	0.473	0.477	0.473	0.445
19.5	0.485	0.311	0.365	0.404	0.118	0.124	0.440	0.449	0.450	0.423
20.0	0.448	0.296	0.329	0.393	0.121	0.117	0.419	0.423	0.425	0.400
20.5	0.424	0.298	0.320	0.402	0.121	0.127	0.451	0.458	0.446	0.419
21.0	0.375	0.270	0.309	0.367	0.092	0.111	0.406	0.419	0.409	0.395
21.5	0.365	0.282	0.312	0.352	0.096	0.109	0.367	0.376	0.367	0.356
22.0	0.355	0.250	0.303	0.296	0.089	0.099	0.345	0.355	0.338	0.317
22.5	0.390	0.228	0.326	0.272	0.108	0.107	0.360	0.375	0.370	0.325
23.0	0.372	0.235	0.300	0.266	0.107	0.097	0.349	0.366	0.355	0.312
23.5	0.360	0.205	0.305	0.221	0.128	0.100	0.333	0.353	0.344	0.276
24.0	0.368	0.160	0.325	0.180	0.125	0.080	0.295	0.320	0.346	0.258
24.5	0.436				0.140	0.082	0.377	0.406	0.426	0.335
25.0	0.365				0.185	0.122	0.327	0.342	0.353	0.310

Table B-4. Near Normal Spectral Reflectance (at 294K) from 0.3 to 2.2μm of Bare and Statically Oxidized Inconel 617 in HTEA Environment

WAVELENGTH (μm)	BARE METAL*		1367K IN ATM OF				1255K
	C	H	263 Pa Air	2630 Pa Air	Vacuum	263 Pa Argon	263 Pa Dried Argon
0.3	0.229	0.202	0.166	0.182	0.212	0.194	0.130
0.4	0.308	0.315	0.143	0.155	0.233	0.158	0.130
0.5	0.350	0.380	0.138	0.147	0.240	0.151	0.130
0.6	0.370	0.420	0.133	0.144	0.242	0.147	0.127
0.65	0.380	0.435	0.134	0.145	0.244	0.147	0.129
0.7	0.383	0.448	0.139	0.147	0.244	0.148	0.130
0.8	0.393	0.475	0.162	0.163	0.260	0.160	0.132
0.9	0.400	0.495	0.160	0.160	0.260	0.157	0.130
1.0	0.410	0.513	0.160	0.160	0.265	0.158	0.130
1.1	0.418	0.537	0.159	0.159	0.276	0.159	0.131
1.2	0.427	0.558	0.157	0.157	0.285	0.158	0.131
1.3	0.433	0.572	0.152	0.155	0.290	0.155	0.131
1.4	0.440	0.595	0.153	0.155	0.299	0.155	0.132
1.5	0.440	0.600	0.150	0.152	0.299	0.152	0.131
1.6	0.448	0.613	0.150	0.153	0.303	0.152	0.132
1.7	0.453	0.626	0.151	0.157	0.307	0.152	0.137
1.8	0.459	0.630	0.157	0.159	0.310	0.157	0.138
1.9							0.140
2.0							0.138
2.1							0.140
2.2							0.144

*C = Cabot, H = Huntington

BEST DOCUMENT AVAILABLE

Table B-5 Near Normal Spectral Reflectance (at 294K) from 2.0 to 25μm of Bare and Statically Oxidized Inconel 617 in HTEA Environment

WAVELENGTH (μm)	BARE METAL*		1367K IN ATM OF				1255K 263 Pa Dried Argon
	C	H	263 Pa Air	2630 Pa Air	vac	263 Pa Argon	
2.0	0.482	0.680	0.171	0.170	0.331	0.169	0.152
2.5	0.517	0.703	0.171	0.171	0.346	0.169	0.158
3.0	0.543	0.721	0.170	0.169	0.358	0.167	0.161
3.5	0.575	0.742	0.169	0.168	0.370	0.165	0.165
4.0	0.617	0.766	0.171	0.171	0.383	0.168	0.172
4.5	0.650	0.783	0.175	0.177	0.397	0.172	0.179
5.0	0.676	0.799	0.178	0.182	0.405	0.176	0.183
5.5	0.698	0.809	0.133	0.196	0.417	0.189	0.191
6.0	0.714	0.817	0.180	0.205	0.426	0.194	0.189
6.5			0.192	0.210	0.441	0.199	0.203
7.0	0.746	0.834	0.193	0.192	0.452	0.198	0.200
7.5			0.194	0.201	0.466	0.204	0.206
8.0	0.774	0.846	0.179	0.203	0.474	0.191	0.206
8.5			0.153	0.192	0.480	0.169	0.207
9.0	0.791	0.855	0.143	0.167	0.487	0.151	0.218
9.5			0.144	0.148	0.496	0.143	0.233
10.0	0.805	0.862	0.145	0.131	0.501	0.146	0.247
10.5			0.143	0.133	0.508	0.156	0.256
11.0	0.827	0.872	0.148	0.145	0.512	0.160	0.255
11.5			0.146	0.146	0.504	0.151	0.239
12.0	0.832	0.878	0.144	0.140	0.483	0.135	0.213
12.5			0.156	0.152	0.473	0.144	0.230
13.0	0.830	.883	0.188	0.170	0.474	0.182	0.324
13.5			0.292	0.266	0.496	0.312	0.385
14.0	0.838	.887	0.457	0.434	0.511	0.496	0.451
14.5			0.484	0.461	0.531	0.519	0.423

*C = Cabot, H = Huntington

Table B-5 Continued

WAVELENGTH (um)	BARE METAL* C	H	1367K IN ATM OF 263 Pa Air	2030 Pa Air	vac	263 Pa Argon	1255K 263 Pa Dried Argon
15.0			0.528	0.502	0.565	0.566	0.462
15.5			0.587	0.562	0.600	0.621	0.550
16.0	0.855	.894	0.561	0.540	0.620	0.569	0.563
16.5			0.380	0.391	0.573	0.413	0.386
17.0			0.566	0.544	0.602	0.586	0.525
17.5			0.621	0.609	0.641	0.634	0.652
18.0	0.857	.899	0.613	0.606	0.658	0.620	0.672
18.5			0.535	0.539	0.655	0.545	0.592
19.0			0.457	0.478	0.616	0.479	0.501
19.5			0.431	0.465	0.605	0.458	0.476
20.0	0.879	.906	0.414	0.448	0.585	0.441	0.457
20.5			0.424	0.456	0.576	0.456	0.474
21.0			0.401	0.451	0.561	0.447	0.431
21.5			0.375	0.451	0.556	0.448	0.396
22.0	0.883	.910	0.348	0.415	0.540	0.412	0.330
22.5			0.376	0.444	0.524	0.454	0.346
23.0			0.349	0.419	0.520	0.434	0.317
23.5			0.321	0.374	0.510	0.408	0.270
24.0	0.815	.903	0.318	0.367	0.473	0.458	0.300
24.5			0.338	0.393	0.497	0.522	0.395
25.0			0.266	0.298	0.490	0.469	0.355

*C = Cabot, H = Huntington

Table B-6. Spectral and Total Normal Emittance of Statically Oxidized HS188

	STATICALLY OXIDIZED				AFTER ARC PLASMA TESTS								
					8 CYCLE			20 CYCLE			38 CYCLE		
TEMPERATURE (K)	543	816	1088	1256	816	1090	1252	812	1088	1259	814	1094	1252
WAVELENGTH (μm)													
1.0	-	0.63	0.81	0.82	0.89	0.98	0.95	0.90	0.91	0.96	0.81	0.84	0.89
1.5	0.70	0.78	0.85	0.86	0.94	0.95	0.97	0.96	0.96	0.95	0.94	0.92	0.95
2.0	0.78	0.80	0.85	0.85	0.85	0.87	0.91	0.93	0.94	0.87	0.91	0.89	0.91
3.0	0.72	0.77	0.82	0.83	0.78	0.79	0.85	0.85	0.88	0.82	0.88	0.87	0.90
4.0	0.65	0.69	0.78	0.81	0.75	0.77	0.82	0.82	0.88	0.81	0.84	0.86	0.90
5.0	0.62	0.66	0.75	0.77	0.67	0.68	0.74	0.72	0.74	0.69	0.81	0.80	0.84
6.0	0.60	0.64	0.74	0.74	0.63	0.64	0.70	0.61	0.64	0.61	0.77	0.72	0.81
7.0	0.46	0.50	0.60	0.61	0.59	0.60	0.65	0.56	0.60	0.58	0.73	0.74	0.77
8.0	0.41	0.45	0.53	0.56	0.57	0.57	0.62	0.57	0.62	0.60	0.69	0.69	0.73
9.0	0.44	0.47	0.57	0.62	0.61	0.62	0.67	0.66	0.71	0.67	0.69	0.68	0.73
10.0	0.46	0.51	0.64	0.69	0.60	0.63	0.68	0.66	0.75	0.69	0.63	0.65	0.69
11.0	0.54	0.62	0.75	0.79	0.62	0.65	0.70	0.65	0.73	0.66	0.61	0.62	0.67
12.0	0.64	0.73	0.85	0.89	0.57	0.62	0.68	0.54	0.65	0.59	0.62	0.64	0.69
13.0	0.57	0.74	0.92	0.93	0.47	0.53	0.58	0.43	0.54	0.46	0.53	0.56	0.59
14.0	0.52	0.65	0.90	0.90	0.41	0.46	0.51	0.36	0.43	0.37	0.49	0.53	0.57
ε_{TN}	0.57	0.68	0.77	0.81	0.68	0.75	0.79	0.74	0.82	0.81	0.79	0.82	0.83

Table B-7. Spectral and Total Normal Emittance of Statically Oxidized HS188 After Radiant Heating Tests

WAVELENGTH (μm)	10 CYCLE			20 CYCLE			50 CYCLE			100 CYCLE		
	#7*	#8	#9	#10	#11	#12	#13	#14	#15	#16	#17	#18
1.0	0.91	0.91	0.89	0.86	0.89	0.88	0.88	0.87	0.89	0.90	0.92	0.93
1.5	0.91	0.92	0.90	0.90	0.90	0.89	0.89	0.91	0.91	0.94	0.96	0.95
2.0	0.87	0.88	0.86	0.86	0.86	0.85	1.04	0.88	0.88	0.93	0.93	0.74
3.0	0.82	0.83	0.82	0.82	0.78	0.81	0.83	0.84	0.84	0.89	0.01	0.90
4.0	0.76	0.77	0.79	0.77	0.78	0.77	0.79	0.81	0.82	0.86	0.89	0.87
5.0	0.76	0.74	0.73	0.73	0.72	0.72	0.74	0.76	0.77	0.81	0.83	0.84
6.0	0.72	0.69	0.73	0.70	0.70	0.70	0.70	0.73	0.73	0.79	0.81	0.81
7.0	0.58	0.63	0.62	0.60	0.65	0.62	0.66	0.68	0.69	0.74	0.77	0.77
8.0	0.53	0.59	0.55	0.56	0.62	0.55	0.60	0.69	0.65	0.71	0.72	0.74
9.0	0.57	0.59	0.56	0.58	0.64	0.58	0.59	0.67	0.63	0.68	0.70	0.75
10.0	0.64	0.60	0.61	0.62	0.64	0.61	0.61	0.64	0.62	0.67	0.68	0.72
11.0	0.74	0.68	0.72	0.69	0.68	0.68	0.66	0.66	0.66	0.69	0.72	0.72
12.0	0.79	0.77	0.80	0.78	0.78	0.76	0.76	0.75	0.75	0.79	0.77	0.77
13.0	0.76	0.77	0.78	0.63	0.81	0.75	0.76	0.82	0.79	0.81	0.84	0.84
14.0	0.61	0.70	0.73	0.74	0.80	0.68	0.70	0.83	0.78	0.82	0.84	0.86
ε_{TN}	0.78	0.79	0.78	0.78	0.78	0.77	0.79	0.80	0.81	0.85	0 97	0.87

*Denotes Sample Number

Table B-8. Near Normal Spectral Reflectance (at 294K) of Statically Oxidized HS188 from 0.3 to 2.2μm

WAVELENGTH (μm)	8 CYCLE			20 CYCLE			38 CYCLE		
	STATIC OXIDATION	AFTER ARC PLASMA	AFTER HTEA	STATIC OXIDATION	AFTER ARC PLASMA	AFTER HTEA	STATIC OXIDATION	AFTER ARC PLASMA	AFTER HTEA
0.3	0.160	0.050	0.058	0.140	0.030	0.052	0.132	0.035	0.045
0.4	0.147	0.076	0.107	0.130	0.037	0.097	0.129	0.040	0.095
0.5	0.142	0.082	0.118	0.128	0.039	0.113	0.130	0.042	0.145
0.6	0.140	0.076	0.087	0.128	0.040	0.086	0.130	0.043	0.160
0.65	0.140	0.080	0.090	0.129	0.039	0.088	0.132	0.043	0.175
0.7	0.140	0.090	0.130	0.130	0.038	0.110	0.135	0.043	0.200
0.8	0.144	0.112	0.138	0.136	0.038	0.124	0.142	0.048	0.244
0.9	0.136	0.118	0.128	0.133	0.039	0.122	0.139	0.057	0.213
1.0	0.140	0.120	0.122	0.138	0.040	0.127	0.142	0.060	0.181
1.1	0.143	0.120	0.120	0.143	0.042	0.130	0.148	0.060	0.167
1.2	0.140	0.117	0.117	0.138	0.039	0.125	0.146	0.052	0.148
1.3	0.134	0.104	0.110	0.130	0.034	0.110	0.137	0.047	0.123
1.4	0.133	0.104	0.110	0.132	0.034	0.110	0.137	0.043	0.117
1.5	0.133	0.106	0.110	0.135	0.034	0.111	0.140	0.043	0.110
1.6	0.135	0.110	0.111	0.137	0.037	0.113	0.141	0.046	0.103
1.7	0.144	0.130	0.130	0.150	0.045	0.148	0.152	0.050	0.117
1.8	0.162	0.147	0.137	0.176	0.059	0.170	0.172	0.056	0.122
1.9		0.160		0.196	0.072	0.178		0.062	0.121
2.0		0.162		0.206	0.079	0.178		0.062	0.119
2.1		0.170		0.219	0.087	0.183		0.067	0.119
2.2		0.180		0.230	0.095	0.190		0.073	0.120

BEST DOCUMENT AVAILABLE

Table B-9. Near Normal Spectral Reflectance (at 294K) of Statically Oxidized HS188 Before and After Arc Plasma Tests

WAVELENGTH (μm)	STATIC OXIDATION	AFTER ARC PLASMA AND HTEA TESTS		
		8 CYCLE	20 CYCLE	38 CYCLE
2.0	0.208	0.156	0.111	0.104
2.5	0.236	0.190	0.140	0.136
3.0	0.258	0.206	0.172	0.171
3.5	0.275	0.222	0.185	0.201
4.0	0.317	0.278	0.206	0.253
4.5	0.350	0.333	0.255	0.305
5.0	0.350	0.366	0.305	0.344
5.5	0.350	0.389	0.352	0.380
6.0	0.373	0.396	0.381	0.403
6.5	0.429	0.407	0.400	0.426
7.0	0.482	0.419	0.411	0.451
7.5	0.532	0.431	0.410	0.474
8.0	0.548	0.432	0.407	0.485
8.5	0.537	0.415	0.375	0.471
9.0	0.512	0.398	0.345	0.457
9.5	0.509	0.407	0.342	0.466
10.0	0.513	0.449	0.400	0.515
10.5	0.500	0.464	0.428	0.540
11.0	0.481	0.482	0.459	0.551
11.5	0.405	0.484	0.502	0.537
12.0	0.391	0.477	0.536	0.525
12.5	0.417	0.511	0.576	0.542
13.0	0.498	0.565	0.626	0.589
13.5	0.423	0.497	0.566	0.602
14.0	0.503	0.412	0.580	0.584
14.5	0.534	0.335	0.565	0.545
15.0	0.555	0.273	0.485	0.478
15.5	0.579	0.230	0.405	0.408
16.0	0.556	0.218	0.422	0.407
16.5	0.417	0.166	0.299	0.393
17.0	0.451	0.220	0.412	0.445
17.5	0.583	0.277	0.508	0.461
18.0	0.629	0.302	0.502	0.455
18.5	0.597	0.270	0.461	0.438
19.0	0.573	0.226	0.371	0.429
19.5	0.525	0.232	0.298	0.452
20.0	0.518	0.184	0.347	0.442
20.5	0.524	0.200	0.388	0.441
21.0	0.437	0.201	0.255	0.458
21.5	0.383	0.203	0.192	0.497
22.0	0.360	0.190	0.185	0.509
22.5	0.400	0.195	0.214	0.526
23.0	0.339	0.203	0.208	0.532
23.5	0.336	0.258	0.298	0.545
24.0	0.403	0.253	0.347	0.545
24.5	0.468	-	-	-
25.0	0.407	0.275	0.346	0.545

Table B-10. Near Normal Spectral Reflectance (at 294K) of Statically Oxidized HS188 from 0.3 to 2.2μm After Radiant and HTEA Testing

WAVELENGTH (μm)	AFTER RADIANT TESTING 10 CYCLES #7 *	20 CYCLES #10	50 CYCLES #13	100 CYCLES #16	CYCLES #19	AFTER HTEA TEST 10 CYCLES #7	20 CYCLES #10	50 CYCLES #13	100 CYCLES #16
0.3	0.157	0.162	0.157	0.088	0.077	0.140	0.155	0.149	0.089
0.4	0.147	0.158	0.150	0.077	0.069	0.123	0.140	0.134	0.020
0.5	0.137	0.148	0.142	0.071	0.066	0.120	0.131	0.123	0.076
0.6	0.135	0.144	0.138	0.071	0.066	0.120	0.130	0.120	0.075
0.65	0.137	0.146	0.139	0.073	0.067	0.122	0.130	0.121	0.076
0.7	0.138	0.148	0.140	0.074	0.070	0.126	0.132	0.123	0.078
0.8	0.143	0.152	0.147	0.080	0.076	0.157	0.154	0.147	0.096
0.9	0.144	0.150	0.144	0.085	0.083	0.163	0.160	0.150	0.107
1.0	0.155	0.159	0.150	0.100	0.098	0.172	0.168	0.158	0.118
1.1	0.161	0.162	0.158	0.105	0.109	0.178	0.171	0.162	0.122
1.2	0.160	0.160	0.155	0.095	0.099	0.178	0.170	0.160	0.114
1.3	0.150	0.153	0.147	0.080	0.078	0.170	0.162	0.152	0.092
1.4	0.151	0.155	0.148	0.078	0.074	0.172	0.164	0.153	0.089
1.5	0.152	0.155	0.149	0.078	0.074	0.173	0.165	0.153	0.088
1.6	0.158	0.160	0.151	0.079	0.075	0.177	0.170	0.157	0.088
1.7	0.165	0.169	0.160	0.087	0.084	0.190	0.183	0.171	0.100
1.8	0.188	0.188	0.180	0.116	0.118	0.210	0.200	0.189	0.135
1.9	0.210	0.208	0.200	0.140	0.142	0.221	0.212	0.200	0.152
2.0	0.216	0.210	0.202	0.143	0.143	0.221	0.212	0.200	0.153
2.1	0.227	0.220	0.213	0.150	0.150	0.230	0.220	0.208	0.160
2.2	0.237	0.228	0.220	0.158	0.158	0.238	0.230	0.217	0.167

*Denotes Sample Number

TABLE B-11. Near Normal Spectral Reflectance (at 294K) of Statically Oxidized HS188 after Radiant Heating and HTEA Tests

WAVELENGTH (μm)	AFTER RADIANT HEATING AND HTEA TESTS			
	10 CYCLE #7	20 CYCLE #10	50 CYCLE #13	100 CYCLE #16
2.0	0.230	0.222	0.209	0.168
2.5	0.249	0.241	0.227	0.184
3.0	0.263	0.256	0.239	0.199
3.5	0.275	0.267	0.251	0.212
4.0	0.314	0.292	0.268	0.223
4.5	0.335	0.327	0.291	0.244
5.0	0.333	0.347	0.318	0.260
5.5	0.342	0.357	0.341	0.279
6.0	0.375	0.375	0.357	0.297
6.5	0.432	0.413	0.385	0.324
7.0	0.483	0.452	0.406	0.342
7.5	0.525	0.490	0.437	0.362
8.0	0.535	0.505	0.456	0.371
8.5	0.518	0.492	0.452	0.369
9.0	0.489	0.466	0.444	0.373
9.5	0.470	0.470	0.450	0.379
10.0	0.467	0.487	0.476	0.416
10.5	0.458	0.488	0.485	0.438
11.0	0.455	0.482	0.484	0.450
11.5	0.452	0.414	0.432	0.449
12.0	0.462	0.400	0.407	0.436
12.5	0.515	0.432	0.425	0.446
13.0	0.608	0.518	0.514	0.508
13.5	0.590	0.498	0.498	0.490
14.0	0.615	0.517	0.514	0.517
14.5	0.595	0.510	0.499	0.465
15.0	0.618	0.538	0.524	0.443
15.5	0.666	0.594	0.574	0.457
16.0	0.600	0.574	0.548	0.430
16.5	0.446	0.431	0.399	0.301
17.0	0.566	0.509	0.491	0.248
17.5	0.709	0.630	0.629	0.452
18.0	0.715	0.667	0.662	0.565
18.5	0.628	0.615	0.603	0.518
19.0	0.571	0.585	0.577	0.479
19.5	0.518	0.548	0.569	0.510
20.0	0.486	0.530	0.556	0.539
20.5	0.477	0.543	0.567	0.566
21.0	0.401	0.461	0.497	0.538
21.5	0.328	0.378	0.410	0.501
22.0	0.290	0.340	0.351	0.430
22.5	0.340	0.395	0.406	0.422
23.0	0.280	0.342	0.340	0.404
23.5	0.297	0.365	0.338	0.324
24.0	0.396	0.457	0.420	0.250
24.5	0.460	0.514	0.492	0.346
25.0	0.387	0.424	0.415	0.380

BEST DOCUMENT AVAILABLE

Table B-12. Near Normal Spectral Reflectance (at 294K) of HS188 Bare Metal and Statically Oxidized After HTEA Testing

WAVELENGTH (μm)	BARE METAL	1367 K IN ATM OF			
		263 Pa AIR	2630 Pa AIR	263 Pa ARGON	VACUUM
0.3	0.338	0.110	0.112	0.100	0.236
0.4	0.433	0.098	0.105	0.092	0.262
0.5	0.468	0.090	0.097	0.083	0.272
0.6	0.486	0.088	0.095	0.081	0.270
0.65	0.492	0.089	0.096	0.082	0.280
0.7	0.503	0.092	0.096	0.084	0.288
0.8	0.525	0.102	0.100	0.100	0.300
0.9	0.544	0.103	0.103	0.107	0.302
1.0	0.565	0.110	0.110	0.115	0.308
1.1	0.589	0.114	0.117	0.121	0.317
1.2	0.611	0.108	0.108	0.115	0.320
1.3	0.630	0.090	0.095	0.098	0.322
1.4	0.650	0.091	0.092	0.090	0.330
1.5	0.660	0.092	0.092	0.099	0.330
1.6	0.676	0.095	0.093	0.100	0.337
1.7	0.688	0.110	0.103	0.118	0.348
1.8	0.698	0.133	0.130	0.147	0.355

BEST DOCUMENT AVAILABLE

Table B-13. Near Normal Spectral Reflectance (at 294K) of Statically Oxidized HS188 Before and After HTEA Testing

WAVELENGTH (μm)	STATICALLY OXIDIZED	STATICALLY OXIDIZED AFTER HTEA TESTS			
		263 Pa Air	2630 Pa Air	Vacuum	263 Pa Argon
2.0	0.207	0.175	0.170	0.560	0.188
2.5	0.242	0.200	0.196	0.580	0.213
3.0	0.270	0.225	0.222	0.592	0.237
3.5	0.314	0.251	0.247	0.616	0.261
4.0	0.350	0.280	0.275	0.633	0.287
4.5	0.339	0.307	0.301	0.652	0.310
5.0	0.345	0.340	0.324	0.673	0.338
5.5	0.395	0.371	0.344	0.690	0.362
6.0	0.473	0.395	0.358	0.700	0.377
6.5	0.545	0.416	0.386	0.713	0.400
7.0	0.588	0.430	0.404	0.719	0.413
7.5	0.609	0.453	0.428	0.723	0.443
8.0	0.604	0.478	0.436	0.720	0.458
8.5	0.576	0.485	0.434	0.715	0.465
9.0	0.535	0.498	0.434	0.703	0.469
9.5	0.510	0.502	0.432	0.701	0.471
10.0	0.503	0.532	0.468	0.709	0.495
10.5	0.482	0.541	0.473	0.717	0.497
11.0	0.488	0.540	0.479	0.722	0.494
11.5	0.491	0.547	0.496	0.728	0.503
12.0	0.509	0.540	0.495	0.741	0.502
12.5	0.555	0.550	0.513	0.758	0.524
13.0	0.635	0.591	0.553	0.779	0.587
13.5	0.575	0.500	0.498	0.774	0.513
14.0	0.650	0.577	0.537	0.758	0.587
14.5	0.663	0.535	0.514	0.766	0.565
15.0	0.664	0.464	0.466	0.778	0.525
15.5	0.667	0.447	0.457	0.796	0.523
16.0	0.619	0.475	0.482	0.797	0.529
16.5	0.356	0.302	0.327	0.721	0.327
17.0	0.475	0.236	0.193	0.754	0.271
17.5	0.681	0.437	0.428	0.790	0.541
18.0	0.682	0.569	0.546	0.811	0.618
18.5	0.623	0.529	0.514	0.783	0.553
19.0	0.517	0.532	0.493	0.748	0.525
19.5	0.487	0.580	0.542	0.738	0.568
20.0	0.526	0.624	0.602	0.727	0.618
20.5	0.503	0.633	0.617	0.722	0.633
21.0	0.396	0.598	0.583	0.712	0.593
21.5	0.343	0.556	0.544	0.701	0.542
22.0	0.306	0.465	0.474	0.689	0.450
22.5	0.322	0.475	0.460	0.683	0.447
23.0	0.258	0.442	0.434	0.682	0.412
23.5	0.250	0.348	0.355	0.694	0.322
24.0	0.305	0.272	0.256	0.695	0.243
24.5	0.365	0.353	0.324	0.693	0.344
25.0	0.340	0.420	0.392	0.678	0.395

BEST DOCUMENT AVAILABLE

Table B-14. Spectral and Total Normal Emittance of R512E Coated Cb752

	AS COATED, 0 EXPOSURE CYCLES						AFTER ARC PLASMA TESTS						AFTER RADIANT HEATING TESTS					
	#2		#3		#4		8 CYCLES #10		20 CYCLES #7		38 CYCLES #8		10 CYCLES #11		20 CYCLES #13		50 CYCLES #7	
TEMPERATURE (K)	1256	1590	1256	1590	1256	1590	1256	1590	1256	1590	1256	1590	1256	1590	1256	1590	1256	1590
WAVELENGTH(μm)																		
1.0	0.74	0.66	0.80	0.65	0.76	0.70	0.72	0.64	0.81	0.66	0.71	0.62	0.80	0.61	0.87	0.66	0.87	0.66
1.5	0.76	0.72	0.79	0.72	0.77	0.74	0.78	0.75	0.85	0.73	0.75	0.72	0.80	0.67	0.87	0.76	0.90	0.77
2	0.77	0.73	0.77	0.73	0.78	0.76	0.80	0.79	0.85	0.75	0.77	0.76	0.77	0.71	0.83	0.78	0.88	0.80
3	0.78	0.76	0.79	0.79	0.79	0.77	0.84	0.85	0.86	0.79	0.82	0.82	0.73	0.75	0.80	0.81	0.85	0.84
4	0.78	0.77	0.78	0.89	0.80	0.75	0.93	0.89	0.89	0.82	0.86	0.87	0.68	0.77	0.77	0.84	0.84	0.88
5	0.79	0.76	0.80	0.32	0.79	0.77	0.88	0.89	0.88	0.80	0.87	0.86	0.73	0.78	0.76	0.83	0.84	0.88
6	0.80	0.78	0.83	0.84	0.79	0.81	0.90	0.91	0.89	0.83	0.91	0.89	0.75	0.80	0.75	0.83	0.86	0.89
7	0.80	0.78	0.82	0.87	0.80	0.85	0.91	0.93	0.88	0.84	0.92	0.92	0.78	0.82	0.79	0.85	0.87	0.90
8	0.93	0.91	0.92	0.95	0.93	0.92	0.97	0.95	0.96	0.94	0.96	0.95	0.91	0.92	0.91	0.93	0.85	0.95
9	0.92	0.92	0.90	0.93	0.93	0.88	0.95	0.92	0.92	0.89	0.92	0.88	0.88	0.90	0.92	0.94	9.93	0.94
10	0.93	0.91	0.90	0.91	0.92	0.91	0.93	0.95	0.89	0.85	0.92	0.91	0.90	0.93	0.92	0.95	0.94	0.96
11	0.92	0.91	0.90	0.91	0.91	0.86	0.92	0.69	0.89	0.89	0.94	0.94	0.89	0.89	0.92	0.93	0.94	0.95
12	0.92	0.89	0.89	0.89	0.90	0.87	0.89	0.94	0.87	0.88	0.91	0.94	0.85	0.87	0.92	0.93	0.95	0.94
13	0.89	0.89	0.88	0.90	0.89	0.82	0.89	0.95	0.83	0.89	0.92	0.95	0.85	0.86	0.90	0.90	0.95	0.94
14	0.89	0.89	0.87	0.89	0.90	0.79	0.89	0.91	0.84	0.90	0.91	0.95	0.83	0.84	0.87	0.89	0.92	0.95
ϵ_{TN}	0.81	0.80	0.81	0.83	0.79	0.81	0.82	0.87	0.86	0.83	0.80	0.84	0.75	0.81	0.79	0.86	0.85	0.87

Table B-15. Near Normal Spectral Reflectance (0.3 to 2.2μm at 294K) of R512E Coated Cb752 before and after Arc Plasma and HTEA Tests

	BEFORE ARC PLASMA TESTS				AFTER ARC PLASMA TESTS				AFTER ARC PLASMA AND HTEA* TEST		
					8 CYCLE	10 CYCLE	20 CYCLE	38 CYCLE			
WAVELENGTH(μm)	#7	#8	#9	#10	#10	#9	#7	#8	#7	#8	#10
0.3	0.102	0.095	0.105	0.120	0.067	0.060	0.090	0.080	0.102	0.049	0.058
0.4	0.120	0.110	0.125	0.135	0.148	0.200	0.102	0.145	0.132	0.056	0.056
0.5	0.140	0.137	0.163	0.170	0.224	0.293	0.102	0.213	0.143	0.082	0.055
0.6	0.155	0.148	0.184	0.190	0.260	0.317	0.101	0.232	0.140	0.082	0.055
0.65	0.170	0.163	0.205	0.210	0.285	0.323	0.101	0.245	0.140	0.082	0.055
0.7	0.175	0.170	0.210	0.217	0.238	0.328	0.101	0.248	0.142	0.083	0.056
0.8	0.220	0.215	0.255	0.277	0.313	0.332	0.094	0.280	0.170	0.107	0.065
0.9	0.245	0.240	0.288	0.303	0.303	0.310	0.095	0.298	0.173	0.127	0.070
1.0	0.262	0.254	0.306	0.320	0.300	0.293	0.102	0.314	0.187	0.150	0.080
1.1	0.277	0.266	0.320	0.334	0.293	0.278	0.108	0.325	0.200	0.182	0.093
1.2	0.238	0.272	0.327	0.342	0.283	0.261	0.110	0.330	0.215	0.220	0.112
1.3	0.293	0.275	0.328	0.345	0.270	0.245	0.112	0.330	0.223	0.257	0.133
1.4	0.297	0.277	0.325	0.347	0.260	0.230	0.116	0.330	0.232	0.298	0.160
1.5	0.288	0.269	0.310	0.337	0.244	0.214	0.114	0.317	0.235	0.318	0.180
1.6	0.284	0.266	0.308	0.331	0.236	0.202	0.115	0.310	0.240	0.340	0.203
1.7	0.230	0.262	0.300	0.325	0.225	0.192	0.117	0.300	0.242	0.355	0.227
1.8	0.272	0.255	0.290	0.317	0.215	0.182	0.115	0.288	0.243	0.363	0.243
1.9	0.265	0.250	0.289	0.305	0.207	0.172	0.117	0.278	0.247	0.372	0.257
2.0	0.257	0.241	0.278	0.293	0.193	0.160	0.114	0.266	0.244	0.373	0.270
2.1	0.257	0.240	0.278	0.297	0.190	0.158	0.118	0.260	0.252	0.380	0.287
2.2	0.258	0.241	0.230	0.299	0.193	0.158	0.122	0.258	0.260	0.395	0.300

*263 Pa Air

B-16. Near Normal Spectral Reflectance (0.3 to 2.2μm at 294K) of R512E Coated Cb752 Before and After Radiant Heating and HTEA Tests

	AS COATED AND OXIDIZED			AFTER HTEA TESTS (263 Pa Air)			AFTER RADIANT HEATING AND HTEA TESTS		
							10 CYCLES	20 CYCLES	50 CYCLES
WAVELENGTH(μm)	#1	#2	#3	#1	#2	#3	#11	#13	#7
0.3	0.098	0.114	0.090	0.083	0.083	0.170	0.100	0.108	0.095
0.4	0.155	0.135	0.097	0.120	0.115	0.150	0.100	0.094	0.080
0.5	0.240	0.150	0.132	0.170	0.160	0.140	0.135	0.090	0.080
0.6	0.275	0.167	0.160	0.185	0.170	0.137	0.133	0.092	0.081
0.65	0.292	0.185	0.190	0.192	0.172	0.137	0.131	0.098	0.085
0.7	0.295	0.192	0.200	0.197	0.173	0.137	0.130	0.100	0.089
0.8	0.317	0.240	0.293	0.230	0.200	0.140	0.150	0.130	0.105
0.9	0.337	0.270	0.345	0.233	0.212	0.134	0.160	0.148	0.118
1.0	0.339	0.287	0.383	0.242	0.224	0.139	0.177	0.167	0.130
1.1	0.340	0.300	0.415	0.251	0.235	0.143	0.198	0.190	0.144
1.2	0.338	0.313	0.440	0.257	0.248	0.151	0.222	0.219	0.162
1.3	0.333	0.320	0.457	0.260	0.256	0.160	0.242	0.243	0.184
1.4	0.333	0.321	0.464	0.260	0.260	0.172	0.264	0.265	0.207
1.5	0.323	0.321	0.455	0.255	0.258	0.179	0.277	0.276	0.221
1.6	0.322	0.322	0.452	0.254	0.257	0.187	0.292	0.290	0.240
1.7	0.320	0.322	0.448	0.253	0.254	0.192	0.305	0.302	0.258
1.8	0.318	0.320	0.440	0.251	0.252	0.195	0.311	0.310	0.271
1.9	0.310	0.315	0.425	0.249	0.250	0.200	0.317	0.317	0.286
2.0	0.312	0.313	0.410	0.247	0.243	0.198	0.318	0.317	0.293
2.1	0.317	0.319	0.413	0.250	0.249	0.200	0.326	0.328	0.311
2.2	0.322	0.330	0.420	0.253	0.250	0.205	0.338	0.338	0.325

BEST DOCUMENT AVAILABLE

Table B-17 Near Normal Reflectance (from 2.0 to 25μm at 294K)
for R512E Coated Cb752

WAVELENGTH (μm)	AFTER ARC PLASMA AND HTEA* TESTS			AFTER RADIANT HEATING AND HTEA* TESTS			AFTER HTEA 263 Pa Argon	AFTER HTEA 263 Pa Air
	8 CYCLE #10	20 CYCLE #7	38 CYCLE #8	10 CYCLE #11	20 CYCLE #13	50 CYCLE #7		
2.0	0.310	0.274	0.361	0.345	0.341	0.311	0.250	0.271
2.5	0.344	0.287	0.378	0.362	0.360	0.347	0.274	0.284
3.0	0.348	0.289	0.374	0.359	0.360	0.338	0.292	0.290
3.5	0.356	0.295	0.380	0.366	0.364	0.350	0.307	0.304
4.0	0.366	0.309	0.390	0.375	0.375	0.357	0.325	0.323
4.5	0.370	0.318	0.390	0.385	0.386	0.359	0.341	0.340
5.0	0.277	0.291	0.292	0.336	0.346	0.308	0.355	0.304
5.5	0.285	0.290	0.292	0.356	0.365	0.318	0.370	0.323
6.0	0.256	0.300	0.276	0.350	0.357	0.280	0.382	0.323
6.5	0.283	0.320	0.292	0.381	0.388	0.308	0.398	0.358
7.0	0.253	0.321	0.260	0.365	0.375	0.280	0.407	0.352
7.5	0.221	0.298	0.223	0.345	0.353	0.242	0.416	0.329
8.0	0.151	0.110	0.155	0.145	0.159	0.100	0.399	0.142
8.5	0.120	0.104	0.148	0.099	0.076	0.077	0.411	0.141
9.0	0.139	0.162	0.192	0.146	0.090	0.105	0.432	0.195
9.5	0.080	0.165	0.113	0.117	0.096	0.083	0.445	0.126
10.0	0.077	0.146	0.101	0.132	0.147	0.108	0.450	0.120
10.5	0.068	0.131	0.093	0.121	0.140	0.116	0.459	0.107
11.0	0.065	0.112	0.088	0.132	0.114	0.115	0.465	0.131
11.5	0.064	0.121	0.083	0.141	0.101	0.100	0.469	0.145
12.0	0.070	0.135	0.082	0.149	0.090	0.062	0.470	0.155
12.5	0.080	0.138	0.086	0.171	0.100	0.044	0.485	0.167
13.0	0.093	0.130	0.096	0.167	0.118	0.056	0.496	0.167
13.5	0.107	0.134	0.102	0.170	0.143	0.072	0.507	0.176
14.0	0.115	0.145	0.109	0.178	0.164	0.085	0.518	0.189
14.5	0.124	0.157	0.117	0.186	0.183	0.100	0.532	0.203
15.0	0.129	0.151	0.121	0.184	0.191	0.111	0.539	0.207
15.5	0.130	0.159	0.125	0.173	0.186	0.113	0.545	0.198
16.0	0.134	0.177	0.136	0.163	0.182	0.114	0.546	0.187
16.5	0.127	0.203	0.127	0.152	0.174	0.110	0.548	0.183
17.0	0.131	0.232	0.128	0.158	0.169	0.107	0.550	0.184
17.5	0.134	0.261	0.134	0.174	0.174	0.113	0.551	0.184
18.0	0.141	0.278	0.143	0.182	0.182	0.124	0.552	0.184
18.5	0.163	0.290	0.176	0.209	0.205	0.163	0.556	0.195
19.0	0.183	0.286	0.211	0.269	0.244	0.182	0.560	0.223
19.5	0.226	0.311	0.254	0.351	0.312	0.222	0.574	0.289
20.0	0.233	0.311	0.267	0.379	0.334	0.226	0.588	0.316
20.5	0.230	0.331	0.264	0.361	0.339	0.235	0.602	0.327
21.0	0.218	0.344	0.253	0.332	0.324	0.230	0.607	0.318
21.5	0.199	0.349	0.229	0.300	0.313	0.218	0.607	0.303
22.0	0.179	0.330	0.202	0.268	0.283	0.197	0.598	0.272
22.5	0.187	0.321	0.205	0.270	0.283	0.210	0.597	0.267
23.0	0.170	0.300	0.193	0.251	0.265	0.195	0.585	0.248
23.5	0.185	0.298	0.203	0.253	0.267	0.208	0.580	0.249
24.0	0.175	0.273	0.194	0.263	0.277	0.221	0.575	0.231
24.5	0.172	0.270	0.192	0.256	0.270	0.220	0.575	0.220
25.0	0.235	0.292	0.255	0.308	0.315	0.275	0.580	0.262

* 263 Pa air

BEST DOCUMENT AVAILABLE

1. Report No.	2. Government Accession No.	3. Recipient's Catalog No.
NASA CR- 3740		

4. Title and Subtitle	5. Report Date
RADIATIVE PROPERTIES OF ADVANCED SPACECRAFT HEAT SHIELD MATERIALS	November 1983
	6. Performing Organization Code

7. Author(s)	8. Performing Organization Report No.
G. R. Cunnington, A. I. Funai, and T. K. McNab	
	10. Work Unit No.

9. Performing Organization Name and Address	11. Contract or Grant No.
Lockheed Palo Alto Research Laboratories Lockheed Missiles and Space Company, Inc. Palo Alto, CA 94304	NAS1-16423
	13. Type of Report and Period Covered
12. Sponsoring Agency Name and Address National Aeronautics and Space Administration Washington, D. C. 20546	Contractor Report
	14. Sponsoring Agency Code

15. Supplementary Notes

NASA Langley Project Manager: Ronald K. Clark
Final Report

16. Abstract Experimental results are presented to show the effects of simulated reentry exposure by convective heating and by radiant heating on spectral and total emittance of statically oxidized Inconel 617 and Haynes HS188 superalloys to 1260 K and a silicide coated (R512E) columbium 752 alloy to 1590 K. Convective heating exposures were conducted in a supersonic arc plasma wind tunnel using a wedge-shaped specimen configuration. Radiant tests were conducted at a pressure of 3×10^{-3} atomospheres of dry air at a flow velocity of several meters per second. Convective heating specimens were subjected to 8, 20, and 38 15-min heating cycles, and radiant heating specimens were tested for 10, 20, 50, and 100 30-min heating cycles. Changes in radiative properties are explained in terms of changes in composition resulting from simulated reentry tests.

The methods used to evaluate morphological, compositional and crystallographic changes include: Auger Electron Spectroscopy (AES); Scanning Electron Microscopy (SEM); X-Ray Diffraction Analysis (XRDA); and Electron Microprobe (EP) analysis. Total normal emittance of oxidized Inconel 617 and HS188 did not significantly change from the statically oxidized conditions after either exposure. Total normal emittance of both materials remained above 0.80 at 1260 K. Significant spectral changes were observed at wavelengths less than 2.0 μm and greater than 15 μm, but these had no significant influence on total emittance at 1260 K. The changes in radiative properties were qualitatively correlated to compositional changes observed after the exposure cycles.

17. Key Words (Suggested by Author(s))	18. Distribution Statement
Radiative Properties Superalloys Heat Shield Materials Thermal Protection Oxidation Emittance	Unclassified-Unlimited Subject Category 26

19. Security Classif. (of this report)	20. Security Classif. (of this page)	21. No. of Pages	22. Price
Unclassified	Unclassified	198	A09

N-305 For sale by the National Technical Information Service, Springfield, Virginia 22161 NASA-Langley, 1983

END

1-11-84